Informatics Control Measurement
in Economy and Environment Protection

4/2021

Informatyka Automatyka Pomiary

www.e-IAPGOS.pl

w gospodarce i ochronie środowiska

ISSN 2083-0157

Kwartalnik Naukowo-Techniczny

fot. arch. TNTU

Ternopil Ivan Puluj National Technical University (Ternopil, Ukraine)

4/2021

październik – grudzień

Wydanie pod redakcją naukową
prof. dr hab. inż. Waldemara Wójcika

INFORMATYKA AUTOMATYKA POMIARY W GOSPODARCE i OCHRONIE ŚRODOWISKA

Informatics Control Measurement in Economy and Environment Protection

p-ISSN 2083-0157, e-ISSN 2391-6761, www.e-iapgos.pl

EDITOR STAFF
ZESPÓŁ REDAKCYJNY

EDITORIAL OFFICE
REDAKCJA

Redakcja czasopisma Informatyka, Automatyka, Pomiary w Gospodarce i Ochronie Środowiska
Katedra Elektroniki i Technik Informacyjnych
Politechnika Lubelska
ul. Nadbystrzycka 38A, 20-618 Lublin
tel. +48 81 53 84 309,
fax: +48 81 53 84 312
iapgos@pollub.pl
www.e-iapgos.pl
iapgos.pollub.pl
ph.pollub.pl/index.php/iapgos

PUBLISHER
WYDAWCA

Politechnika Lubelska
ul. Nadbystrzycka 38D
20-618 Lublin
tel. +48 81 53 84 100
www.pollub.pl
ph.pollub.pl

EDITORIAL BOARD
KOMITET REDAKCYJNY

INTERNATIONAL PROGRAMME COMMITTEE
RADA PROGRAMOWO-NAUKOWA

PRINTING HOUSE – DRUKARNIA

Soft Vision Mariusz Rajski
https://www.printone.pl

nakład: 100 egzemplarzy

OTHER INFORMATION – INNE INFORMACJE

Czasopismo jest indeksowane w bazach:

DOAJ	doaj.org
BazTech	baztech.icm.edu.pl
IC Journals Master List	www.journals.indexcopernicus.com
Google Scholar	scholar.google.pl
POL-index	pbn.nauka.gov.pl
Sherpa RoMEO	www.sherpa.ac.uk
OAJI	oaji.net

Czasopismo *Informatyka, Automatyka, Pomiary w Gospodarce i Ochronie Środowiska* zostało objęte finansowaniem przez Ministerstwo Nauki i Szkolnictwa Wyższego w ramach programu *Wsparcie dla czasopism naukowych* w latach 2019-2020.

Czasopismo znajduje się w wykazie czasopism naukowych opublikowanym w Komunikacie Ministra Edukacji i Nauki z dnia 1 grudnia 2021 r., Unikatowy Identyfikator Czasopisma: 200167 – z przypisaną liczbą punktów przyznawanych za publikację artykułu równą 20.

Zasady publikowania artykułów, przygotowania tekstów, zasady etyczne, procedura recenzowania, wykazy recenzentów oraz pełne teksty artykułów dostępne są na stronie internetowej czasopisma:

www.e-iapgos.pl

W celu zwiększenia oddziaływania czasopisma w środowisku naukowym redakcja zaleca:

- w artykułach publikowanych w IAPGOS cytować artykuły z renomowanych czasopism międzynarodowych (szczególnie indeksowanych w bazach Web of Science oraz Scopus) używając oficjalnych skrótów nazw czasopism,
- w artykułach publikowanych w innych czasopismach (zwłaszcza indeksowanych w bazach Web of Science oraz Scopus) cytować prace publikowane w IAPGOS – zwłaszcza posługując się numerami DOI, np.:
  Kluszczyński K. *Modelowanie – umiejętność czy sztuka?* Informatyka, Automatyka, Pomiary w Gospodarce i Ochronie Środowiska – IAPGOS, 1/2016, 4–15, https://doi.org/10.5604/20830157.1193833.

CONTENTS – SPIS TREŚCI

http://doi.org/10.35784/iapgos.2836

SINGULAR INTEGRATION IN BOUNDARY ELEMENT METHOD FOR HELMHOLTZ EQUATION FORMULATED IN FREQUENCY DOMAIN

Tomasz Rymarczyk[1,2], **Jan Sikora**[1,2]

[1]Research & Development Centre Netrix S.A., Lublin, Poland, [2]University of Economics and Innovation in Lublin, Faculty of Transport and Informatics, Lublin, Poland

Abstract. *Two ways of approximation of the BEM kernel singularity are presented in this paper. Based on these approximations extensive error analysis was carried on. As a criterion the preciseness and simplicity of approximation were selected. Simplicity because such approach would be applied for the tomography problems, so time of execution plays particularly significant role. One of the approximations which could be applied for the wide range of the arguments of the kernel were selected.*

Keywords: partial differential equations, numerical analysis, function approximation, integral equations

CAŁKI OSOBLIWE W METODZIE ELEMENTÓW BRZEGOWYCH DLA RÓWNANIA HELMHOLTZA SFORMUŁOWANEGO W PRZESTRZENI CZĘSTOTLIWOŚCI

Streszczenie. *Dwie metody aproksymacji osobliwości funkcji Greena zaproponowano w tej pracy. Bazując na tych aproksymacjach dokonano wnikliwej analizy błędów. Jako kryterium wybrano dokładność i prostotę zaproponowanych aproksymacji. Prostotę dlatego, że takie podejście będzie proponowane w zagadnieniach tomograficznych. Tak więc czas odgrywa zasadniczą rolę. Wybrano aproksymację, która może być stosowana dla szerokiego zakresu argumentów.*

Słowa kluczowe: równania różniczkowe cząstkowe, analiza numeryczna, aproksymacja funkcji, równania całkowe

Introduction

Singular integrals are an especially important question for the Boundary Element Method. Only for the Laplace's equation and for the basic boundary elements of the zero order, such an integral could be calculated analytically (see for example [11]). But the second order boundary element demands a special treatment [11]. Many technical problems described by Helmholtz equation [5, 7] demands integration of difficult functions like for example the Green function. Then, particularly useful is the procedure of approximation. In this paper some difficulties associated with this procedure will be presented. Unfortunately, there is no one single universal approximation for the Green function. Below, following [1, 6] we will show a simple approximation which could be useful for Helmholtz integral formulation in a frequency domain. As simple as possible because the approximation function should be easily integrable. But the kind of approximation depend on the value of the Green function arguments as it will be presented in this paper.

1. Treatment of singularity

For the small arguments $|x| \to 0$ the modified Bessel function (see for example Diffuse Optical Tomography (DOT) [2]) becomes, asymptotically simple power of their arguments [1]:
for n = 0:

$$K_0(x) \cong -\ln(x) = \ln\frac{1}{x} \tag{1}$$

and for n > 0:

$$K_n(x) \cong \frac{(n-1)!}{2}\left(\frac{x}{2}\right)^{-n} \tag{2}$$

So, for the first order we will get:

$$K_1(x) \cong \frac{(1-1)!}{2}\left(\frac{x}{2}\right)^{-1} = \frac{1}{x} \tag{3}$$

Modified Bessel functions and their approximation for the small arguments are shown in Fig. 1.

As we can see in the next figure – Fig. 2 the approximation of the modified Bessel function of the second kind and first order is much better than for the same function but zero order. So, the small parameter in the case of the Helmholtz equation (DOT problems for example) mean that the arguments should not exceed value of 0.1.

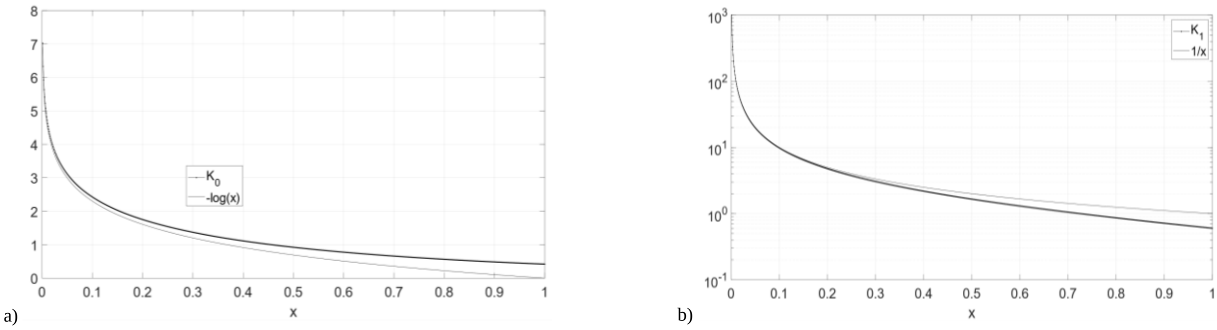

Fig. 1. Comparison for the small arguments between the modified Bessel function of the second kind and their approximation for a) zero order and b) first order (in semi-logarithmic scale)

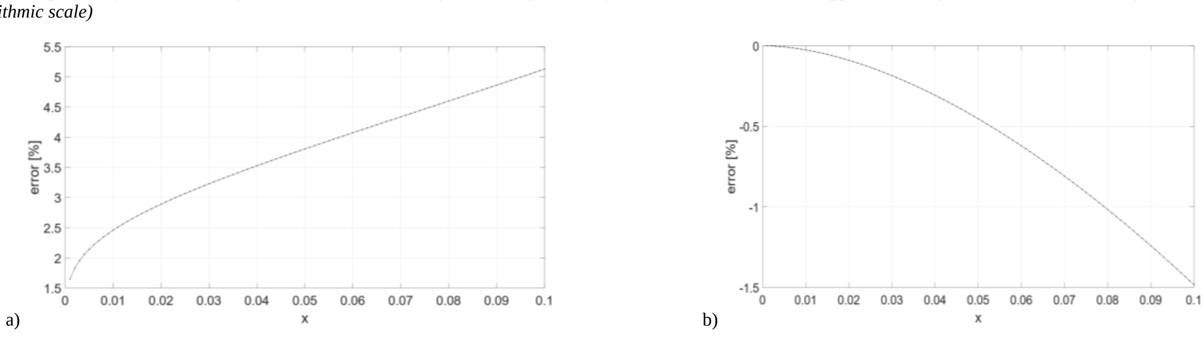

Fig. 2. Relative error of approximation for the small arguments for the modified Bessel function of the second kind a) zero order and b) first order

If the arguments become higher than more sophisticated approximations are required. Exists plenty of excellent approximations, for example in [1, 6, 12]. Following the [1] we have selected simple but effective approximation:

$$\widetilde{K}_0(x) = -\left\{\ln\left(\frac{1}{2}x\right) + \gamma\right\} I_0(x) + \frac{\frac{1}{4}x^2}{(1!)^2} + \left(1 + \frac{1}{2}\right)\frac{\left(\frac{1}{4}x^2\right)^2}{(2!)^2} + \left(1 + \frac{1}{2} + \frac{1}{3}\right)\frac{\left(\frac{1}{4}x^2\right)^3}{(3!)^2} + \cdots \quad (4)$$

where: $\widetilde{K}_0$ and $\tilde{I}_0$ stands for approximation, γ is the Euler-Mascheroni constant [12].

The approximation of the function $\tilde{I}_0$ is the modified Bessel function of the first kind and zero order which could be approximated by [1]:

$$\tilde{I}_0(x) = 1 + \frac{\frac{1}{4}x^2}{(1!)^2} + \frac{\left(\frac{1}{4}x^2\right)^2}{(2!)^2} + \frac{\left(\frac{1}{4}x^2\right)^3}{(3!)^2} + \ldots \quad (5)$$

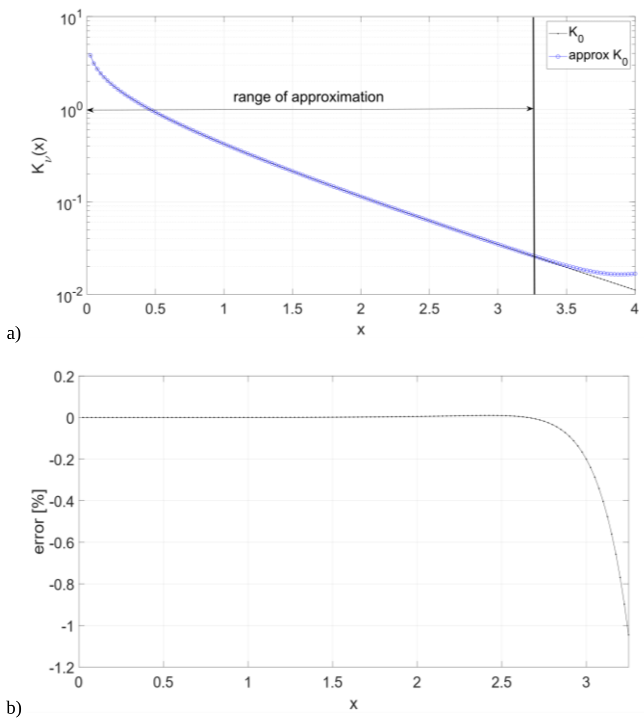

Fig. 3. a) approximation of the modified Bessel function of the second kind and zero order for the arguments less than 4 in a semilogarithmic scale and b) relative error of such approximation

The approximation proposed by Eq. (4) and (5) extend the range of arguments significantly and the approximation error does not exceed low value for example 0.3% as it is shown in Fig. 3b.

2. Governing equations

As an example of the problem leading to the Hemholtz equation let us consider the light transport in biological tissue [2].

The governing equation describing the light transport is a Boltzman equation approximated by diffusion equation (see for example [2]). For harmonic excitation it could be formulated in a frequency domain:

$$\nabla^2\varphi(\boldsymbol{r},\omega) - k^2\varphi(\boldsymbol{r},\omega) = q \quad (6)$$

where $k = \sqrt{\frac{\mu_a}{D} - i\frac{\omega}{cD}}$ [mm] – is the wave number, c speed of light, ω angular frequency, $D = \frac{1}{2(\mu_s' + \mu_a)}$ [mm] for 2D space, μ_s', μ_a the optical parameters of the tissue and $q = \frac{q_s}{D}$ right hand side of Eq. (6) containing source of light.

On the external boundary the Robin boundary conditions are imposed:

$$\varphi(\boldsymbol{r},\omega) + 2Dn \cdot \nabla\varphi(\boldsymbol{r},\omega) = 0 \qquad \forall\, \boldsymbol{r} \in \boldsymbol{\Gamma} \quad (7)$$

After discretization for the Boundary Element Method, one must deal with a couple of unknowns in one node – $\varphi(\boldsymbol{r},\omega)$ and $\frac{\partial\varphi(\boldsymbol{r},\omega)}{\partial n}$, so it is convenient to present the boundary conditions in the following form:

$$\frac{\partial\varphi(\boldsymbol{r},\omega)}{\partial n} = -\frac{1}{2D}\,\varphi(\boldsymbol{r},\omega) \qquad \forall\, \boldsymbol{r} \in \boldsymbol{\Gamma} \quad (8)$$

The fundamental solution for BEM of the problem described by Eq. (6) is given by the Green function of the form (consult [2,3,6]):

$$G(|\boldsymbol{r} - \boldsymbol{r}'|,\omega) = \frac{1}{2\pi} K_0(k|\boldsymbol{r} - \boldsymbol{r}'|,\omega) \quad (9)$$

where K_0 – is the modified Bessel function of the second kind of zero order.

Using the Green's second identity to arrive at a boundary integral equation:

$$c(\boldsymbol{r})\varphi(\boldsymbol{r},\omega) + \int_{\boldsymbol{\Gamma}} \frac{\partial G(|\boldsymbol{r} - \boldsymbol{r}'|,\omega)}{\partial n}\varphi(\boldsymbol{r}',\omega)d\boldsymbol{\Gamma} = \int_{\boldsymbol{\Gamma}} G(|\boldsymbol{r} - \boldsymbol{r}'|,\omega)\frac{\partial\varphi(\boldsymbol{r}',\omega)}{\partial n}d\boldsymbol{\Gamma} + - \int_{\boldsymbol{\Gamma}} G(|\boldsymbol{r_{is}} - \boldsymbol{r}'|,\omega)\, q\, d\Omega \quad (10)$$

where $\boldsymbol{r}$ and $\boldsymbol{r}' \in \boldsymbol{\Gamma}$, $\boldsymbol{r_{is}} \in \Omega$, and $G(|\boldsymbol{r_{is}} - \boldsymbol{r}'|,\omega)$ is the value of the fundamental solution at the point $\boldsymbol{r_{is}}$.

In optical tomography, concentrated light (point) sources are frequently used and modelled by Dirac delta function in a following way:

$$q = Q_{is}\delta_{is} \quad (11)$$

where Q_{is} is the magnitude of the light source and $\delta_{is}(|\boldsymbol{r_{is}} - \boldsymbol{r}'|,\omega)$ is the Dirac delta function which integral is equal to 1 at the point $\boldsymbol{r_{is}}$ and zero elsewhere.

Assuming that there are no light sources, the equation (10) could be written:

$$c(\boldsymbol{r})\varphi(\boldsymbol{r},\omega) + \int_{\boldsymbol{\Gamma}} \frac{\partial G(|\boldsymbol{r} - \boldsymbol{r}'|,\omega)}{\partial n}\varphi(\boldsymbol{r}',\omega)d\boldsymbol{\Gamma} = \int_{\boldsymbol{\Gamma}} G(|\boldsymbol{r} - \boldsymbol{r}'|,\omega)\frac{\partial\varphi(\boldsymbol{r}',\omega)}{\partial n}d\boldsymbol{\Gamma} \quad (12)$$

Now the boundary integral equation (12) for constant boundary elements can be written in terms of local coordinate ξ instead of the boundary line $\boldsymbol{\Gamma}$, as follows:

$$c(\boldsymbol{r})\varphi(\boldsymbol{r}) + \sum_{j=1}^{M}\varphi_j(\boldsymbol{r}')\int_{-\boldsymbol{1}}^{+1}\frac{\partial G(|\boldsymbol{r}-\boldsymbol{r}'|)}{\partial n}J(\xi)d\xi = \sum_{j=1}^{M}\frac{\partial\varphi_j(\boldsymbol{r}')}{\partial n}\int_{-1}^{+1}G(|\boldsymbol{r} - \boldsymbol{r}'|)J(\xi)d\xi \quad (13)$$

where M – is the total number of constant elements, and $J(\xi)$ – is the Jacobian of transformation:

$$J(\xi) = \frac{d\boldsymbol{\Gamma}}{d\xi} = \sqrt{\left(\frac{dx(\xi)}{d\xi}\right)^2 + \left(\frac{dy(\xi)}{d\xi}\right)^2} = \sqrt{\left(\frac{x_3 - x_1}{2}\right)^2 + \left(\frac{y_3 - y_1}{2}\right)^2} = \frac{1}{2}L \quad (14)$$

where x_3, y_3 and x_1, y_1 are the coordinates of the edge points of the zero-order boundary element and x_2, y_2 is a middle node when state function and its derivative is fixed, L is the length of element.

The functions under integral sign which contain the kernels can be substituted by the functions $A_{i,j}$ and $B_{i,j}$ as follows:

$$c(\boldsymbol{r})\varphi(\boldsymbol{r}) + \sum_{j=1}^{M}\varphi_j(\boldsymbol{r}')\,A_{i,j}(\boldsymbol{r},\boldsymbol{r}') = \sum_{j=1}^{M}\frac{\partial\varphi_j(\boldsymbol{r}')}{\partial n}B_{i,j}(\boldsymbol{r},\boldsymbol{r}') \quad (15)$$

To form a set of linear algebraic equations, we take each node in turn as a load point $\boldsymbol{r}$ and perform the integrations indicated in Eq. (13). This will result in the following system of algebraic equations:

$$[\boldsymbol{A}][\boldsymbol{\varphi}] = [\boldsymbol{B}]\left[\frac{\partial\boldsymbol{\varphi}}{\partial n}\right] \quad (16)$$

where the matrices $[\boldsymbol{A}]$ and $[\boldsymbol{B}]$ contain the integrals of the kernel's normal derivative $\frac{\partial G(|\boldsymbol{r}-\boldsymbol{r}'|)}{\partial n}$ and the kernels $G(|\boldsymbol{r} - \boldsymbol{r}'|)$ respectively, i.e. the functions $A_{i,j}$ and $B_{i,j}$ of Eq. (15).

It is apparent that the kernels in Eq. (12) may be written in more explicit form:

$$\frac{\partial G(|\boldsymbol{r}-\boldsymbol{r}'|,\omega)}{\partial n}=\frac{\partial}{\partial n}\left(\frac{1}{2\pi}K_0(k|\boldsymbol{r}-\boldsymbol{r}'|,\omega)\right)=$$
$$=-\frac{k}{2\pi}K_1(k|\boldsymbol{r}-\boldsymbol{r}'|,\omega)\frac{\partial R}{\partial n} \tag{17}$$

where K_1 is the modified Bessel function of the second kind of order one.

The derivative of the radius R with respect to the unit outward normal n at the point $\boldsymbol{r}'$ is calculated as follows:

$$\frac{\partial R}{\partial n}=\frac{\partial R}{\partial x}\frac{\partial x}{\partial n}+\frac{\partial R}{\partial y}\frac{\partial y}{\partial n}=\frac{\partial R}{\partial x}n_x+\frac{\partial R}{\partial y}n_y \tag{18}$$

where

$$\frac{\partial R}{\partial x}=\frac{x\prime-x}{R} \quad \text{and} \quad \frac{\partial R}{\partial y}=\frac{y\prime-y}{R}.$$

Now, the kernel from Eq. (13) can be rewritten more explicitly:

$$\frac{\partial G(|\boldsymbol{r}-\boldsymbol{r}'|,\omega)}{\partial n}=-\frac{k}{2\pi}K_1(k|\boldsymbol{r}-\boldsymbol{r}'|,\omega)\left(\frac{x\prime-x}{R}n_x+\frac{y\prime-y}{R}n_y\right) \tag{19}$$

When we put Eq. (17) into Eq. (13) than it can be solved numerically. However, the problem arises when the $\boldsymbol{r}'->\boldsymbol{r}$ than the singularity of the integrand must be specially treated.

3. Singular integration for constant element

The singular integrals are a particularly important problem for integral formulation for the partial differential equations [4]. For the Dirichlet problem and for the Diffuse Optical Tomography (DOT) it was already solved [6,10,11]. However, for DOT integrand singularity only in case a small argument of the kernel, where successfully solved. Then the function in Eq. (10) which is the Bessel function was approximated by a quite simple equation (see for example Eq. (1)).

For many other problems like for example the acoustic ones [7, 8] it is insufficient and more sophisticated approximation is necessary (see for example Eq. (4) and Eq. (5)). After some mathematical operations Eq. (4) could be presented in the following form [1]:

$$\widetilde{K}_0(x)=-\ln\left(\frac{1}{2}x\right)I_0(x)-\gamma+0.42278420*\left(\frac{x}{2}\right)^2+$$
$$+0.23069756*\left(\frac{x}{2}\right)^4+0.03488590*\left(\frac{x}{2}\right)^6+0.00262698*$$
$$*\left(\frac{x}{2}\right)^8+0.00010750*\left(\frac{x}{2}\right)^{10}+0.00000740*\left(\frac{x}{2}\right)^{12}+\epsilon \tag{20}$$

where $|\epsilon|<10^{-8}$.

The Bessel function of the first kind and zero order $I_0(x)$ appearing in the first term of Eq. (20) has the following shape and is completely covered by its approximation – Fig. 4.

In Fig. 4 it is clearly visible that function $I_0(x)$ it is not singular within the interesting us range of independent variable and its approximation is very precise (consult Fig. (4b)).

So, still we are facing the problem of integration of singular integrals because the first term of approximation is the logarithmic one. Some term of the kernel could be integrated in an analogous way as for the Laplace's equation, but the rest term of integrand could be calculated using the Gauss quadrature. For this case, the $A_{i,j}$ coefficients are equal zero and the $B_{i,j}$ integrals can be calculated analytically and numerically as well. The distance between point $\boldsymbol{r}$ and point $\boldsymbol{r}'(\xi)$ depends on local coordinate system in a following way: $R(\xi)=|\boldsymbol{r}-\boldsymbol{r}'(\xi)|$.

The entries of the matrices in Eq. (13) are:

$$B_{i,j}(\boldsymbol{r},\boldsymbol{r}')=\int_{-1}^{+1}G(|\boldsymbol{r}-\boldsymbol{r}'|)J(\xi)d\xi=$$
$$=\int_{-1}^{+1}\widetilde{K}_0\big(k\,R(\xi)\big)\,J(\xi)d\xi \tag{21}$$

where $\boldsymbol{r}$ depends on index i and $\boldsymbol{r}'$ depends on index j and $J(\xi)=\frac{L}{2}$ is a Jacobian of transformation defined by Eq. (14), so:

$$B_{i,j}\big(k\,R(\xi)\big)=\int_{-1}^{+1}\widetilde{K}_0\big(k\,R(\xi)\big)\,J(\xi)d\xi=$$
$$=\frac{L}{2}\int_{-1}^{+1}\Bigg[-\ln\left(\frac{1}{2}k\,R(\xi)\right)I_0\big(k\,R(\xi)\big)-\gamma+$$
$$+0.42278420*\left(\frac{k\,R(\xi)}{2}\right)^2+0.23069756*\left(\frac{k\,R(\xi)}{2}\right)^4+$$
$$+0.03488590*\left(\frac{k\,R(\xi)}{2}\right)^6+0.00262698*\left(\frac{k\,R(\xi)}{2}\right)^8+$$
$$+0.00010750*\left(\frac{k\,R(\xi)}{2}\right)^{10}+0.00000740*\left(\frac{k\,R(\xi)}{2}\right)^{12}\Bigg]d\xi \tag{22}$$

To simplify consideration let us divide the integrand on two parts. The first one consists of the logarithmic term and the second one consists of the rest of the Eq. (20) as follows:

$$B_{i,i}\big(k\,R(\xi)\big)=\frac{L}{2}\int_{-1}^{+1}\left[-\ln\left(\frac{1}{2}k\,R(\xi)\right)I_0\big(k\,R(\xi)\big)-\gamma\right]d\xi=$$
$$=\frac{L}{2}\int_{-1}^{+1}\Bigg[0.42278420*\left(\frac{k\,R(\xi)}{2}\right)^2+$$
$$+0.23069756*\left(\frac{k\,R(\xi)}{2}\right)^4+0.03488590*\left(\frac{k\,R(\xi)}{2}\right)^6+$$
$$+0.00262698*\left(\frac{k\,R(\xi)}{2}\right)^8+0.00010750*\left(\frac{k\,R(\xi)}{2}\right)^{10}+$$
$$+0.00000740*\left(\frac{k\,R(\xi)}{2}\right)^{12}\Bigg]d\xi \tag{23}$$

The integral of the first part is the logarithmic type so we could calculate it analytically in the similar (integration by parts must be involved) way as for the Laplace's equation but for more complex cases a special logarithmically weighted numerical integration formula can be used [11]. Note that the limits of integration are from 0 to 1 instead of the –1 to +1 range used in the non–singular integrals of Boundary Integral Equations (BIE).

The remained part is not singular so it could be calculated numerically by the standard Gaussian rule.

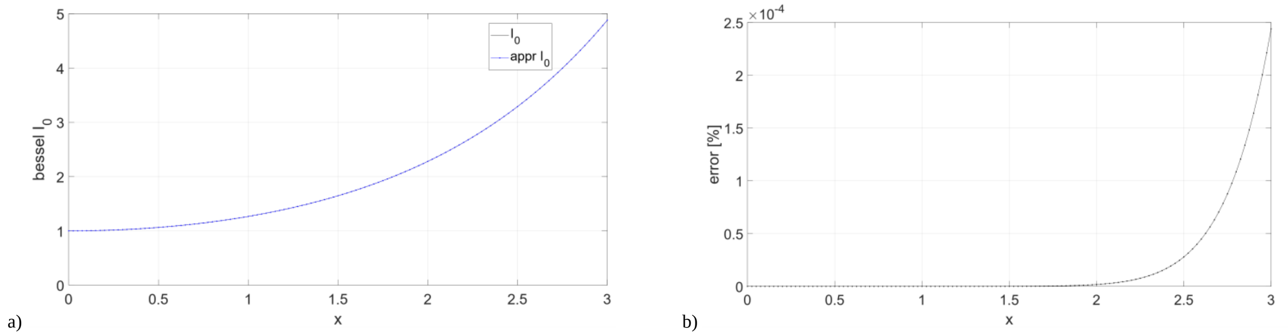

Fig. 4. a) The modified Bessel function of the first kind of zero order for the small arguments and b) relative error of approximation (see Eq. (5))

4. Benchmark solution

To solve the Helmholtz equation in the frequency domain, let us consider the excellent benchmark problem suggested by P. Jablonski in his monograph [6].

Inside the domain which is the interior of a rectangle of the width a and the height b as it is denoted in Fig. 5. On the boundary the following Neumann boundary conditions are imposed:

$$\frac{\partial\varphi}{\partial n} = \begin{cases} 0 & \text{when } y = 0, \\ 100 & \text{when } x = a, \\ 0 & \text{when } y = b, \\ 0 & \text{when } x = 0. \end{cases} \tag{24}$$

The analytical solution of the state function φ (see Eq. (6) and boundary conditions Eq. (7) and Eq. (24)) is equal to:

$$\varphi(\boldsymbol{r}(x,y)) = \frac{100}{k}\frac{cosh(2k)}{sinh(ak)} \tag{25}$$

where k is the wavelength, a=4 is the length of the rectangular area (Fig. 5).

Solutions of the problem (6) with the boundary conditions (7) for different wavelength are presented in the Fig. 6 and in the Fig. 7.

The bigger wave number the more rapid state function diminishing along the x axis direction.

Interesting is the error distribution of the state function along the boundary. In Fig. 9 it can be observed as the error rapidly erase on two corners where the Neumann boundary conditions were imposed. But only up to the value of 1.17%. It is quite satisfactory especially that no special treatment of the sharp corners was applied.

As the exact analytical solution exists it is possible to control exactness of the numerical solution within the internal points of the region.

In Fig. 9 for different wave numbers relative error was calculated for the point in the centre of the region. Coordinates of this point were: (a/2, b/2). The error was calculated for two cases:

1) for the logarithmic approximation of the kernel,
2) for the approximation by the series suggested in [1].

The second case is much more precise for the Helmholtz equation than the simple logarithmic approximation as it is visible in the Fig. 9.

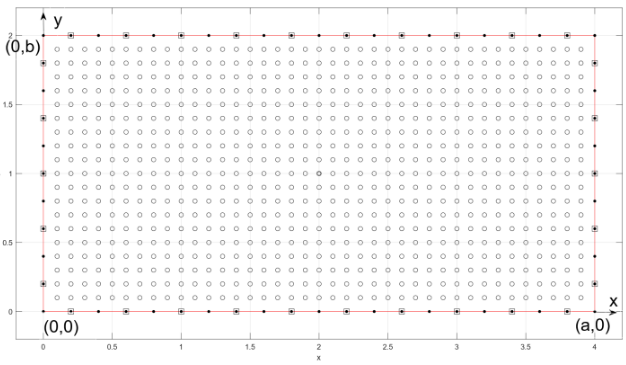

Fig. 5. Discretization of the region of interest with the internal points where the state function is calculated

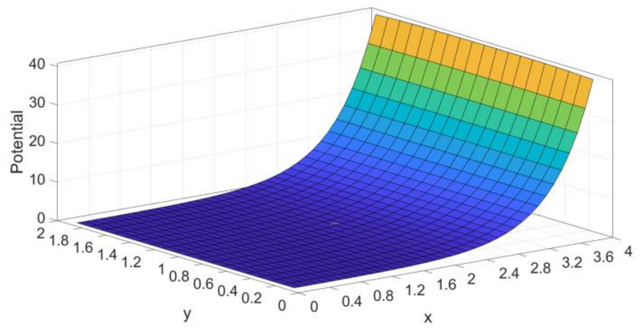

Fig. 6. Numerical solution for $k = \sqrt{4}$

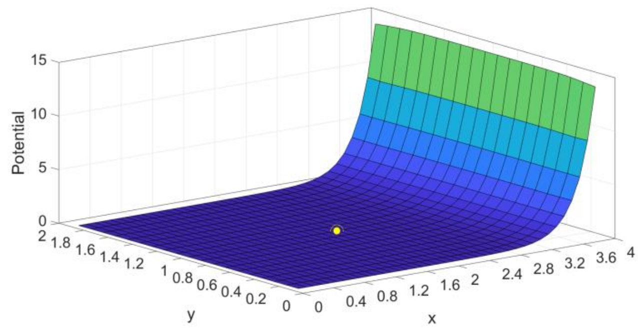

Fig. 7. Numerical solution for $k = \sqrt{20}$

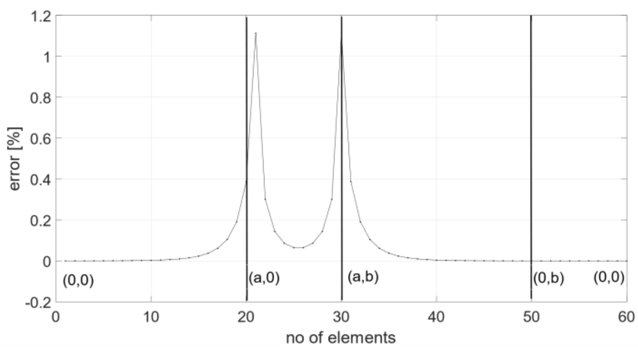

Fig. 8. Relative error distribution along the boundary

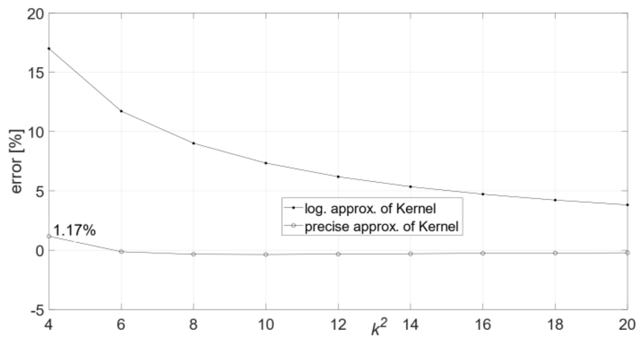

Fig. 9. Relative error distribution as a function of the wavelength with power two

5. Conclusions

Two ways of approximation of the kernels for the Helmholtz equation in the frequency domain were presented in this paper. Based on the benchmark provided in [6] error analysis was carried on for two cases of approximation of BEM singular integrands. The second one represents exceedingly high precision so it could be suitable for the imaging method for the different kind of tomography [9].

References

[1] Abramowitz M., Stegun I. A.: Handbook of mathematical functions with formulas, graphs, and mathematical tables. John Wiley, New York 1973.
[2] Arridge S. R.: Optical tomography in medical imaging. Inverse Problems 15(2), 1999, R41–R93.
[3] Becker A. A.: The boundary Element Method in Engineering. A complete course. McGraw-Hill Book Company, 1992.
[4] Harrison J.: Fast and Accurate Bessel Function Computation. [https://www.cl.cam.ac.uk/~jrh13/papers/bessel.pdf] (last access 20.07.2021).
[5] Jackson J. D.: Classical Electrodynamics (3rd ed.). Wiley, New York 1999.
[6] Jabłoński P.: Metoda Elementów Brzegowych w analizie pola elektromagnetycznego. Częstochowa University of Technology, Częstochowa 2003.
[7] Kirkup S.: The Boundary Element Method in Acoustics: A Survey. Applied Sciences 9(8), 1642 [http://doi.org/10.3390/app9081642].
[8] Krawczyk A.: Fundamentals of mathematical electromagnetism. Instytut Naukowo-Badawczy ZTUREK, Warszawa 2001.
[9] de Munck J. C., Faes T. J. C., Heethaar R. M.: The boundary element method in the forward and inverse problem of electrical impedance tomography. IEEE Trans Biomed Eng. 47(6), 2000, 792–800 [http://doi.org/10.1109/10.844230].
[10] Rymarczyk T.: Tomographic Imaging in Environmental, Industrial and Medical Applications. Innovatio Press Publishing Hause, Lublin 2019.
[11] Sikora J.: Boundary Element Method for Impedance and Optical Tomography. Warsaw University of Technology Publishing Hause, Warsaw 2007.
[12] https://mathworld.wolfram.com/Euler-MascheroniConstant.html (last access 10.07.2021).

Prof. D.Sc. Ph.D. Eng. Tomasz Rymarczyk
e-mail: tomasz@rymarczyk.com

He is the director in Research and Development Centre in Netrix S.A. and the director of the Institute of Computer Science and Innovative Technologies in the University of Economics and Innovation, Lublin, Poland. He worked in many companies and institutes developing innovative projects and managing teams of employees. His research area focuses on the application of non-invasive imaging techniques, electrical tomography, image reconstruction, numerical modelling, image processing and analysis, process tomography, software engineering, knowledge engineering, artificial intelligence, and computer measurement systems.

http://orcid.org/0000-0002-3524-9151

Prof. D.Sc. Ph.D. Eng. Jan Sikora
e-mail: sik59@wp.pl

Prof. Jan Sikora (PhD. DSc. Eng.) graduated from Warsaw University of Technology Faculty of Electrical Engineering. During 44 years of professional work, he has proceeded all grades, including the position of full professor at his alma mater. Since 1998 he has worked for the Institute of Electrical Engineering in Warsaw. In 2008, he has joined Electrical Engineering and Computer Science Faculty in Lublin University of Technology. During 2001-2004 he has worked as a Senior Research Fellow at University College London in the prof. S. Arridge's Group of Optical Tomography. His research interests are focused on numerical methods for electromagnetic field. He is an author of 8 books and more than 180 papers published in the international journals and conferences.

http://orcid.org/0000-0002-9492-5818

otrzymano/received: 02.12.2021 *przyjęto do druku/accepted: 15.12.2021*

http://doi.org/10.35784/iapgos.2822

APPLICATION OF THE THREAT INTELLIGENCE PLATFORM TO INCREASE THE SECURITY OF GOVERNMENT INFORMATION RESOURCES

Bohdan Nikolaienko[1], Serhii Vasylenko[2]

[1]Institute for Special Communication and Information Protection of the National Technical University of Ukraine "Igor Sikorsky Kyiv Polytechnic Institute", Department of Telecommunication Systems, Kyiv Ukraine, [2]Institute for Special Communication and Information Protection of the National Technical University of Ukraine "Igor Sikorsky Kyiv Polytechnic Institute", Research Center, Kyiv, Ukraine

Abstract. *With the development of information technology, the need to solve the problem of information security has increased, as it has become the most important strategic resource. At the same time, the vulnerability of the modern information society to unreliable information, untimely receipt of information, industrial espionage, computer crime, etc. is increasing. In this case, the speed of threat detection, in the context of obtaining systemic information about attackers and possible techniques and tools for cyberattacks in order to describe them and respond to them quickly is one of the urgent tasks. In particular, there is a challenge in the application of new systems for collecting information about cyberevents, responding to them, storing and exchanging this information, as well as on its basis methods and means of finding attackers using integrated systems or platforms. To solve this type of problem, the promising direction of Threat Intelligence as a new mechanism for acquiring knowledge about cyberattacks is studied. Threat Intelligence in cybersecurity tasks is defined. The analysis of cyberattack indicators and tools for obtaining them is carried out. The standards of description of compromise indicators and platforms of their processing are compared. The technique of Threat Intelligence in tasks of operative detection and blocking of cyberthreats to the state information resources is developed. This technique makes it possible to improve the productivity of cybersecurity analysts and increase the security of resources and information systems.*

Keywords: Threat Intelligence, cybersecurity, cyberdefense

ZASTOSOWANIE PLATFORM THREAT INTELLIGENCE DO ZWIĘKSZENIA OCHRONY ZASOBÓW INFORMACJI PUBLICZNEJ

Streszczenie. *Wraz z rozwojem technologii informacyjnych wzrosła potrzeba rozwiązania problemu bezpieczeństwa informacji, gdyż stała się ona najważniejszym zasobem strategicznym. Jednocześnie wzrasta podatność współczesnego społeczeństwa informacyjnego na nierzetelną informację, nieterminowe otrzymywanie informacji, szpiegostwo przemysłowe, przestępczość komputerową itp. W związku z tym, jednym z ważniejszych zadań jest szybkie wykrywania zagrożeń, w kontekście pozyskiwania informacji o napastnikach, możliwych technikach i narzędziach cyberataków, wraz z metodami ich opisu i szybkiego reagowania na nie. W szczególności wyzwaniem jest zastosowanie nowych systemów zbierania informacji o cyberzagrożeniach, reagowania na nie, przechowywanie i wymiana tych informacji, a także, na ich podstawie, metod i środków znajdowanie napastników z wykorzystaniem zintegrowanych systemów lub platform. W celu rozwiązania tego typu problemów badany jest obiecujący kierunek Threat Intelligence jako nowy mechanizm pozyskiwania wiedzy o cyberatakach. Zdefiniowano Threat Intelligence w problemach cyberbezpieczeństwa. Dokonano analizy wskaźników cyberataków i narzędzi ich pozyskiwania. Porównywano standardy opisu wskaźników kompromisów oraz platformy ich przetwarzania. Opracowano technikę Threat Intelligence w zadaniach operacyjnego wykrywania i blokowania cyberzagrożeń dla zasobów informacyjnych państwa. Technika ta pozwala na zwiększenie produktywności analityków cyberbezpieczeństwa oraz zwiększenie bezpieczeństwa zasobów i systemów informatycznych.*

Słowa kluczowe: Threat Intelligence, ceberbezpieczeństwo, cyberochrona

Introduction

Several years ago, the main vectors of cyberthreats that cybersecurity experts worked with were mass cyberattacks. Today, these attacks are seen as secondary threats that simply create "noise" in the network. For the most part, organizations and institutions successfully protect themselves from them by analyzing the first cases of cyberattacks, forming their indicators of compromise (IoC) and rapidly disseminating these indicators. The most serious violations of cybersecurity are due to well-planned, complex attacks targeting specific companies or industries. Well-funded attackers make it difficult to detect their attacks by using social engineering techniques that cannot be identified by simple indicators of compromise or blocked by traditional means of protection.

In addition, the number of cyberthreats themselves is growing rapidly. Attacks and, as a result, compromise computer networks can take minutes, and the process of detecting, responding to, and eliminating the effects of an attack takes days, weeks, and even months. Most often, detection occurs after the state information resources are compromised. According to Cisco's annual information security report [13], security professionals are able to process only 56% of incoming threat messages during their business day, and only one in two (i.e. 28%) is considered valid. Thus, 44% of incidents go completely unnoticed. At the same time, organizations critically lack not only resources to handle all incidents, but also a common system that would make it possible to respond to them at an early stage - ideally before operation, as well as to accumulate distributed knowledge about threats, share data. To investigate the causes of threats and respond to them immediately. Data from a variety of sources should be used to gather information about potential threats more quickly. It is important that this information is standardized, i.e. standards and protocols for data transmission and provision must be defined in advance for all players. One of the most important functions of effective protection of the organization's information system is threat tracking. Threat Intelligence (TI) is used to mitigate adverse events in cyberspace [10]. The TI system allows you to detect threats and attacks before they can affect the system. In the event that an incident does occur, TI allows you to analyze and, based on the investigation, expand your knowledge base with context, mechanisms, indicators of compromise, and threat analysis.

At the same time, it is not necessary to translate the concept of Threat Intelligence verbatim and understand it as the investigation of threats in cyberspace in the sense specified in [7]. The word "Intelligence" in English, in addition to the meaning of "intelligence", in the sense of a military unit or the process of obtaining hidden information about countries, companies, etc., also means "the ability to understand, study, form judgments and opinions based on facts." Therefore, along with the definition of Threat Intelligence as threat intelligence, it is advisable to use analogues – the acquisition of knowledge about threats, or knowledge about threats in general. It is in this context that Threat Intelligence is one of the processes of cybersecurity.

1. Analysis of recent research and publications

In [19] provides information on the limitations that arise when exchanging information about cyberthreats within TI platforms, as well as ways to address these limitations and options for using TI platforms. The best practices for the use of TI, trends in this regard and the main definitions in the field of TI are given in [5].

The question of the relationship between the tasks of Threat Intelligence and Threat Hunting in the investigation of cyberattacks, reproduction of tactics of attackers according to the model MITER ATT & CK and tools that can be used in this case are given in [2]. At the same time, the issue of increasing the security of state information resources through the use of the TI platform directly in the tasks of rapid detection and blocking of cyberthreats in the known literature was not considered.

Therefore, the purpose of this article is to consider the possibility of increasing the security of public information resources through the use of Threat Intelligence in the tasks of operational detection and blocking of cyberattacks and cyberthreats.

2. Presenting main material

Threat intelligence, the acquisition of knowledge about threats (Threat Intelligence) is defined as a set of knowledge that is built on observations, and includes indicators of compromise, mechanisms and context of attacks, as well as practical recommendations for eliminating identified and potential threats. Cyberintelligence services combine cybermonitoring infrastructure with the findings of specialists from the centers of investigation and response to incidents. Data for the nfrastructure comes from a distributed monitoring network, Honeypot-traps, the results of botnet analysis, various conferences, private groups on social networks, as well as the exchange of information between associations to combat cyberthreats [14].

An important component of effective protection against threats is information about them, which allows you to anticipate attacks and prepare for them in advance, rather than dealing with costly and long-term elimination of their consequences. By processing and analyzing data from hundreds of sources, you can get personalized, verified and meaningful information about current threats.

The information obtained during TI is diverse – from network artifacts and indicators of compromise to the identification of the attacker. Moreover, for example, for technicians to configure the means of protection is more important information about the indicators of compromise. Therefore, there is a need to separate certain levels of TI and information that is extracted and processed at these levels. Currently, there is no generalized distribution of TI levels, so, based on the analysis of existing representations of TI levels by different organizations [15, 16, 18], TI levels and source information processed at these levels in specific organizations have been generalized (Table 1).

As we see in table 1, these sources define 3 (tactical, operational, strategic), or 4 (tactical, technical, operational, strategic) levels of TI. The definition of such levels is due to the different nature of the data extracted and processed during TI. The same data are assigned to different specialists. For example, a national activity report cannot be compared to an IP address, and cannot be applied in the same way. Summarizing the information obtained during the analysis of TI levels and data on these levels, taking into account the existing levels of martial arts in Threat Intelligence, we distinguish three separate levels (strategic, operational and tactical) and consider them in more detail.

At the strategic level, high-level information is processed, on the basis of which specific management decisions are made to counter the threat. The purpose of the TI strategic level is to help strategists understand current and probable risks, obtain the attributes of attackers, identify them, define their strategies and goals. Intelligence materials are often presented in the form of reports describing the geopolitical situation, the activity of ART groups in the direction of the organization, trends in cyberattacks, high-level risks, the likelihood of their implementation and ways to address these risks. This information is obtained from open source intelligence (OSINT), obtained from reports of analytical organizations, from computer incident response teams (CERT) and cybersecurity companies in the form of "feeds" [17]. It should be noted that from these sources it is possible to obtain relevant information for the operational and tactical levels of TI. Threat hunting technologies and network forensic analysis are also used to obtain information that is assessed at the strategic level. This information provides analysts with a strategic level of understanding of the threat landscape in their infrastructure.

At the operational level, information is obtained about possible attacks on the organization, their possible tactics, as well as techniques and procedures that have already taken place. This information is obtained by analyzing events detected by network security tools (firewalls, Honeypots and Honeynets network lures), end device security tools. These protections typically act as data sources for the SIEM network event and message management system, through which professionals can aggregate, correlate, and process detected events to identify tactics, techniques, and procedures for attacks that have already taken place. At the same time, information obtained from open sources or "feeds" on possible complex ART attacks is used to configure these protections.

At the tactical level, during threat detection, based on data from intrusion detection and prevention systems (IDS/IPS), network sensors, server log file data, end devices, specialized security tools (eg, Security E-mail Gateway), network artifacts and identifiers of computer network compromise and the hypothesis of attack tools. The use of a network scanner and a vulnerability scanner provides information about existing vulnerabilities in computer network components. OSINT also provides information on vulnerabilities and compromise identifiers that are specific to an organization's computer network. Based on the data obtained, network administrators or information security specialists can respond to a cyberattack, configure and adjust the rules for detecting attacks in computer network security systems. The described levels of TI are summarized in table 2.

Table 1. TI-levels and source information processed at these levels in specific organizations

Organizations	TI levels	Source information
National Center for Cyber Security of the United Kingdom (NCSC)	1. Tactical	methodologies, tools and tactics, actions and more about attackers
	2. Technical	indicators of certain malware
	3. Operational	details of a specific incoming attack, assessment of the organization's ability to identify future cyberthreats
	4. Strategic	high-level risk reduction information (strategic shifts) - senior management assesses threat assessments
Threat Connect	1. Technical	indicators of compromise, detection of signatures
	2. Tactical	methodologies, tools and tactics
	3. Operational	compromise indicators
	4. Strategic	risk reduction due to threat models, capabilities of attackers
National Institute of Standards and Technology (NIST)	1. Tactical	security alerts, signature detection, and in advanced cases, some form of kill chain analysis based on information about attackers or network behavior
	2. Operational	identification of botnets, malware, phishing, etc.
	3. Strategic	determining the intentions and capabilities of attackers
Fortinet	1. Operational	structured data, indicators of compromise
	2. Tactical	low-level reports or structured data, understanding of attackers' tactics, techniques and procedures
	3. Strategic	high-level reports, models of attackers, their intentions, motivation, plans

The analyzed sources and generalized levels of TI provide an understanding only of what information is extracted, processed and used at each of these levels. This corresponds to the approaches to building an organizational and technical model of cybersecurity, given in [3]. Of course, the ultimate goal of both TE and cyberattack investigation is to identify the perpetrator and his intentions. To achieve this goal, we use formalized models to detect intruders in cyberspace, which directly operate on the information obtained during TI on the basis of Q- and Diamond models [6]. Consider these models in terms of their application in TI.

The Q-model is designed as a map of the attribution process: it allows, not having sufficient technical base, to implement a detailed attribution of a cyberattack (Fig. 1) [4].

Table 2. TI-levels

	Levels	Source information
Threat Intelligence	Strategic	Identification of the enemy, his possible names, pseudonyms, e-mail addresses, etc. Defining intentions and opportunities, reducing risks by studying threat models
	Operative	Understanding the tactics, techniques and procedures of the enemy, responding to attacks, writing rules for defense mechanisms
	Tactical (technical)	Tools, network artifacts, compromise indicators

The use of the Q-model allows scientists, as well as politicians or managers, to increase significant technical detail and communicate meaningfully with technicians. The model also allows forensic experts to assess the strategic and political context. The model itself has three levels (strategic, operational, tactical) and is divided into three stages (conceptual, empirical, communicative). The first stage is conceptual: it presents attribution as a process of discussing the model in general terms, introducing several critical differences and dynamics. During this stage, specialists must answer the questions of how (tactical level), who (operational), why (strategic level) carried out the attack, what was his goal, strength and means. The empirical level raises clarifying, specific questions to the conceptual level, providing answers to which it is possible to find indicators of compromise for a more accurate attribution of the attacker. The communication stage determines the completeness of information and the subjects to whom it is transmitted during the exchange of research results, as well as the order of this exchange. The ultimate goal of attribution in the Q-model is to define an organization or government, not individuals. But through labeling, unification, and geotagging, individual indicators can be powerful evidence links between artifacts and specific organizations.

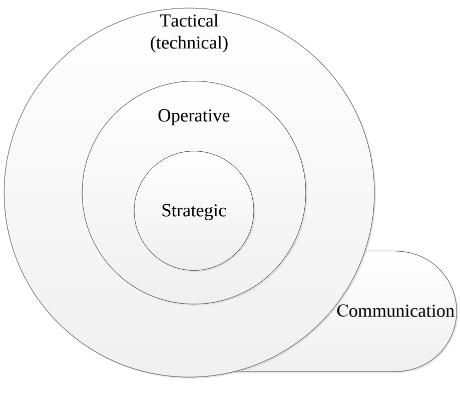

Fig. 1. Q-model

The diamond model describes a cyberattack as part of four main functions: attacker, infrastructure, capability, and victim [11]. These features are associated with the vertices, which represent their main relationship and are located in the shape of a diamond (Fig. 2).

This model also defines additional functions to support higher-level constructs, such as combining events together in activity streams and their subsequent integration. The model establishes a formal method that applies scientific principles to intrusion analysis, including measurement, testing, and repeatability. This scientific approach and simplicity can improve analytical efficiency and accuracy. Finally, this model provides the ability to integrate real-time threat intelligence to protect the network, automatically correlate and classify events. In its simplest form (Fig. 2), the model describes the enemy's ability to attack the victim's infrastructure. These elements are called events and are filled in by the analyst in case they are detected during threat investigation or cyberattack investigation. The vertices are connected by edges and distinguish connections between functions. Going along the edges and vertices, analysts find more information about the operations of the attacker and discover new capabilities (capabilities), infrastructure and victims. The event determines only one step in the series that the opponent must perform to achieve his goal.

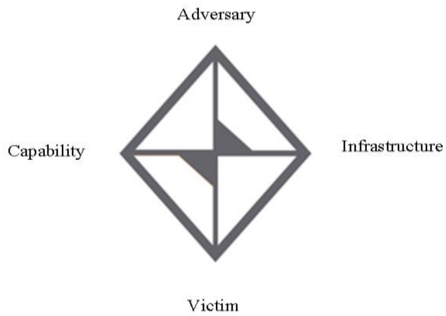

Fig. 2. Diamond model

In addition to the Q- and Diamond models, which directly describe the process of conducting TI, it should be noted the existence of such models as Kill Chain and MITER ATT & CK, which describe the behavior of the attacker during a cyberattack. Thus, the Kill Chain model determines the typical course of action of the attacker to achieve the goals [1]. To succeed, an attacker must usually go through all eight stages (intelligence, weapons, delivery, infection, installation, management, action, destruction of traces). The MITER ATT & CK matrix is a structured list of known behaviors of attackers, divided into tactics, techniques and procedures, expressed in the form of tables (matrices). Matrices for different situations and types of attackers are published on the MITER website [3]. The ATT & CK matrix can be useful for cyberintelligence because it allows you to standardize and describe the behavior of attackers.

As mentioned above, the information obtained during the TI, the identified indicators of compromise and threats, the order and format of the exchange of messages and reports need to be standardized. There are the following standards of description [8]:

- low level data (PCAP, CEF);
- indicators of compromise (MAEC, MMDEF, Snort rule, CybOX);
- enumeration (CVE, CWE, CPE);
- quantitative description of threats (CVSS, XCCDF);
- report formats (CVRF, IODF, STIX).

By using one of the standard formats, an organization can minimize the ambiguity of information, as well as use tools that support the exchange of these standards. However, there are other important technical considerations for the exchange of information, in particular the transport mechanisms used to request and transmit data. In addition, when using non-standard data formats, the choice of sorting method can have significant implications for overall performance and ease of integration with existing tools. Table 3 presents the standards, their levels, the ability to present information and an example of programs that use them.

Table 3. Standards and tools for information exchange and processing

Standard level	The name of the standard	Ability to present information	Programs that use the standard
Low level data	PCAP	packet taken from the network	Tcpdump, Wireshark
	CEF	event logging by hardware	ArcSight SIEM
Indicators of compromise	MAEC	characteristics of SPZ and their actions	Anubis, ThreatExpert, Cuckoo Sandbox
	MMDEF	file names, hash files, SPZ behavior	Cuckoo Sandbox
	Snort rules	IP addresses, ports, protocol, destination, HTTP request and response parameters	Snort, Suricata
	CybOX	network streams, network artifacts, files, SMS, images, emails	python-cybox
Enumeration	CVE	description of threats	STIX, VERIS
	CWE	a description of frequently used threats	IODEF-SC
	CPE	names of operating systems, software packages, classes of hardware devices	MAEC, CybOX
Quantitative description of threats	CVSS	threat assessment from 0 to 10	IODEF-SC, Cuckoo Sandbox
	XCCDF	full description and environment in which the threat is realized	SCAP
Report formats	CVRF	describes the entire lifecycle of vulnerability processing	Used within supplier communications
	IODEF	XML format, incident information exchange	ArcSight
	STIX	a full description of events by one of the above standards	CRITs, Microsoft Interflow

Currently, there is a critical lack not only of resources to handle all cybersecurity incidents, but also of common systems to respond to them in the early stages of cyberattacks, as well as to extract and accumulate distributed knowledge about threats, share data, investigate causes of attacks, respond to them and find perpetrators. Therefore, the main cyberintelligence platforms (Threat Intelligence Platform – TIR) that perform these tasks were considered, as well as a table on the capabilities of these platforms according to TI levels (table 4). The capabilities, functions and purpose of each platform are covered in detail in the public domain.

Thus, the threat intelligence platform can be deployed as software as a service to facilitate cyberintelligence management, accumulation and exchange of information about objects such as attackers, companies, incidents, vulnerabilities and TTP [12]. This is determined by its ability to perform four key functions: aggregation of intelligence from multiple sources; adjustment, normalization, enrichment and risk assessment; integration with existing security systems; analysis and exchange of information on threats. At the same time, not all TIRs can collect, process and exchange information at all levels of TIs, nor are general methods of the TI process known. Therefore, the following TI technique is proposed in the tasks of operative detection and blocking of cyberthreats to state information resources (Fig. 3).

Table 4. Comparison of major intelligence platforms according to TI-levels

Platform	Type	Levels		
		Tactical	Operational	Strategic
MISP	open	+	+	-
CRITs	open	+	+	-
TheHeroic	open	+	+	+
YETI	open	+	+	-
GOSINT Framework	open	+	+	+
R-Vision	open	+	+	+
ThreatStream	commercial	+	+	+
IBM QRadar Security TI	commercial	+	+	-

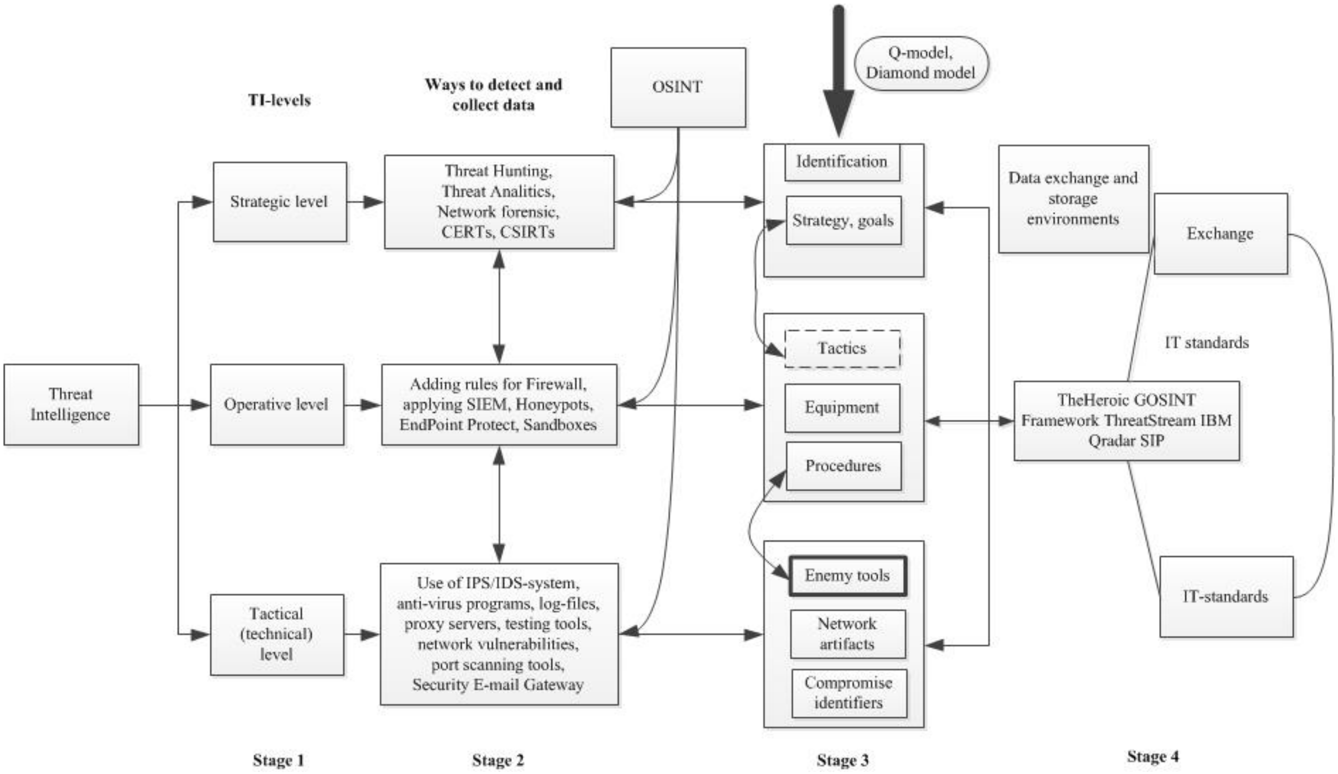

Fig. 3. TI methodology

The proposed TI technique (Fig. 3) is divided into four stages:

In the first stage, it is proposed to divide threat intelligence into three levels: tactical (technical), operational and strategic, according to which the tools for detection and data collection are determined (stage 2).

In the second stage, the analysis of attacks is performed using tools to detect and collect data. Stage 2, according to the model of the sequence of actions of the enemy's attack, has three sub-stages, namely: collection of attack data, processing, response and definition of strategies and goals of the attacker.

Attack data collection involves the use of IPS / IDS, SIEM, anti-virus programs, log files, proxy servers, network vulnerability testing tools, port scanning tools, Security E-mail Gateway and others.

After collecting all possible data on the cyberattack, they are processed and responded to incidents. This is possible by adding rules for Firewall, using SIEM, Honeypots, Honeynets, EndPoint Protect, Sandboxes, etc.

The last step of stage 2 is to determine possible data about the enemy, his strategies and goals . To do this, TI analysts use Threat Hunting methods, conduct network investigations using OSINT tools. OSINT tools can also be used during the third step to search for enemy data and possible threats.

In the third stage, threat attributes are identified and standardized according to TI levels. As malefactors have various motives, the purposes, ways, tools, for their identification it is necessary:

- collect and characterize all evidence using threat description standards (compromise indicators, network data and enemy tools);
- on the basis of the collected data and tools of cyberattack to define tactics, techniques and procedures according to which malefactors realize the purposes and to take measures for reaction to incidents;
- show the purpose of the attackers and how they will achieve the desired result, try to identify the attacker or group of attackers.

To perform these tasks, different models of detection and response to intrusion (Q- and Diamond models) should be used.

The final stage involves defining the storage environment and sharing the attributes of threats collected in the previous phase. Formalization of the exchange of such data is provided by special standards, which are considered in Table 3.

3. Conclusions

Built complex information security system, information security systems and information security management system on the objects of information activities, which process state information resources, the binding nature of which is defined in [20] require increasing their efficiency through the use of computerized methods and tools. Such tools allow automating the processes of data collection, detection and processing of new threats, their blocking and further study in order to develop general recommendations for protection against them.

The paper considers the essence of TI as a new type of intelligence, defines the levels of intelligence and their representation by different organizations, analyzes the main models for detecting intruders, based on the ontological approach shows the features of the offender's tactics, techniques and procedures for targeted cyberattacks. Provide a description and formalization of the exchange of indicators of compromising cyberattacks, as well as determine the purpose of the most well-known cyberintelligence platforms and the possibility of their work.

Based on the analysis, the TI methodology was developed for the tasks of rapid detection and blocking of threats to public information resources, which will improve the efficiency of cybersecurity analysts, as well as increase the security of public information resources and systems.

References

[1] Hutchins E. M. et al.: Intelligence-Driven Computer Network Defense Informed by Analysis of Adversary Campaigns and Intrusion Kill Chains. Lockheed Martin Corporation, 2010.

[2] Palacín V.: Practical Threat Intelligence and Data-Driven Threat Hunting. Packt Publishing Ltd., 2021.

[3] Potiy O. et al.: Conceptual principles of implementation of organizational and technical model of cyber defense of Ukraine. Information protection 23(1), 2021.

[4] Rid T. et al.: Attributing Cyber Attacks. The Journal of Strategic Studies 38(1-2), 2015, 4–37.

[5] Shackleford D.: Who's Using Cyberthreat Intelligence and How? SANS Institute 2015.

[6] Zhylin M. et al.: Functional model of cybersecurity situation center. Information Technology and Security 6(2), 2018, 51–67 [http://doi.org/10.20535/2411-031.2018.6.2.153490].

[7] Exploring the opportunities and limitations of current Threat Intelligence Platforms. Public version 1.0, ENISA, December 2017.

[8] Standards and tools for exchange and processing of actionable information. European Union Agency for Network and Information Security, 2017.

[9] https://attack.mitre.org

[10] https://rvision.pro/blog-posts/chto-takoe-threat-intelligence-iv-chem-ego-tsennost

[11] https://threatconnect.com/blog/diamond-model-threat-intelligence-star-wars/

[12] https://www.anomali.com/resources/what-is-a-tip

[13] https://www.cisco.com/c/uk_ua/products/security/security-reports.html

[14] https://www.forcepoint.com/cyber-edu/threat-intelligence

[15] https://www.fortinet.com/ru

[16] https://www.ncsc.gov.uk

[17] https://www.ncsc.gov.uk/content//files/protected_files/guidance_files//MWR_Threat_Intelligence_whitepaper-2015.pdf

[18] https://www.nist.gov

[19] https://zakon.rada.gov.ua/laws/show/2163-19#Text

[20] https://zakon.rada.gov.ua/laws/show/518-2019-%D0%BF#Text

Ph.D. Bohdan Nikolaienko
e-mail: nikolaenko_iszzi@ukr.net

Nikolaenko Bohdan Anatoliyovych, Candidate of Technical Sciences, Senior Lecturer at the Special Department No. 3 of the Institute of Special Communication and Information Protection of the National Technical University of Ukraine "Igor Sikorsky Kiev Polytechnic Institute", Kyiv, Ukraine.

http://orcid.org/0000-0002-6888-5947

Ph.D. Serhii Vasylenko
e-mail: vasylenko.phd@gmail.com

Vasylenko Serhii Viktorovych, Candidate of Technical Sciences, Head of the Research Laboratory of the Research Center of the Institute of Special Communications and Information Protection of the National Technical University of Ukraine "Igor Sikorsky Kiev Polytechnic Institute", Kyiv, Ukraine.

http://orcid.org/0000-0001-6779-8246

otrzymano/received: 15.11.2021 *przyjęto do druku/accepted: 15.12.2021*

http://doi.org/10.35784/iapgos.2812

INDIRECT INFORMATION HIDING TECHNOLOGY ON A MULTIADIC BASIS

Volodymyr Barannik[1], Natalia Barannik[2], Oleksandr Slobodyanyuk[3]
[1]V.N. Karazin Kharkiv National University, Kharkiv, Ukraine, [2]National University of Civil Defence of Ukraine, Kharkiv, Ukraine, [3]Kamianets-Podilskyi Ivan Ohiienko National University, Kamianets-Podilskyi, Ukraine

Abstract. *It is shown that the current direction of increasing the safety of information resources when transmitting information in info-communication systems is the use of methods of steganographic instruction in video imagery. The effectiveness of such methods is significantly increased when used in a complex of methods of concealment, which are based on the principles of inconsistent and cosmic communication. At the same time, existing methods of steganographic are used in the process of insertion of information mainly only laws, empty features of visual perception of video images. So, it is justified that the scientific and applied problem, which is to increase the density of embedded messages in the video container with a given level of their reliability, is relevant. The solution of this problem is based on the solution of the contradiction, which concerns the fact that increasing the density of embedded data leads to a decrease in the bit rate of the video container, steganalysis stability, reliability of special information, and video container. Therefore, the research aims to develop a methodology for the steganographic embedding of information, taking into account the regularities of the video container, which are generated by its structural and structural-statistical features. The solution to the posed problem of applying steganographic transformations is proposed to be realised by methods of indirectly embedding parts of the hidden message in certain conditions or functional relationships. The possibility of creating steganographic transformations regarding the indirect embedding and extraction of hidden information in a multiadic basis by modifying the underlying basis system within an admissible set is demonstrated. It is shown that the multiadic system, which is created in the spectral space of DCT transforms, has the potential to form a set of admissible modifications of basis systems.*

Keywords: steganographic transformations, video container, video compression, indirect embedding

TECHNOLOGIA POŚREDNIEGO UKRYWANIA INFORMACJI NA ZASADZIE MULTIADYCZNEJ

Streszczenie. *Wykazano, że aktualnym kierunkiem zwiększania bezpieczeństwa zasobów informacyjnych przy przesyłaniu informacji w systemach info-komunikacyjnych jest stosowanie metod instrukcji steganograficznej w obrazach wideo. Skuteczność tych metod znacznie wzrasta, gdy są one stosowane w zespole metod ukrywania, które opierają się na zasadach bezpośredniego i pośredniego osadzania komunikatów. Jednocześnie istniejące metody steganografii wykorzystują w procesie osadzania informacji głównie wzorce generowane przez cechy percepcji wizualnej obrazów wideo. Tak więc, uzasadnione jest, że istotnym jest problem naukowy i praktyczny polegający na zwiększeniu gęstości osadzonych wiadomości w kontenerze wideo z danym poziomem ich wiarygodności. Sednem tego problemu jest rozwiązanie kontrowersji, że wzrost gęstości osadzonych danych prowadzi do spadku przepływności kontenera wideo, odporności na steganoanalizę, wiarygodności informacji specjalnych i kontenera wideo. Dlatego celem pracy jest opracowanie metodyki steganograficznego osadzania informacji uwzględniającej prawa kontenera wideo, które są generowane przez jego cechy strukturalne i konstrukcyjno-statystyczne. Rozwiązanie postawionego problemu w zakresie zastosowania przekształceń steganograficznych proponuje się zrealizować metodami pośredniego osadzania części ukrytego komunikatu w pewnych warunkach lub zależności funkcjonalnych. Wykazano możliwość tworzenia przekształceń steganograficznych odnośnie pośredniego wbudowania i ekstrakcji ukrytych informacji w bazie wieloaddycznej poprzez modyfikację podstawowego układu bazowego w ramach dopuszczalnego zbioru. Udowodniono, że układ wieloadyczny, który powstaje w przestrzeni spektralnej transformat DCT, ma potencjał do tworzenia zbioru dopuszczalnych modyfikacji układów bazowych.*

Słowa kluczowe: transformacje steganograficzne, kontener wideo, kompresja wideo, pośrednie osadzanie

Introduction

One of the actual directions for increasing the security of information resources during transmission in info-communication systems is the use of methods of steganographic embedding of information in video images. The efficiency of such methods significantly increases when used in a set of concealment methods, which are based on the principles of direct and indirect embedding of messages. It allows [1–3] to create conditions for localizing the imbalance between the timeliness of the delivery of hidden information (special information) and the indicator of its reliability [4, 5, 7, 8].

At the same time, the existing methods of steganography are used in the process of embedding information mainly only the regularities generated by the features of visual perception of video images. In turn, this leads to the fact that with the use of modern telecommunication technologies and coding technology video container H26* creates conditions for the organization of the hidden message channel, which allows you to embed a message at 3 – 20 Mpixels for PSNR in 20 dB. This accordingly creates conditions for hiding FullHD video images [9–11]. However, in this case, the level of PSNR is 20 dB, which means that there are significant distortions of the video container. So, such PSNR level does not satisfy the required level of video information fidelity in critical infrastructure management systems. On the contrary, for a given level of fidelity (the PSNR value reaches 40 dB) conditions are created for hiding messages with a bit volume of only 1.5 Mbytes. This allows hiding CIF and SD format video images. But this format of video images does not meet the requirements regarding the completeness of video information [12–16].

So, the scientific and applied problem, which is to increase the density of embedded messages in the video container with a given level of reliability, is relevant.

The solution to this problem is based on the solution of a contradiction, which concerns the fact that increasing the density of embedded data leads to a decrease in the bit rate of the video container, steganalysis stability, reliability of special information, and video container [15, 17, 18].

To resolve this contradiction, it is proposed to develop steganographic methods that allow message embedding under conditions of exclusion of necessity (or limitation) in the use of psychovisual regularities. That is, the process of message embedding should not be accompanied by additional distortions in the video container [19–21].

Therefore, the purpose of the study is the development of the methodology of steganographic information with the take into account the regularities of the video container, which are empty of its structural and structural-statistical characteristics.

1. The reasoning of the direction for creating steganographic systems with video container distortion exclusion

The solving of the formulated problem in the field of application of steganographic transformations is proposed to realize with the use of methods of indirect embedding of some condition or functional dependence to the bit of scrambled message [22–26].

But in turn, the existing methods of indirect steganographic transformations are characterized by a drawback, which is the insufficient value of the density of embedded data according to modern requirements [25, 27, 28].

To eliminate the disadvantages of indirect steganographic embedding, it is proposed to develop an approach that allows using not only psychovisual but also structural redundancy of video containers for concealment [6, 29–33].

To build a steganographic system under the conditions of fulfilling the requirements, it is proposed to use multiadic transformation [35–37]. In this case, the following is achieved.

1. The regularities appear adaptively for each data set with the structural-combinatorial origin and are described quantitatively in the form of estimates of the dynamic ranges of the data set elements. That is.

$$\psi_i = \max_{1\le i\le m}\{a_{i,j}\}+1 \qquad j=\overline{1,n}\,.$$

here $a_{i,j}$ - j-th item i-th row of the array A.

2. There is a possibility of restored data array elements to establish with given integrity of the appropriate conditional dependence. This provides a condition for extracting a hidden message without loss of information [38, 39].

In this case, the process of removing hidden information will be carried out by analyzing the values of the initial and modified service information.

Modifications in the field of structural-combinator patterns create an opportunity to avoid its impact on the value of video elements. Therefore, there is potential relative to the avoidance of distortions in the masses of video data [40, 41].

The data array is proposed to be considered as a container for indirect embedding information in the spectral region. This is because the DCT transformant creates conditions for identifying and reducing more structural and combinatorial redundancy than in the space-time domain [42, 43]. Consequently, DCT transformants increase the potential for the embedding of the hidden message due to modification in the field of patterns according to dynamic ranges in the conditions of the presence of the corresponding amount of structural and combinatorial redundancy.

Thus, a selection of a multiadic system is substantiated to organize indirect hiding information in terms of avoidance of losses as built-in information, and additional distortion of the container.

2. Creation of methodology of the steganographic system of indirect hiding information.

Multiadic system (MAS) – system $F_{mads}(A_j;\, E_j;\, \Psi; \delta_j = 0)$ mutual one-to-one $(\delta_j = 0)$ formation of code values E_j for sequences A_j in multiadic space with the set system of bases Ψ. Here δ_j – average deviation of elements of decoded multiadic number relative to elements of initial IODM number. This is described by the expression:

$$\delta_j = \sqrt{\frac{\sum_{i=1}^{m}(a_{i,j}^{(\theta)} - a_{i,j})^2}{m}}\,,$$

where m – number of elements in multiadic number;

$a_{i,j}^{(\theta)}$ - $(i;\, j)$-th item for θ-th an option to recover the initial multiadic number A_j;

$A_{\theta,j}$ - j-th multiadic number for θ-th variant of system building Ψ_θ basis, $A_{\theta,j} = (a_{1,j}^{(\theta)};...;a_{i,j}^{(\theta)};...;a_{m,j}^{(\theta)})$.

The multiadic system consists of two basic operators $\phi_{emad}(A_j;\, \Psi)$, $\phi_{dmad}(E_j;\, \Psi)$. Therefore:

$$F_{mads}(A_j;\, E_j;\, \Psi; \delta_j = 0) = \{\phi_{emad}(A_j;\, \Psi);\, \phi_{dmad}(E_j;\, \Psi)\}\,.$$

Here $\phi_{emad}(A_j;\, \Psi)$, $\phi_{dmad}(E_j;\, \Psi)$ - operators, which are implemented according to the technology of direct (encoding) and reverse (decoding) of multiadic transformations.

Let's introduce the concept of basic MAS. The basic (reference) multiadic system is understood as such a system that is formed directly for a particular data set (video data block, transformant).

So, in this case, the ***basic system*** Ψ of bases ψ_i is such a system, the values of bases of which are determined by the rules of:

$$\psi_i = \max_{1\le j\le n}\{a_{i,j}\}+1\,,\ i = \overline{1,\, m}$$

That is, the value of bases ψ_i for the base system Ψ is defined as dynamic ranges of elements in the rows of the data array.

Defining the basics ψ_i by dynamic range not for individual elements $a_{i,j}$ multiadic numbers, but by the set of elements in rows, i.e. $A_i = \{a_{i,1};...;a_{i,j};...;a_{i,n}\}$, due to the need to reduce the bit volume of the service component. Then, on average, each element of the column of the data array (transformers) will fall on average $(\ell og_2\psi_i / n)$ binary digits. Wherefore, as the number of columns grows, the value $(\ell og_2\psi_i / n)$ will decrease. Therefore, the total bit volume of the compression representation of the data array (transformers) will be reduced as a result of the multiadic encoding of its columns.

It is clear that for the possibility of indirect concealment of information in a multiadic system at the level of structural meta-features, MAS must possess the following property (characteristic).

3. Property of MAS

Multiadic System Property (MASP) on the possibility of forming and without erroneous restoration of one multiadic number A_j by multiple code values $E_{\theta,j}$ in a different system of bases Ψ_θ.

That is, relative to the error-free direct and inverse transformations of a single multiadic number A_j in various multiadic systems $F_{mads}(A_j;\, E_j;\, \Omega(\Psi);\, \delta_j = 0)$. Here $\Omega(\Psi)$ – a set of multiadic bases Ψ_θ, for which this MAS property is provided.

To prove this property of MAS, we will formulate and then prove the following statement.

To generalize the conclusions of the statement, we will carry out its examination without reference to a specific transformation or a set of video data. There is A_j initial one-dimensional multiadic (IODM) number, $A_j = \{a_{1,j};...;a_{i,j};...;a_{m,j}\}$ in a basis $\Psi = \Psi_\theta$ of bases $\psi_i = \psi_i^{(\theta)}$, $i=\overline{1,\, m}$, for which is the code value $E_j = E_{\theta,j}$.

So in this case this formulation of the statement corresponds.

The statement about the existence of a plurality of admissible multiadic systems for one sequence (about the modification of the system of bases).

There are so set of systems $\Omega(\Psi)$ of bases Ψ_θ, $\theta = \overline{1,\Theta}$, for which with the help of the set $\Omega(E)$ corresponding code values $E_{\theta,j}$, $\theta = \overline{1,\Theta}$ for one sequence A_j mutually unambiguous (without false) direct and reverse multiadic transformation is achieved, namely:

$$A_j = \phi_{dmad}(E_{\theta,j};\, \Psi_\theta)\,,\ \text{for}\ \ E_{\theta,j} = \phi_{emad}(A_j;\, \Psi_\theta)$$

There is $W_{\theta,i}$ – a weight coefficient of the i-th element of the sequence A_j in case of use θ-th variant of system bases construction Ψ_θ.

This statement allows establishing the conditions of modification of the system of bases of the multiadic space, for which restoration of elements of the initial sequence without loss of information is provided. So there's a set $\Omega(\Psi)$ of variants of system basis modifications Ψ_θ, which eliminates the loss of information in the process of reconstruction of elements of multiadic (IODM) numbers using the corresponding code values. The mutual one-valued conversion between the code values $E_{\theta,j}$ and related IODM number A_j will be executed in the case of:

- the choice of the system of bases Ψ_θ, which is included in the admissible set $\Omega(\Psi)$ of options for the construction of;
- the formation of appropriate code values $E_{\theta,j}$ in the permissible systems of bases Ψ_θ.

In the particular case of two admissible systems of bases Ψ_θ, Ψ_ϑ, i.e. $\Psi_\vartheta, \Psi_\theta \in \Omega(\Psi)$, $\theta \neq \vartheta$, in the conditions of the formation of code values by expressions:

$$E_{\theta,j} = \phi_{emad}(A_j; \Psi_\theta); \quad E_{\vartheta,j} = \phi_{emad}(A_j; \Psi_\vartheta)$$

will be achieved decoding the original sequence without loss of information, such as:

$$\phi_{dmad}(E_{\theta,j}; \Psi_\theta) = \phi_{dmad}(E_{\vartheta,j}; \Psi_\vartheta) = a_{i,j} \in A_j, \quad i = \overline{1,m}, \quad j = \overline{1,n}.$$

At the same time, it should be taken into account that according to the technological requirements for digitization of full-color video images, the element values of each color component cannot exceed the value of 255. Then the dynamic range of each element will be in the following limits: $0 \le a_{i,j} \le 255$.

What is the meaning of base $\psi_i^{(\theta)}$ will be limited to a maximum value of 256, such as:

$$a_{i,j} \le \psi_i^{(\theta)} - 1 \le 255, \quad i = \overline{1,m} \quad (1)$$

The inequalities (1) describe the conditions for the formation of an admissible set of $\Omega(\Psi)$ systems of Ψ_θ bases, which creates conditions for the construction of mutually one-valued multiadic systems.

From expression (1) we obtain the value ${}_\Delta\psi_i^{(\theta)}$, which defines the range of acceptable changes in the values of the bases relative to the elements $a_{i,j}$ multiadic number, i.e.

$${}_\Delta\psi_i^{(\theta)} \le 256 - \psi_i^{(\theta)}$$

In general, we obtain the following relation, which limits the values of the quantities ${}_\Delta\psi_i^{(\theta)}$:

$$1 \le {}_\Delta\psi_i^{(\theta)} \le 256 - \psi_i^{(\theta)}$$

This allows us to determine the volume $|\Omega(\Psi)|$ of the acceptable systems of the basics set $\Omega(\Psi)$ in relation to the values of the elements $a_{i,j}$ IODM number, such as:

$$|\Omega(\Psi)| = \Theta = \prod_{i=1}^{m} ({}_\Delta\psi_i^{(\theta)} - 1) \quad (2)$$

From the analysis of formula (2), it follows that $|\Omega(\Psi)| > 1$ if $({}_\Delta\psi_i^{(\theta)} - 1 \ge 1)$. The last condition is reached when $a_{i,j} <<< 255$ that is when elements of multiadic numbers have a limited dynamic range $\psi_i^{(\theta)}$. The volume of the set $\Omega(\Psi)$ depends on the amount of structural-combinatorial redundancy generated by the finiteness of the dynamic ranges of the elements of multiadic numbers.

At the same time, as practical studies show, the formation of a multiadic basis in the spectral space using the discrete cosine transform (DCT) provides the presence of patterns of such origin.

It follows that the multiadic system, which is created in the spectral space of the transformant DCT, has the potential for the formation of a set of admissible modifications of the systems of bases. In turn, this characteristic feature creates the possibility for the construction of indirect steganographic transformations on the multiadic basis based on a modification of structural meta-features

4. Conclusions

1. It has been proven that it is possible to create steganographic transformations to indirect embedding and removal of hidden information on a multiadic basis by modifying the basic system of bases within the permissible set.
2. There has been a proven existence of multiple permissible multiadic systems for the same continuity in a way that achieves mutually unambiguous (without erroneous) direct and reverse code transformation. This allows you to establish the conditions for modifying the system of multiadic space for which the recovery of the elements of the initial sequence without loss of information, namely:
   - selection of the system of bases, which is part of the permissible set of constructing options;
   - formation of the corresponding code values in allowable systems of bases.
3. It is substantiated that the multiadic system that is created in the spectral space transformant DCT has the potential for the formation of a set of permissible modifications of bases. In turn, such a characteristic feature creates an opportunity to build indirect steganographic transformations in a multiadic based on the modification of structural meta-features.

References

[1] Alam, M. A.: Faster Image Compression Technique Based on LZW Algorithm Using GPU Parallel Processing. Joint 7th International Conference on Informatics, Electronics & Vision (ICIEV) and 2nd International Conference on Imaging, Vision & Pattern Recognition (icIVPR), 2018, 272–275 [http://doi.org/10.1109/ICIEV.2018.8640956].

[2] Announcing the ADVANCED ENCRYPTION STANDARD (AES), Federal Information Processing Standards Publication 197, 2001.

[3] Barannik V.: Fast Coding of Irregular Binary Binomial Numbers with a Set Number of Units Series. IEEE 2nd International Conference on Advanced Trends in Information Theory (IEEE ATIT 2020), 2020, 29–33 [http://doi.org/10.1109/ATIT50783.2020.9349356].

[4] Barannik D.: Stegano-Compression Coding in a Non-Equalible Positional Base. IEEE 2 nd International Conference on Advanced Trends in Information Theory, 2020, 83–86 [http://doi.org/10.1109/ATIT50783.2020.9349328].

[5] Barannik N., Ryabukha Yu.: Method of Indirect Steganographic Coding of Information without Visual Distortion of the Video Container series. IEEE 2 nd International Conference on Advanced Trends in Information Theory, 2020, 57–61 [http://doi.org/10.1109/ATIT50783.2020.9349262].

[6] Barannik V., Hahanova A., Krivonos V.: Coding tangible component of transforms to provide accessibility and integrity of video data. International Symposium, East-West Design & Test Symposium (EWDTS), 2013, 1–5 [http://doi.org/10.1109/EWDTS.2013.6673179].

[7] Barannik V. V., Karpinski M. P., Tverdokhleb V. V., Barannik D. V., Himenko V. V., Aleksander M.: The technology of the video stream intensity controlling based on the bit-planes recombination. 4th IEEE International Symposium on Wireless Systems within the International Conferences on Intelligent Data Acquisition and Advanced Computing Systems (IDAACS-SWS), 2018, 25–28 [http://doi.org/10.1109/IDAACS-SWS.2018.8525560].

[8] Barannik V., Barannik D., Fustii V., Parkhomenko M.: Technology for Protecting Video Information Resources in the Info-Communication Space. IEEE 3rd International Conference on Advanced Information and Communications Technologies (IEEE AICT 2019), 2019, 248–250 [http://doi.org/10.1109/AIACT.2019. 8847820].

[9] Barannik, V., Barannik, N., Ryabukha, Yu., Barannik, D. Indirect Steganographic Embedding Method Based On Modifications of The Basis of the Polyadic System. 15 th IEEE International Conference on Modern Problems of Radio Engineering, Telecommunications and Computer Science, 2020, 699–702 [http://doi.org/10.1109/TCSET49122.2020.235522].

[10] Barannik V., Himenko V., Babenko Yu., Hahanova A., Fustii V.: Technology of Composite Code Forming in The Spatial-Spectral Description Significant Microsegments. IEEE 15th International Conference on Advanced Trends in Radioelectronics, Telecommunications and Computer Engineering, 2020, 703–706 [http://doi.org/10.1109/TCSET49122.2020.235523].

[11] Barannik V., Jancarczyk D., Babenko Yu., Stepanko O., Nikodem J., Zawislak S.: A Model for Representing Significant Segments of a Video Image Based on Locally Positional Coding on a Structural Basis. IEEE 5nd International Symposium on Smart and Wireless Systems within the Conferences on Intelligent Data Acquisition and Advanced Computing Systems (IEEE IDAACS-SWS 2020), 2020, 1–5 [http://doi.org/10.1109/IDAACS-SWS50031.2020.9297068].

[12] Barannik V., Kharchenko N., Othman Shadi O., Musienko A.: A method to control bit rate while compressing predicted frames. IEEE International Conference on The Experience of Designing and Application of CAD Systems in Microelectronics (IEEE CADSM 2015), 2015, 36–38 [http://doi.org/10.1109/CADSM.2015.7230789].

[13] Barannik V., Kharchenko N., Tverdokhleb V., Kulitsa O.: The issue of timely delivery of video traffic with controlled loss of quality. 13th International Conference on Modern Problems of Radio Engineering, Telecommunications and Computer Science (TCSET), 2016, 902–904 [http://doi.org/10.1109/TCSET.2016.7452220].

[14] Barannik V., Shulgin S., Krasnorutsky A., Slobodyanyuk O., Gurzhii P., Korolyova N.: Methodological Fundamentals of Deciphering Coding of Aerophotography Segments on Special Equipment of Unmanned Complex. IEEE 2 nd International Conference on Advanced Trends in Information Theory, 2020, 38–43 [http://doi.org/10.1109/ATIT50783.2020.9349257].

[15] Barannik V., Sidchenko S., Barannik N., Khimenko A.: The method of masking overhead compaction in video compression systems. Radioelectronic and Computer Systems 2, 2021, 51–63. [https://doi.org/10.32620/reks.2021.2.05].

[16] Belikova T.: Decoding Method of Information-Psychological Destructions in the Phonetic Space of Information Resources. Proceedings of the 2nd IEEE International Conference Advanced Trends in Information Theory (ATIT), 2020, 87–91 [https://ieeexplore.ieee.org/document/9349300].

[17] Bui V., Chang L., Li D., Hsu L., Chen M.: Comparison of lossless video and image compression codecs for medical computed tomography datasets. IEEE International Conference on Big Data, 2016 3960–3962 [http://doi.org/10.1109/BigData. 2016.7841075].

[18] Chen T.-H., Wu Ch.-S.: Efficient multi-secret image sharing based on Boolean operation. Signal Processing 91(1), 2011, 90–97 [http://doi.org/10.1016/j.sigpro.2010.06.012].

[19] Deshmukh M., Nain N., Ahmed M.: An (n, n)-Multi Secret Image Sharing Scheme Using Boolean XOR and Modular Arithmetic. IEEE 30 th International Conference on Advanced Information Networking and Applications (AINA), 2016, 690–697 [http://doi.org/10.1109/aina.2016.56].

[20] Djelouah A., Campos J., Schaub-Meyer S., Schroers C.: Neural Inter-Frame Compression for Video Coding. IEEE/CVF International Conference on Computer Vision (ICCV), 2019, 6420–6428 [http://doi.org/10.1109/ICCV.2019.00652].

[21] Dong W., Wang J.: JPEG Compression Forensics against Resizing. IEEE Trustcom/BigDataSE/IвSPA, 2016, 1001–1007 [http://doi.org/10.1109/TrustCom.2016.0168].

[22] Gonzales R. C., Woods R. E.: Digital image processing. Prentice Inc., Upper Saddle River 2002.

[23] Honda T., Murakami Y., Yanagihara Y., Kumaki T., Fujino T.: Hierarchical image-scrambling method with scramble-level controllability for privacy protection. IEEE 56th International Midwest Symposium on Circuits and Systems, 2013, 1371–1374 [http://doi.org/10.1109/MWSCAS.2013.6674911].

[24] Ieremeiev O., Lukin V., Okarma K.: Combined visual quality metric of remote sensing images based on neural network. Radioelectronic and computer systems 4, 2020, 4–15 [http://doi.org/10.32620/reks.2020.4.01].

[25] Information technology – JPEG 2000 image coding system: Secure JPEG 2000, International Standard ISO/IEC 15444-8, ITU-T Recommendation T.807, 2007.

[26] JPEG Privacy & Security Abstract and Executive Summary, 2015 [https://jpeg.org/items/20150910_privacy_security_summary.html].

[27] Komolov D., Zhurbynskyy D., Kulitsa O.: Selective Method For Hiding of Video Information Resource In Telecommunication Systems Based on Encryption of Energy-Significant Blocks of Reference I-Frame. 1st International Conference on Advanced Information and Communication Technologies (AICT'2015), 2015, 80–83.

[28] Li F., Krivenko S., Lukin V.: Two-step providing of desired quality in lossy image compression by SPIHT. Radioelectronic and computer systems 2, 2020, 22–32 [http://doi.org/10.32620/reks.2020.2.02].

[29] Naor M., Shamir A.: Visual Cryptography. Proceedings of the Advances in Cryptology – EUROCRYPT'94. Lecture Notes in Computer Science 950, 1995, 1–12 [http://doi.org/10.1007/bfb0053419].

[30] Narmatha C., Manimegalai P., Manimurugan S.: A LS-compression scheme for grayscale images using pixel based technique. International Conference on Innovations in Green Energy and Healthcare Technologies (IGEHT), 2017, 1–5 [http://doi.org/10.1109/IGEHT.2017.8093980].

[31] Richter T.: Error Bounds for HDR Image Coding with JPEG XT. Data Compression Conference, 2017, 122–130 [http://doi.org/10.1109/DCC.2017.7].

[32] Rippel O.: Learned Video Compression. IEEE/CVF International Conference on Computer Vision (ICCV), 2019, 3453–3462 [http://doi.org/10.1109/ICCV.2019.00355].

[33] Rivest R. L., Shamir A., Adleman L. M.: A method for obtaining digital signatures and public-key cryptosystems. Communications of the ACM 21(2), 1978, 120–126 [http://doi.org/10.1145/359340.359342].

[34] Sharma R., Bollavarapu S.: Data Security using Compression and Cryptography Techniques. International Journal of Computer Applications 117(14), 2015, 15–18 [http://doi.org/10.5120/20621-3342].

[35] Wang S., Kim S. M., Yin Z., He T.: Encode when necessary: Correlated network coding under unreliable wireless links. ACM Transactions on Sensor Networks 13(1), 2017, article 7, 1–22 [http://doi.org/10.1145/3023953].

[36] Wang S., Zhang X., Liu X., Zhang J., Ma S., Gao W.: Utility Driven Adaptive Preprocessing for Screen Content Video Compression. IEEE Transactions on Multimedia 19(3), 2017, 660–667.

[37] Wang X., Xiao J., Hu R., Wang Z.: Cruise UAV Video Compression Based on Long-Term Wide-Range Background. Data Compression Conference (DCC), 2017, 466–467 [http://doi.org/10.1109/DCC.2017.71].

[38] Watanabe O., Uchida A., Fukuhara T., Kiya H.: An Encryption-then-Compression system for JPEG 2000 standard. IEEE International Conference on Acoustics, Speech and Signal Processing (ICASSP), 2015, 1226–1230 [http://doi.org/10.1109/ICASSP.2015.7178165].

[39] Wu H., Sun X., Yang J., Zeng W., Wu F.: Lossless Compression of JPEG Coded Photo Collections. IEEE Transactions on Image Processing 25(6), 2016, 2684–2696 [http://doi.org/10.1109/TIP.2016.2551366].

[40] Xiao W., Wan N., Hong A., Chen X.: A Fast JPEG Image Compression Algorithm Based on DCT. IEEE International Conference on Smart Cloud, 2020, 106–110 [http://doi.org/10.1109/SmartCloud49737.2020.00028].

[41] Yang Ch.-N., Chen Ch.-H., Cai S.-R.: Enhanced Boolean-based multi secret image sharing scheme. Journal of Systems and Software 116, 2016, 22–34 [http://doi.org/10.1016/j.jss.2015.01.031].

[42] Yuan L., Korshunov P., Ebrahimi T.: Secure JPEG Scrambling enabling Privacy in Photo Sharing. 11 th IEEE International Conference and Workshops on Automatic Face and Gesture Recognition (FG), 2015, 1–6 [http://doi.org/10.1109/FG.2015.7285022].

[43] Zhou J., Liu X., Au O. C., Tang Y. Y.: Designing an Efficient Image Encryption-Then-Compression System via Prediction Error Clustering and Random Permutation. IEEE Transactions on Information Forensics and Security 9(1), 2014, 39–50 [http://doi.org/10.1109/TIFS.2013.2291625].

Prof. Volodymyr Barannik
e-mail: vvbar.off@gmail.com

Doctor of Technical Sciences, Professor
Department of Artificial Intelligence and Software
V. N. Karazin Kharkiv National University
Number of articles in national databases – 750
Number of articles in international databases – 112

http://orcid.org/0000-0002-2848-4524

M.Sc. Natalia Barannik
e-mail: barannik11121972@gmail.com

Postgraduate student
Scientific Researcher Scientific Organizing Department
National University of Civil Defence of Ukraine, Ukraine
Number of articles in national databases – 17
Number of articles in international databases – 10

https://orcid.org/0000-0001-6420-1838

Ph.D. Oleksandr Slobodyanyuk
e-mail: slobodyanyuk.olexandr@kpnu.edu.ua

Associate professor at the Department of Computer Science in Kamianets-Podilsky Ivan Ohiienko National University.
Oleksandr Slobodyanyuk is the author more than 50 publications. His research interests include cybersecurity, data processing, algorithms and methods of video data compression.

http://orcid.org/0000-0001-5195-3053

otrzymano/received: 8.11.2021 *przyjęto do druku/accepted: 15.12.2021*

http://doi.org/10.35784/iapgos.2804

SELECTED APPLICATIONS OF DEEP NEURAL NETWORKS IN SKIN LESION DIAGNOSTIC

Magdalena Michalska-Ciekańska
Lublin University of Technology, Department of Electronics and Information Technology, Lublin, Poland

Abstract. *The article provides an overview of selected applications of deep neural networks in the diagnosis of skin lesions from human dermatoscopic images, including many dermatological diseases, including very dangerous malignant melanoma. The lesion segmentation process, features selection and classification was described. Application examples of binary and multiclass classification are given. The described algorithms have been widely used in the diagnosis of skin lesions. The effectiveness, specificity, and accuracy of classifiers were compared and analyzed based on available datasets.*

Keywords: dermatoscopic images, neural networks, melanoma, skin lesions

WYBRANE ZASTOSOWANIA GŁĘBOKICH SIECI NEURONOWYCH W DIAGNOZIE ZMIAN SKÓRNYCH

Streszczenie. *Artykuł zawiera przegląd wybranych zastosowań głębokich sieci neuronowych w diagnostyce zmian skórnych z obrazów dermatoskopowych człowieka z uwzględnieniem wielu chorób dermatologicznych, w tym bardzo niebezpiecznej z nich malignant melanoma. Został opisany proces segmentacji zmiany, selekcji cech i klasyfikacji. Uwzględniono przykłady binarnej i wieloklasowej klasyfikacji. Opisane algorytmy znalazły szerokie zastosowanie w diagnostyce zmian skórnych. Porównano i przeanalizowano skuteczność, specyficzność i dokładność klasyfikatorów w oparciu o dostępne zestawy danych.*

Słowa kluczowe: obrazy dermatoskopowe, sztuczne sieci neuronowe, melanoma, zmiany skórne

Introduction

In modern diagnostics of skin diseases, neural networks find a wide range of continguits. They are slowly displacing classical methods [4, 30]. These include methods based on: ABCD, Hunter, Menzies method [25], 7-point checklist [3], TDS, scale Glasgow, scale Hunter and many others [2, 6, 18].

Artificial intelligence is widely used in supporting diagnostic tools in dermatology. Deep learning and machine are effective in distinguishing melanoma from benign skin lesions based on clinical dermatoscopic images. Neural networks are also used in the classification process of dermatoscopic images [13, 11, 36].

An overview of the available methods using the networks has been provided in the [35]. In order for the process to run properly, you need to pay attention to many aspects. One of them is the preliminary preparation of dermatoscopic images. Many available dermatological databases contain images with artifacts: medical markers, applied scale, dark hair, air bubbles, are of poor quality (no contrast in them or are overexposed), the image does not cover the entire outline of the lesion. The next stage is to prepare an appropriate database of training and test images for a given class. Images previously diagnosed correctly by doctors based on a biopsy.

Deep neural networks consist of many layers, each of which identifies more complex elements of the input image. Figure 1 shows an example of a four-layer structure that analyse dermatoscopic images. The input picture of the skin lesion can be classified as a benign birthmark, or melanoma. The layers of the network are interconnected, they have been given appropriate weights. Each node (blue circle) in a layer is connected to each node in the next layer. In fact, the deep network is a much more complex structure than this shown example in figure 1.

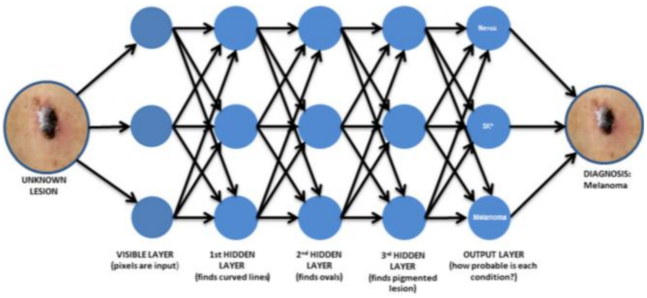

Fig. 1. Diagram of building a neural network [26]

Neural networks contain deep learning algorithms [8], deep convolutional neural networks DCNN [20], synergic deep learning. Great effectiveness achieve algorithms based on neural networks. A more complex structure becomes more effective for data with greater diversity. Also are made hybrid systems [37], witch connecting a model combining synergistic models and deep convolutional neural networks.

1. Segmentation and classification methods

Melanoma occurs in different areas of the body on the neck, torso, arms or legs. The resulting dermatoscopic images are of different quality and contain many artifacts. Therefore, for this, segmenting the entire skin lesion from the image is not an easy task. Traditional segmentation methods such as: adaptive thresholding, Otsu's thresholding, level set active contour, region growing become insufficient.

Increasingly, they are used for this purpose DCNN to train and perform region segmentation in melanoma test images [12, 27, 28]. Images with disease are used to trained model. Training images do not even require often preprocessing. For this purpose, they were used a hybrid deep learning approach based on CNN and recurrent neural network (RNN) [5]. Often researchers use use deep learning [9, 36] and a Deep Residual Network (DRN or ResNet). Efficiency of implementation deep region based convolutional neural network (RCNN) with Fuzzy C-mean (FCM) clustering was checked in [27]. Before the segmentation stage, regions of interest (ROI) are designated, which includes the skin lesion. Containing a fully convolutional neural network (FCN) and a specific convolutional neural network (CNN) in [5] allowed to obtain the result of accuracy 92%, a specificity 93% and a sensitivity 94%. The 28-layer FCN structure made segmentation and with a mask for (ROI).

In [19] researchers implemented neural networks for segmentation, superpixel masks for dermoscopic feature extraction and annotations for images classification procces. Dermatoscopic images from the ISIC database have been segmented and classified using multi-scale fully-convolutional residual networks and a lesion index calculation unit (LICU). Images are classified into three categories: melanoma, seborrheic keratosis and nevus. Scientists have developed framework is named as Lesion Indexing Network (LIN) shown in figure 2. It consists of two FCRN and a calculation unit for lesion index. The next step is bilinear interpolaction for two different images size to get SUM. LICU is result of algorithm, which include possibility and distance maps. The JA and AUC of LIN for segmentation and three categories classification get 0.753 and 0.912.

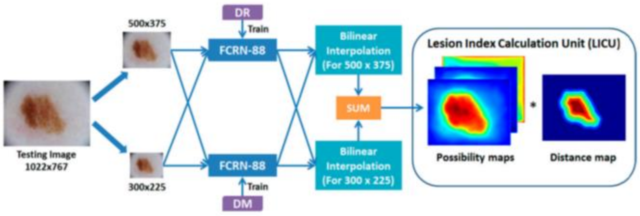

Fig. 2. Lesion Indexing Network (LIN) implementation in [19]

However CNN-based framework, named Lesion Feature Network (LFN) is responsible for dermoscopic feature extraction. The effectiveness of the implemented networks with different number of layers and different parameters, such as batch normalization, weighted softmax, was also studied. In [38] CNN was used to image feature learning and test segmentation results. Figure 3 shows the results of the segmentation algorithm. Binary images are test and real images, designated TP, FN, FN and TN. Classification was made in [10] using CNN based on over 120,000 clinical images.

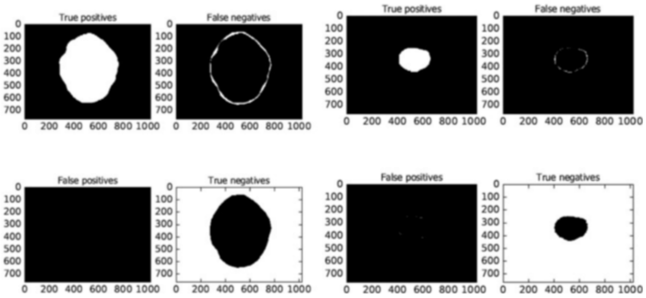

Fig. 3. Results of melanoma test segmentation (FP, TN, TP, FN) [38]

2. Lesions classification process

Deep learning is the basis for numerous applications in dermatology. International projects are also being created to collect a diverse database, and then finding an effective classification method for skin lesions. Such projects are of great interest among scientists. It is made multiclass classification and binary classification. Binary assumes only two classes: melanoma versus benign nevi or benign nonpigmented skin lesions [14]. More extensive classifications allow you to assess more skin diseases causing the formation of various birthmarks.

2.1. Binary classification

Research teams most often work on binary classification based on extensive databases of dermatoscopic images. In most works, the number of training images reaches 900 or even 2000. The images were previously diagnosed by doctors. Their diagnoses were confirmed by histopathological examinations. Gathering such large databases is not easy, it requires a lot of cooperation between scientists and dermatologists.

The mainly diagnosed skin disease that causes the formation of skin lesions is maliganat melanoma. It is diagnosed most often versus no-melanoma lesions or begin nevi. Neural networks are trained on two sets of data, marked as healthy and sick. Table 1 cites six works based on binary classification.

The cited works are characterized by a high level of sensitivity, AUC and specificity. In [29], images from mobile phones were even tested so that anyone with it could make a preliminary diagnosis of lesion using an application on the basis of a photo taken of the property.

Table 1. Binary classification results for dermatoscopic images [35]

Study	Dataset/No. of images	Classification task	Algorithm
[9]	1,279 (900 train, 379 test)	Melanoma versus melanocytic nevi	82% sensitivity, 62% specificity, AUC 0.84
[22]	1,279 (900 train, 379 test)	Melanoma versus melanocytic nevi	82% sensitivity, 76% specificity AUC 0.86
[12]	>100,000	Melanoma versus benign melanocytic nevi	AUC 0.86 (more difficult test-set-100); AUC 0.95 (test-set-300)
[7]	12,378	Melanoma versus atypical nevi	74.1% sensitivity, 86.5% specificity
[17]	Training set: 4,204 biopsyproven melanoma and nevi (1:1) Test set: 804 biopsy-proven melanoma and nevi (1:1)	Melanoma versus nevi	82.3% sensitivity, 77.9% specificity
[29]	Training set: not reported Test set: 551 biopsied lesions (including 125 melanoma) and 999 control lesions (assumed benign)	Melanoma versus nonmelanoma	100% sensitivity, 64.8% specificity with iPhone 6s images

2.2. Multiclass classification

Increasing interest in the processes of diagnosing skin lesions using artificial intelligence has resulted in the development of its use for the diagnosis of many skin diseases. More extensive network models were created, allowing for classification 3, 5, 7 and even 10 different disease. Of course, the introduction of more classes is associated with increased difficulties in solving the algorithm. Multiclass classification mostly helps diagnose nevus, dermatofibroma, melanoma, vascular lesions, benign keratosis, solar lentigo, benign keratosis. Examples of applications for this type of classification are presented in table 2.

Table 2. Multiclass classification results for dermatoscopic images [35]

Study	Dataset/No. of images	Classification task	Algorithm
[23]	Training set: 2,000 Test set: 150	3 disease classes (SK, melanoma, and nevus)	76% sensitivity, 85% specificity AUC 0.87
[24]	Training set: 11,444 Test set: 300 biopsy-verified	5 disease classes (AK, intraepithelial carcinoma, benign keratosis, melanocytic nevi, and melanoma)	AUC 0.96 macro-mean AUC for multiclass AUC 0.93 for benign versus malignant
[33]	Training set: 10,015 Test set: 1,195	7 disease classes (intraepithelial carcinoma including AK and Bowen's disease; BCC; benign keratinocytic lesions including solar lentigo, SK, and LPLK; dermatofibroma; melanoma; melanocytic nevi; and vascular lesions)	81.9% sensitivity, 96.2% specificity (top three algorithms of 139 challenge submissions)
[15]	Images from multiple sources	10 disease classes (nevus, angioma/angiokeratoma, SK, dermatofibroma, solar lentigo, AK, Bowen's disease, melanoma, BCC, and SCC)	95.0% sensitivity, 80.4% specificity for benign versus malignant

In [15], the highest number of class disease was diagnosed. Figure 4 shows boxplots ranked from begin to more malignat categories. Awarded probability scores in scale from 0 (lower probability of malignancy) to 1 (higher probability of malignancy).

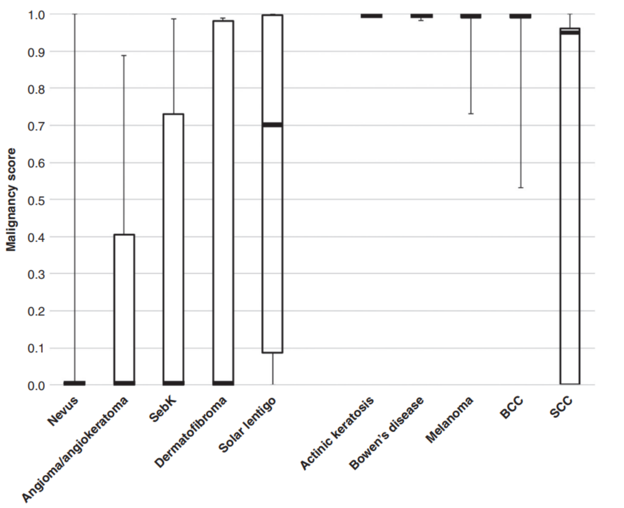

Fig. 4. CNN's melanoma probability scores for benign and malignant categories [15]

3. Features extraction

Convolutional networks have achieved great success in the features selection. There are three types convolutional neural network. First of them are convolution. Mostly they are sets of filters, which are learned for feature extractor to get representative map activation. Next to Pooling – statistically represent the previous layer, that helps to significantly reduce without loss images. The last one is Fully Conected Layer [1].

It is currently being used more and more to smaller receptive window size and smaller stride of the first layer. During training and testing the networks are used the whole image and multiple scales. It is also worth paying attention to the number of layers in the structure of the entire network – its depth. The number of layers should be selected according to the function performed and use of very small convolution filters in all layers. Another important element to fixing other parameters. Networks apply to other sets of images. They achieve excellent performance. That's way convolutional filters numbers of kernel size is kept on maximum small level. Figure 5 shows sparse CNN – Module inception construction. Networks uses convolutions of different sizes to capture details on scales (5×5, 3×3, 1×1).

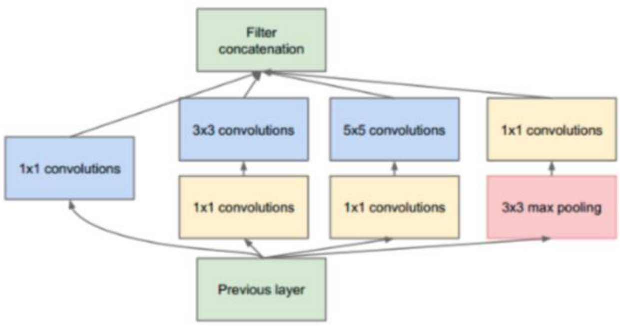

Fig. 5. Module inception construction [32]

In [34] in the first stage, the algorithms were given a modified 7-point method based on the ResNet-50 based supervised deep learning networks (figure 6). Obtained extracted features from dermatoscopic images. Next step is multimodal deep learning framework for automatic malignat melanoma and begin lesions detection by combining deep convolutional neural networks. Based on the obtained features was made clinically constrained classifier chain (CC).

In [34] in the first stage, the algorithms were given a modified 7-point method based on the ResNet-50 based supervised deep learning networks. Reached extracted features from dermatoscopic images. Next step is making multimodal deep learning framework for automatic malignat melanoma and begin lesions detection by combining deep convolutional neural networks. Based on the obtained features got clinically constrained classifier chain (CC).

Commonly known neural network structures are being modified, but new methods are also being used to support them. The applications of new methods are interesting. In [22] a new method called Lesion-classifier. It is based on pixel-wise binary classification on melanoma and non-melanoma cases. All model based on deep convolution encoder-decoder network is shown on figure 7.

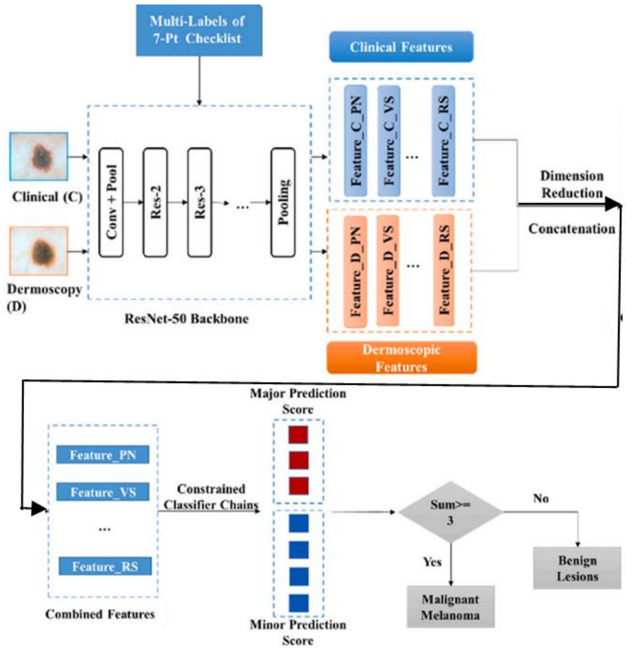

Fig. 6. Operation of the algorithm based on deep learning networks for features extraction [34]

```
procedure Encoder(X)      ▷ X: x (L, B, H) is an input
image with dimension L, B, H
    Extract the feature map F_map from the input image;
    For i = 0 to M-1:
    Set F_ci = Conv(F_map);
    Set F_ri = Relu(F_ci);
    Set F_pi = Pooling(F_ri);
    if i <= M then
    Set F_pi+1 = F_pi;
    else return F_pi
    end if
    end for
procedure Decoder(F_pi)      ▷ F_pi is the downsampled
feature maps
    For i =M−1 to 0:
    Set F_di = Upsamp(F_pi);
    Set F_ri = Relu(F_di);
    Set F_ci = Conv(F_ri);
    if i <= M AND i != 0 then
    Set F_pi−1 = F_ci;
    else return F_ci
    end if
    end for
Predictedpixels= softmaxclassifier(F_ci)   ▷ F_ci which is
the output from the decoder is sent to softmax classifier
function for pixel-wise prediction
Pi= cluster(Predictedpixels)   ▷ The predicted pixels are
clustered into segmented output
Finalresults= Pi      ▷ Final Segmented Output Display
Finalresults
```

Fig. 7. Algorithm based on DCN for binary classification from [1]

Many convolutional neural network from Keras library as VGG16 (512), VGG19 (512), ResNet50 (2048), InceptionV3 (2048) has been used for features extraction in many works [16, 21, 31, 32] – table 3. Artificial neural network structures used The best results were achieved by Logistic Regression using features extracted by the VGG19 with accuracy of 92.5% and F1-score (balance between precision and sensitivity) of 80% (the best result). Precision found by InceptionV3 with Logistic Regression was the best (87.88%).

Table 3. Results deep learning architectures with different classificators [21]

Architecture	Classifier	Accuracy	Precision	Recall	Specificity	F1-Score
InceptionV3	Logistic Regression	0.9250	0.8788	0.7250	0.9750	0.7945
	SVM Linear	0.9200	0.8333	0.7500	0.9625	0.7895
	Naive Bayes	0.7800	0.4750	0.9500	0.7375	0.6333
	SVM RBF	0.8700	0.8889	0.4000	0.9875	0.5517
	AdaBoost	0.7800	0.4500	0.4500	0.8625	0.4500
	Random Forest	0.8250	0.6923	0.2250	0.9750	0.3396
ResNet50	SVM Linear	0.9100	0.8438	0.6750	0.9688	0.7500
	Logistic Regression	0.9000	0.7941	0.6750	0.9563	0.7297
	Random Forest	0.8850	0.7931	0.5750	0.9625	0.6667
	Naive Bayes	0.8100	0.5152	0.8500	0.8000	0.6415
	SVM RBF	0.8850	0.9048	0.4750	0.9875	0.6230
	AdaBoost	0.8300	0.5750	0.5750	0.8938	0.5750
VGG16	Logistic Regression	0.9150	0.7949	0.7750	0.9500	0.7848
	SVM Linear	0.9100	0.7750	0.7750	0.9438	0.7750
	SVM RBF	0.8950	0.7317	0.7500	0.9313	0.7407
	Random Forest	0.8950	0.7714	0.6750	0.9500	0.7200
	Naive Bayes	0.8400	0.5667	0.8500	0.8375	0.6800
	AdaBoost	0.8700	0.6944	0.6250	0.9313	0.6579
VGG19	**Logistic Regression**	**0.9250**	**0.8571**	**0.7500**	**0.9688**	**0.8000**
	SVM Linear	0.9050	0.8182	0.6750	0.9625	0.7397
	Random Forest	0.9100	0.8929	0.6250	0.9813	0.7353
	SVM RBF	0.8950	0.8276	0.6000	0.9688	0.6957
	Naive Bayes	0.8150	0.5246	0.8000	0.8188	0.6337
	AdaBoost	0.8450	0.6452	0.5000	0.9313	0.5634

4. Discussion and conclusions

The process of diagnosing skin lesions based on neural networks is an issue of interest to many research teams, many works have been created in this field and further research is still being conducted. Currently, an important problem in the use of deep neural networks is the preparation of an appropriate database of dermatoscopic images, their initial preparation, taking an effective segmentation method and using a well-chosen structure for the lesion classification. In the future, most likely, the classic methods of diagnosing skin lesions based on geometry, shape of the lesion using segmentation will begin to be replaced by diagnostics based on the analysis of lesion texture.

References

[1] Adegun A., Viriri S.: Deep learning-based system for automatic melanoma detection. IEEE Access 8/2020, 7160–7172.
[2] Alendar F. et al.: Clear definitions, simple terminology, no metaphoric terms. Expert Rev Dermatol 3/2008, 27–29.
[3] Argenziano G. et al.: Epiluminescence microscopy for the diagnosis of doubtful melanocytic skin lesions. Comparison of the ABCD rule of dermatoscopy and a new 7-point checklist based on pattern analysis. Archives of Dermatology 134/1998, 1563–1570.
[4] Argenziano G. et al.: Dermoscopy of pigmented skin lesions: results of a consensus meeting via the Internet. Journal of American Academy of Dermatology 48(5)/2003, 679–693.
[5] Attia M. et al.: Skin melanoma segmentation using recurrent and convolutional neural networks. Biomedical Imaging (ISBI 2017) – 14th International Symposium, IEEE, 2017, 292–296.
[6] Blum H., Ellwanger U.: Digital image analysis for diagnosis of cutaneous melanoma. Development of a highly effective computer algorithm based on analysis of 837 melanocytic lesions. British Journal of Dermatology 151(5)/2004, 1029–1038.
[7] Brinker T. J. et al.: Deep learning outperformed 136 of 157 dermatologists in a head-to-head der moscopic melanoma image classification task. Eur J Cancer 113/2019, 47–54.
[8] Codella N., Cai J., Abedini M., Garnavi R., Halpern A., Smith J. R.: Deep Learning, Sparse Coding, and SVM for Melanoma Recognition in Dermoscopy Images. In: Zhou L., Wang L., Wang Q., Shi Y. (eds) Machine Learning in Medical Imaging. MLMI 2015. Lecture Notes in Computer Science 9352. Springer, Cham 2015 [http://doi.org/10.1007/978-3-319-24888-2_15].
[9] Codella N. et al.: Deep learning ensembles for melanoma recognition in dermoscopy images. 2016 [http://arxiv.org/abs/1610.04662] (accessed 4 October 2019).
[10] Esteva A. et al.: Dermatologist-level classification of skin cancer with deep neural networks. Nature 542/2017, 115–118.
[11] Esteva A.: Dermatologist-level classification of skin cancer with deep neural networks. Nat. Res. 542(7639), 2017, 115–118.
[12] Ge Y. et al.: Melanoma segmentation and classification in clinical images using deep learning. Proceedings of the 2018 10th International Conference on Machine Learning and Computing, 2018, 252–256.
[13] Ge Z. et al.: Skin disease recognition using deep saliency features and multimodal learning of dermoscopy and clinical images. Springer, Cham LNCS 10435, 2017, 250–258.
[14] Haenssle H. A. et al.: Man against machine: diagnostic performance of a deep learning convolutional neural network for dermoscopic melanoma recognition in comparison to 58 dermatologists. Ann Oncol 29/2018, 1836–1342.
[15] Haenssle H. A. et al.: Man against machine reloaded: performance of a market-approved convolutional neural network in classifying a broad spectrum of skin lesions in comparison with 96 dermatologists working under less artificial conditions. Ann Oncol 31/2020, 137–143.
[16] He K., Zhang X, Ren, S., Sun J.: Deep residual learning for image recognition, Proceedings of the IEEE conference on computer vision and pattern recognition, 2016, 770–778.
[17] Hekler A. et al.: Deep learning outperformed 11 pathologists in the classification of histopathological melanoma images. Eur J Cancer 118, 2019, 91–96.
[18] Kittler H. et al.: Dermatoscopy of unpigmented lesions of the skin: A new classification of vessel morphology based on pattern analysis. Dermatopathology: Practical & Conceptual 14(4), 2008, 3.
[19] Li Y., Shen L.: Skin lesion analysis towards melanoma detection using deep learning network. Sensors 18, 2018, 556.
[20] Lopez A. R. et al.: Skin lesion classification from dermatoscopic images using deep learning techniques. Biomedical Engineering 852, 2017, 852-053 [http://doi.org/10.2316/P.2017.852-053].
[21] Maia L. et al.: Evaluation of melanoma diagnosis using deep features. 25th International Conference on Systems, Signals and Image Processing (IWSSIP), 2018, 1–4.
[22] Marchetti M. A. et al.: Results of the 2016 international skin imaging collaboration international symposium on biomedical imaging challenge: comparison of the accuracy of computer algorithms to dermatologists for the diagnosis of melanoma from dermoscopic images. J Am Acad Dermatol 78, 2018, 270–277.
[23] Marchetti M. A. et al: Computer algorithms show potential for improving dermatologists' accuracy to diagnose cutaneous melanoma: results of the international skin imaging collaboration 2017. J Am Acad Dermatol 82, 2020, 622–627.
[24] Maron R. C. et al.: Systematic outperformance of 112 dermatologists in multiclass skin cancer image classification by convolutional neural networks. Eur J Cancer 119, 2019, 57–65.
[25] Menzies S. et al.: Frequency and morphologic characteristics of invasive melanomas lacking specific surface microscopic features. Archives of Dermatology 132, 1996, 1178–1182.
[26] Murphree D. H. et al.: Deep learning for dermatologists: Part I. J Am Acad Dermatol 2020, 1–9, [http://doi.org/10.1016/j.jaad.2020.05.05].
[27] Nida N. et al.: Melanoma lesion detection and segmentation using deep region based convolutional neural network and fuzzy C-means clustering. International Journal of Medical Informatics 124, 2019, 37–48.
[28] Nijeweme-d'Hollosy W. et al.: Evaluation of three machine learning models for self-referral decision support on low back pain in primary care. Int. J. Med. Inform. 110, 2018, 31–41.
[29] Phillips M. et al.: Assessment of accuracy of an artificial intelligence algorithm to detect melanoma in images of skin lesions. JAMA Netw Open 2, 2019, 1913436.
[30] Rosendahl C., Cameron A., McColl I., Wilkinson I.: Dermatoscopy in routine practice. Chaos and Clues. Australian Family Physician 41(7), 2012.
[31] Simonyan K., Zisserman A.: Very deep convolutional networks for large-scale image recognition. arXiv preprint arXiv:1409.1556, 2014.
[32] Szegedy C. et al.: Going deeper with convolutions. Proceedings of the IEEE conference on computer vision and pattern recognition, 2015, 1–9.
[33] Tschandl P et al.: Comparison of the accuracy of human readers versus machine-learning algorithms for pigmented skin lesion classification: an open, webbased, international, diagnostic study. Lancet Oncol 20, 2019, 938–947.
[34] Wang Y. et al.: Incorporating clinical knowledge with constrained classifier chain into a multimodal deep network for melanoma detection. Computers in Biology and Medicine 137, 2021, 104812.
[35] Young A. T. et al.: Artificial intelligence in dermatology: A Primer. Journal of Investigative Dermatology 140, 2020, 1504–1512.
[36] Yu L. et al.: Automated melano-ma recognition in dermoscopy images via very deep residual networks. IEEE transactions on medical imaging 36(4), 2017, 994–1004.
[37] Zhang J. et al.: Skin lesion classification in dermoscopy images using synergic deep learning. Springer Nature Switzerland, LNCS 11071, 2018, 12–20.
[38] Zhang X.: Melanoma segmentation based on deep learning. Computer Assisted Surgery 22, 2017, 267–277.

M.Sc. Magdalena Michalska-Ciekańska
e-mail: magdalena.michalska@pollub.edu.pl

Ph.D. student at Department of Electronics and Information Technology, Lublin University of Technology. Recent graduate Warsaw University of Technology The Faculty Electronics and Information Technology. Her research interests include medical image processing, optoelectronics, spectrophotometry.

http://orcid.org/0000-0002-0874-3285

otrzymano/received: 29.10.2021 *przyjęto do druku/accepted: 15.12.2021*

http://doi.org/10.35784/iapgos.2817

EFFICIENT LINE DETECTION METHOD BASED ON 2D CONVOLUTION FILTER

Paweł Kowalski, Piotr Tojza
Gdansk University of Technology, Faculty of Electrical and Control Engineering, Gdańsk, Poland

Abstract. *The article proposes an efficient line detection method using a 2D convolution filter. The proposed method was compared with the Hough transform, the most popular method of straight lines detection. The developed method is suitable for local detection of straight lines with a slope from -45˚ to 45˚. Also, it can be used for curve detection which shape is approximated with the short straight sections. The new method is characterized by a constant computational cost regardless of the number of set pixels. The convolution is performed using the logical conjunction and sum operations. Moreover, design of the developed filter and the method of filtration allows for parallelization. Due to constant computation cost, the new method is suitable for implementation in the hardware structure of real-time image processing systems.*

Keywords: image processing, real-time processing, Hough transform, straight lines detection

EFEKTYWNA METODA WYKRYWANIA LINII Z WYKORZYSTANIEM KONWOLUCYJNEGO FILTRU 2D

Streszczenie. *W artykule zaproponowano efektywną metodę wykrywania prostych z wykorzystaniem dwuwymiarowego filtru konwolucyjnego. Zaproponowana metoda została porównana z transformatą Hough, najpopularniejszą metodą wykrywania linii prostych. Opracowana metoda pozwala na wykrywanie linii prostych o nachyleniu od -45˚ to 45˚. Może również zostać wykorzystana do wykrywania krzywych, których kształt jest aproksymowany za pomocą krótkich prostych odcinków. Zaproponowana metoda charakteryzuje się stałym kosztem obliczeniowym, niezależnym od liczby pikseli. Splot wykonywany jest z wykorzystaniem logicznej koniunkcji oraz sumowania. Ponadto konstrukcja opracowanego filtru oraz zastosowana metoda filtracji pozwala na zrównoleglenie. Ze względu na stały koszt obliczeniowy, zaproponowana metoda nadaje się do implementacji w strukturze sprzętowej systemów przetwarzania obrazu w czasie rzeczywistym.*

Słowa kluczowe: przetwarzanie obrazu, przetwarzanie w czasie rzeczywistym, transformacja Hough, wykrywanie prostych

Introduction

Colinear pixels detection is often used in image processing. For example, for recognizing objects consisting of straight edges. The most commonly used method is the Hough transform [8]. It is characterized by high efficiency and low sensitivity to disturbances, as well as insensitivity to line discontinuity [5, 6]. The main part of this method is the voting procedure, in which each input image pixel is transformed into Hough space. Such a transformation requires determining a set of lines passing through a given pixel. It allows performing some kind of voting in two-dimensional Hough space. The voting results contain information about the number of pixels lying on each straight line. The high efficiency of this method and low noise sensitivity resulted in its modifications for the detection of more complex shapes. For instance, curve or circles detection [11, 12]. This is commonly achieved by extending the Hough space and the voting table to three dimensions. Similarly, the method can be extended to other shapes by broadening the number of dimensions, but this escalates computational cost [1, 8, 11, 12].

Hough transform can also be done by neutral networks, where it also extends the possibilities of detection [4, 7, 10] but due to multiplications during processing it may escalate computational cost.

In another approach, the method itself is not modified but is used for local detections. This approach allows the curve detection if the curve has got a slight curvature and locally is similar to a straight line. The computational cost of the global and local Hough method is similar. Detecting curves requires additional steps to connect the detected straight pieces together. This approach is often less computationally expensive than using the three-dimensional Hough method.

In both cases, broadening the dimensions of the voting matrix or connecting local parts together, allows the detection of more complex shapes, but enlarges the computational cost. The aim of the proposed method is reducing the computational cost compared to the standard Hough transform. The proposed method is dedicated to detect straight sections with an slope from -45˚ to 45˚. The main part of the proposed method is a 2D filtration with a developed set of masks. It is performed using the logical conjunction and sum operations.

1. Hough Transform

1.1. Cartesian space

Two-dimensional Cartesian Space allows to describe the position of a point by two coefficients (*x*,*y*). The origin of the coordinate system is represented as a point (0,0). By Cartesian space coefficients, it is possible to determine the position of all pixels in an image. A line in Cartesian space image can be represented as set of pixels described by formula (1)

$$y = ax + b\ . \tag{1}$$

Also, the line can be determined by the perpendicular vector Ψ connecting the straight line and the point (0,0). Such a vector has got the constant beginning (0, 0), so Ψ can be described using two coefficients: α and ρ, where α is the angle of the vector Ψ, and ρ is the length of the vector Ψ (Fig. 1).

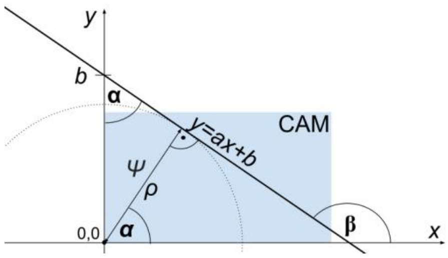

Fig. 1. Diagram of a line and Ψ vector in Cartesian space

The relation of the angle α and the coefficient a is defined in the formula (2)

$$a = -ctg(\alpha) \tag{2}$$

The length of the vector Ψ is defined as ρ (3)

$$\rho = sin\alpha\ \cdot y + cos\alpha\ \cdot x \tag{3}$$

1.2. Hough space

The Hough space is two-dimensional space closely related to the Cartesian space. The line from Cartesian space is established by a single point in Hough space. Such a point is defined as a pair of coefficients α and ρ. This representation allows voting in the Hough space.

1.3. Voting in the Hough space

The main part of the Hough transformation is the voting procedure, where each pixel in the Cartesian space votes on the lines that pass through it. A single line is defined as a pair α and ρ and calculated by point position x, y and specified α. The set of lines is determined by specifying a set of α coefficients. It is common practice to determine the set of angles α divisible by the selected *step* value. For example, selecting *step* = 1˚, each pixel of the Cartesian space will vote on 360 different lines. Saving the votes is performed by increasing the value of the cell (α, ρ) of the Hough space matrix. The result of the vote is a two-dimensional Hough space matrix, where the cell position dictates α and ρ and the cell value contains the number of votes.

1.4. Inverse transformation

The transformation of the vector (α, ρ) into the form (1) is called the inverse transformation. In this case, the coefficient a is defined by relation (2), and the coefficient b is determined by relation (4)

$$b = \frac{\rho}{sin\alpha} \tag{4}$$

Using the formula (1) allows determining all the pixels from the Cartesian space lying on the line. It can be used to draw this line in the image, for instance by changing the colour of these pixels.

2. New method

The new method was designed for the local detection of straight lines. For this purpose, the image is divided into vertical sections (Fig. 2). Straight lines are detected in each of these sections. Connecting short lines allows to identify straight lines and curves.

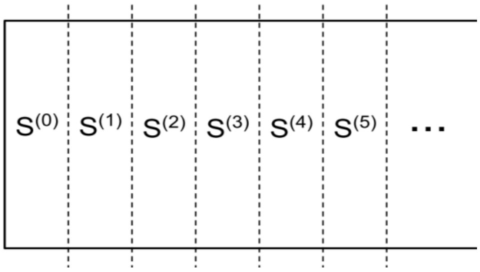

Fig. 2. The division of the image on the vertical sections

In the new method, the multiplication of the real numbers was eliminated. There is also no need to determine the values of the trigonometric functions. In the presented method, calculations are performed in the form of a two-dimensional filter using a predefined set of masks. Each mask contains a fragment of one straight line. Convolution of the masks and the window is achieved using logical conjunction. The result is a set of bits. The number of set bits in the string indicates the number of pixels lying on the straight line, which is similar to the results in standard Hough method.

2.1. Masks

The masks are designed to detect lines with slope from -45˚ to 45˚. A single mask is expressed by a binary matrix of the size $M_w \times M_h$, where $M_h = 2M_w - 1$. Each mask has been marked with identifiers *id*. The masks are created using (5)

$$m_{x,y}^{id} = \begin{cases} 1 \; if \; y \approx \frac{id - M_w}{M_w - 1}x + M_w - 1 \\ 0 \; else \end{cases} \tag{5}$$

where $m_{x,y}^{id}$ is the cell (x,y) of the mask M_h^{id}. Pixels lying on the line (5) take the value 1, and the rest of them the value 0. A graphical representation of the set of 15 masks of size 8×15 is shown in Fig. 3. The set bits are represented by white pixels.

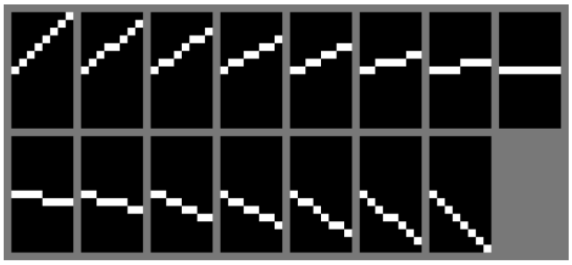

Fig. 3. Set of 15 masks with the size of 8 × 15

2.2. Convolution

The convolution is performed by moving the window W around the images and convoluting with a set of masks. Image is divided into sections (Fig. 2), where single section can be treated as image S with a width of M_w pixels. The size of the window W and the mask M in the presented algorithm are identical ($M_w \times M_h$). While processing, window W is moving in section S only vertically, so its position can be defined as single variable j. Each pixel in window W^j is described by formula (6)

$$w_{x,y}^{j} = s_{x,y+j-M_w+1} \tag{6}$$

where $w_{x,y}^{j}$ is the single pixel of window W^j, j is the window position, (x,y) is the position of the pixel in the window and $s_{x,y+j-M_w+1}$ is the pixel $x, y + j - M_w + 1$ of the section S.

The convolution with single mask was divided into two steps. First, the intermediate result is obtained by a logical conjunction of binary matrices M and W (7)

$$C = M \wedge W \tag{7}$$

Then the set bits in C are counted. It should be noted that the mask M includes only M_w set bits, so the result of the conjunction (7) can be saved in a sequence of M_w bits. The next step is counting set bits in the received binary string. Methods of counting bits was presented in section 2.3. The results from all convolutions are stored in table R in form presented in formula (8)

$$r_{j,id} = cb(M^{id} \wedge W^j) \tag{8}$$

where *id* means the mask *id*, j the position of the window W in section S, and *cb* the function of counting set bits in a binary string.

2.3. Counting set bits

The most time-consuming part of the new method is counting set bits in the binary string. In the simplest approach, the bits are added sequentially. For the n bit sequence it requires a n-1 summations.

Another example of a sequential algorithm is the Brian Kernighan algorithm [9]. Execution of this algorithm requires $4{\cdot}z$ elementary operations to determine the number of set bits, where z is the number of set bits in the string.

The quickest way is to store all results of counting bits of n bits strings in an array called a lookup table. Then the determination of the number of set bits is performed by reading the value directly from the memory. But it may require large amount of memory to keep the lookup table.

Counting the set bits may also be performed using a parallel algorithm. In this approach, all pairs of cells will be summed in each cycle. In each cycle, the number of cells summed is doubled. In that case it requires $\lceil log_2 n \rceil$ cycles.

Another approach is a hybrid method combining techniques with the use of partial results, called lookup table and the simple sequential algorithm. In the hybrid method, the input string is divided into sections of m bits. For each section, the number of set bits is determined by simply reading from the lookup table. It takes $\lceil M_w / \lfloor log_2 m \rfloor \rceil$ operations to obtain $\lceil M_w / \lfloor log_2 m \rfloor \rceil$ subsets. Simple addition of these results needs $\lceil M_w / \lfloor log_2 m \rfloor \rceil - 1$ operations. All in all, this procedure for counting the set bits takes $2 \cdot \lceil M_w / \lfloor log_2 m \rfloor \rceil - 1$ elementary operations. It is faster than simple summation for $m \geq 3$.

Another way to count bits is a combination of a parallel technique and a lookup table. In this case, the string is divided into m bit packets and the partial results are determined by parallel readings from the lookup table. The counting of bits in each section is also performed parallel. In this case, it takes $\lceil log_2 \lceil m/n \rceil \rceil + 1$ cycles and requires $\lceil n/m \rceil$ threads.

2.4. Searching for straight lines in the results

The detection of straight lines for both, the standard Hough method and the new method is similar. In both cases, the cell in the result array represents a single straight line, and the value determines the number of pixels lying on that line. Searching for straight lines is usually performed by thresholding the result table [6]. There is slight difference is the size of the resulting arrays of standard Hough method and new method. In the case of Hough, it is $M_h \times \sqrt{{S_h}^2 + {M_h}^2}$ cells, and in new method, it is $M_h \times S_h$.

3. Computational cost comparison of the new method and the standard Hough transform

The new method is dedicated for a narrow range of applications. Therefore, both methods are compared in detecting lines with M_h different slopes from -45˚ to 45˚. In the new method, the image S is divided vertically into sections of M_w pixels width (Fig. 2). Each section can be treated as a separate binary image of size $S_h \times M_w$. A similar computation will be performed for each section, so the single section processing cost will be compared. The comparison was divided into three sections, where memory cost, calculation cost and parallel efficiency were compared.

3.1. Memory cost

In both algorithms, a significant amount of memory is occupied by the result table and the lookup table. In the case of the standard Hough transform, using a lookup table to store all necessary *sin* and *cos* values reduces the computational cost [2, 3]. The size of such an array is $2M_h$. Additionally, for each section, one voting matrix of the size of $M_h \times \sqrt{{S_h}^2 + {M_h}^2}$ cells is created. The total memory cost is equal to $2M_h + M_h\sqrt{{S_h}^2 + {M_h}^2}$ cells.

In the case of the new method, for the comparison the lookup table for counting set bits in hybrid counting algorithm will be same size as the lookup table of the Hough method, $2M_h$.

The processing results of each section are kept in the matrix of size $M_h \cdot S_h$. The total cost is equal to $2M_h + M_h \cdot S_h$ memory cells. It can be seen that the new approach has got slightly lower memory requirements. The results of the memory cost comparison were shown in Table 1.

Table 1. Memory cost comparison

	Hough	New Method
lookup table	$2M_h$	$2M_h$
results table	$M_h \times \sqrt{{S_h}^2 + {M_h}^2}$	$M_h \cdot S_h$
total cost	$2M_h + M_h \cdot \sqrt{{S_h}^2 + {M_h}^2}$	$2M_h + M_h \cdot S_h$

3.2. Calculation cost

The exact calculation cost depends on the platform, which is being used to run the method. For comparative purposes, the impact of platform constraints on the results, such as the time of reading data from memory, was ignored. The computational cost was determined as the number of elementary operations, where each operation such as addition, multiplication or comparison costs one clock cycle.

The standard Hough transform requires three procedures. First, the set bits are searched for. This requires the $M_w \cdot S_h$ comparison operations. For each of the z bits found, a set of M_h straight lines is determined. This means computing a set of ρ coefficients. Each demands two multiplications by the *sin* and *cos* values from the lookup table and single sum operation (3). It means that determining the set of coefficients ρ takes $M_h \cdot z \cdot 3$ elementary operations. Determination of coefficients α is not included in the cost, because they are constant. Each pair of coefficients α and ρ votes by incrementing one cell of the result matrix. This requires the $z \cdot M_h$ increment operations. In total, performing the Hough transformation requires $M_w \cdot S_h + 4M_h \cdot z$ basic operations.

The new method is performed by the convolution of window size $M_w \times M_h$ with the set of M_h masks. After each convolution the window moves one pixel down. Processing the entire image requires $S_h \cdot M_h$ convolutions with masks. Convolution of the window with the single mask requires a single conjunction operation and then the set bits counting. The hybrid algorithm with lookup table of size $2M_h$ performs counting in $2 \cdot \lceil M_w / \lfloor log_2(2M_h) \rfloor \rceil - 1$ elementary operations. So processing the image $S_h \times M_w$ with the new algorithm requires $S_h \cdot M_h \cdot (2 \cdot \lceil M_w / \lfloor log_2(2M_h) \rfloor \rceil - 1)$ basic operations.

Fig. 4 shows the dependence of the number of the set pixels on the computational cost of the processing a single image section of size 32×1080 pixels. In the standard approach, the number of operations is proportional to the number of set pixels z. In contrast, the number of operations for the new method is regardless of the number of set pixels. For the amount of about 6% set pixels, the number of operations of both methods is equal. Above this threshold (6%), the new method requires less operations than the standard method. But below the threshold, the new method requires more operations than the standard method.

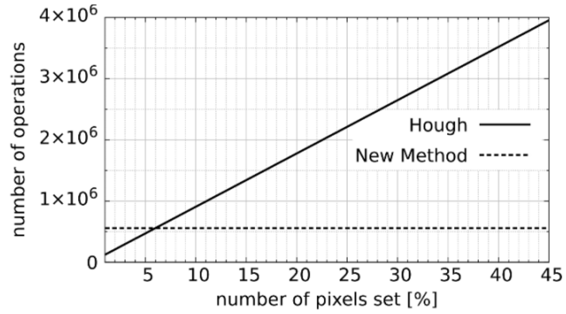

Fig. 4. The computational cost of processing a 32-pixel wide section of an image

Fig. 5 indicates the dependence of the image section width S_w on the threshold, where the number of operations of both methods is equal. This threshold is the highest, approximately 6%, for the 20-pixel section width. For sections, which are over 32 pixels wide, the threshold is less than 6%.

It should be noted that the standard method involves the multiplication of the real numbers, and the new algorithm uses only conjunction operations and the addition of integers.

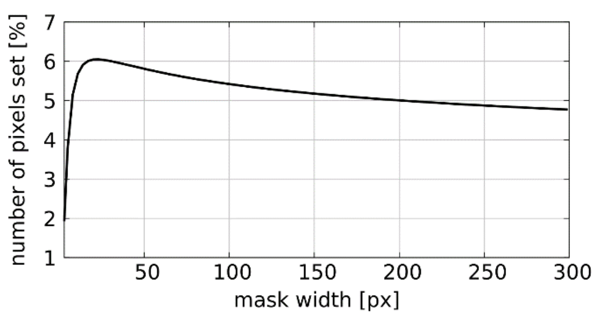

Fig. 5. Comparison of the computational cost of image processing using the standard Hough transform and the new algorithm

3.3. The cost of parallel processing

The standard approach requires a procedure of set pixels searching, determining ρ, and voting. Parallel search for set pixels in one cycle requires $S_w \times M_h$ threads. Each thread performs one comparison operation. Once the z set pixels are found, for each set pixel M_h coefficients ρ are determined. It requires $z \cdot M_h$ threads and 3 clock cycles. Then, each of the threads votes. Multiple threads will modify one cell of the result array, this requires thread synchronization. Even using memory, which allows parallel access to each memory location, the blocking time is equal to M_h operations.

In the case of the new method, the image processing is performed by the convolution procedure. It is composed of the conjunction of windows with masks and counting of set bits. This requires $S_h \cdot M_h$ threads. Each thread will perform a single conjunction operation. Then, the set bits are counted. Parallel counting requires $S_h \times M_h \cdot M_h/2$ threads and $log_2 M_h$ clock cycles. An alternative is the hybrid method, which requires $S_h \cdot M_h$ threads and $2 \cdot \lceil M_w / \lfloor log_2(M_h) \rfloor \rceil - 1$ clock cycles. Each result is stored in a different memory location, so all results can be saved simultaneously. It requires $S_h \cdot M_h$ threads and a single clock cycle. The results of the comparison were depicted in table 2.

Table 2. Parallel processing cost comparison

method	Threads OW	$\frac{operations}{thread}$	Bloking time
Hough, $z \le S_h/2$	$S_h \cdot M_h$	5	$2M_h$
Hough, $z > S_h/2$	$z \cdot M_h$	5	$M_h \cdot S_h$
New Method, parallel	$\frac{S_h \cdot M_h^2}{2}$	$\log_2 M_h$	
New Method, hybrid	$S_h \cdot M_h$	$2 \cdot \left\lceil \frac{M_h}{\lfloor log_2(2M_h) \rfloor} \right\rceil - 1$	

With the parallel Hough transform and fully parallel new method, the number of threads varies during processing. Moreover during the voting procedure of parallel Hough transform the threads sleep most of the time. By the contrast, with the new hybrid algorithm, a fixed number of threads is used throughout the entire process, and no one thread is sleeping at any time. Such effective use of computational capabilities makes this method suitable for hardware implementation in a real-time image processing system.

4. Comparison of basic operations

4.1. Line extension in the next section

The input image is split into sections with the width of M_w (Fig. 2). Lines are detected independently in each section. It makes the detection of the curved lines possible. The shape of a curved line can be approximated as many short straight lines, each in a separate section (Fig. 6).

To obtain the curve, the appropriate short sections must be connected. The convenient approach is to divide the image with sections overlapping by 1 pixel. In this case, the absolute position of the last pixel of the line in section $S^{(i)}$ is the same as the first pixel of the connected line in the section $S^{(i+1)}$. In order to find a connected line, first the position of the rightmost pixel of a given line should be calculated. Then, the straight line from the next section going through that pixel should be found. The cost of this procedure was compared for the results from standard Hough method and the new method.

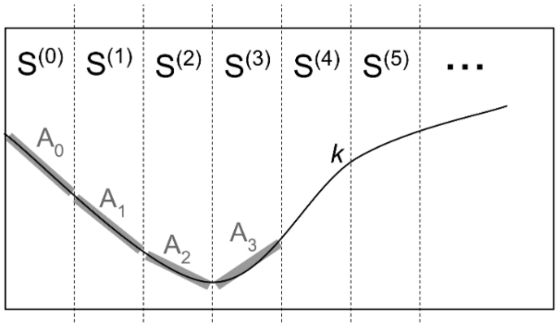

Fig. 6. Curve in sections

In the case of the Hough method, each section is associated with the Hough space voting results. The rightmost pixel of a line (α,ρ) in a section $S^{(i)}$ can be found by inverse transformation and using the formula (1). After locating this pixel in the next section $S^{(i+1)}$, it needs to be transformed to the Hough space getting M_h lines passing through this pixel. Then it should be checked, which of these lines has the most votes in the result table of section $S^{(i+1)}$. Such a procedure requires two operations for the inverse transformation, two operations for determining the point position in the section $S^{(i+1)}$, $3 \cdot M_h$ operations for the Hough transformation, and M_h operations for checking the voting table. In total, it requires $3 \cdot M_h + 4$ basic operations.

In the case of the new algorithm, the results from the section $S^{(i)}$ are stored in the array R of size $S_h \times M_h$. The straight line $r_{y,id}$ means that the line segment starts at the point (0,y) of the section and ends at the point (M_w,$y - M_w + id$). The continuation of the $r_{y,id}$ line from the $S^{(i)}$ section is $r_{y-M_w+id,k}$ from the $S^{(i+1)}$ section, where $k \in <0;\ M_h - 1>$ indicates M_h lines with different slopes. This procedure requires two operations to find the pixel in the next section and $M_h - 1$ operations to find the straight line with the highest score. In total, it requires $M_h + 1$ basic operations.

Straight line extension search for the standard approach requires an $3 \cdot M_h + 4$ operations. However, in the case of the new algorithm, it requires only $M_h + 1$ operations. In this case, the new method is much faster.

4.2. Check if a line from the result table passes through the selected point

In the case of the Hough method, the line is described by coefficients α_L, ρ_L and in case of new method by y_L, id_L. The basic operations is to check if a given point $P = (x_P, y_P)$ from the input image is part of the selected line.

In the case of the standard Hough transform, it consists in the inverse transformation and checking if the pixel P matches the obtained formula (1). This requires two operations for the inverse transformation and three operations to check if the point matches the formula. In total, this requires 5 basic operations.

In case of new method, checking if a line from the result table passes through the selected point requires inserting a pixel P into a blank window. It can be performed by single assignment operation. Then, the conjunction of this window with the mask id_L is made and check if the obtained result contains set bit. This procedure requires one operation to insert a pixel into the window, a single operation of window and mask conjunction, and a single operation to check if the result contains set bit. In total, this requires 3 basic operations. In both cases, the check can be done quickly.

4.3. Drawing the line in Cartesian space

After lines detection, drawing found lines in Cartesian space image is the common procedure. In the case of the standard Hough method, the inverse transformation should be performed. Then, for each x factor of the image, the y factor is calculated using the formula (1), and the M_w pixels are changed to make a line visible. The inverse transformation requires 2 operations. Determining the set of M_w points (x,y) requires $2 \cdot M_w$ operations. In total, this requires $2 \cdot M_w + 2$ basic operations.

In the case of the new algorithm, masks can be used for drawing. A single line in the voting matrix corresponds to a single mask. Drawing this line can be executed by logical disjunction of the appropriate mask and the appropriate part of the image. It can be done by a single logical operation. It is much faster than drawing a line based on standard Hough transformation results.

4.4. Parallel lines search

One of the common procedures of the detected lines processing is searching for parallel lines. In the case of standard Hough transform, lines $L1 = (\alpha_{L1}\rho_{L1})$ and $L2 = (\alpha_{L2}\,\rho_{L2})$ are parallel if $\alpha_{L1} = \alpha_{L2}$. Finding lines in Hough space with identical α coefficient can be done by a single column search of the result matrix. It requires $\sqrt{{S_h}^2 + {M_h}^2}$ comparison operations.

In the case of the new algorithm, The lines $L1 = (y_{L1}, id_{L1})$ and $L2 = (y_{L2}, id_{L2})$ are parallel if $id_{L1} = id_{L2}$. Finding the lines with identical id can be done by checking a single column of the result matrix. This requires S_h comparison operations.

In both cases, the search is performed with only comparison operations. The standard method requires $\sqrt{{S_h}^2 + {M_h}^2}$ comparisons, and the new method S_h comparisons.

5. Experiments

The developed method was used to detect overhead lines in photos with an environmental background. The test procedure is composed of the Canny edge detection algorithm and the developed method, which divides the image into sections 64 pixels wide. Straight lines are detected in each section. The results of processing sample photos are shown in Fig. 7, 8 and 9. Each example contains three images: a raw image (a), an image after edge detection with the Canny method (b), and an image with straight lines detected by the developed method (c).

Fig. 7. An example of image processing using the developed method: a) input image, b) Canny edge extraction, c) straight lines extraction by a developed method

Fig. 8. Curved wire detection: a) input image, b) Canny edge extraction, c) straight lines extraction by a developed method

Fig. 9. Detection of wires in front of trees: a) input image, b) Canny edge extraction, c) straight lines extraction by a developed method

6. Conclusion

The paper presents a new method of collinear pixels detection. The method is suitable for detecting straight lines with a slope from -45˚ to 45˚. An example of the method's application is detecting curves whose shape is locally approximated using short straight lines. The proposed method is characterized by a constant computational cost regardless of the number of set pixels. It is achieved by two-dimensional filtering using a dedicated set of masks performed using conjunction and sum operations. It eliminates real numbers multiplication. Due to constant computation cost, the new method is suitable for hardware implementation in a real-time processing system. The computational cost of selected operations performed after detecting straight lines was also compared. It has been shown that using the results of the new algorithm, it is faster to perform operations such as:

- line extension in the next section,
- checking whether a line passes through a selected point,
- drawing a line in the Cartesian space,
- searching for parallel lines.

The comparison was presented in table 3.

Table 3. Comparison of calculation costs of selected procedures after detecting straight lines

procedure	Hough	New Method
Line extension	$3 \cdot M_h + 4$	$M_h + 1$
Checking if a line passes through the point	5	3
Drawing a line in Cartesian space	$2 \cdot M_h + 2$	1
Parallel line search	$\sqrt{{S_h}^2 + {M_h}^2}$	S_h

References

[1] Ballard D. H.: Generalizing the hough transform to detect arbitrary shapes. Pattern recognition 13(2), 1981, 111–122.

[2] Elhossini A., Moussa M.: Memory efficient FPGA implementation of hough transform for line and circle detection. 25th IEEE Canadian Conference on Electrical and Computer Engineering (CCECE), 2012, 1–5

[3] Guan J., An F., Zhang X., Chen L., Mattausch H. J.: Real-time straight-line detection for xga-size videos by hough transform with parallelized voting procedures. Sensors 17(2), 2017, 270.

[4] Han Q., Zhao K., Xu J., Cheng M. M.: Deep hough transform for semantic line detection. 2020, arXiv preprint arXiv:2003.04676.

[5] Illingworth J., Kittler J.: A survey of the hough trans form. Computer vision, graphics, and image processing 44(1), 1988, 87–116.

[6] Kowalski P., Smyk R.: Straight lines detection in digital image using hough transform. Zeszyty Naukowe Wydziału Elektrotechniki i Automatyki Politechniki Gdanskiej 61, 2018, 45–48.

[7] Milletari F., Ahmadi S. A., Kroll C., Plate A., Rozanski V., Maiostre J., Levin J., Dietrich O., Ertl-Wagner B., Bötzel K., et al.: Hough-cnn: deep learning for segmentation of deep brain regions in mri and ultrasound. Computer Vision and Image Understanding 164, 2017, 92–102.

[8] Mukhopadhyay P., Chaudhuri B. B.: A survey of hough transform. Pattern Recognition 48(3), 2015, 993–1010.

[9] Ritchie D. M., Kernighan W., Lesk M. E.: The C programming language. Prentice Hall Englewood Cliffs, 1988.

[10] Serra P. L., Masotti P. H., Rocha M. S., de Andrade D. A., Torres W. M., de Mesquita R. N.: Two-phase flow void fraction estimation based on bubble image segmentation using randomized hough transform with neural network (rhtn). Progress in Nuclear Energy 118, 2020, 103133.

[11] Shehata Hassanein A., Mohammad S., Sameer M., Ehab Ragab M.: A survey on hough transform, theory, techniques and applications. 2015, arXiv:1502.02160.

[12] Ye H., Shang G., Wang L., Zheng M.: A new method based on hough transform for quick line and circle detection. IEEE 8th International Conference on Biomedical Engineering and Informatics (BMEI), 2015, 52–56.

Ph.D. Eng. Paweł Kowalski
e-mail: pawel.kowalski@pg.edu.pl

Assistant professor at the Department of Electrical and High Voltage Engineering, Faculty of Electrical and Control Engineering, Gdańsk University of Technology. His research interest include computer vision, real time image processing and embedded systems and hardware structures in FPGA.

http://orcid.org/0000-0002-0913-1408

Ph.D. Eng. Piotr M. Tojza
e-mail: piotr.tojza@pg.edu.pl

Piotr Tojza finished his M.Sc. in 2011 at Gdansk University of Technology in the field of Control Engineering and Robotics. In 2016 he obtained his Ph.D. in Bioengineering. His main field of scientific interests are: biomechatronics, medical diagnostic systems and decision supporting systems. From 2016 he is an adjunct professor at Gdansk University of Technology, Department of Biomechatronics. From 2017 he is also a medical student at the Medical University of Gdansk, Faculty of Medicine.

http://orcid.org/0000-0002-0837-0976

otrzymano/received: 10.11.2021 *przyjęto do druku/accepted: 15.12.2021*

http://doi.org/10.35784/iapgos.2788

FACTOR ANALYSIS METHOD APPLICATION FOR CONSTRUCTING OBJECTIVE FUNCTIONS OF OPTIMIZATION IN MULTIMODAL TRANSPORT PROBLEMS

Serhii Zabolotnii[1], Artem Honcharov[2], Sergii Mogilei[3]

[1]Cherkasy State Business-College, Cherkasy, Ukraine, [2]Cherkasy State Technological University, Cherkasy, Ukraine, [3]Rauf Ablyazov East European University, Cherkasy, Ukraine

Abstract. *The paper regards a specific class of optimization criteria that possess features of probability. Therefore, constructing objective function of optimization problem, the importance is attached to probability indices that show the probability of some criterial event or events to occur. Factor analysis has been taken for the main method of constructing objective function. Algorithm for constructing objective function of optimization is done for criterion of minimization risk level in multimodal transportations that demanded demonstration data. The application of factor analysis in classical problem solution was shown to give the problem a more distinct analytical interpretation in solving it.*

Keywords: factor analysis, risk function, optimization criterion, multimodal transportation

ZASTOSOWANIE METODY ANALIZY CZYNNIKOWEJ DO KONSTRUOWANIA FUNKCJI CELU OPTYMALIZACJI W PROBLEMACH TRANSPORTU MULTIMODALNEGO

Streszczenie. *Artykuł dotyczy szczególnej klasy kryteriów optymalizacyjnych, które posiadają cechy prawdopodobieństwa. W związku z tym, przy konstruowaniu funkcji celu problemu optymalizacyjnego pierwszorzędne znaczenie mają wskaźniki prawdopodobieństwa wystąpienia określonego zdarzenia lub zbioru zdarzeń. Jako główną metodę konstruowania takiej funkcji celu wybrano analizę czynnikową. Algorytm konstrukcji funkcji celu optymalizacji wykonano dla kryterium minimalizacji poziomu ryzyka w przewozach multimodalnych – w tym celu wykorzystano dane demonstracyjne. Wykazano, że zastosowanie analizy czynnikowej w klasycznym sformułowaniu problemu badawczego pozwala nadać mu bardziej wyrazistą interpretację analityczną w jego rozwiązywaniu.*

Słowa kluczowe: analiza czynnikowa, funkcja ryzyka, kryterium optymalizacji, transport multimodalny

Introduction

World globalization is inevitably affecting all human spheres. Besides, scientific and applied provision of human lives is to cater modern demands. Transportation in this respect appears to be a most urgent one. Passengers and goods deliveries are made for longer and longer distances and are required to be fast and of high quality, and also safe and inexpensive. Transportation costs being provided through free market economy competition the transportation safety risks are to be specially regarded.

Long distance transportations often require complicated logistics solutions. In passenger transportations, at least a changing or several of them are to be made, and in case of freight transportations, transmitting transportation knots (hubs or terminals) are to be arranged. However, their feature in common is that they both use several transportation means. Hence, transportations that consequently, or one by one, use several means of transportation are called intermodal. Those that use the means of transport simultaneously, or in parallel order, are called multimodal. Combined or mixed transportations are both intermodal and multimodal.

Dealing with transportation safety, presume the issue of risk level for multimodal freight transportations to be discovered in the paper. Multimodal transport problems as a separate class of optimization problems are taken for main models of these transportations. Hence, the research focuses on the problem of constructing objective functions to minimize risks in multimodal transportations.

Some analysts [13] consider intermodal transportations to be a part of multimodal ones. Such approach seems to be quite reasonable, though, to stick to distinct terminology, the notions of intermodal and multimodal transportations should be applied in the above mentioned sense.

Multimodal transportations are given quite a few investigations [1, 2, 5, 7, 8, 16, 18, 22], whereas a multimodal transport problem gets a vast mathematical analysis involved into the solution as well as possibilities of modern information technologies. Thus, in [9] a multimodal transport problem is revealed through various program means, while the problem regarded in the paper may be much more complex and applied to practical needs. It is presumably to be done through combining different optimization functions of a multimodal transport problem, for instance, a risk function.

While creating objective functions for minimizing risk in multimodal transportations, it should be for the first thing singled out what are parameters and variables of the objective function in a certain multimodal transport problem. Alike with a classical transport problem, the variables are to be indices of transportations amount between departure and delivery points, whereas this paper is focused on methods of finding out parameters of the risk objective function. Thus, in [20] there was an attempt of analyzing the issue under consideration, and, as a prospective research method, a method of group factor analysis was suggested [12]. However, this paper regards as the main method not a group, but an ordinary factor analysis.

The choice of research method accounts for several reasons. Firstly, factor analysis is the one quite spread and well-studied in applied science. It is especially popular in psychology and biomedicine [3, 10, 11]. Secondly, a group factor analysis applied, for instance, in machine training [19, 23] really seems to be quite a perspective, but cannot be fully applied in the given context.

1. Problem statement and solution by factor analysis method

Classical criterion for minimizing summary cost of multimodal transportations corresponds to objective minimization function given in [21] as follows:

$$S=\sum_{i,j=1}^{m,n}a_{ij}x_{ij}+\sum_{i,j=1}^{m,n}b_{ij}y_{ij}+\sum_{i,j=1}^{m,n}c_{ij}z_{ij}\rightarrow\min \qquad (1)$$

where $i=\overline{1,n},\ j=\overline{1,m}$ are n of departure points and m of delivery points correspondingly;

x_{ij}, y_{ij}, z_{ij} – number of goods transported from i departure point to j delivery point by automobile, railroad and river means of transport correspondingly;

a_{ij}, b_{ij}, c_{ij} – cost of transporting 1 item of goods from i departure point to j delivery point by automobile, railroad and river means of transport correspondingly;

S – cost function.

Objective function for a multimodal transport problem according to the criterion of minimal risk level is given in [20] and constructed similarly to objective function of minimizing cost for a classical (multimodal) transport problem. Therefore, this research regards the problem as a classical one.

With 3 means of transport, the objective function given in [21] as follows:

$$R=\sum_{i,j=1}^{m,n} f_{ij}x_{ij}+\sum_{i,j=1}^{m,n} g_{ij}y_{ij}+\sum_{i,j=1}^{m,n} h_{ij}z_{ij} \to \min \quad (2)$$

where f_{ij}, g_{ij}, h_{ij} – risk coefficient of goods transportation from i point of departure to j point of delivery by means of automobile, railroad or river transport correspondingly;

R – transportation risk function.

There is a number of ways to find out risk parameters f_{ij}, g_{ij}, h_{ij} while constructing objective function (2). Here are two of them:

1. Risk in transporting one unit of load.

The method is a logical consequence of the problem under consideration: hence, each parameter f_{ij}, g_{ij}, h_{ij} in (2) stands for damage risk while transporting 1 unit of load from i point of departure to j point of delivery by automobile, railroad and river means correspondingly.

Regard the example: in case transportation risk level of a load unit is 0.1 (10%) then transportation risk level for 2 units will be 0.01 (1%) etc. In mathematical aspect, it is obviously wrong but the problem does not require exact calculations of risk level, instead, it presupposes option of the least among all possible values. Therefore, such an approach to the problem can be considered as correct.

2. The grades of risk level according to number of transportations.

If to calculate yet more exact coefficients f_{ij}, g_{ij}, h_{ij} within classical approach, the grades of risk level according to number of transportations might be suggested.

In this case, objective function (2) is to be illustrated by grade coefficients tables, for example (Table 1).

Table 1. The grades of risk level for automobile transportations

Gradation level	$\min x_{ij}$	$\max x_{ij}$	Risk level
1	0	p	f_{ij}^{1}
2	p+1	l	f_{ij}^{2}
3	l+1	q	f_{ij}^{3}
4	q+1	…	…

In Table 1, indices $\min x_{ij}$ and $\max x_{ij}$ stand for minimal and maximal value for the number of automobile transportations correspondingly, whereas $p, l, q \in R$ and $0<p<l<q$.

For railroad and river transportations, the related tables are similarly created.

The main advantage of applying classical approach to the problem is unification of functions (1) and (2). That may be necessary for a multicriteria multimodal transportation problem solution within which both objective functions (1) and (2) would appear simultaneously as optimization criteria.

In any case, there appears a necessity of calculating coefficients values f_{ij}, g_{ij}, h_{ij} analytically. To this effect, factor analysis method, or factor approach, would be applied.

Expression (2) is written as follows:

$$R=R_a+R_r+R_w \to \min \quad (3)$$

where $R_a=\sum_{i,j=1}^{m,n} f_{ij}x_{ij}$, $R_r=\sum_{i,j=1}^{m,n} g_{ij}y_{ij}$, $R_w=\sum_{i,j=1}^{m,n} h_{ij}z_{ij}$ – is a summary risk for transportation loads from i point of departure to j point of delivery by means of automobile, railroad and river transport (taken separately), correspondingly.

Next, additional variables are to be introduced to mark risk factors: $\alpha_{ij}^k, \beta_{ij}^k, \gamma_{ij}^k$, which are values for k risk factor when goods are transported from i departure point to j delivery point by means of automobile, railroad and river transport correspondingly.

According to methodology suggested in [12], it may be written as:

$$f_{ij}=\sum_{i,j,k=1}^{m,n,v} \alpha_{ij}^k w_\alpha^k + o_{ij}^f$$

$$g_{ij}=\sum_{i,j,k=1}^{m,n,v} \beta_{ij}^k w_\beta^k + o_{ij}^g \quad (4)$$

$$h_{ij}=\sum_{i,j,k=1}^{m,n,v} \gamma_{ij}^k w_\gamma^k + o_{ij}^h$$

where $w_\alpha^k, w_\beta^k, w_\gamma^k$ are weight coefficients of introducing (factor weights) of k risk factor to general index of transportation risk by automobile, railroad and river transport (taken for certain);

$o_{ij}^f, o_{ij}^g, o_{ij}^h$ – "Gaussian noise" or in other words a value that does not essentially affect the ultimate calculated result and the value of which could be neglected.

Besides, in general case, it could be admitted:

$$0<w_\alpha^k, w_\beta^k, w_\gamma^k<1,\; w_\alpha^k+w_\beta^k+w_\gamma^k=1.$$

Next, coming from (4) back to (3):

$$R_a=\sum_{i,j,k=1}^{m,n,v} (\alpha_{ij}^k w_\alpha^k + o_{ij}^f)x_{ij}$$

$$R_r=\sum_{i,j,k=1}^{m,n,v} (\beta_{ij}^k w_\beta^k + o_{ij}^g)y_{ij} \quad (5)$$

$$R_w=\sum_{i,j,k=1}^{m,n,v} (\gamma_{ij}^k w_\gamma^k + o_{ij}^h)z_{ij}$$

Through neglecting in (5) the values of components in "Gaussian noise", the ultimate expression is:

$$R=\sum_{i,j,k=1}^{m,n,v} (\alpha_{ij}^k w_\alpha^k x_{ij} + \beta_{ij}^k w_\beta^k y_{ij} + \\ +\gamma_{ij}^k w_\gamma^k z_{ij}) \to \min \quad (6)$$

Taking into account that since $\alpha_{ij}^k, \beta_{ij}^k, \gamma_{ij}^k$ are matrix values for cases i and j, and each of the elements $w_\alpha^k, w_\beta^k, w_\gamma^k$ is a vector, for instance, of the type $w_\alpha^k=(w_\alpha^1; w_\alpha^2; ...; w_\alpha^v)$, therefore, the following equation is applied:

$$f_{ij}=(\alpha_{ij}^1)\cdot w_\alpha^1+(\alpha_{ij}^2)\cdot w_\alpha^2+...+(\alpha_{ij}^v)\cdot w_\alpha^v \quad (7)$$

For parameters g_{ij}, h_{ij} (7) is given in the same way.

That demonstrates that through factor analysis method the analytical expression which reveals the criterion of minimization of risk objective function for multimodal transport problem could be considerably specified. Besides, factor approach to the problem solution is proved to be a logical consequence of classical approach.

2. Problem solution for model example

The solution of the given problem could be done by applying model data which would be a preparatory stage for ultimate risk transportation function (2) or (6) that could be solved through program aids [4, 6, 14, 15, 17].

Main propositions for the problem are as follows:

1) Departure and delivery points are the same in number and are equal to 3: $m = n = 3$.
2) Risk factors are as well 3 in number: $v = 3$.
   Among risk factors are: damage ($k = 1$), disorder ($k = 2$), force majeur ($k = 3$).
3) Vectors of weight factors are as follows (for each transport means):
   Automobile: $\bar{w}_\alpha^k = (w_\alpha^1; w_\alpha^2; w_\alpha^3) = (0.5; 0.4; 0.1)$
   Railroad: $\bar{w}_\beta^k = (w_\beta^1; w_\beta^2; w_\beta^3) = (0.6; 0.25; 0.15)$
   River: $\bar{w}_\gamma^k = (w_\gamma^1; w_\gamma^2; w_\gamma^3) = (0.45; 0.5; 0.05)$
4) Values for indices $\alpha_{ij}^k, \beta_{ij}^k, \gamma_{ij}^k$ are given as matrices (for each transport means):

Automobile:

$$\alpha_{ij}^1 = \begin{pmatrix} 0.1 & 0.2 & 0.15 \\ 0.3 & 0.17 & 0.11 \\ 0.15 & 0.07 & 0.13 \end{pmatrix}$$

$$\alpha_{ij}^2 = \begin{pmatrix} 0.2 & 0.23 & 0.14 \\ 0.31 & 0.07 & 0.21 \\ 0.16 & 0.03 & 0.1 \end{pmatrix}$$

$$\alpha_{ij}^3 = \begin{pmatrix} 0.15 & 0.12 & 0.25 \\ 0.13 & 0.1 & 0.12 \\ 0.19 & 0.08 & 0.09 \end{pmatrix}$$

Railroad:

$$\beta_{ij}^1 = \begin{pmatrix} 0.3 & 0.02 & 0.17 \\ 0.13 & 0.08 & 0.1 \\ 0.25 & 0.04 & 0.03 \end{pmatrix}$$

$$\beta_{ij}^2 = \begin{pmatrix} 0.02 & 0.15 & 0.11 \\ 0.21 & 0.27 & 0.1 \\ 0.06 & 0.23 & 0.01 \end{pmatrix}$$

$$\beta_{ij}^3 = \begin{pmatrix} 0.05 & 0.13 & 0.4 \\ 0.14 & 0.19 & 0.12 \\ 0.17 & 0.04 & 0.19 \end{pmatrix}$$

River:

$$\gamma_{ij}^1 = \begin{pmatrix} 0.2 & 0.1 & 0.12 \\ 0.13 & 0.07 & 0.21 \\ 0.19 & 0.01 & 0.11 \end{pmatrix}$$

$$\gamma_{ij}^2 = \begin{pmatrix} 0.3 & 0.22 & 0.17 \\ 0.11 & 0.03 & 0.2 \\ 0.19 & 0.04 & 0.01 \end{pmatrix}$$

$$\gamma_{ij}^3 = \begin{pmatrix} 0.16 & 0.2 & 0.05 \\ 0.14 & 0.15 & 0.23 \\ 0.13 & 0.18 & 0.19 \end{pmatrix}$$

According to (7), they result in:

$$f_{ij} = (\alpha_{ij}^1)\cdot w_\alpha^1 + (\alpha_{ij}^2)\cdot w_\alpha^2 + (\alpha_{ij}^3)\cdot w_\alpha^3$$
$$g_{ij} = (\beta_{ij}^1)\cdot w_\beta^1 + (\beta_{ij}^2)\cdot w_\beta^2 + (\beta_{ij}^3)\cdot w_\beta^3$$
$$h_{ij} = (\gamma_{ij}^1)\cdot w_\gamma^1 + (\gamma_{ij}^2)\cdot w_\gamma^2 + (\gamma_{ij}^3)\cdot w_\gamma^3$$

Either, substituting exact values:

$$f_{ij} = \begin{pmatrix} 0.145 & 0.204 & 0.156 \\ 0.287 & 0.123 & 0.151 \\ 0.158 & 0.055 & 0.114 \end{pmatrix}$$

$$g_{ij} = \begin{pmatrix} 0.1925 & 0.069 & 0.1895 \\ 0.1515 & 0.144 & 0.103 \\ 0.1905 & 0.0875 & 0.049 \end{pmatrix}$$

$$h_{ij} = \begin{pmatrix} 0.248 & 0.165 & 0.1415 \\ 0.1205 & 0.054 & 0.206 \\ 0.187 & 0.0335 & 0.064 \end{pmatrix}$$

Coefficients $w_\alpha^k, w_\beta^k, w_\gamma^k$ could as well be presented as matrices, which would be valid in case values of factor weights are dependent on concrete points of departure and delivery. However, it does not especially affect the principle of finding out coefficients f_{ij}, g_{ij}, h_{ij}.

Thus, the model example demonstrates algorithm for calculating parameters f_{ij}, g_{ij}, h_{ij} for objective function (2).

3. Conclusions

The paper regards the objective risk function of multimodal transport problem. It presents algorithm for calculating this function's parameters, together with factor analysis method for their definition.

The obtained results perfectly correlate with classical solution for a multimodal transport problem and could be further applied for solving multicriteria multimodal transportation problems. Risk objective function is constructed for three transport means: automobile, railway, river. Though, the problem considered in this form could be extended for any finite number of goods delivery. For a classical problem, application of factor analysis method results in more concrete analytical interpretation of this type of solution in the course of solving the problem. Correspondingly, similar approach could be applied for solving other problems of the type.

Further studies could be devoted to application of elements of this method as a group factor analysis while finding out values of parameters of minimization risk function. For example, creating different hierarchies of influence factors should be regarded to affect the ultimate risk objective function in the problem given.

References

[1] Ayed H., Galvez-Fernandez C., Habbas Z., Khadraoui D.: Solving time-dependent multimodal transport problems using a transfer graph model. Computers and Industrial Engineering 61, 2011, 391–401 [http://doi.org/10.1016/j.cie.2010.05.018].

[2] Ayed H., Habbas Z., Khadraoui D., Galvez-Fernandez C.: A parallel algorithm for solving time dependent multimodal transport problem. IEEE Conference on Intelligent Transportation Systems, Proceedings, ITSC, 2011, 722–727 [http://doi.org/10.1109/ITSC.2011.6082973].

[3] Boyd K. C.: Factor analysis. The Routledge Handbook of Research Methods in the Study of Religion 2013, 204–216 [http://doi.org/10.4324/9780203154281-22].

[4] Chandrakantha L.: Using excel solver in optimization problems. John Jay College of Criminal Justice of CUNY, 2014, 42–49.

[5] Elias D., Nadler B., Nadler F., Hauger G.: OPTIHUBS – Multimodal Hub Process Optimization by Means of Micro Simulation. Transportation Research Procedia 14, 2016, 457–466 [http://doi.org/10.1016/j.trpro.2016.05.098].
[6] Ezeokwelume O.: Solving linear programming problems and transportation problems using excel solver. International Journal of Scientific & Engineering Research 7(9), 2016, 134–142.
[7] Flórez J. E., Torralba A., García J., Linares López C., García-Olaya A., Borrajo D.: TIMIPLAN: An Application to Solve Multimodal Transportation Problems. Scheduling and Planning Applications Workshop 2010.
[8] García J., Florez J. E., Torralba A., Borrajo D., López C. L., García-Olaya A., Sáenz J.: Combining linear programming and automated planning to solve intermodal transportation problems. European Journal of Operational Research 227, 2013, 216–226.
[9] Honcharov A., Mogilei S.: Solving multimodal transportation problems by different program means. Bulletin of Cherkasy State Technological University 3, 2020, 67–74.
[10] Jennrich R. I., Bentler P. M.: Exploratory Bi-Factor Analysis. Psychometrika 76(4), 2011, 537–549 [http://doi.org/10.1007/s11336-011-9218-4].
[11] Journal I., Factor I.: Computational and Mathematical Methods in Medicine. Bio Med Research International 1, 2015, 2–4.
[12] Klami A., Virtanen S., Leppaaho E., Kaski S.: Group Factor Analysis. IEEE Transactions on Neural Networks and Learning Systems 26(9), 2015, 2136–2147 [http://doi.org/10.1109/TNNLS.2014.2376974].
[13] Lin C. C., Lin S. W.: Two-stage approach to the intermodal terminal location problem. Computers and Operations Research 67, 2016, 113–119 [http://doi.org/10.1016/j.cor.2015.09.009].
[14] Ovcharuk V., Vovkodav N., Kryvets T., Ovcharuk I.: Linear programming in Mathcad on the example of solving the transportation problem. Scientific Works of NUFT 21(4), 2015, 110–117.
[15] Sengamalaselvi J.: Solving transportation problem by using Matlab. International Journal of Engineering Sciences & Research Technology 6(1), 2017, 374–381 [http://doi.org/10.5281/zenodo.259588].
[16] Slavova-Nocheva M.: Competitiveness of the transport market in Bulgaria. Economic Studies 21(3), 2012, 15–24.
[17] Vats B., Kumar Singh A.: Solving transportation problem using excel solver for an optimal solution. MIT International Journal of Mechanical Engineering 6(1), 2016, 18–20.
[18] Verga J., Silva R. C., Yamakami A.: Multimodal transport network problem: Classical and innovative approaches. Studies in Fuzziness and Soft Computing, Springer Verlag 358, 2018, 299–332 [http://doi.org/doi:10.1007/978-3-319-62359-7_14].
[19] Virtanen S., Klami A., Khan S.A., Kaski S.: Bayesian group factor analysis. The Journal of Machine Learning Research 22, 2012, 1269–1277.
[20] Zabolotnii S., Mogilei S., The methods for determining the parameters of the objective function of multimodal transportation risk. Proceedings of V International Scientific-Practical Conference "ITEST-2020", 2020, 114–115.
[21] Zabolotnii S., Mogilei S.: Optimization of the method of constructing reference plans of multimodal transport problem. Technological audit and production reserves 2(45), 2019, 15–20 [http://doi.org/10.15587/2312-8372.2019.154561].
[22] Zelenika R., Sever D., Zebec S., Pirš B.: Logistic operator: Fundamental factor in rational production of services in multimodal transport. Promet - Traffic&Transportation 17(1), 2005, 43–53.
[23] Zhao S., Gao C., Mukherjee S., Engelhardt B. E.: Bayesian group factor analysis with structured sparsity. Journal of Machine Learning Research 17, 2016, 1–47.

D.Sc. Serhii Zabolotnii
e-mail: zabolotniua@gmail.com

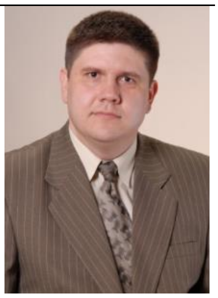

Serhii Zabolotnii was born in 1973 in Cherkasy, Ukraine. In 1995 he graduated the Department of informational technologies of Cherkasy State Technological University. Doctor of Technical Sciences (2015).
Job: professor of the Department of Computer Engineering and Informational Technologies in Cherkasy State Business-College. Scientific interests: statistical data processing, computer modeling.
Author/co-author of more than 150 publications, 1 monography and 7 patents.

http://orcid.org/0000-0003-0242-2234

Ph.D. Eng. Artem Honcharov
e-mail: a.honcharov@chdtu.edu.ua

Graduated the Department of Electronic Technologies of Cherkasy State Technological University in 2001. First Vice-Rector of Cherkasy State Technological University. Associate professor of the Department of Robotic and Telecommunication Systems and Cyber Security in Cherkasy State Technological University. Scientific interests: signal processing, computer modeling.

https://orcid.org/0000-0003-4043-5300

M.Sc. Sergii Mogilei
e-mail: sergiymogiley@gmail.com

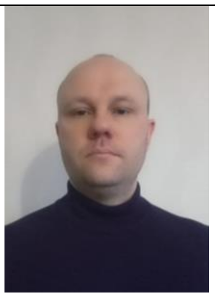

Sergii Mogilei is a Ph.D. student in Cherkasy State Technological University and works as a tutor in Rauf Ablyazov East European University (Cherkasy, Ukraine). His main scientific interests include mathematical and computer modeling, business analysis, mathematical programming, decision making theory and logistics.

http://orcid.org/0000-0002-9296-6827

otrzymano/received: 20.10.2021 *przyjęto do druku/accepted: 15.12.2021*

http://doi.org/10.35784/iapgos.2751

QUALITY OF SATELLITE COMMUNICATION IN SELECTED MOBILE ANDROID SMARTPHONES

Przemysław Falkowski-Gilski
Gdansk University of Technology, Faculty of Electronics, Telecommunications and Informatics, Gdansk, Poland

Abstract. *Today, thanks to mobile devices, satellite communication is available to anyone and everywhere. Gaining information on one's position using GNSS (Global Navigation Satellite Systems), particularly in unknown urban environments, had become an everyday activity. With the widespread of mobile devices, particularly smartphones, each person can obtain information considering his or her location anytime and everywhere. This paper is focused on a study, considering the quality of satellite communication in case of selected mobile terminals. It describes a measurement campaign carried out in varying urban environments, including a set of Android-powered smartphones coming from different manufacturers. Based on this, respective conclusions and remarks are given, which can aid consumers as well as device manufacturers and application developers.*

Keywords: mobile applications, mobile communication, satellite communication, satellite navigation systems

DOKŁADNOŚĆ KOMUNIKACJI SATELITARNEJ W WYBRANYCH MOBILNYCH SMARTFONACH ANDROID

Streszczenie. *Obecnie, dzięki urządzeniom mobilnym, komunikacja satelitarna jest dostępna dla każdego niezależnie od położenia. Pozyskiwanie informacji o własnej pozycji z wykorzystaniem systemów GNSS (Global Navigation Satellite Systems), szczególnie w nieznanych środowiskach miejskich, stało się codzienną aktywnością. Wraz z wszechobecnością urządzeń mobilnych, w szczególności smartfonów, każda osoba może pozyskać informacje dotyczące jego lub jej położenia zawsze i wszędzie. Praca ta skupia się na badaniu, dotyczącym jakości komunikacji satelitarnej w przypadku wybranych terminali mobilnych. Opisuje kampanię pomiarową przeprowadzoną w zmiennym środowisku miejskim, z wykorzystaniem zestawu smartfonów pracujących pod kontrolą systemu Android pochodzących od różnych dostawców. Na podstawie tego wyciągnięto wnioski i wskazówki, które mogą wspomóc zarówno konsumentów jak i producentów sprzętu i programistów aplikacji.*

Słowa kluczowe: aplikacje mobilne, komunikacja mobilna, komunikacja satelitarna, systemy nawigacji satelitarnej

Introduction

Due to the technological development, mobile terminals have evolved into functionally-sophisticated devices, such as smartphones. The Android platform has become one of the most popular operating system, with millions of new users each year. At present, there is a growing demand for positioning services, ranging from pedestrian navigation to consumer behavior analysis. These systems have been successfully used in many applications and have become very popular in recent years. A review of selected wireless positioning solutions, operating in both indoor and outdoor environments, including fundamentals of positioning techniques, methods, systems, as well as information processing mechanisms, may be found in [9].

1. Positioning and Navigation with Mobile Devices

Most often, the 2.4 and 5 GHz band, utilized by Bluetooth and Wi-Fi devices, is also used for indoor and/or outdoor (together with GNSS) navigation purposes. An analysis of the positioning accuracy in the aforementioned band, along with a comparison of indoor and outdoor navigation techniques, for selected ISM (Industrial, Scientific and Medical) bands, is available in [5].

Currently, many solutions make use of the RSSI (Received Signal Strength Indicator) parameter, most often related to beacons. An analysis of localization performance, concerning BLE (Bluetooth Low Energy) for tracking the movement of individuals, e.g. in order to indicate popular paths in an interactive art installation, is available in [1].

Other researchers focus on RFID (Radio-Frequency Identification) tags, e.g. a three-dimensional indoor positioning system based on a multiple trilateration algorithm [12]. Whereas some utilize UWB (Ultra Wideband) technology, mainly due to the fact that UWB signals are well-suited for communication and tracking systems, as they provide increased tolerance to localization errors due to the finite time resolution of the transmitted pulses and their large bandwidth. An investigation of UWB and hybrid-UWB schemes may be found in [2].

As shown, mobile navigation along with positioning technologies can lead to the development of various services, such as: disaster recovery, content delivery, and efficient point-to-point communication. As a result, different algorithms and techniques have been developed, in order to minimize the localization error.

In [6] authors investigated the performance of mobile personal positioning devices, utilized for pedestrian navigation in urban environments. They focused mainly on blind and visually impaired individuals. Due to the fact that GNSS-based devices suffer from a decrease in accuracy in urbanized areas, related to frequent NLOS (Non-Line-of-Sight) conditions, particularly in the vicinity of multistory buildings and other man-made objects. Thanks to a hybrid GPS-Galileo module, authors developed a prototype system in order to improve the comfort of everyday life.

Another group of authors [11] investigated a method of tracing massive amounts of people and providing them with visual information. This system was based on the HAIP (High Accuracy Indoor Positioning) technology by Nokia. The aforementioned studies inspired this one, considering the quality of satellite communication among popular consumer devices, namely smartphones.

2. About the study

Due to the widespread and mobility of portable devices, it seemed interesting to investigate the precision that modern smartphones can offer. Particularly, what is the quality of satellite positioning and navigation systems for urban mobility applications. That is why this study, concerning Android-powered terminals, was carried out.

2.1. Tested mobile device

The study was carried out using two mobile devices, particularly smartphones, released to the market in 2019. They came from different manufacturers, and are further labeled as smartphone 1 and smartphone 2.

The first one had an 8-core CPU (2.2 GHz), 3 GB of RAM, and was powered by Android Pie (9.0). The integrated GNSS module was compatible with GPS, GLONASS, Galileo, BeiDou, and QZSS.

The second device had also an 8-core CPU (2.3 GHz), 4 GB of RAM, and was powered by Android Pie (9.0). The integrated GNSS module was compatible with GPS, GLONASS, Galileo, and BeiDou.

2.2. Tested scenarios

In the first scenario, the route resembled a square. It was evaluated with a bicycle at an average speed of 8 km/h, and a car at an average speed of 35 km/h. This route went along 3 streets in the city of Gdansk. It varied in type of structure and its closest neighborhood. Some part of it was surrounded by buildings, and some of it was next to an open terrain.

In the second scenario, the route resembled a straight line. As previously, it was evaluated with a bicycle at an average speed of 8 km/h, and a car at an average speed of 35 km/h. This route, based on the type of surrounding buildings, could be divided into 2 parts. The first part had high buildings on one side, whereas the second part was an open terrain.

All obtained data were recorded in the raw format [13], and then processed using the GNSS Measurement Tool [14] as well as Matlab software. During both measurement and processing, a custom software was utilized, in order to obtain as much data as possible. The measurement campaign included 2 types of routes (square-shaped and straight line), 2 types of communication means (bicycle – low speed, car – high speed), and of course 2 smartphones.

3. Obtained results

To start with, obtained results will be described taking into consideration the type of route (square-shaped and straight line), type of mobility (bicycle and car), and utilized smartphone (smartphone 1 and smartphone 2). Next, obtained results will be compared and discussed.

Square-shaped route – bicycle excursion – smartphone 1

During this bicycle excursion, as shown in figure 1, the device observed 39 satellites from 4 constellations: GPS, GLONASS, Galileo, and BeiDou. Among them 29 were monitored (see figure 2), as some were on the outskirts of the horizon. Due to this, signals from those 10 satellites did not reach the reference threshold signal level. The average CNR (Carrier-to-Noise Ratio) for 4 strongest satellites' signal strength was equal to: GPS – 26.8 dBHz, GLONASS – 21.8 dBHz, Galileo – 22.8 dBHz, BeiDou – 28.8 dBHz (best geometry). As shown, the strongest signal was observed for BeiDou.

The signal with the strongest CNR was observed for satellite C27 from the BeiDou constellation. This satellite, like C28 and C22, was observed only during the first few seconds of measurement. The signal strength from other BeiDou satellites was equal to approx. 20–25 dBHz. The signal strength itself was unstable.

Square-shaped route – bicycle excursion – smartphone 2

In this case, as shown in figure 3, the smartphone observed 40 satellites, where 22 of them were monitored. It is worth mentioning that signals from 2 GPS satellites were omitted, as well as most of the signals from Galileo and BeiDou systems (see figure 4). The average CNR for 4 strongest satellites' signal strength was equal to: GPS – 38.1 dBHz (best geometry), GLONASS – 36.5 dBHz, Galileo – 24.5 dBHz, BeiDou – 21.1 dBHz.

It should be pointed out that BeiDou and Galileo satellites were not monitored during most of the time. Biases in the clock itself had a significant impact as well.

Square-shaped route – car excursion – smartphone 1

During this drive, as shown in figure 5, 46 satellites were observed, considering GPS, GLONASS, Gaileo, and BeiDou, 40 of which were monitored (see figure 6). The CNR values did not reach the reference values, which was caused by additional attenuation by the car itself, as the mobile device was located inside of it. The average CNR for 4 strongest satellites' signal strength was equal to: GPS – 34.4 dBHz (best geometry), GLONASS – 29.0 dBHz, Galileo – 24.6 dBHz, BeiDou – 29.2 dBHz.

During approx. half of the time, the clock was not concise, resulting in a discontinuous time of satellite observation, especially in case of BeiDou and Galileo. The best reception quality was observed for G16, G27, and G20, which were located on more than 45 degree elevation.

Square-shaped route – car excursion – smartphone 2

In this case, as shown in figure 7, 32 satellites were observed, whereas 18 of them were monitored. Satellites from BeiDou, as well as G29 and G30 from GPS, were omitted, although they were on the 5th degree of elevation (see figure 8). Additionally, C12 was not monitored, although it was on the highest position. The average CNR for 4 strongest satellites' signal strength was equal to: GPS – 37.7 dBHz (best geometry), GLONASS – 33.8 dBHz, BeiDou – 33.9 dBHz.

Straight line route – bicycle excursion – smartphone 1

When examining the route shown in figure 9, the device registered 40 satellites, with 30 of them being monitored. They came from GPS, GLONASS, Galileo, and BeiDou constellations. The omitted satellites came from Galileo and BeiDou, and were recorded below the 5th degree of elevation (see figure 10).
Furthermore, the E02 Galileo satellite was also omitted, although being on the 15th degree of elevation. The average CNR for 4 strongest satellites' signal strength was equal to: GPS – 34.4 dBHz (best geometry), GLONASS – 29.4 dBHz, Galileo – 27.9 dBHz, BeiDou – 30.8 dBHz.

Straight line route – bicycle excursion – smartphone 2

In this case, as shown in figure 11, this device also registered 40 satellites form GPS, GLONASS, Galileo, and BeiDou constellations, from which 31 were monitored (see figure 12). In case of the 3 first systems, they offered stable reception conditions. The average CNR for 4 strongest satellites' signal strength was equal to: GPS – 38.0 dBHz (best geometry), GLONASS – 35.6 dBHz, Galileo – 28.4 dBHz, BeiDou – 24.4 dBHz.

This mobile device enabled stable reception for GPS and GLONASS constellations. The CNR value did not change much, equal too approx. 38-45 dBHz over time. A degradation in reception quality was observed in case of satellites G18, G11, and G30, which were situated on the 30th degree of elevation.

Straight line route – car excursion – smartphone 1

In this case, as shown in figure 13, 42 satellites were observed, including GPS, GLONASS, Galileo, and BeiDou constellations, from which 31 were monitored (see figure 14). The average CNR for 4 strongest satellites' signal strength was equal to: GPS – 32.8 dBHz (best geometry), GLONASS – 30.8 dBHz, Galileo – 32.5 dBHz, BeiDou – 32.5 dBHz.
In case of BeiDou, the C19 satellite exceeded the reference signal level. However, the signal from this satellite was only observed for a limited time period.

Straight line route – car excursion – smartphone 2

When examining the route shown in figure 15, this device observed 34 satellites, where 20 of them were monitored. They included GPS, GLONASS, Galileo, BeiDou, and even 1 QZSS (quite surprisingly, although according to the technical specification this constellation was supposed to be not supported). In case of those satellites that were not monitored, 12 of them came from Galileo. All of them had a high elevation, e.g. C12 was in the zenith, the other 7 on elevation of above 15 degrees. The smartphone did not monitor satellites G30 and G29, which were on elevation below 5 degrees (see figure 16).

The received signal strength values were high, although being recorded inside a car. The average CNR for 4 strongest satellites' signal strength was equal to: GPS – 40.3 dBHz (best geometry), GLONASS – 35.9 dBHz, BeiDou (and QZSS) – 33.3 dBHz. The received signal strength level was stable, especially when examining GPS satellites at a height of above 30 degrees, i.e. G12.

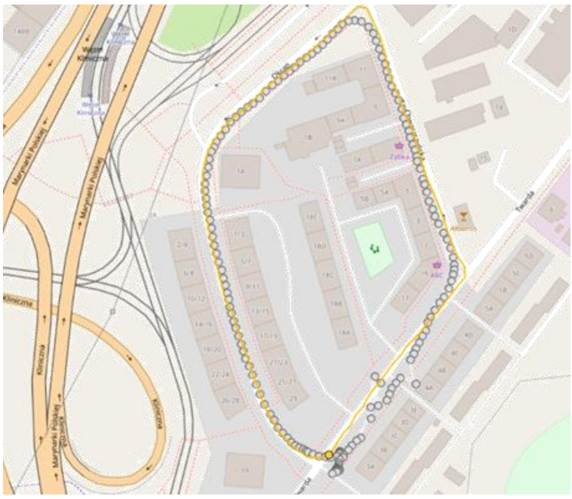

Fig. 1. Bicycle excursion along the square-shaped route with smartphone 1: yellow – real route, dot – measured route

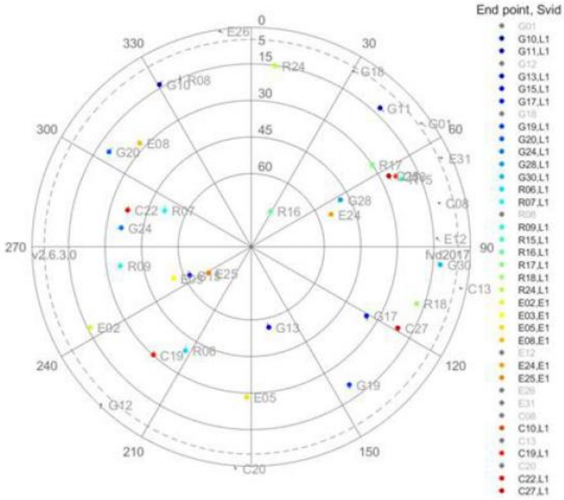

Fig. 2. Observed satellites – bicycle excursion along the square-shaped route with smartphone 1

Fig. 3. Bicycle excursion along the square-shaped route with smartphone 2: yellow – real route, dot – measured route

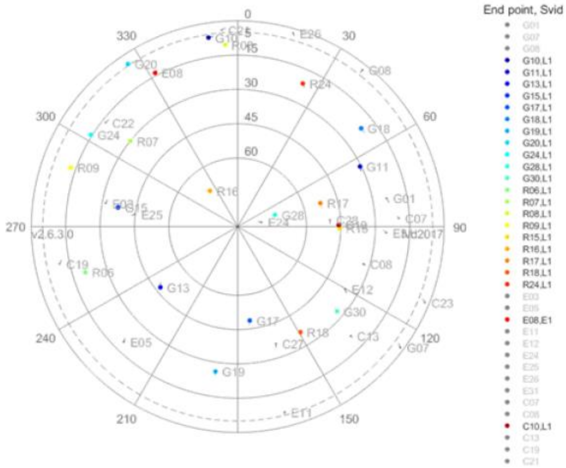

Fig. 4. Observed satellites – bicycle excursion along the square-shaped route with smartphone 2

Fig. 5. Car excursion along the square-shaped route with smartphone 1: yellow – real route, dot – measured route

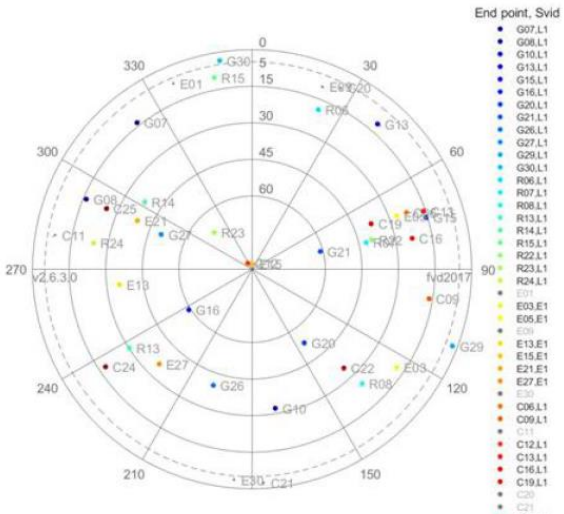

Fig. 6. Observed satellites – car excursion along the square-shaped route with smartphone 1

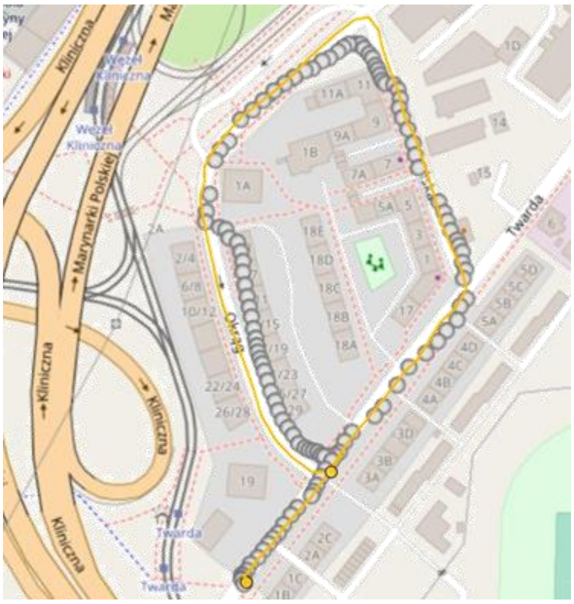

Fig. 7. Car excursion along the square-shaped route with smartphone 2: yellow – real route, dot – measured route

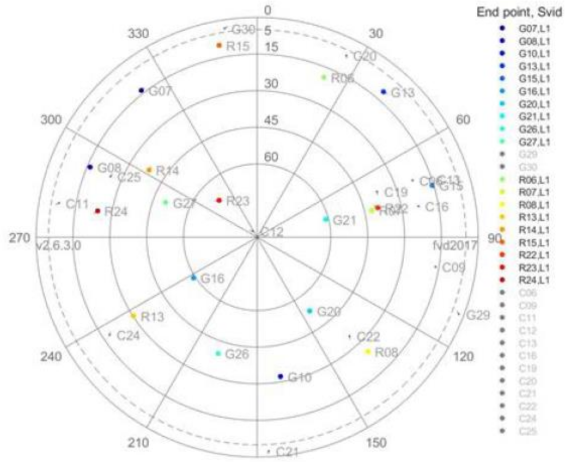

Fig. 8. Observed satellites – car excursion along the square-shaped route with smartphone 2

Fig. 9. Car excursion along the straight line route with smartphone 1: yellow – real route, dot – measured route

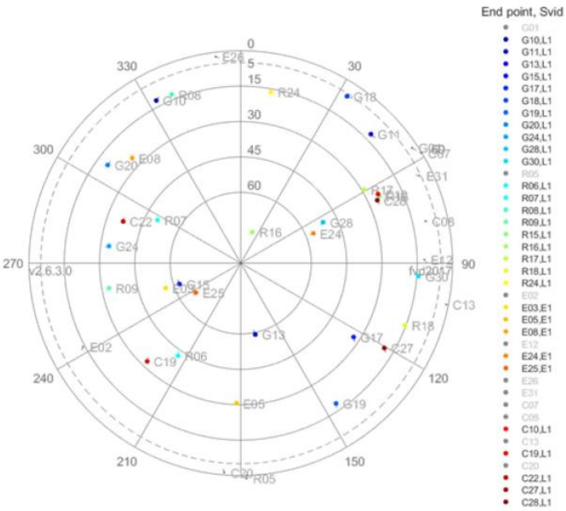

Fig. 10. Observed satellites – bicycle excursion along the straight line route with smartphone 1

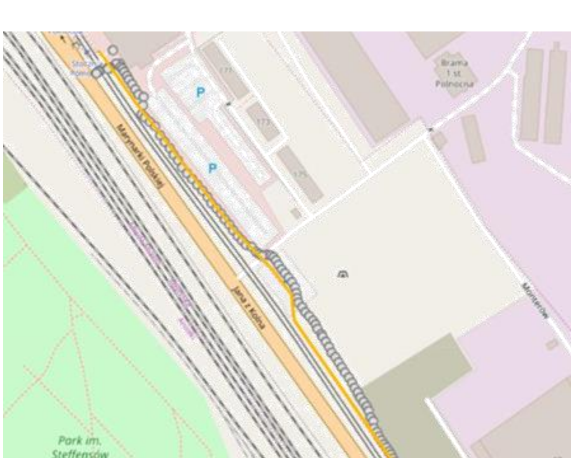

Fig. 11. Bicycle excursion along the straight line route with smartphone 2: yellow – real route, dot – measured route

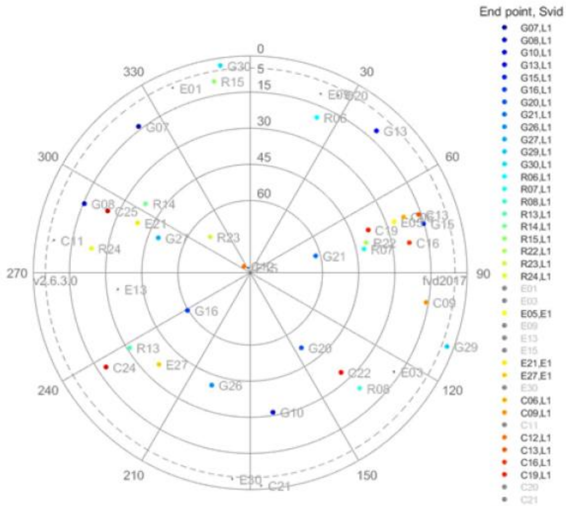

Fig. 12. Observed satellites – bicycle excursion along the straight line route with smartphone 2

Fig. 13. Car excursion along the straight line route with smartphone 1: yellow – real route, dot – measured route

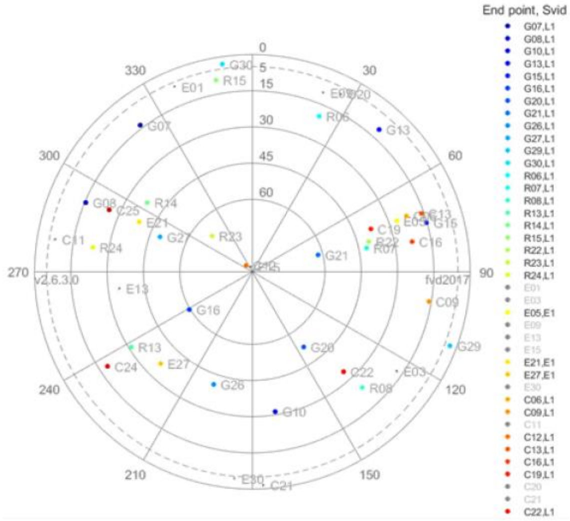

Fig. 14. Observed satellites – car excursion along the straight line route with smartphone 1

Fig. 15. Car excursion along the straight line route with smartphone 2: yellow – real route, dot – measured route

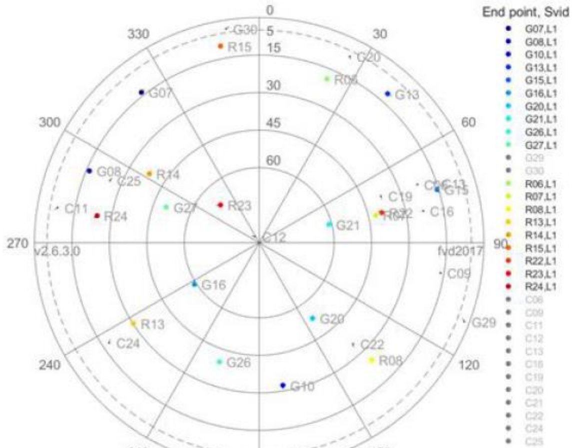

Fig. 16. Observed satellites – car excursion along the straight line route with smartphone 2

4. Summary

This work describes results of a study, focused on the precision of GNSS systems using smartphones, their quality, reliability, related to signal reception. The tested devices, coming from 2 different manufacturers, were all Android-powered devices operating on version 9.0 (Pie). The measurement campaign itself was carried out in different conditions, including surrounding buildings, terrain topology, and urban fabric.

The devices came from a medium-end segment, most popular among consumers. Although indexed at the same level, considering their quality and price, they proved to be different, e.g. when going along a straight line or taking turns. As a result, obtained results were completely unlike, although tested in the same research scenario. As shown, a number of differentiators had been noticed.

The first differentiator was the number of observed satellites, summarized in table 1. In case of smartphone 1, the total number of observed satellites (respective signals) was equal to 167, from which 130 were monitored (78% of all). Whereas smartphone 2 received signals from 146 satellites, from which 91 were monitored (62% of all).

This difference is also clearly visible in case of satellite parameters. Satellites with low elevation values were neglected (excluded) by both devices. Additionally, the second device favored GPS and GLONASS constellations. Moreover, surprisingly smartphone 2 recorded a QZSS satellite, although according to the technical specification the build-in components were not compatible with this constellation. It should be pointed out that smartphone 1 was compatible with QZSS, and yet it did not observe any of them during the whole study.

Next was the stability of signal reception itself. The first smartphone seldom provided a signal level above the referenced CNR. Whereas the second one received at least over 10 such signals (above reference level), from which only 1 came from a constellation other than GPS or GLONASS.

As the number and availability of smartphones continues to grow, every year new mobile devices, coming from a broad range of manufacturers, emerge on the market. One must note that the type of utilized inner components, and not only screen size or amount of memory, has an enormous impact on the efficiency and quality of operation of a mobile device. Further studies could include a broader range of user devices, types of motion, shape of the path, types of terrain, surroundings (both man-made and natural), urban fabric, etc. Additional information on mobile devices, including consumption of content and quality-related issues, is available in [3, 7, 8]. A source of inspiration for future studies may be found in [10].

Table 1. Number of observed (monitored) satellites

Device	Square-shaped route	Straight line route
smartphone 1	Bicycle excursion: 39(29) Car excursion: 46(40)	Bicycle excursion: 40(30) Car excursion: 42(31)
smartphone 2	Bicycle excursion: 40(22) Car excursion: 32(18)	Bicycle excursion: 40(31) Car excursion: 34(20)

References

[1] Ashby S., Hanna J., Rodrigues R.: Using BLE beacons to simulate proxemic surveillance for an interactive art installation. Proceedings of the 2017 Conference Extended Abstracts on Human Factors in Computing Systems CHI I, 2017, 1486–1493 [http://doi.org/10.1145/3027063.3053096].

[2] Bogdani E., Vouyioukas D., Nomikos N.: Localization error modeling of hybrid fingerprint-based techniques for indoor ultra-wideband systems. Telecommunication Systems 63, 2016, 223–241.

[3] Boz E., Finley B., Oulasvirta A., Kilkki K., Manner J.: Mobile QoE prediction in the field. Pervasive and Mobile Computing 59, 2019, 101039.

[4] Chruszczyk Ł., Zając A., Grzechca D.: Comparison of 2.4 and 5 GHz WLAN network for purpose of indoor and outdoor location. International Journal of Electronics and Telecommunications 62(1), 2016, 71–79.

[5] Chruszczyk Ł., Zając A.: Comparison of indoor/outdoor, RSSI-based positioning using 433, 868 or 2400 MHz ISM bands. International Journal of Electronics and Telecomunications 62(4), 2016, 395–399.

[6] Drypczewski K., Moszyński M., Demkowicz J., Bikonis K., Stepnowski A.: Design of the dual constellation GPS/GALILEO mobile device for improving navigation of the visually impaired in an urban area. Polish Maritime Research 22, 2015, 15–20 [http://doi.org/10.1515/pomr-2015-0065].

[7] Falkowski-Gilski P., Uhl T.: Current trends in consumption of multimedia content using online streaming platforms: a user-centric survey. Computer Science Review 37, 2020, 100268.

[8] Falkowski-Gilski P.: On the consumption of multimedia content using mobile devices: a year to year user case study. Archives of Acoustics 45(2), 2020, 321–328 [http://doi.org/10.24425/aoa.2020.133152].

[9] Gilski P., Stefański J.: Survey of radio navigation systems. International Journal of Electronics and Telecommunications 61(1), 2015, 43–48.

[10] Jeena Jacob I., Kolandapalayam Shanmugam S., Piramuthu S., Falkowski-Gilski P. (Eds.): Data intelligence and cognitive informatics: proceedings of ICDICI 2020. Springer, Singapore 2021.

[11] Ryu A., Nelson M., Mehtala A., Nyberg T., Xiong G.: Non-GPS positioning sensor network in social manufacturing. Proceedings of the 2016 IEEE International Conference on Service Operations and Logistics, and Informatics SOLI I, 2016, 47–52 [http://doi.org/10.1109/SOLI.2016.7551660].

[12] Xu H., Ding Y., Wang R., Shen W., Li P.: A novel radio frequency identification threedimensional indoor positioning system based on trilateral positioning algorithm. Journal of Algorithms and Computational Technology 10(3), 2016, 158–168 [http://doi.org/10.1177/1748301816649078].

[13] https://developer.android.com/guide/topics/sensors/gnss.html (available: 7.09.2021).

[14] https://github.com/google/gps-measurement-tools (available: 07.09.2021).

Ph.D. Przemysław Falkowski-Gilski
e-mail: przemyslaw.falkowski@eti.pg.edu.pl

Przemysław Falkowski-Gilski is a graduate of the Faculty of Electronics, Telecommunications and Informatics (ETI), Gdansk University of Technology. Currently he works as an assistant professor.
Member of a number of organizational, scientific, technical and program committees of national and international conferences, as well as a reviewer in numerous Polish and English-language journals.

http://orcid.org/0000-0001-8920-6969

otrzymano/received: 20.09.2021 *przyjęto do druku/accepted: 15.12.2021*

http://doi.org/10.35784/iapgos.2805

CHROMATIC DISPERSION COMPENSATION IN EXISTING FIBER OPTIC TELECOMMUNICATION LINES WITH THE GROWING BIT RATES NEEDS OF DWDM SYSTEM

Tomasz Bobruk
Cellnex Telecom, Warsaw, Poland

Abstract. *The article presents an analysis of the methods of chromatic dispersion compensation in the existing, already built fiber optic telecommunications lines, based on ITU G.652 A and B fibers with the constantly growing demand for bit rates in DWDM systems. Due to the enormous investment costs, it is impossible to replace the cables used with NZDSF, hence the chapter analyzes methods of improving the bandwidth without replacing all cables. Typical models of the optimization of chromatic dispersion in the existing lines are presented.*

Keywords: chromatic dispersion, optical fiber dispersion, compensation, DWDM

KOMPENSACJA DYSPERSJI CHROMATYCZNEJ W ISTNIEJĄCYCH ŚWIATŁOWODOWYCH LINIACH TELEKOMUNIKACYJNYCH Z ROSNĄCYM ZAPOTRZEBOWANIEM PRZEPŁYWNOŚCI W SYSTEMACH DWDM

Streszczenie. *W artykule przedstawiono problematykę kompensacji dyspersji chromatycznej w istniejących, już wybudowanych światłowodowych liniach telekomunikacyjnych, opartych o włókna w standardzie ITU G.652 A i B z ciągle rosnącym zapotrzebowaniem na przepływności w systemach DWDM. Ze względu na ogromne koszty inwestycyjne wymiana zastosowanych kabli na NZDSF jest niemożliwa, stąd w artykule analizowane sa sposoby poprawy pasma bez wymiany wszystkich kabli. Przedstawiono typowe modele procesu optymalizacji dyspersji chromatycznej w istniejących liniach.*

Słowa kluczowe: dyspersja chromatyczna, dyspersja światłowodowa, kompensacja, DWDM

Introduction

The publication concerns the existing DWDM telecommunications network with optical crossconnects (OXC), which has been developed for years by telecommunication operators based on single mode fiber on the ITU G.652 A and B standard. These networks are constantly expanded by adding new fiber optic lines based on the latest ITU G.652 D standards.

While the current development of the network consisting in increasing the transmission speed to 10 Gbit/s and increasing the number of optical channels was possible assuming the typical characteristics of single mode fibers (G.652), the use of new generation systems with a bit rate of 40 Gbit/s and the ever-increasing demand for a wider bandwidth will require a detailed analysis and verification of the existing network resources, especially in terms of chromatic dispersion [6] and polarization dispersion which is non-linear and depends on the geometry of the fibers used [2, 7].

Optical transmission in DWDM systems is transmitted over sections of up to several hundred kilometers, there is a need to measure and compensate the chromatic dispersion, taking into account the fiber standards used in the network, in search of increasing the bandwidth to a specified level, with the minimum allowable additional attenuation [4, 9].

The main limitation is the existing infrastructure built on the basis of G.652 A and B fibers. These fibers have a relatively large dispersion. Replacing these cables with the newer NZDSF is not possible due to the enormous investment costs.

Another thing, NZDSF type fibers have lower dispersion than standard fibers, but some of them have a higher dispersion characteristic slope, which makes proper compensation of dispersion in long lines using DWDM technique a critical problem [6].

The publication explores ways to improve bandwidth without replacing all existing cables.

1. Optical transmission systems

1.1. DWDM (Dense Wavelength Division Mulitplexing)

The optical transmission system most often used in telecommunications is the DWDM system (Dense Wavelength Division Mulitplexing), which enables transmission with a total bit rate calculated in Tbit/s.

The DWDM system is the simultaneous introduction to the fiber of several dozen or several hundred optical signals, with wavelengths shifted between each other by 200 GHz or a fraction of it (100 GHz, 50 GHz, 25 GHz).

The first implemented DWDM systems are a simple point-to-point transmission multiplication. Transmitters with lasers of different wavelengths are placed at the beginning of the line. The signals are summed in a multiplexer connected to a single mode optical fiber. At the other end of the fiber optic line there is a demultiplexer that distributes the waves to different receivers. Between the nodes of this network, optical amplifiers are placed, significantly increasing the transmission range, and ADM devices (Add Drop Multiplexer), enabling the separation of one or more waves from the fiber for local customer. The amplifiers increase the ranges, but don't eliminate the distortion of the pulses caused by chromatic dispersion or polarization. The phenomenon of non-linearity causes inter-channel interference (FWM – Four Wave Mixing), which highly reduces the range or bit rate of channels [10].

The DWDM system uses the C and L optical bands in the 1530 nm to 1610 nm range [10].

1.2. MetroDWDM (Metropolitan DWDM)

Optical networks for urban agglomerations for which MetroDWDM systems (Metropolitan DWDM) have been developed are less demanding in terms of transmission range. The total bit rate of the system is over 2000 Gbit/s. The essence of these systems is the use of DWDM wave multiplication in closed ring configuration, increased bit rate in relation to DWDM, the possibility of creating connections in a mesh configuration, smaller distances between nodes, greater variety of interfaces, flexible management system, quick reconfiguration for traffic management or connecting new customers to the network [10].

2. Dispersion compensation and its application in telecommunications optical fiber lines

2.1. DCF-SMF

The most popular method of chromatic dispersion compensation in telecommunications optical fiber lines is the use of a DC-SMF (Dispersion Compensating Single Mode Fiber) fiber. A fragment of such optical fiber is inserted into the existing line [3]. Fig. 1 shows a diagram of such a solution.

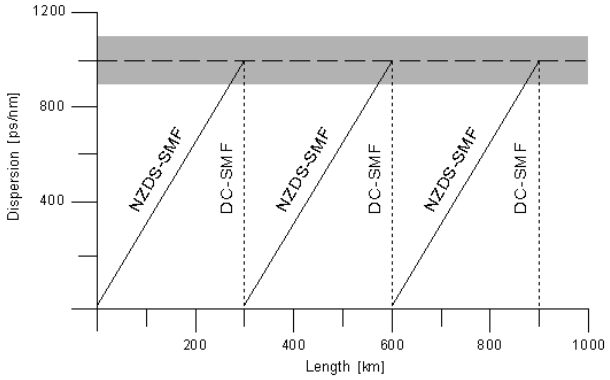

Fig. 1. Dispersion compensation of NZDS-SMF optical fiber with applied DC-SMF [5]

It turns out that for a line built of NZDS-SMF fibers, transmission with a speed of 10 Gbit/s can be transferred up to 360 km. Introducing the 3 km section of the DC-SMF fiber to the line results in receiving an unexpanded pulse at the output.

On the other side, in DWDM systems based on DC-SMF lines, the simultaneous use of EDFA amplifiers is a limitation, because the compensation factor isn't a constant value and depends on the transmitted power level and the bit rate [5, 15].

2.2. Fiber Bragg Grating

Grating with a variable period are also perfect for dispersion compensation, which, due to their application, are also called for short DCG (Dispersion Compensating Gratings). Due to the uneven distribution of the grating, different wavelengths are reflected in different places, so they travel different paths and, consequently, each wavelength experiences a different exit delay:

$$\tau(\lambda) \approx \frac{(\lambda_0 - \lambda)}{\Delta\lambda_{chirp}} \cdot \frac{2L_g}{v_g} \tag{1}$$

where $\Delta\lambda_{chirp} = 2n_{eff} \cdot \Delta\Lambda_{chirp}$, and l_0 mid-wavelength of grating, v_g average group speed of the light in the fiber.

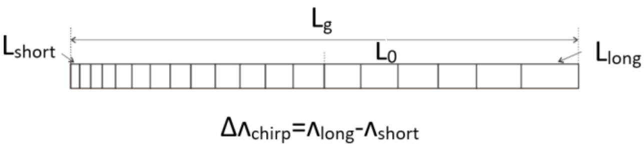

Fig. 2. Fiber Bragg Grating with variable period [8]

Fiber Bragg Graiting are used to create narrow- and wideband dispersion compensators and compensators for the slope of the dispersion characteristic. Such compensators are characterized by low losses and introduce relatively small delays. Therefore, they are perfect for use in long distance WDM and DWDM systems. Moreover, mesh adaptive compensators are manufactured, intended for use in undersea lines without multiplication, with a throughput of up to 40 Gbit/s [1, 16].

The methods of installing the Fiber Bragg Grating in the system are presented in Fig. 3. As for compensating fibers (DCF), we can use grating compensators to precompensate, post-compensate or use them in any other available place for compensation of a single section.

On the basis of the Fiber Bragg Grating, in addition to the classic narrow-band compensators, there are also manufactured elements compensating the slope of the dispersion characteristic for WDM and DWDM systems, as well as adjustable compensators [12].

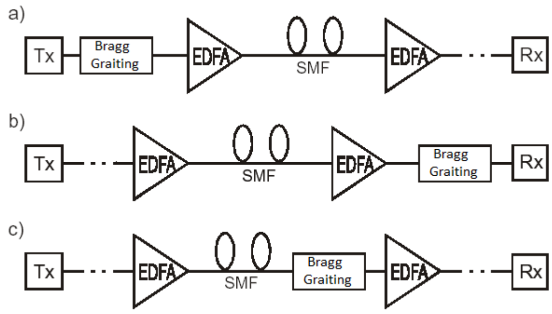

Fig. 3. Places of Fiber Bragg Grating installation as dispersion compensator: a) precompensation; b) post-compensation; c) compensation of one section [11]

The tunability of the compensator based on the Fiber Bragg Grating allows you to change the chromatic dispersion coefficient in the range from 940 ps/nm to even 8770 ps/nm [13].

2.3. DC-PCF

The methods of chromatic dispersion compensation presented they allow for optimal compensation in only one transmission window.

The use of photonic optical fibers with a double cladding structure (DC-PCF) allows to control dispersion in the full range of the transmission band, by modeling the wavelength at zero dispersion λ_0 and the dispersion slope coefficient [11].

Figure 4 shows the cross-section of a DC-PCF fiber with a double cladding and different coefficients of efficiency. The inner cladding has a hole diameter d_1 and a distance between the centers of the holes Λ_1, and the outer hole diameter d_2 and a distance there between Λ_2; a_1 the outer radius of the inner cladding, a_2 the inner radius of the outer cladding. The presented DC-PCF optical fiber has a central core, which are air holes in the inner cladding, and a second core, which is the area between a_1 and a_2. They come from here the parameters R_a and R_n:

$$R_a = \frac{a_2}{a_1} \tag{2}$$

$$R_n = \frac{n_{cl2} - n_{cl1}}{n_{cl1}} \tag{3}$$

where n_{cl1} and n_{cl2} are the effective cladding coefficients, R_a corresponds to the width of the second core, while R_n is the wavelength dependent on the relative coefficient between the inner and outer cladding.

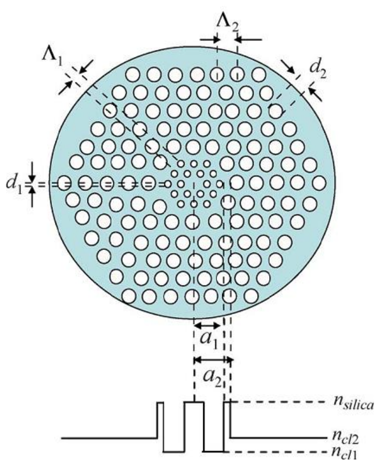

Fig. 4. DC-PCF fiber cross section and effective coefficient index profile [11]

The first requirement when designing a dispersion compensating fiber is to match the slope of the characteristic for a SMF at a wavelength of 1550 nm. Another variable taken into consideration is the wavelength value at zero dispersion λ_0 attenuating the dispersion insufficiency λ_0 at SMF. These two requirement lead to compensation – the dispersion of the DC-PCF fiber decreases as the wavelength increases.

That means, the dispersion characteristics in photonic optical fibers with small distances between holes depend on the distance between the centers of the holes and their size. When designing a DC-PCF fiber, a 1% change in the distance between the centers of the holes Λ_1 causes a 1% change in the zero dispersion length λ_0. It can be assumed that the poor quality of the surface of the air holes will cause dispersion and additional losses and multi-pass interference. Therefore, a more precise fabrication process would require an additional firing technique. Moreover, the improvement of the splicing technique, through the use of taper fibers, will be needed to reduce the loss of splices between DC-PCF and the standard SMF fiber [11].

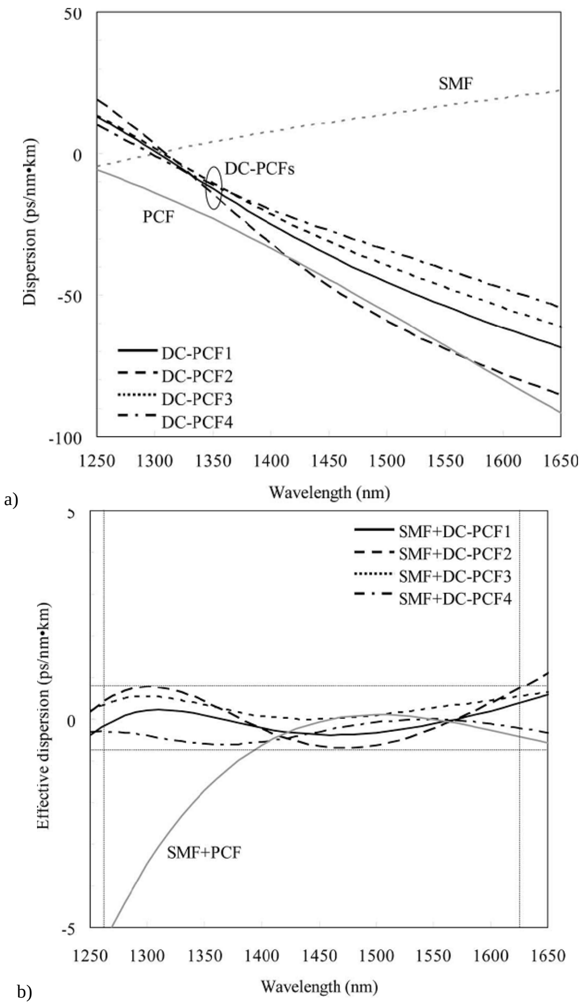

Fig. 5. Characteristics of the designed DC-PCF fiber. (a) properties of the designed DC-PCF fiber compared to conventional DCF and SMF fiber, (b) Effective dispersion of SMF + DC-PCF and SMF + PCF fiber [11]

Figure 5a shows the dispersion characteristics in the designed DC-PCF optical fiber. The figure also shows the dispersion in the PCF fiber (solid gray line). The dotted curve follows the dispersion in a conventional SMF fiber. Figure 5b also shows the effective dispersion for the SMF + DC-PCF and SMF + PCF fiber. The SMF coefficient fiber length and optical fiber compensation result in even smaller changes in the effective dispersion in the all telecommunications band. Figure 5b confirms that the design of the DC-PCF was achieved by efficient dispersion ±0.8 ps·nm·km in the all telecommunications band [11, 14].

3. Optimization of the compensation process in telecommunications optical lines

Typical possibilities of optimizing the chromatic dispersion compensation process in operator telecommunication lines are presented below.

3.1. SMF line without compensation

The first variant concerns the existing telecommunication line built on the basis of optical fibers in the G.652 A standard.

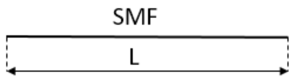

Fig. 6. SMF line

The attenuation of this line is given by the formula:

$$A = \alpha \cdot L \tag{4}$$

where α – attenuation of the SMF line [dB/km], L – length of the SMF line [km],
while the total dispersion of the SMF line is:

$$d = D \cdot L \tag{5}$$

where D – unit dispersion of the SMF line [ps/nm·km].

3.2. SMF line with DCF compensator

In this model, a DCF optical fiber was used to compensate for the SMF line, which was wound on a drum and placed in a telecommunications node.

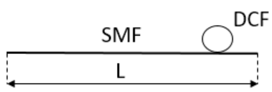

Fig. 7. SMF line with DCF compensator

The attenuation of such a line is:

$$A = \alpha \cdot L + \alpha_c \cdot L_c \tag{6}$$

where α_c – compensator attenuation [dB/km], L_c – compensator length [km],
while the total dispersion of the line with the applied DCF compensator is:

$$d = D \cdot L + D_c \cdot L_c \tag{7}$$

where D_c – unit dispersion of the compensator [ps/nm·km]

3.3. SMF line with the SMF line section replaced with DCF cable

In this model, the SMF line of L-L_c length assumed the replacement of a section of the existing SMF cable with a DCF cable of L_c length.

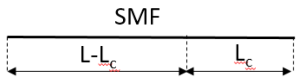

Fig. 8. SMF line with the SMF line section replaced with DCF cable

Then the attenuation of such a line will be:

$$A = \alpha \cdot (L - L_c) + \alpha_c \cdot L_c \tag{8}$$

and total line dispersion:

$$d = D \cdot (L - L_c) + D_c \cdot L_c \tag{9}$$

3.4. SMF line with DCG compensator attached at the end of the line

In this model, DCG was used to compensate for the dilution, which was placed at the end of the line.

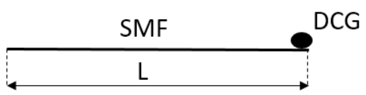

Fig. 9. SMF line with DCG compensator attached at the end of the line

The attenuation of such a line will be:

$$A = \alpha \cdot L + A_B \qquad (10)$$

where A_B – DCG attenuation [dB],
and the total line dispersion is:

$$d = D \cdot L + d_B \qquad (11)$$

where d_B denotes DCG dispersion [ps/nm].

The graph and the calculated values of A and d by 1550 nm for an exemplary 100 kilometer line are shown Fig. 10 and 11. The following values were adopted for the calculations α = 0.2 dB/km, α_c = -0.5 dB/km, D = 17 ps/nm·km, D_c = -90 ps/nm·km, A_B = 10 dB, d_B=-1670 ps/nm.

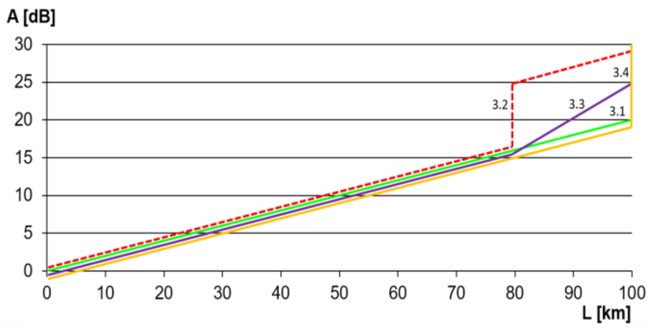

Fig. 10. Graph of the dependence of the attenuation on the length of the fiber optic line, taking into account the dispersion compensator

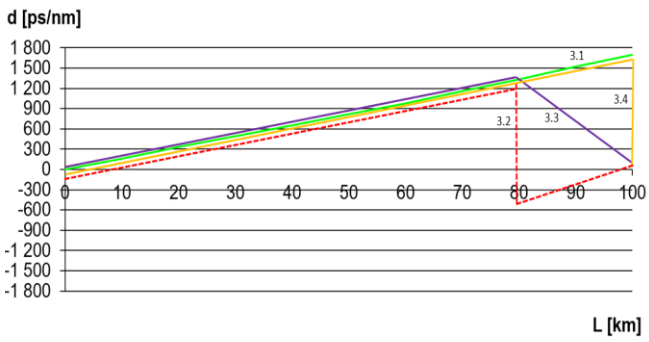

Fig. 11. Graph of the dependence of the total line dispersion on the length of an optical fiber line, taking into account the dispersion compensator

4. Conclusion

The presented results of the analyzes show that using method 3.3 it is possible to obtain the lowest line attenuation, while from the point of view of the telecommunications network operator, taking into account the current expenditures, the best way to optimize the process of chromatic dispersion compensation in the existing optical fiber lines is the method presented in point 3.2. The DCF compensator, wound on the drum and placed in the node, at the current market prices of several thousand zlotys, guarantees effective compensation of dispersion to a level around 0 ps/nm.

The optimization method presented in point 3.3, also allows to achieve good levels of compensation, but with slightly higher investment costs (the current level is 8–10 thousand zlotys per kilometer).

Of course, presented methods of dispersion compensation, are not able to shape the dispersion characteristics of the line in the all available band, which is especially important in DWDM systems. They do not correct dispersion evenly, they only correct it for a specific wavelength (most often it is the "middle wavelength" for the C band, that is 1550nm), while the adjacent wavelengths will be overcompensated or insufficiently compensated [6].

In some optical fibers there is a 2-3 times difference in dispersion values for the C-band wavelengths. Thus, proper management of line dispersion is the process of balancing it with positive and negative dispersion along the length of the line over the entire spectral range of interest so that the total dispersion value is close to zero or within predetermined limits.

This means that it is necessary to precisely measure the total dispersion for each optical telecommunication line and select the compensation (for example DCF fiber length) in order to obtain a dispersion characteristic appropriate for a given telecommunications line in a wide range.

References

[1] Andreev V. et al.: Chromatic dispersion monitoring based on Bragg notch filter central frequency polyharmonic probing. Proc. SPIE 11146/2019, 111461M, 7–9.
[2] Bo L. et al.: Optical frequency comb generation for DWDM transmission over 25- to 50-km standard single-mode fiber. Optical Engineering 57(1), 2018, 1–12.
[3] Bobruk T., Wójcik W., Smolarz A.: Dispersion and its compensation in telecommunication optical fibers. Proc. SPIE 6608, 2007, 660814.
[4] Chorchos Ł., Turkiewicz J.: SSMF 1310 nm dispersion characteristic influence on the 400 Gbit/s and 1000 Gbit/s ethernet physical layer design, Proc. SPIE 10445, 2017, 104450E.
[5] Drabik Z.: Procedura wyznaczania niepewności pomiaru dyspersji chromatycznej Laboratorium Badawczego OTO. OTO Lublin, Lublin 2000.
[6] Drabik Z., Koper Z.: Wyzwania dla sieci optycznej TPSA stawiane przez technikę transmisji 10Gbit/s. Researchgate 2003.
[7] Fischer G. et al.: Automatic polarization mode dispersion compensation in 40 Gb/s optical transmission system. Ei.Uni-Paderborn, August 2016, 1–5.
[8] Hayami S., Mukasa K., Sugizaki R.: Dispersion-Managed Transmission Lines with Reverse-Dispersion Fiber. Furukawa Review 19, 2000, 6–8.
[9] Huang Y., Yang H., Mao Y.: Design of linear photonic crystal fiber with all-positive/negative ultraflattened chromatic dispersion for the whole telecom band. Optical Engineering 60(7), 2021, 1–3.
[10] Kowalski A.: Modern optical networks and systems. Proc. SPIE 6608, 2007, 660811.
[11] Matsiu T., Nakajima K., Sankawa I.: Dispersion Compenastion Over All the Telecomunication Bands With Double–Cladding Photonic-Crystal Fiber. Lightwave Technology 25(3), 2007, 1–5.
[12] Nguyen H. et al.: Ultra-flattened chromatic dispersion in all-solid hybrid micro-structured optical fibers for mid-infrared lightwave generation. Proc. SPIE 10902, 2019, 109021Q.
[13] Perlicki K.: Systemy Transmisji Optycznej WDM. WKŁ, Warszawa 2007.
[14] Song P., Wang J., Zhou C.: High birefringence and near-zero dispersion photonic crystal fiber at the wavelength of 1.55 μm. Proc. SPIE 10255, 2017, 102553O.
[15] Szymańska A.: Łącza światłowodowe – budżet mocy. Politechnika Warszawska, Ośrodek Kształcenia na Odległość OKNO, Warszawa 2018.
[16] http://www.teraxion.com (available 1.10.2021).

M.Sc. Tomasz Bobruk
e-mail: tomaszbobruk@gmail.com

Ph.D. student at the Lublin University of Technology. He professionally build fiber optic networks for telecommunications operators.

https://orcid.org/0000-0001-8265-9228

otrzymano/received: 5.11.2021 *przyjęto do druku/accepted: 15.12.2021*

http://doi.org/10.35784/iapgos.2828

FIBRE OPTIC BRAGG STRUCTURES WITH MONOTONIC APODISATION CHARACTERISTICS

Jacek Klimek
Lublin University of Technology, Faculty Electrical Engineering and Computer Science, Lublin, Poland

Abstract. *The article discusses the principle of operation and the structure of chirped and uniform gratings. It presents the method of producing gratings with monotonic apodisation characteristics, and compares the spectral features of produced gratings with the those obtained by mathematical modelling.*

Keywords: apodised Bragg gratings, optical fibre sensors, FBG, CFBG

ŚWIATŁOWODOWE STRUKTURY BRAGGA O MONOTONICZNEJ CHARAKTERYSTYCE APODYZACJI

Streszczenie. *W artykule omówiono zasadę działania i budowę siatek chirpowych oraz siatek jednorodnych., przedstawiono sposób wytwarzania siatek o monotonicznej charakterystyce apodyzacji, porównano charakterystyki spektralne siatek wytworzonych z charakterystykami uzyskanymi metodą modelowania matematycznego.*

Słowa kluczowe: apodyzowane siatki Bragga, czujniki światłowodowe, FBG, CFBG

Introduction

Sensors using fibre-optic Bragg gratings as measuring transducers enable non-invasive measurements in medicine and industry [6]. Due to their small dimensions and insensitivity to the external electromagnetic field, the area of application of this type of sensors is constantly increasing [2, 3, 10]. Research on their applications has been going on for several decades.

The most frequently used method of producing Bragg structures on optical fibres is the phase mask inscription method. It is a well-known method, the advantages of which are the small number of elements necessary to produce the grating and low vibration sensitivity. The disadvantage, however, is the cost of phase masks and the inscription of the structure to a specific wavelength.

The conducted works allow to determine the possibility of shaping the spectral characteristics of structures, and thus influencing the metrological properties of sensors based on them. This is important because the commercially available Bragg gratings are characterised by a limited range of available parameters. Such structures are often optimised for use in telecommunications.

Some types of Bragg gratings, such as tilted fibre Bragg gratings, are not commercially available. Due to the sensitivity to temperature and stress, Bragg gratings are used as sensors of these physical quantities [1, 16]. The most frequently used phenomenon is the shift of the Bragg resonance wavelength under the influence of temperature or stress [12, 13, 17].

There are many types of Bragg gratings, the most important of which, due to the geometric distribution of the refractive index, are: uniform fibre Bragg gratings (FBGs), tilted fiber Bragg gratings (TFBGs), chirped fiber Bragg gratings (CFBGs) and long-period gratings (LPGs).

Each type of grating can have different distribution profiles of the refractive index change along the length of the grating, i.e. apodisation. Grating apodisation changes its spectral characteristics and the potential area of its applications [8, 9, 13, 18].

Figure 1 shows examples of the spectral transmission characteristics obtained from numerical calculations in the OptiGrating Optiwave Systems Inc. environment. Figure 1a shows the spectral characteristics of a uniform grating with an apodisation profile described by the constant function *f(x)* = 1, Figure 1b shows the spectral characteristics of a grating with a Gauss apodisation profile.

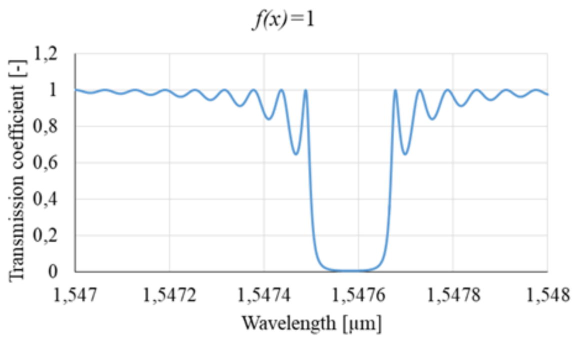

a)

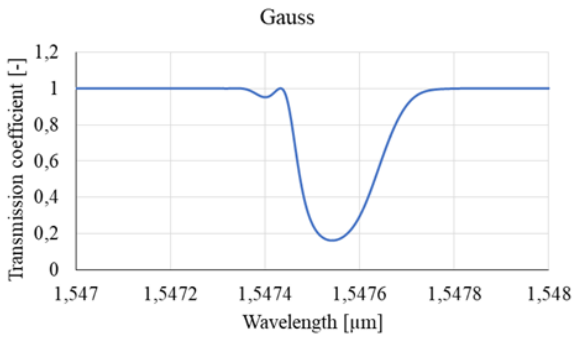

b)

Fig. 1. Spectral characteristics of gratings with different apodisation functions: a) apodisation by f(x) = 1, b) apodisation by Gaussian function

For the apodisation described by the constant function *f(x)* = 1, the transmission characteristic shows sidebands which are strongly damped on the Gauss-type transmission characteristics. The most commonly used apodisation profiles in the production technology of Bragg gratings are presented in the form of equations (1-5).

Gauss profile:

$$T = exp\left[-a\left(\frac{z}{L}\right)^2\right] \qquad -\frac{L}{2} \le z \le \frac{L}{2} \tag{1}$$

Hamming profile:

$$\mathrm{T} = \frac{1+\mathrm{a}\cos\left(\frac{2\pi z}{\mathrm{L}}\right)}{1+\mathrm{a}} \qquad -\frac{\mathrm{L}}{2} \le \mathrm{z} \le \frac{\mathrm{L}}{2} \tag{2}$$

cosine profile:

$$T = cos^{\,a}\left(\frac{\pi z}{L}\right) \qquad -\frac{L}{2} \le z \le \frac{L}{2} \tag{3}$$

hyperbolic tangent profile:

$$T = \begin{cases} \dfrac{1}{\tanh(a)} tanh\left(\dfrac{2a\left(z+\left(\frac{L}{2}\right)\right)}{L}\right) & -\dfrac{L}{2} \le z < 0 \\ \dfrac{1}{\tanh(a)} tanh\left(\dfrac{2a\left(-z+\left(\frac{L}{2}\right)\right)}{L_g}\right) & 0 \le z \le \dfrac{L}{2} \end{cases} \tag{4}$$

Cauchy profile:

$$T = \frac{1-\left(\frac{2z}{L}\right)^2}{1-\left(\frac{2az}{L}\right)^2} \qquad -\frac{L}{2} \le z \le \frac{L}{2} \tag{5}$$

Parameter a is used to control the shape of the apodisation profile, z is the axis along which the grating is written, L is the length of the grating. Unfortunately, the main problem in the selection of apodisation is the inverse relationship between the *FWHM* parameter and the noise characteristics of the group delay ripple (GDR), because apodisation reduces the reflectance and reduces the effective length of the grating [18]. Smoother and more concentrated, with larger values in the middle, the apodisation profile for chirped gratings reduces the spectral reflectance and the value of the half-width of the grating [4].

1. Modification of the distribution of the apodisation function

The apodisation characteristic is one of the main parameters influencing the spectral properties of the optical Bragg grating. It results from the magnitude of changes in the refractive index along the length of the entire structure, affecting the effective refractive index in the optical fibre core [5]. One way to obtain a specific apodisation is to use a spatially differentiated distribution of the radiation intensity of the laser beam used to produce Bragg sieves. Changing the distribution of the apodisation function enables the elimination of unfavourable spectral properties such as, for example, sidebands [7, 19], as well as enables the shaping of the spectral characteristics of the produced grating and its modification for a specific application. The transverse distribution of the laser beam is described by the Gauss function. Modification of this type of profile in order to obtain a monotonic apodisation function is possible through the use of a slit and a selective selection of a part of the radiation intensity distribution characteristic of the rising or falling slope.

An uncomplicated method of controlling the apodisation shape of the produced periodic structures was developed. A method has been proposed in which the change of the apodisation profile can be easily achieved by placing a slot in the laser beam that records the structures. Such a slit should cover the laser beam in a strictly defined place. Figure 2 shows the method of controlling the apodisation shape of the produced periodic structures. The laser beam is 12.5 mm wide, while the produced Bragg structures, after using the slit, have a length of 5 mm.

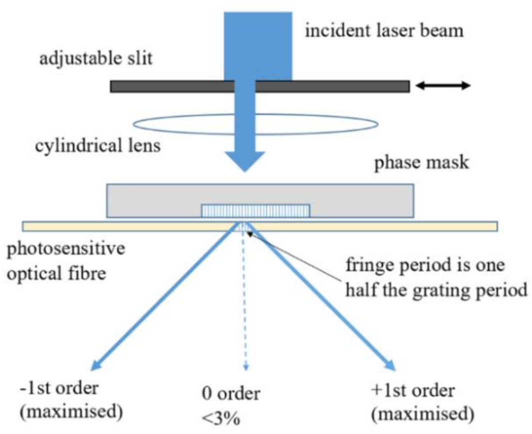

Fig. 2. Modification of the apodisation profile

The aperture that modifies the intensity distribution of the UV laser radiation has the ability to change its position along the mask as shown in Figure 2. It is located between the phase mask and the source of UV radiation. On the characteristic showing the distribution of the intensity of the UV laser radiation, this aperture is located on one of the slopes of this characteristic (Fig. 3a and Fig. 3b). As can be seen, the shape of the radiation intensity distribution of the entire laser beam is described by the Gaussian curve, while selecting the appropriate part of the beam, a monotonic profile of radiation intensity changes is obtained.

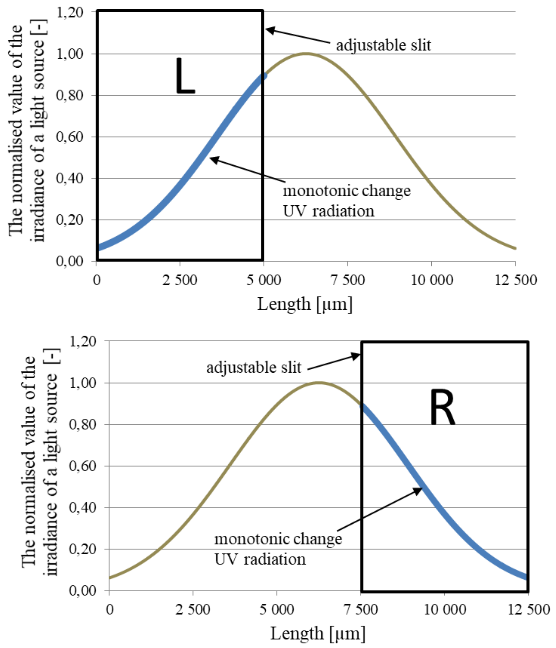

a)

b)

Fig. 3. Change of apodisation by means of a slot of adjustable width located on a) rising profile of the laser beam marked as L, b) falling profile of the laser beam R

With the help of appropriate masks, uniform or chirped gratings are obtained. The principle of the chirped grating is that waves of different length are reflected in different parts of the grating depending on the period of change of the refractive index. In this way, shorter wavelengths are reflected in the part of the grating where the period is smaller and similarly longer waves are reflected in the part of the grating where the period is longer, as shown in Figure 4a. For comparison, the grating without chirp is shown in Figure 4b.

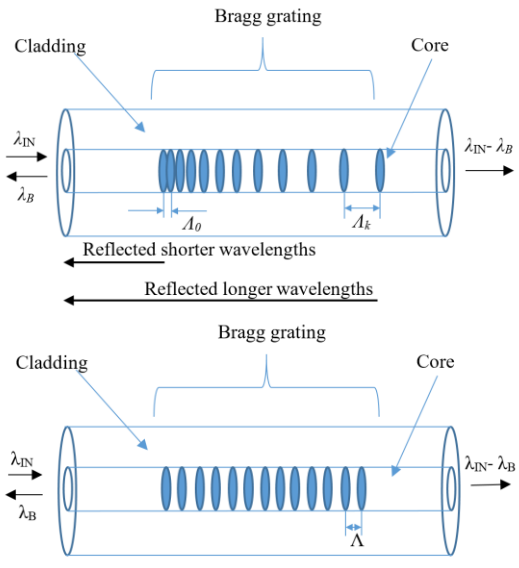

a)

b)

Fig. 4. Scheme and principle of operation of a fibre Bragg grating: a) with chirp, b) without chirp

In the described case, the distance travelled by shorter waves is smaller than in the case of longer waves. The opposite case can be obtained by changing the direction of the optical signal input (input on the right), then longer waves will be reflected earlier, thus they will travel a shorter distance. The measure of the phase mask chirp used to produce the chirped grating is the change in the period of the mask in relation to its length and is expressed in the unit nm/cm. For a mask with a length of 25 mm, a 1 nm/cm chirp and a central period of the mask, e.g. 1060 nm, the period at the beginning of the mask is 1.25 nm lower than 1060 nm, and at the end of the mask is 1.25 nm higher. For the produced gratings, their chirp will assume half the chirp value of the phase mask. This type of grating is produced by changing the period along the length of the optical fibre or by changing the effective refractive index depending on the length of the grating, and by both of these effects simultaneously, as shown in equation 6.

$$\lambda_B(z)=2n_{eff}(z)\Lambda(z) \tag{6}$$

The simplest chirped gratings are those whose period changes linearly according to the equation below:

$$\Lambda(z)=\Lambda0+\Delta\Lambda z, \tag{7}$$

where Λ_0 is the initial period and $\Delta\Lambda$ is the linear change of the period along the fibre length *z*.

2. Obtained results

Research has been carried out on the influence of changes in the period of the gratings on their spectral characteristics. For this purpose, models of Bragg structures were built without chirp and corresponding to the chirp values of phase masks provided by the laboratory, i.e. 0.05 nm/cm, 0.5 nm/cm and 5 nm/cm. Then, their spectral characteristics were determined numerically (Fig. 5, Fig. 6) and compared with the actual spectral characteristics of the gratings that were produced (Fig. 7). The value of the refractive index modulation amplitude determined by the equation was adopted for the calculations:

$$\Delta n_{AC} = \frac{\lambda_B \cdot \mathrm{atanh}(\sqrt{R_{max}})}{\pi L \Gamma}, \tag{8}$$

where R_{max} is the maximum value of the grating reflection coefficient, *L* is the grating length, and the parameter Γ determines what part of the energy is propagated in the fibre core; this parameter takes a value from 0 to 1 and is described by the equation:

$$\Gamma = \frac{\pi^2 d^2 N^2}{\lambda_B^2+\pi^2 d^2 N^2}, \tag{9}$$

where *d* is the diameter of the core and *N* is a numerical aperture.

For the SMF-28 fibre, the parameter Γ takes the value of 0.7, which means that 30% of the energy is propagated in the cladding and 70% in the core [15].

In order to analyse the influence of changing the grating's physical parameters on its spectral characteristics, numerical calculations were performed in the OptiGrating Optiwave Systems Inc. environment. The analysis concerned parameters such as chirp and grating apodisation. OptiGrating is an environment that enables the design and analysis of sensors based on fibre Bragg gratings. Figure 5 shows the transmission characteristics of the gratings obtained by mathematical modelling with the use of the OptiGrating software. Gauss apodization profile was used for uniform gratings without chirp, with 0.05 nm/cm chirp, 0.5 nm/cm chirp and 5 nm/cm chirp. Gratings chirp have been matched to the appropriate masks provided by the laboratory in order to easily compare the parameters of the simulated and produced gratings.

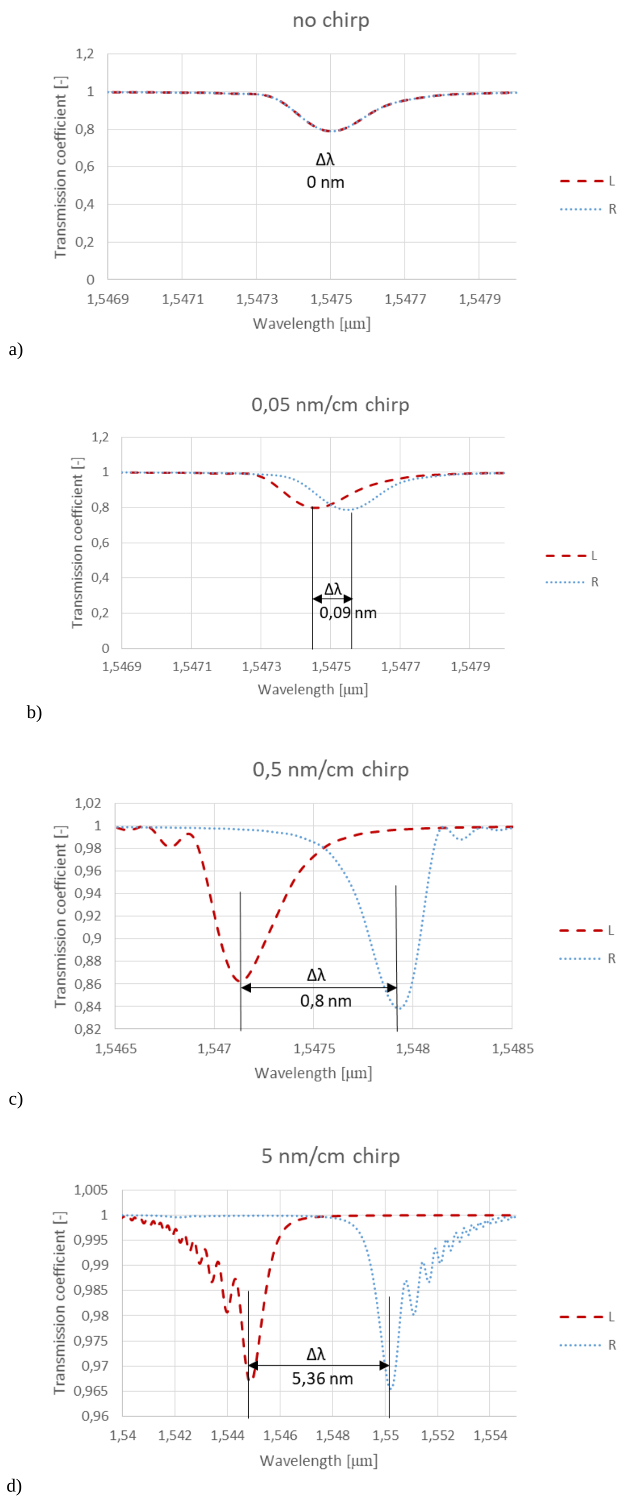

Fig. 5. Spectral characteristics of grids with Gauss apodisation profile, a) without chirp, b) with a 0.05 nm/cm chirp, c) with a 0.5 nm/cm chirp, d) with a 5 nm/cm chirp

Gauss apodisation shortens the effective length of the grating and affects the shape of the spectral characteristics, it is visible for gratings with a higher chirp value (Fig. 5d). For gratings recorded with chirp masks, a shift in the central Bragg resonance length for the *L* and R positions is visible. The shift is the greater the greater the chirp value of the phase mask used. The smallest Bragg resonance shift value was obtained for gratings with a 0.05 nm/cm chirp, this shift is 0.09 nm, for gratings with a 0.5 nm/cm chirp the shift is 0.8 nm, while for gratings with a 5 nm/cm chirp the shift is the largest and amounts to 5.36 nm.

Figure 6 shows the transmission characteristics of the gratings obtained from mathematical modelling with the use of the Optigrating software. The apodisation profile described by the function *f(x)* = 1 was used for the calculations.

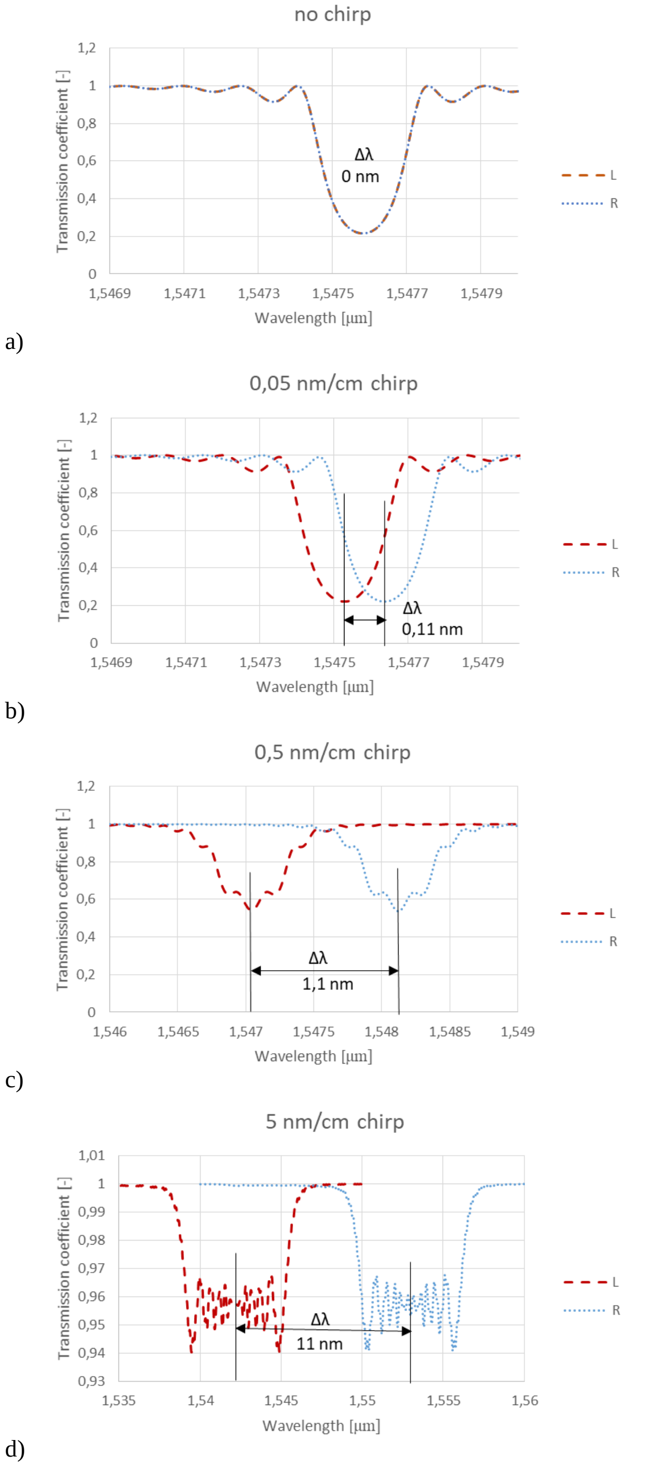

Fig. 6. Spectral characteristics of grids with apodisation profile f(x) = 1, a) without chirp, b) with a 0.05 nm/cm chirp, c) with a 0.5 nm/cm chirp, d) with a 5 nm/cm chirp

The effective length of the grating recorded with apodisation with the profile *f(x)*=1 is the same as the slot, i.e. 5 mm. There is a visible decrease in transmissivity for the Bragg resonance wavelength. The shift for the *L* and *R* edges for gratings with a chip is greater than for a Gaussian grating. The shift is the greater the higher the chirp value of the phase mask used, similar to the case of Gaussian gratings. The smallest Bragg resonance shift value was obtained for gratings with a 0.05 nm/cm chirp, his shift is 0.11 nm, for gratings with a 0.5 nm/cm chirp the shift is 1.1 nm, while for gratings with a 5 nm/cm chirp the shift is the largest and amounts to 11 nm.

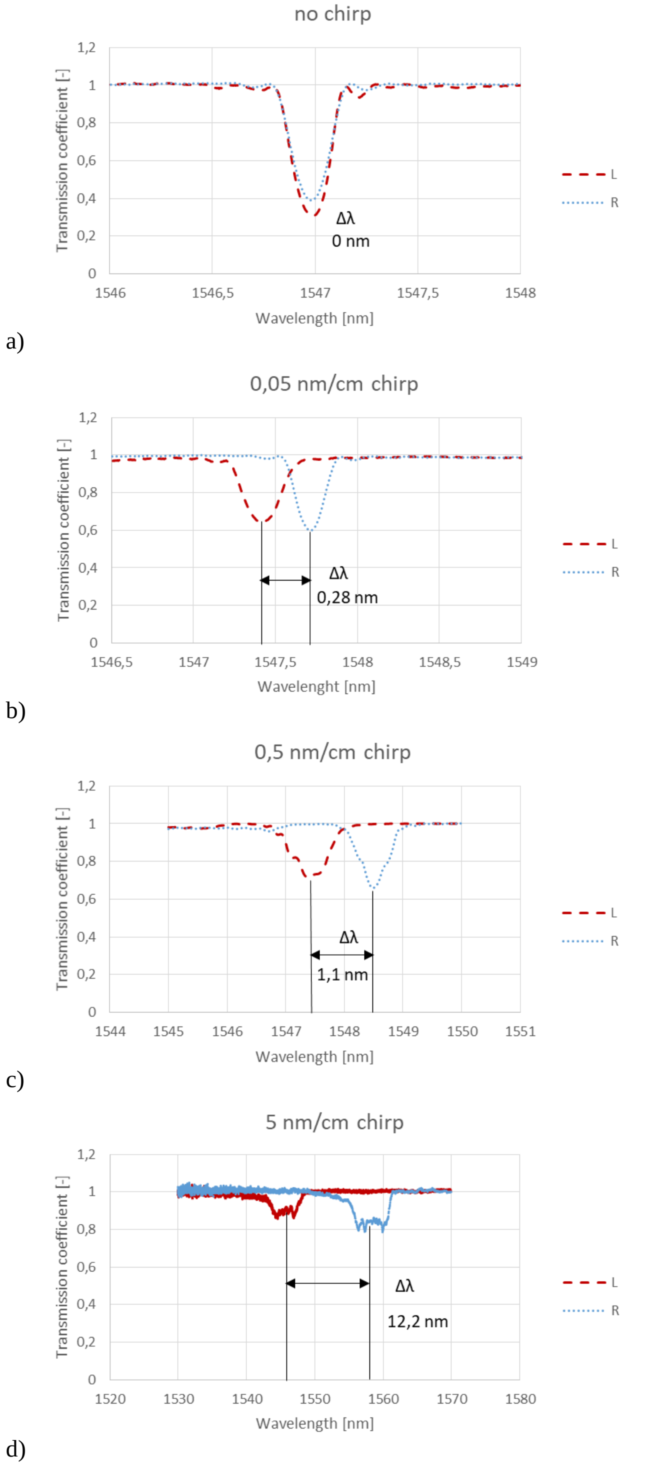

Fig. 7. Spectral characteristics of gratings produced in the laboratory, a) without chirp, b) with a 0.05 nm/cm chirp, c) with a 0.5 nm/cm chirp, d) with a 5 nm/cm chirp

The spectral characteristics of the produced gratings are similar to those of the gratings modelled with the *f(x)* = 1 profile. For the gratings with a 0.5 nm/cm chirp, the identical shift for the *L* and *R* slopes was obtained, amounting to 1.1 nm, for the gratings with a 5 nm/cm chirp, the difference between the produced and modelled gratings was 1.2 nm, while for the gratings with a 0.05 nm/cm chirp, the difference was 0.17 nm.

3. Summary and conclusions

For gratings recorded with chirp masks, a shift in the central Bragg resonance length is visible for the *L* and *R* positions, i.e. the rising and falling slopes. The shift is the greater the higher the chirp value of the applied phase mask. The smallest Bragg resonance shift values below 1 nm were obtained for gratings with a chirp of 0.05 nm/cm, which is related to a small change in the period of the phase mask along its length. The greatest change in wavelength, amounting to a dozen or so nanometers, was obtained for gratings with a chirp of 5 nm/cm. When inscription uniform gratings – without chirp, no shift in the Bragg resonance wavelength for the *L* and *R* slopes was demonstrated. The above method of modifying the apodisation profile can be used to shape the spectral characteristics as well as to control the central Bragg resonance wavelength. The correct position of the slit relative to the phase mask as well as the slit width can change the shape of the spectrum as well as the Bragg resonance wavelength.

References

[1] Chehura E., James S. W., Tatam R. P.: Temperature and strain discrimination using a single tilted fibre Bragg grating. Optics Communications 275, 2007, 344–347.

[2] Dong B. et al.: Simultaneous measurement of temperature and force based on a special strain-function-chirped FBG. Sensors and Actuators A 147, 2008, 169–172.

[3] Ecke W. et al.: Optical fiber grating sensor network for monitoring refractive index and temperature distributions in fluids. Proc. SPIE 3783, 1999, 176–183.

[4] Ennser, K., Zervas, N., Laming, R. L.: Optimization of apodized linearly chirped fiber gratings for optical communications. IEEE Journal of Quantum Electronics 34(5), 1998, 770–778.

[5] Gillooly A. M. et al.: Implementation Of Chirped Fiber Bragg Gratings (CFBG) As Optical Wear Sensors. Lasers and Electro-Optics Society. The 16th Annual Meeting of the IEEE 2003.

[6] Guo T.: Fiber Grating-Assisted Surface Plasmon Resonance for Biochemical and Electrochemical Sensing. Journal of Lightwave Technology 35(16), 2017, 3323–3333.

[7] Hill K., Meltz G.: Fibre Bragg grating technology fundamentals and overview. Jr. Lightwave Techno. 15, 1997, 1263–1276.

[8] Hwang G. S. et al.: Numerical Study on Reflection Spectra of an Apodized Fiber Bragg Grating Subjected to Strain Gradients. Procedia Engineering 79, 2014, 631–639.

[9] Khalid K. S. et al.: Simulation and analysis of Gaussian apodized fiber Bragg grating strain sensor. Journal of Optical Technology 79(10), 2012, 667–673.

[10] Kinet D. et al.: Fiber Bragg Grating Sensors toward Structural Health Monitoring in Composite Materials: Challenges and Solutions. Sensors 14, 2014, 7394–7419.

[11] Kisała P.: Metrological conditions of strain measurement optoelectronic method by the use of fibre Bragg gratings. Metrology and Measurement Systems 19(3), 2012, 471–480.

[12] Kisala P., Cieszczyk S.: Method of simultaneous measurement of two direction force and temperature using FBG sensor head. Applied Optics 54(10), 2015, 2677–2687.

[13] Lin Z. et al.: A novel method for fabricating apodized fiberber Bragg gratings. Optics and Laser Technology 35, 2003, 315–318.

[14] Markowski K. et al.: Custom FBGs inscription using modified phase mask method with precise micro- and nano-positioning. Proc. of SPIE 10031, 2016, 100311H.

[15] Waluyo T. et al.: The effect of macro-bending on power confinement factor in single mode fiber. Journal of Physics: Conference Series 985, 2017, 012001.

[16] Weilin L. et al.: Real-Time Interrogation of a Linearly Chirped Fiber Bragg Grating Sensor for Simultaneous Measurement of Strain and Temperature. IEEE Photonics Technology Letters 23(18), 2011, 1340–1342.

[17] Zhan Y. et al.: A linearity interrogation technique with enlarged dynamic range for fiber Bragg grating sensing. Optics Communications 283, 2010, 3428–3433.

[18] Zhang H.: A novel method of optimal apodization selection for chirped fiber Bragg gratings. Optik – International Journal for Light and Electron Optics 125(5), 2014, 1646–1649.

[19] Zychowicz Ł. et al.: Methods of producing apodized fiber Bragg gratings and examples of their applications. Informatyka, Automatyka, Pomiary w Gospodarce i Ochronie Środowiska 89(1), 2018, 60–63.

Ph.D. Jacek Klimek
e-mail: j.klimek@pollub.pl

Assistant at the Faculty of Electrical Engineering and Computer Science of the Lublin University of Technology, author of many publications on fibre optics. He obtained his Ph.D. in 2021. His research focuses on the fabrication and study of optical periodic structures called Bragg gratings. Current research interests focus on issues related to complex periodic structures.

http://orcid.org/0000-0001-8141-6136

otrzymano/received: 25.11.2021 *przyjęto do druku/accepted: 15.12.2021*

http://doi.org/10.35784/iapgos.2816

ON THE CAPACITY OF SOLAR CELLS UNDER PARTIAL SHADING CONDITIONS

Mateusz Bartczak
Wroclaw University of Technology, Chair of Electronic and Photonic Metrology, Wrocław, Poland

***Abstract**. A photovoltaic system under uniform illumination conditions has only one global maximum power point, but the same panel in the case of partial shading conditions can have more maxima on the power-voltage curve. The author presents the simulations and results of measurements on a photovoltaic system under different lighting conditions. Impact of nonlinear capacitance on the shape of the response to excitation in the form of a load is presented. The paper also describes which photovoltaic cell parameters influence the shape of the C-V curve. The author proposes to analyze the voltage response of the system in order to extract information about partial shade condition.*

Keywords: MPPT, PSC, partial shading, I-V curve, solar capacitance, solar cell model

O POJEMNOŚCI OGNIW FOTOWOLTAICZNYCH W WARUNKACH CZĘŚCIOWEGO ZACIEMNIENIA

***Streszczenie.** System fotowoltaiczny w warunkach równomiernego oświetlenia ma tylko jeden globalny punkt mocy maksymalnej, ale ten sam panel w przypadku warunków częściowego zacienienia może mieć więcej maksimów na krzywej moc-napięcie. Autor przedstawia symulacje i wyniki pomiarów systemu fotowoltaicznego w różnych warunkach oświetlenia. Przedstawiono wpływ pojemności nieliniowej na kształt odpowiedzi na wzbudzenie w postaci obciążenia. W artykule opisano również jakie parametry ogniwa fotowoltaicznego wpływają na kształt krzywej C-V. Autor proponuje analizę odpowiedzi napięciowej systemu w celu wydobycia informacji o stanie częściowego zacienienia.*

Słowa kluczowe: MPPT, PSC, częściowe zacienienie, krzywa I-V, pojemność ogniw fotowoltaicznych, jednodiodowy model ogniwa fotowoltaicznego

Introduction

Recently renewable energy has caught more and more scientific research attention due to popularity of solar power, prosumer activities. The process of replacing conventional electricity production systems with photovoltaic systems (PV) has progressed in recent years, due to characteristics such as: environmentally friendly, reliability, renewability, etc. Every year there is an increase in the share of electricity produced by photovoltaic panels compared to other energy sources [7]. In recent years, a lot of low-cost maximum power point (MPP) trackers are emerging. In these devices we can find different types of DC-DC converters, a cross section of these converters can be found in these articles [5, 16]. Simplified diagram of the maximum power point tracker (MPPT) is presented in Fig. 1.

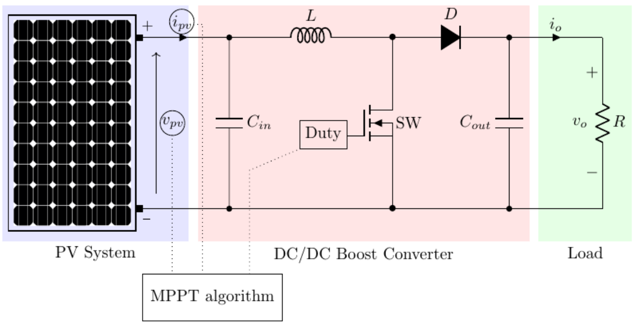

Fig. 1. Schematic diagram of PV System with MPPT

The PV System from Fig. 1 is an assembly of photovoltaic cells and bypass diodes. Temperature, illumination, partial shade condition (PSC), number of bypass diodes, the way individual PV cells are connected, have the greatest influence on the I-V characteristics of a PV system [11]. The single diode solar cell equivalent model is presented in Fig. 2**.** This model is very well known in the scientific literature, there are a number of papers describing the individual effects of the elements of this model on the I-V characteristics [1, 15] and methods of extracting the parameters of this model [14]. This model is commonly used in the design of photovoltaic systems, because it can be used to determine with sufficient accuracy the power delivered by the photovoltaic module to the load. However, for modelling the physical phenomena that occur inside photovoltaic cells, the single diode model is incomplete. It concerns an ideal cell in which the only processes occurring in the semiconductor region are leakage (negligibly small) and diffusion of current carriers, which finds its reference in the diode d_1.

$$I = I_{ph} - I_{d1}\left(e^{\frac{q(V-R_sI)}{nKT}} - 1\right) - \frac{V-R_sI}{R_{sh}} \tag{1}$$

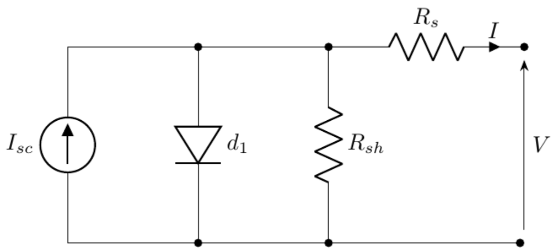

Fig. 2. Solar Cell Single diode model

Publications also include studies on the two-diode model [3, 12]. The effect of recombination in the space charge region of the junction was considered by including a second diode d_2 in the circuit, in parallel with diode d_1. The diode ideality factor (n) for d_1 is not included in this model. It was assumed to have a constant value equal to 1 for the diffusion component, which corresponds to the absence of recombination phenomenon, making diode d_1 reflect an ideal photovoltaic cell. The diode d_2 reflects the recombination component of the dark saturation current. The ideality factor for a d_2 diode is 2, because there are no phenomena other than recombination. Equation (2) is showing the relation between diode currents.

$$I = I_{ph} - I_{d1}\left(e^{\frac{q(V-R_sI)}{KT}} - 1\right) - I_{d2}\left(e^{\frac{q(V-R_sI)}{2KT}} - 1\right) - \frac{V-R_sI}{R_{sh}} \tag{2}$$

1. Description of the problem

Extraction of electrical power from solar photovoltaic (PV) systems under nonuniform irradiance such as partial shading (PSC) is the most challenging task for the solar PV engineers & researchers. The output power of the solar panel, which was reduced due to shading (since the cells are connected in series, shading one cell will reduce the current in the others), was corrected with a bypass diode [10]. The impact of PSC on the I-V characteristic and the P-V characteristic is presented in Fig. 4Fig. 5. They have been generated from a single diode model and reflect the three photovoltaic panels with bypass diodes connected to form one photovoltaic system. The connection is shown in Fig. 3. Each module is made of 20 cells connected in series and has bypass diode connected to the output terminals, therefore the total open-circuit voltage is about 35 V.

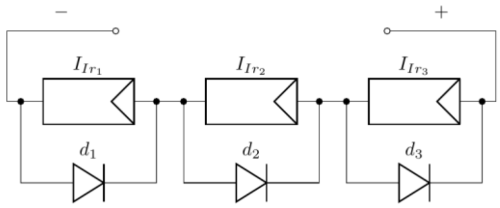

Fig. 3. Bypass diodes connected with solar modules

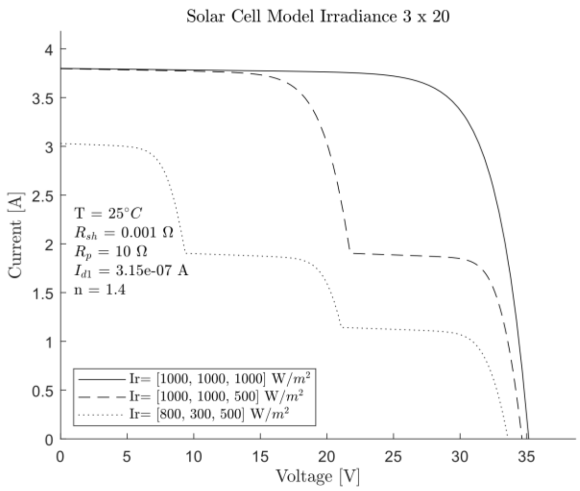

Fig. 4. PSC impact on the PV system I-V characteristic

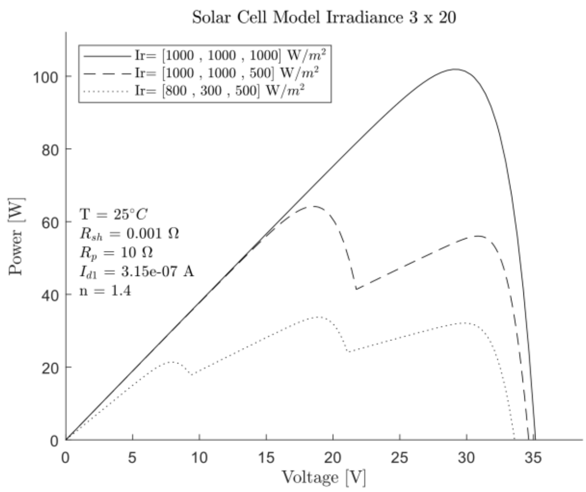

Fig. 5. PSC impact on the PV system P-V characteristic

At non-uniform irradiance conditions local maxima appears on the P-V characteristics which make it difficult for the MPPT controller to search for the maximum power point. There are various types of MPPT techniques used to run PV modules on maximum power. Researchers are constantly creating or improving existing MPPT algorithms. In the research mainstream, algorithms can be divided into couple of groups: classical (Constant Voltage, Perturb & Observe, Incremental Conductance, etc.), intelligent (Artificial Neural Network, Fuzzy Logic, Sliding Mode Controller etc.), optimization (Particle Swarm Optimization, Cuckoo Search etc.). A review of this techniques is presented in following article [4].

2. Experiment setup

One of the classical & conventional simple MPPT is Fractional Short-Circuit Current (FSCC) algorithm. This method assumes that the ratio of I_m (current at MPPT) to I_{sc} (short-circuit current) is approximately a constant value, hence I_m and I_{sc} have a linear relationship (3), where of K is approximately given in the interval $K \in (0.78\,, 0.92)$ [8].

$$I_m = K \cdot I_{sc} \tag{3}$$

In the context of Fig. 1, if the Short-Circuit Current MPPT type algorithm performs the measurement of current I_{sc}, it must close the SW key, then measure the current flowing from the PV System. In the next step the algorithm calculates the I_m, based on it, sets the corresponding duty cycle on the SW gate. Then the key is opened and the voltage returns to the V_{pv} returns to voltage determined by load resistance. In this paper, the author measures the return of this voltage to the operating voltage at time.

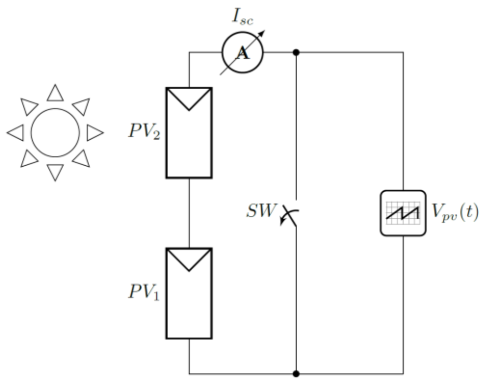

Fig. 6. Simplified schema of measurement setup

Fig. 6 shows a simplified scheme of the measuring system for V_{pv}(t). Two photovoltaic panels were exposed to sunlight. The irradiance of the sunlight was verified using an intensity meter (SOLAR POWER METER TM-206, Accuracy: typically within ± 10 W/m^2 or ±5%). Additionally, the radiation intensity was confirmed by measuring the I_{sc}, because the short-circuit current has linear relation to the solar radiation intensity. V_{pv}(t) has been measured on the oscilloscope (Rigol DS1054Z 50MHz, 1 GSa/sec). The data has been collected from two connected in series solar panels (STP010-12/Kb 10 W, I_{sc} = 0.65 A, V_{oc} = 21.6 V).

3. Results

Using a photovoltaic cell model, so as to simulate the voltage return, a linear charging of the capacitor with a current source is expected. The experimental data show a different shape of $V_{pv}(t)$ Fig. 7**.** The panels had uniform lighting conditions, measurement has been performed for different irradiances.

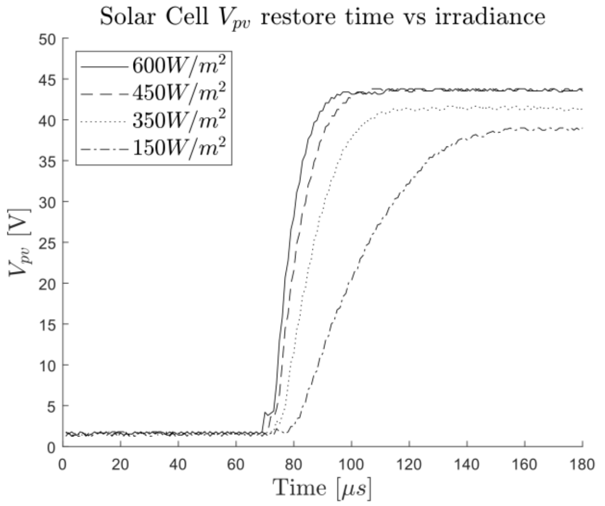

Fig. 7. Restore time of two connected in series STP010-12/Kb 10 W panels

Measurements were also made for non-uniform lighting conditions. When the lighting conditions between two panels are significantly different, one is fully illuminated the other is almost darkened, a fold will start to form on the system response as shown in Fig. 8**.** The voltage response has this shape, because it is the sum of the responses from the two panels.

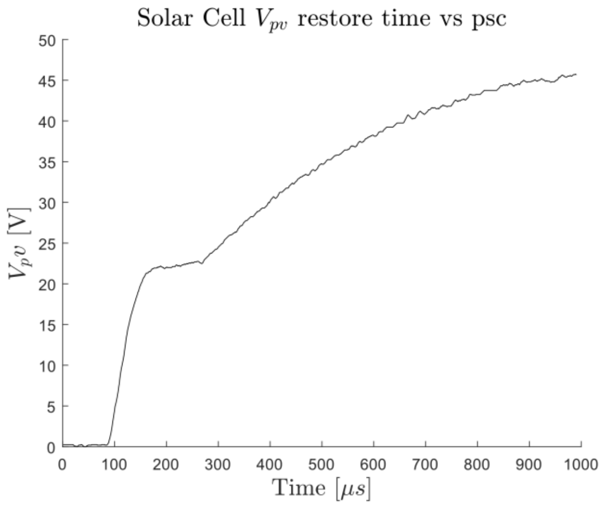

Fig. 8. Output voltage restore time of two connected in series STP010-12/Kb 10 W panels when one of the panels is 90% covered by shade

Shape, rise time of the curve are results from the phenomenon of nonlinear capacitance which occurs at the junction of p-n layers. The two layers of p-n junction can be considered as a capacitor [2]. The capacitance can be so expressed as following equation (4).

$$C = \frac{\varepsilon A}{W} \tag{4}$$

Figures 9–10 presents the non-linear capacitance value in relation to cell voltage, figures data have been generated by the use of a computer program SCAPS. This software can be used to the simulation of solar cells based on different materials types. The software allows to solve numerically the Poisson's equation coupled with continuity equations for both charged carrier electrons and holes [6]. Data has been generated for uniform donor and acceptor density in semiconductor layers and assuming the structure has no defects.

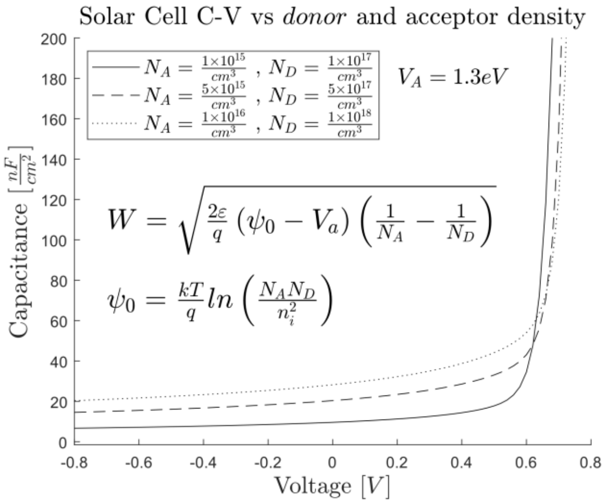

Fig. 9. Solar cell C-V vs donor and acceptor density

The doping density of p and n layers has also an effect on the capacitance of the silicon solar cell Fig. 9. The impact of electric gap on the nonlinear capacitance is presented on Fig. 10. When the solar cell is illuminated, there is a photogeneration process which drives the recombination and diffusion of electrons. The diffusion induces a charge variation into the solar cell accompanied by a charge in the voltage across the cell. It is this charge variation that induces mainly the capacitance of the solar cell under illumination [2].

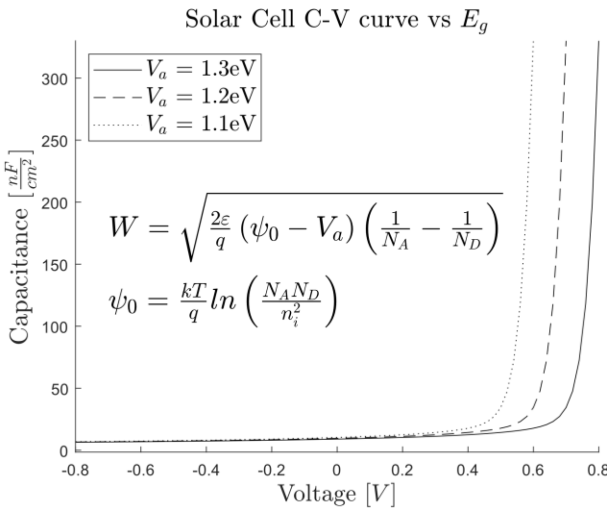

Fig. 10. Solar cell C-V curve vs energy gap of semiconductor

Since the voltage rises Fig. 7Fig. 8 when the SW key Fig. 6 is opened, there is a change in the overall capacitance of the PV System. Capacitance increases as this voltage builds up. When the voltage on the cell is less than 0.6 V, this corresponds to short circuit (I_{sc}) operation of the cell and the capacity is then lower. It is driven by the massive flow of minority carriers through the junction. However, if the voltage is above 0.6 V then the cell is closer to open circuit voltage (V_{oc}). Capacitance increases exponentially, this can be explained by a large storage of carriers in the junction. voltage, the carriers cannot easily move to and cross the junction. A larger number of carriers causes an increase in electrical field, they cannot easily move to and cross the junction.

Analysing the system response in terms of voltage rise time and shape can give information about the insolation state of the system in particular whether there is a PSC. The detection of partial shading conditions is not a major topic in the literature, authors of [13] are using neural network to obtain shade condition. Using the Fill Factor calculation, partial shading can be distinguished from the uniform shading situation [9].

4. Conclusions

The nonlinear capacitance that occurs in photovoltaic systems is worth attention. If there is a need to simulate dynamic load changes and observe voltage changes on a photovoltaic cell, it is worth considering nonlinear capacitance in the photovoltaic cell model. The author proposes an analysis of the voltage response, in terms of changes in shape caused by partial shading of the system. Information about partial shading condition can be valuable from MPPT algorithm point of view, allowing the selection of the type of algorithm. Also, creation of hybrids of MPPT algorithms is possible, for example Fractional Short-Circuit Current (FSCC) algorithm can be combined with Cuckoo Search (CS). The analysis also allows the detection of various defects in the photovoltaic system. The implementation of the voltage rise analysis algorithm does not require drastic changes to the DC-DC converter circuit, the converter has its own capacitance which must be considered.

References

[1] Azzouzi M. et al.: Modeling of electrical characteristics of photovoltaic cell considering single-diode model. Journal of Clean Energy Technologies 4(6), 2016, 414–420.
[2] Barro F. I. et al.: On the capacitance of crystalline silicon solar cells in steady state. Turkish Journal of Physics 39(2), 2015, 122–127.
[3] Bollipo R. B. et al.: Critical review on PV MPPT techniques: classical, intelligent and optimisation. IET Renewable Power Generation 14(9), 2020, 1433–1452.
[4] Bollipo R. B. et al.: Critical review on PV MPPT techniques: classical, intelligent and optimisation. IET Renewable Power Generation 14(9), 2020, 1433–1452.
[5] Bubovich A.: The comparison of different types of DC-DC converters in terms of low-voltage implementation. 5th IEEE Workshop on Advances in Information, Electronic and Electrical Engineering (AIEEE), 2017, 1–4, [http://doi.org/10.1109/AIEEE.2017.8270560].
[6] Burgelman M. et al.: Modelling polycrystalline semiconductor solar cells. Thin solid films 361, 2000, 527–532.
[7] Cozzi L. et al.: World Energy Outlook 2020 – IEA, Organization for Economic Co-operation and Development (OECD) / IEA, Paris, France, 2020 [https://www.iea.org/reports/world-energy-outlook-2020] (available: 10.10.2021).
[8] Danoune M. B. et al.: Study and performance analysis of three conventional MPPT algorithms used in photovoltaic applications. International Conference on Communications and Electrical Engineering (ICCEE). IEEE, 2018.
[9] Davies L. et al.: Automatic detection and characterization of partial shading in PV system. IEEE 7th World Conference on Photovoltaic Energy Conversion (WCPEC) (A Joint Conference of 45th IEEE PVSC, 28th PVSEC & 34th EU PVSEC), 2018.
[10] Fadliondi F. et al.: Bypass diodes for improving solar panel performance. International Journal of Electrical and Computer Engineering 8(5), 2018, 2703.
[11] Franjo P., Virtič P.: Power production comparison of photovoltaic modules. Przegląd Elektrotechniczny 90(12), 2014, 284–287 [http://doi.org/10.12915/pe.2014.12.72].
[12] Humada A. M. et al.: Solar cell parameters extraction based on single and double-diode models: A review. Renewable and Sustainable Energy Reviews 56, 2016, 494–509.
[13] Mekki H. et al.: Artificial neural network-based modelling and fault detection of partial shaded photovoltaic modules. Simulation Modelling Practice and Theory 67, 2016, 1–13.
[14] Rhouma M. B. H. et al.: A simple method for extracting the parameters of the PV cell single-diode model. Renewable Energy 113, 2017, 885–894.
[15] Shannan N. M. et al.: Single-diode model and two-diode model of PV modules: A comparison. IEEE International Conference on Control System, Computing and Engineering, 2013.
[16] Singh S. P. et al.: Performance comparison of MPPT techniques using Cuk converter for photovoltaic energy conversion system. 3rd International Conference on Computational Intelligence & Communication Technology (CICT), 2017, 1–6 [http://doi.org/10.1109/CIACT.2017.7977369].

M.Sc. Eng. Mateusz Bartczak
e-mail: mateusz.bartczak@pwr.edu.pl

Ph.D. student and employee of Wroclaw University of Technology. At this moment assistant professor of Department of Electronic and Photonic Metrology. His scientific interest is mainly focused on renewable energy sources in particular photovoltaic cells, PV modules, DC/DC converters. He works on algorithms for maximum power point tracking and modeling of photovoltaic systems.

http://orcid.org/0000-0003-4459-4173

otrzymano/received: 10.11.2021 *przyjęto do druku/accepted: 15.12.2021*

http://doi.org/10.35784/iapgos.2833

CONTROLLING A FOUR-WIRE THREE-LEVEL AC/DC CONVERTER WITH INDEPENDENT POWER CONTROL IN EVERY PHASE

Bartłomiej Stefańczak
Lublin University of Technology, Faculty of Electrical Engineering and Computer Science, Department of Electrical Drives and Machines, Lublin, Poland

Abstract. *The article presents the design of a four-wire, three-level AC/DC converter. The converter was controlled with the use of a proportional-resonant controllers based voltage oriented control (VOC). The implemented topology of the AC/DC converter allows to control each of the phases separately. This translates into the possibility of independent control of active and reactive power in each of the phases. In addition, the DC bus of the AC/DC converter is connected in parallel with the energy storage via an isolated DC/DC converter and with a renewable energy sources. The tests were carried out with the use of the designed converter, DSP controller and Matlab/SIMULNIK platform, which was used for automatic code generation. The results obtained show that independent control of each of the phases is possible, however, the operation with large power unbalances on each of the phases leads to large current pulsation on the DC bus. This is a phenomenon that threatens the correct operation of the energy storage. As a result, the level of asymmetry between phases should be limited to the level acceptable by the energy storage.*

Keywords: three-level four-wire converter, control of a 4-wire converter, independent power control in each phase, energy storage

STEROWANIE CZTEROPRZEWODOWYM TRÓJPOZIOMOWYM PRZEKSZTAŁTNIKIEM AC/DC Z NIEZALEŻNĄ KONTROLĄ MOCY W KAŻDEJ Z FAZ

Streszczenie. *W artykule przedstawiono projekt czteroprzewodowego trójpoziomowego przekształtnika AC/DC. Sterowanie przekształtnika zrealizowano z wykorzystaniem regulatorów proporcjonalno-rezonansowych opartych na sterowaniu zorientowanym napięciowo (VOC). Zaimplementowana topologia przekształtnika AC/DC pozwala na sterowanie każdą z faz z osobna. Przekłada się to możliwość niezależnej kontroli mocy czynnej i biernej w każdej z faz. Ponadto szyna DC przekształtnika AC/DC połączona jest równolegle z magazynem energii poprzez izolowaną przetwornicę DC/DC oraz odnawialne źródło energii. Badania przeprowadzono z wykorzystaniem zaprojektowanego przekształtnika, sterownika DSP oraz platformy Matlab/SIMULNIK, którą wykorzystano do automatycznej generacji kodu. Otrzymane wyniki wskazują, że sterowanie niezależne każdą z faz jest możliwe jednakże, praca z dużymi asymetriami mocy na każdej z faz prowadzi do dużej pulsacji prądu na szynie DC. Jest to zjawisko zagrażające poprawności działania magazynu energii. W skutek tego poziom asymetrii między fazami powinien być ograniczony do poziomu akceptowalnego przez magazyn energii.*

Słowa kluczowe: przekształtnik trójpoziomowy czteroprzewodowy, sterowanie przekształtnikiem 4-przewodowym, niezależna kontrola mocy w każdej z faz, magazynowanie energii

Introduction

Due to the rapidly developing renewable energy sources (RES) industry, more and more generation sources are connected to the power grid by the three-phase inverters, but also single-phase inverters, the operation of which delivers energy only into one of the three phases [2–6, 11, 14]. Adding to this the fact that most household appliances use pulse power supplies, the current consumed by the consumer is asymmetric and non-linear in nature. Another issue is increasing number of loads with simple supply system, which draws the reactive power from the utility grid. The presented phenomena are undesirable and are described in the distribution grid operation and maintenance manual. When tg ϕ is greater than 0.4, where tg ϕ is the ratio of reactive power to active power, the operator imposes a penalty on the consumer. In a case, where the consumer has a generation source installed and connected to the power grid, e.g. a photovoltaic installation, he becomes a prosumer, a recipient who can also deliver energy into the grid. In this way, thanks to the use of a four-wire AC/DC converter with independent power control in each of the phases, it can affect the quality of power in the grid, i.e. reduce the THD of the current drawn from and delivered to the grid. For this purpose, there is a need to develop a control algorithm that will ensure the limitation of the THD of the current delivered by the converter with the connected electronic devices consuming the current in a non-linear manner. Additionally, the algorithm should be able to compensate the power reactive power independently in each of the phases. It is also recommended that the converter corrects the symmetry of the phase voltages in order to maintain the correct symmetry of the power grid. For the presented reasons, the aim of the article is to develop a converter control algorithm and to select a topology that will be able to meet the desired requirements.

The algorithm described in the paper is based on proportional-resonant regulators and band-pass filters [7, 13]. Their task is to selectively eliminate higher harmonics with independent power control in each of the phases. The actual tests were carried out with the use of a four-wire, three-level converter and a Texas Instruments TMS28379D DSP microcontroller. The algorithm was implemented with the use of automatic code generation via the Matlab / SIMULINK platform. The tests were conducted with the mapping of the power grid characterized by strong asymmetry in the load of individual phases.

1. Four-wire, three-level AC/DC converter with a proportional – resonance algorithm

The system in which a four-wire three-level AC/DC converter can function is shown in figure 1. This figure shows the configuration of an AC/DC converter with a connected chain of PV panels indirectly controlled by the MPPT algorithm [2, 3] The connection of both systems was made by means of a non-isolated DC/DC converter. An electrochemical energy storage was connected in parallel to the DC bus of the converter, through an isolated bidirectional DC/DC converter [1, 8, 10, 12], which is designed not only to charge and unload the storage, but also to provide galvanic separation between the storage and the converter and to guarantee a constant voltage on the DC bus independently from the voltage on the chain of PV panels. On the AC side of the converter, a single-phase voltage control scheme is illustrated. Such a simplification was performed for the sake of clarity of the drawing. In order to build a three-phase control system with the properties described in the first part, the algorithm(the area marked with a red frame in the figure 1) should be duplicated three times for each of the phases. Figure 2 shows the topology of the designed AC/DC converter. The control is based on proportional-resonant regulators responsible for the 1, 3, 5, 7, 9 harmonic in turn. Additionally, a PI controller was connected in parallel, thanks to which the possibility of a constant component is eliminated.

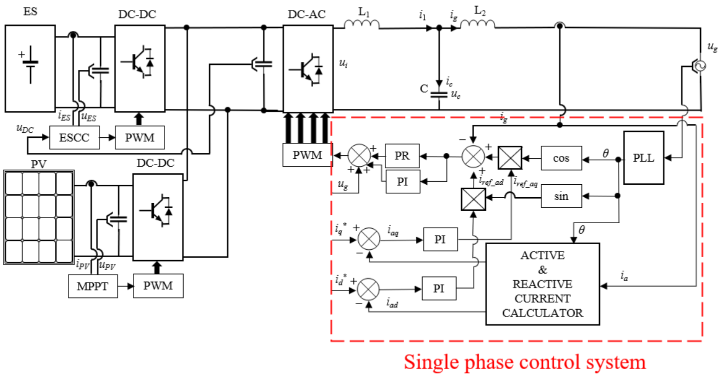

Fig. 1. Simplified algorithm of proportional – resonance converter control for one phase

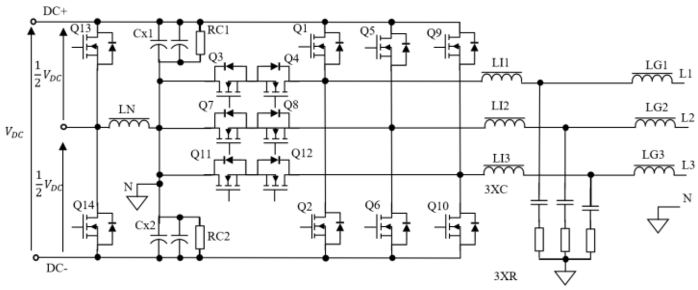

Fig. 2. Diagram of TNPC topology of the DC/AC converter

The parameters of the AC/DC converter are presented table 1.

Table 1. Technical parameters of the four-wire three-level converter AC/DC

Parameter	Value
System output power [kW]	10
DC bus voltage of the AC/DC converter [V]	750
Idle voltage of photovoltaic panels [V]	400
Rated energy storage voltage [V]	48
Capacity of DC bus [mF]	10
Cut-off frequency of the output LCL filter [kHz]	2.8
LCL filter parameters [mH uF mH]	1.2+5+0.38
THDi (at load above 50%) [%]	<3

The energy storage was connected to the converter via a DC/DC converter. The operating range of the converter enforces a bidirectional topology. An algorithm based on Phase-Shift Control (PSC) [1, 9] was used for control. By using such a control method and the topology of the DC/DC converter, the stability of the voltage on the DC bus of the AC/DC converter can be ensured. This is done by taking the excess energy generated by the photovoltaic panels and not converted by the AC/DC converter, or providing energy when the energy generated by the solar panels is insufficient to meet the energy requirements of the AC/DC converter. The task of the modeled AC/DC converter is to provide high-quality energy. The three-level topology of the AC/DC converter allows to reduce the size of the output filter, which eliminates the interference caused by transistor switching noise. Correct connection of the AC/DC converter to the power grid requires reliable synchronization. For this purpose, the Decoupled Double Synchronous Reference Frame Phase Locked Loop (DDSRF-PLL) [15, 17] algorithm was used. The proposed control method is based on feedback, so that even strong interferences present in the network do not threaten the generation of a high-quality synchronization signal [1]. The synchronization signal has a sawtooth shape and is in the range of <0.2π>. The signal is then converted into a sinusoidal signal with an amplitude of 1. The difference between the setpoint and the feedback is sent to a proportional-resonant controller which consists of a plurality of interconnected resonant proportional controllers [3, 7]. The resonant frequency of the regulator is equal to the base frequency of the power grid. As a result, the controller only amplifies the fundamental harmonic signal. Regulators connected in parallel are responsible for 3, 5, 7, 9 harmonics in turn. The transfer function describing the control algorithm as well as the amplitude-phase characteristic, taking into account the LCL output filter of the converter is presented in eq. 1.

$$G_i = \left(K_{pI\_1H} + \sum_{n=1,3,5,7,9}^{N} \frac{K_{iI\_nH} 2\omega_{rcI\_nH} s}{s^2 + 2\omega_{rcI\_nH} s + \omega_{o\_nH}^2}\right)\left(\frac{G_d}{K_{vdc\_fdbk}}\right) G_{LCL}\, G_n \quad (1)$$

where: G_i – transfer function system, K_{pI_1H} – PI regulator gain, n – the harmonic order, ω_{rcl_nH} – the cut-off frequency, K_{iI_nH} – individual resonant gain for the n-th harmonic, ω_0 – base frequency of the filter, K_{vdc_fdbk} – gain due to voltage on the DC bus, G_d – gain of power converter, G_{LCL} – transfer function LCL filter, G_n– transfer function notch filter.

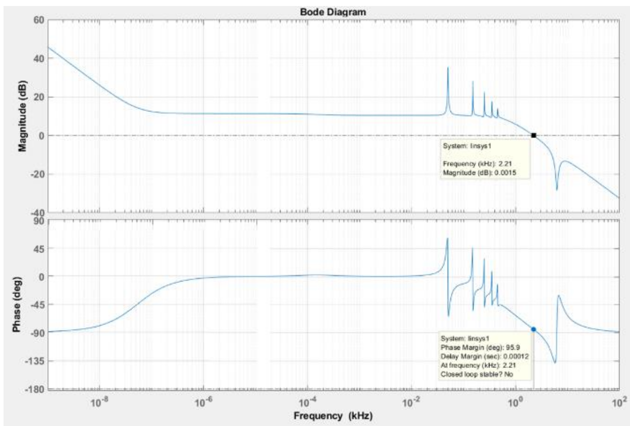

Fig. 3. Amplitude-phase characteristic of the control algorithm

The figure 3 shows the characteristics of the control system. For the most part of the characteristic, the system has a gain of 1. The situation changes when the frequency reaches values equal to the base frequency and the third, fifth, seventh and ninth harmonics, respectively. For the frequencies above the harmonics, the circuit behaves as a low-pass filter. Additionally, a notch filter [17] was used to eliminate the resonant frequency of the LCL filter. The structure of the proportional-resonant filter is based on a filter with an infinite impulse response (IIR). The settings of the regulators are selected in such a way that the regulator obtains the maximum harmonic amplification for a given frequency while maintaining the appropriate phase reserve. When selecting the controller settings, a compromise should be made between the maximum gain and the error resulting from frequency deviations in the power grid. The block named "Active & Reactive block calculator" uses the power calculation method base on the Orthogonal Signal Generator (OSG) [16]. The active power P and reactive power Q for a single-phase application can be calculate with the help of OSG systems. Formulas describing the method used (2), (3). The subscripts “gα” and “gβ” denote the “α” and “β” components of the grid voltage/current in a αβ-stationary reference frame. The subscripts “gα” and “gβ” denote the “α” and “β” components of the grid voltage/current in a αβ-stationary reference frame. Figure 4 show structure of power calculation method.

$$P = \frac{1}{2}\left(v_{g\alpha} i_{g\alpha} + v_{g\beta} i_{g\beta}\right) \tag{2}$$

$$Q = \frac{1}{2}\left(v_{g\beta} i_{g\alpha} - v_{g\alpha} i_{g\beta}\right) \tag{3}$$

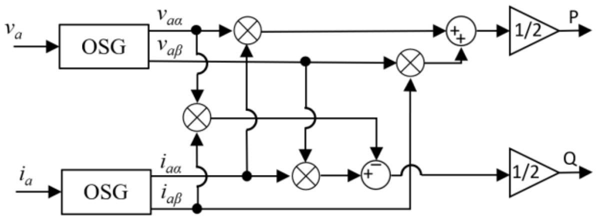

Fig. 4. System for measuring active and reactive power based on orthogonal signal generator for single phase systems

The construction of the OSG system is based on the use of a delay unit which introduces a phase shift of 90° corresponding to the fundamental component of the input signal. The OSG system based on the SOGI filter is used in this implementation because it is an adaptive filtering system and behaves as a generalized integrator. The use of the OSG system allowed for a lower computational load thanks to the quick and accurate response.

Due to the described properties, the proposed control method enables the delivery and drawing of energy from the grid with the use of a converter. The used control system ensures very good dynamics, which translates into a very low THDi at the level of 1–2% at the converter load above 50% of the rated load.

2. Laboratory research

The laboratory stand on which the tests were carried out consists of five parts:

- four-wire, three-level power module made in TNPC topology,
- LCL filter with EMC filter,
- energy storage emulator in the form of a bidirectional ITECH IT6012-C power supply,
- three isolation transformers,
- a controller based on the TI TMS320F28379D microcontroller with Hall sensors for voltage and current measurement.

The constructed stand is illustrated in figure 5.

The obtained test results are shown in the oscillograms in figure 6.

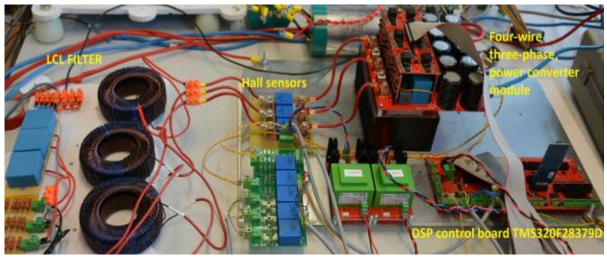

Fig. 5. Laboratory stand on which the research was carried out

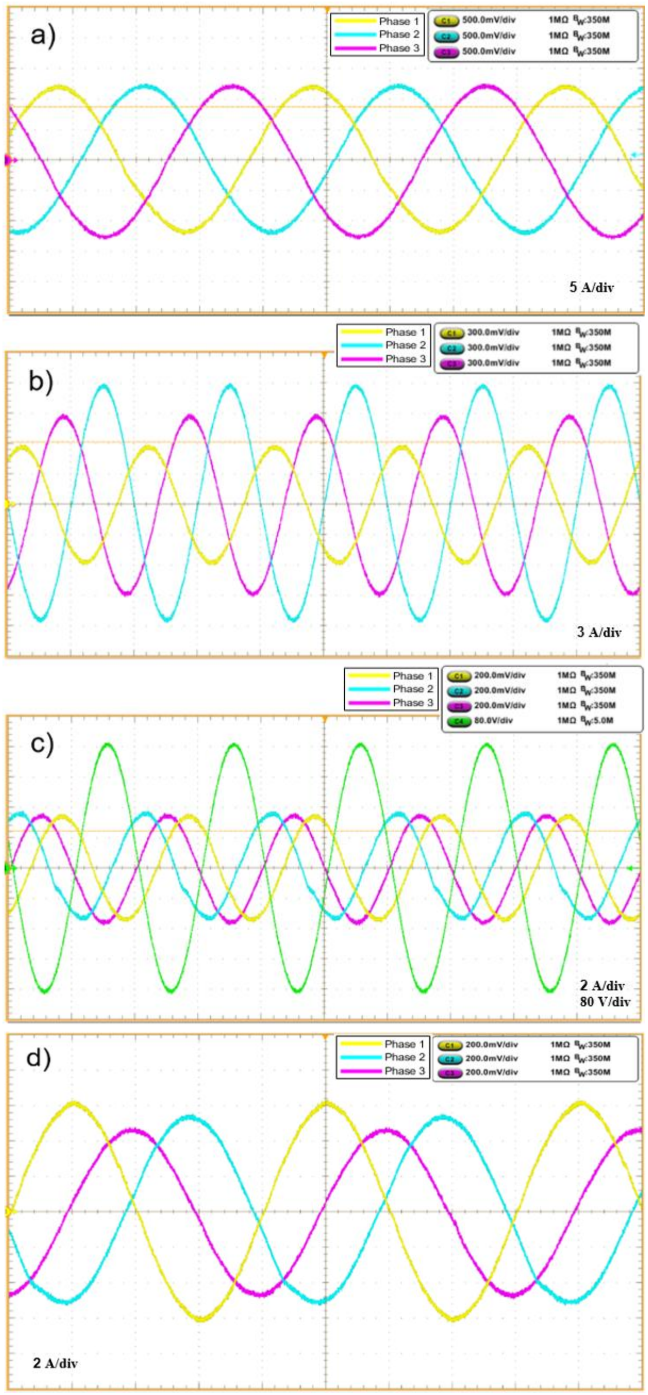

Fig. 6. Oscillograms of the converter operation: a) three-phase currents during inverter operation, symmetrical operation of 2 kW per phase, b) asymmetrical operation, L1 = 1 kW, L2 = 2 kW, L3 = 1.5 kW, c) three-phase currents and L3 phase voltage, L1 and L2 phase inverter operation, L3 phase rectifier operation, d) three-phase currents, L3 phase only active power, L1 and L2 phases with additional reactive power

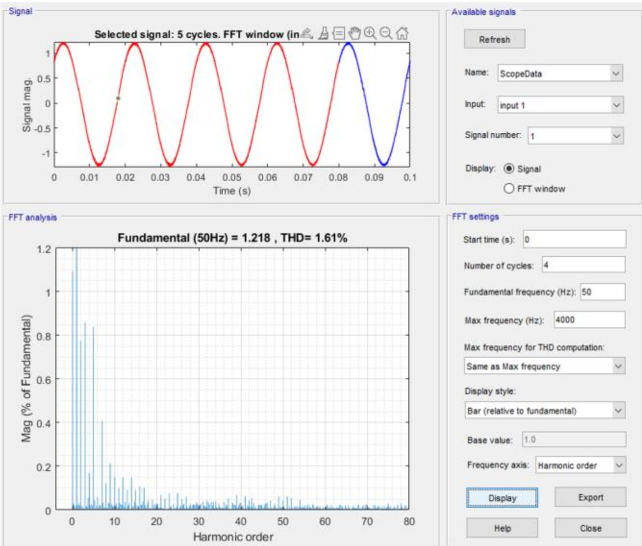

Fig. 7. Analysis of the current output to the network by the converter AC/DC THD current is 1.61%.

The obtained results confirmed the correctness of the applied topology and the selected control method. During tests with high asymmetry, the ITECH 6012-C power supply was used as the DC source. The used power supply has the function of emulating an energy storage. In the case of asymmetric operation, a current with pulsation of 100 Hz, dangerous for the energy storage, was observed, the amplitude of which increased with the increase of induced asymmetry. This problem is being considered and the ways of eliminating the phenomenon will be described in the next article.

3. Conclusions/summary

The article discusses the problem with the stability of the low-voltage electrical network caused by the increasing number of renewable energy sources and loads that draw current in a non-linear manner while consuming reactive power. As a result, these devices cause deterioration of grid parameters and voltage asymmetry between phases. In the following part of the paper, an AC/DC four-wire three-level converter with parallel energy storage is proposed as a solution to the problem. The control algorithm was based on proportional-resonant filters specifically targeting odd harmonics. Multiresonant control combined with DDSRF-PLL synchronization allowed for accurate control of active and reactive power produced and consumed by the AC/DC converter. The performed tests confirmed the validity of the assumptions. The article presents four cases of the converter operation. With symmetrical work and load of the converter in 60% THD of the issued current was 1,61% (figure 7). In the further part the asymmetric operation with phase loading in the ratio L1 = 50%, L2 = 75%, L3 = 100% was shown. The induction of such asymmetry resulted in current flow in the neutral wire. It was observed that the higher the asymmetry, the higher the current amplitude in the neutral conductor. The next oscillogram shows the extreme case where the phases L1 and L3 are delivering power to the grid, while phase L2 draws power from the grid. In this case, the current in the neutral wire is equal to twice the phase current. Such a large current in the neutral conductor results in a large current pulsation on the DC bus of the converter. Its frequency is 100 Hz. The current with such parameters is a threat to the correct operation of the energy storage. Therefore, a power supply with the ability to emulate the energy storage was used in the study. After the tests it was found that such a large current in the neutral line is not a problem for power electronics components. Only a small temperature spike on the DC bus capacitors was reported. The last oscillogram shows the operation of the converter in the mode delivering and drawing reactive power. The converter, thanks to its characteristics, can successfully work as a reactive power compensator. In conclusion, based on the literature analysis, the selection of the converter topology and control method proved to be correct. The device in this configuration can successfully guarantee the prosumer adequate parameters of the LV grid. Further research should focus on solving the problem of the DC bus current pulsation at operation with high asymmetry.

References

[1] Barlik R., Nowak M., Grzejszczak P.: Power transfer analysis in a single phase dual active bridge. Bulletin of the Polish Academy of Sciences: Technical Sciences 61(4), 2013, 809–828 [http://doi.org/10.2478/bpasts-2013-0088].

[2] Brito M. A. G. de, Galotto L., Sampaio L. P., Melo G. d. A. e, Canesin C. A.: Evaluation of the Main MPPT Techniques for Photovoltaic Applications. IEEE Transactions on Industrial Electronics 60(3), 2013, 1156–1167.

[3] Chatterjee A., Mohanty K. B.: Development of stationary frame PR current controller for performance improvement of grid tied PV inverters. 9th International Conference on Industrial and Information Systems (ICIIS), 2014, 1–6 [http://doi.org/10.1109/ICIINFS.2014.7036586].

[4] Govind D., Suryawanshi H. M., Nachankar P., Narayana C. L.: Performance Comparison of Standalone AC Microgrid with Inner Loop Proportional Integral and Proportional Resonant Current Controllers. IEEE First International Conference on Smart Technologies for Power, Energy and Control (STPEC), Nagpur 2020, 1–5 [http://doi.org/10.1109/STPEC49749.2020.9297686].

[5] Grijalva S., Costley M., Ainsworth N.: Prosumer-based control architecture for the future electricity grid. IEEE International Conference on Control Applications, 2011, 28–30 [http://doi.org/10.1109/CCA.2011.6044467].

[6] Ikeda S., Kurokawa F.: Isolated Bidirectional Boost Full Bridge DC-DC Converter for Energy Storage System, 2018 20th European Conference on Power Electronics and Applications, 2018, P.1–P.8.

[7] Islam S., Zeb K., Din, W., Khan I.: Design of a Proportional Resonant Controller with Resonant Harmonic Compensator and Fault Ride Trough Strategies for a Grid-Connected Photovoltaic System. Electronics 7, 2018, 451.

[8] Jarzyna W., Zieliński D., Gopakumar K.: An evaluation of the accuracy of inverter sync angle during the grid's disturbances. Metrology and Measurement Systems 27(2), 2020, 355–371 [http://doi.org/10.24425/mms.2020.132780].

[9] Kumar B. M., Kumar A., Bhat A. H., Agarwal P.: Comparative study of dual active bridge isolated DC to DC converter with single phase shift and dual phase shift control techniques. Recent Developments in Control, Automation & Power Engineering, 2017, 453–458 [http://doi.org/10.1109/RDCAPE.2017.8358314].

[10] Lee J., Jeong Y. and Han B.: A Two-Stage Isolated/Bidirectional DC/DC Converter With Current Ripple Reduction Technique. IEEE Transactions on Industrial Electronics 59(1), 2012, 644–646.

[11] Patil S. N., Prasad R. C.: Design and development of MPPT algorithm for high efficient DC-DC converter for solar energy system connected to grid. International Conference on Energy Systems and Applications, 2015, 228–233.

[12] Penghui Jing, Cong Wang, Wei Jiang, Guopeng Zhang.: Performance analysis of isolated three-level half-bridge bidirectional DC/DC converter, Proceedings of 7th International Power Electronics and Motion Control Conference, 2012, 1527–1531 [http://doi.org/10.1109/IPEMC.2012.6259058].

[13] Praneeth A. V. J. S., Azeez N. A., Patnaik L., Williamson S. S.: Proportional resonant controllers in on-board battery chargers for electric transportation. IEEE International Conference on Industrial Electronics for Sustainable Energy Systems, 2018, 237–242 [http://doi.org/10.1109/IESES.2018.8349880].

[14] Przytuła K., Zieliński D.: Influence of power converters on increasing the share of renewable energy sources. Acta Energetica 1(26), 2016, 125–131 [http://doi.org/10.12736/issn.2300-3022.2016111].

[15] Wu X., Huang T., Chen X., Hu H., He G.: Frequency Characteristic and Impedance Analysis on Three-Phase Grid-Connected Inverters Based on DDSRF-PLL. 10th International Conference on Power Electronics and ECCE Asia, 2019, 1053–1058.

[16] Yang Y., Blaabjerg, F.: A new power calculation method for single-phase grid-connected systems. 2013 IEEE International Symposium on Industrial Electronics, 2013, 1–6 [http://doi.org/10.1109/ISIE.2013.6563684].

[17] Zieliński D., Lipnicki P, Jarzyna W.: Synchronization of voltage frequency convert-ers with the grid in the presence of notching. International Journal for Computation and Mathematics in Electrical and Electronic Engineering – COMPEL 34(3), 2015, 657–673 [http://doi.org/10.24425/mms.2020.132780].

M.Sc. Eng. Bartłomiej Stefańczak
e-mail: b.stefanczak@pollub.pl

Graduated from the Faculty of Electrical Engineering and Computer Science of the Lublin University of Technology in 2019. Since then also employed as assistant lecturer at the university's Department of Electrical Drives and Machines. His research focuses on AC/DC power converters with energy storage. He is a member of the team working on National Centre for Research and Development projects.

http://orcid.org/0000-0001-7071-9131

otrzymano/received: 28.11.2021 *przyjęto do druku/accepted: 15.12.2021*

http://doi.org/10.35784/iapgos.2814

METHOD OF MEASUREMENT AND REDUCTION OF THE ELECTROMAGNETIC DISTURBANCES INDUCTED BY SWITCHING SURGES IN LV CIRCUITS

Patryk Dariusz Wąsik
Wrocław University of Science and Technology, Faculty of Electronics, Photonics and Microsystems, Chair of Electronic and Photonic Metrology, Wrocław, Poland

Abstract. *This paper presents a fast, reliable and portable method for measuring electromagnetic disturbances in LV circuits (overcurrent circuit breakers). The experiment was carried out under conditions reflecting the real measurement environment. The method was verified and confirmed by a series of measurements with passive components reducing the disturbance. The results of the measurements made it possible to obtain suitable EMI reduction solutions, which can be used to protect commutators or end consumers. The results obtained make it possible to apply the method to measurements of multichannel circuit breakers, in which measuring the turn-on time of individual channels is important for the correct operation of the devices.*

Keywords: EMI, circuit breaker, fast measurement method, LV circuits

METODA POMIARU I REDUKCJI ZABURZEŃ ELEKTROMAGNETYCZNYCH INDUKOWANYCH PRZEZ PRZEPIĘCIA ŁĄCZENIOWE W OBWODACH NN

Streszczenie. *W artykule przedstawiono szybką, niezawodną i przenośną metodę pomiaru zaburzeń elektromagnetycznych w obwodach nN (wyłączniki nadprądowe). Eksperyment przeprowadzono w warunkach odzwierciedlających rzeczywiste środowisko pomiarowe. Metoda została zweryfikowana i potwierdzona serią pomiarów z elementami pasywnymi redukującymi zaburzenia. Wyniki pomiarów pozwoliły na uzyskanie odpowiednich rozwiązań redukcji zaburzeń elektromagnetycznych. Dobrane komponenty mogą być wykorzystane do ochrony komutatorów lub odbiorników końcowych. Uzyskane wyniki pozwalają na zastosowanie metody do pomiarów wyłączników wielobiegunowych, w których pomiar czasu załączenia poszczególnych biegunów jest istotny dla poprawnej pracy urządzeń.*

Słowa kluczowe: EMI, wyłącznik nadprądowy, szybka metoda pomiarowa, obwody nN

Introduction

Correct operation, reliability of electrical equipment and apparatus has a direct impact on the protection systems performance. Factors that have a significant influence on the equipment operation are electromagnetic disturbances, which can be emitted into the environment, inducing safety and reliability problems [1]. The common phenomenon nature of the electromagnetic interference determines the need for research on devices in terms of meeting the defined standards adapted to a given device type, and also for research on metrological solutions which can be used not only in laboratory conditions.

One of the protection systems for electrical installations is overcurrent circuit breakers, commonly used in household electrical grids. Commutators used in installation, power solutions, and industrial are used to obtain the desired circuitry in the electrical installation in order to enable the operation of power consumers. The result of an overcurrent switch (commutator) work, apart from switching on the circuit, is a generation of high frequency electromagnetic noise and overvoltage spikes [2, 5]. The most frequently generated noise are groups of impulses and are characterized by high irregularity of amplitude, duration, and repetition period [4, 11, 12].

The electric current conduction through the contact in a commutator is a very complex mechanism [8] and depends on the material of the contacts, the contact surface, the connectors contact force etc [3, 12]. The contact surface is micro-porous [3], because that current flow does not occur on the whole contact surface, but only on a small part of it. The connection resistance is determined not only by the actual surface used for conduction, but also by the resistance of the film on the contact surface [3]. During switching action, the contacts can bounce off each other repeatedly, causing interruption of the flowing current and the formation of an electric arc [7, 9].

Once the arc is ignited, the contact resistance as such ceases to exist [2, 7]. The erosion of the contact material as a result of the arc is determined by the energy released in the arc path when the contact "bounces" [2, 3]. However, the discharge duration is short enough to prevent the formation of a thermally balanced plasma, and the arc is not permanent and does not permanently erode the contact. Due to the length of such an arc, this phenomenon can be called sparking.

Electromagnetic disturbances are generated during the switching system operation [2, 7]. The interference level depends on the value of switched voltage, technical commutator condition, and properties of the circuit (load). In general, the signal spectrum can reach up to 50 MHz and sometimes above this frequency. Regarding the frequency spectrum and propagation conditions, most of the disturbance spectrum in the range up to 10 MHz. The generated disturbance may interfere with the circuit to which the breaker is connected [8, 10].

Measurements of circuit breakers – apart from laboratory tests – take place in switchgear, which limits the choice of measuring tools. Compact solutions of possibly high accuracy class should be chosen. The proposal measurement methodology should create a model of physical phenomena that occurs in the tested object. The information obtained will allow not only to visualize the phenomena but also to further improve the measurement process and to create an explicit model of behavior, due to which – for a given apparatus – it will be possible to create a solution to the problem. The described measurement methodology is consistent with the article [6].

Due to the short duration of the described switching phenomenon, the required mobility of the solution, the use of a spectrum analyzer may give inaccurate results – scanning the required frequency range takes longer, or the initial bandwidth is too low [15]. A fast, reliable method, giving results while the commutator is running, is to use a precision portable oscilloscope and obtain a frequency spectrum.

This paper is divided into two main parts: chapter 1 describes the test methodology and measurement results of the selected commutator. Chapter 2 contains possible solutions based on popular passive components and verification of the proposed method. The solutions are arranged on the basis of the proposal – test result, next proposal – next test result, etc.

1. Measurement methodology

The assumption for the proposed methodology outlined at the end of introduction is simplicity. It can be release by construction of the model bench that reflects the actual measurement conditions as closely as possible. The created model is shown in Fig. 1. The measuring device of the circuit is PicoScope 3405D oscilloscope [14]. The probes used for measurements are the included TA375, set to the x10 operating variant. Additionally, for measurements of current and possible detection of radiated emission, a current probe was used, marked TA189 [16].

The power supply of the system was realized in a safe way (against electric shock). Impulse power supply with an output voltage of 12 V and maximum current 45 A was used for generating direct current. 300 VA mains transformer generating the alternating current – output voltage is 12 V. The load characteristic is shown in the Fig. 2.

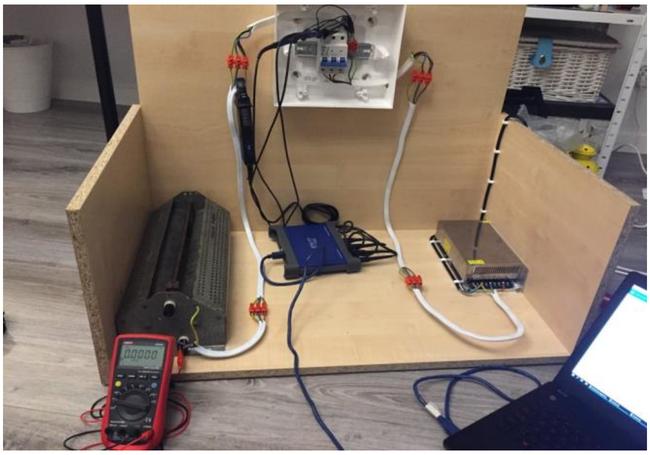

Fig. 1. Test bench model

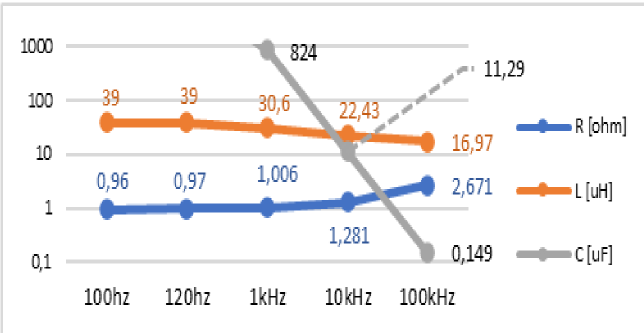

Fig. 2. Load characteristic used in circuit

Circuit breaker selection was based on measurements of 16 circuit breakers with different tripping classes and the number of poles. Similar correlations were observed between the frequencies of disturbances at different currents. Disturbances were in the form of broadband noise, mostly composed of voltage pulses of different duration. The difference was in the power of the noise described. Therefore, the commutator most similar to the average results has been chosen. Characteristics of the selected switch [13]. The measurement results are described below. The first one presented is the measurement of the circuit breaker at 12 V DC.

The graphs from figure 3 contain in each case an increased number of voltage peaks, in each measurement attempt a disturbance was also observed in the circuit of current measurement realized with the use of current probe (current clamps) – the phenomena may suggest the generation of radiated disturbances as well. The switching time was 85.25 µs, the maximum noise voltage reached the value of 19.48 V. The circuit is characterized by a noise band, from 0 to 15 MHz, with a peak at 4.2 MHz. Low power disturbances were also observed in the 35 to 49 MHz range.

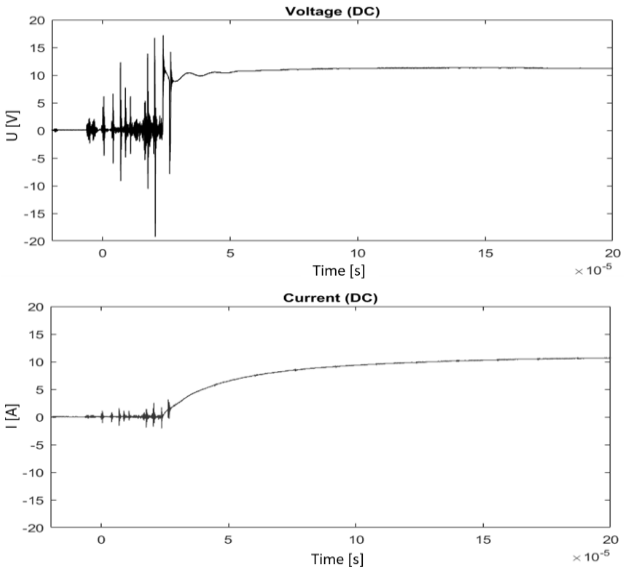

Fig. 3. Time waveforms from commutator test – direct current

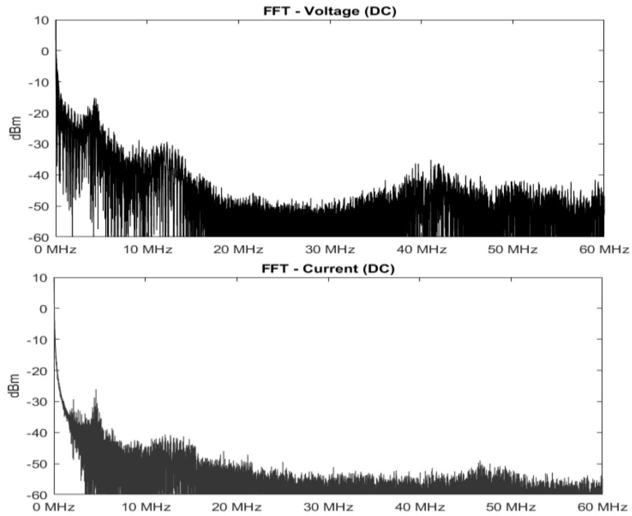

Fig. 4. Time waveforms from commutator test – direct current

Next measurement option – alternating current.

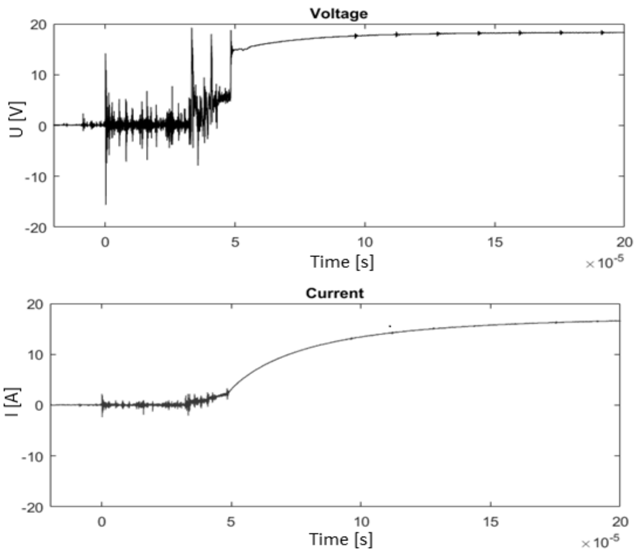

Fig. 5. Time waveforms from commutator test – alternating current

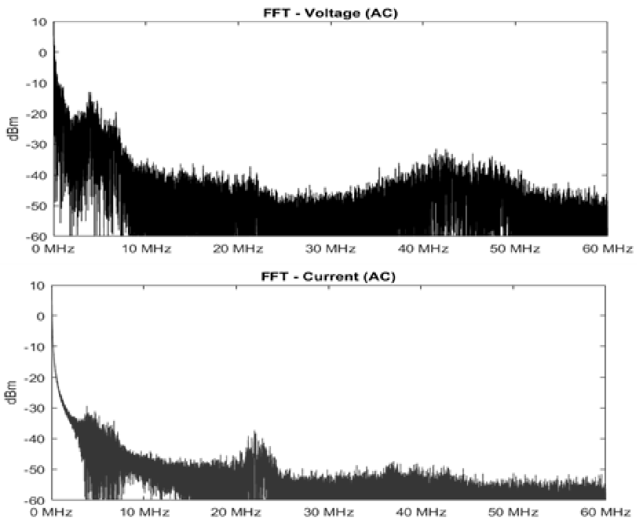

Fig. 6. Observed disturbance spectrum for alternating current

In the case of an AC supply to the commutator, it can be observed that the oscillograms are less disturbed (compare Fig. 3 and Fig. 5), which is as expected. The switch-on time was 337.8 µs, the maximum noise voltage was 19.54 V.

The frequency analysis shown in Figure 6 partially confirms the conclusions drawn from the oscillograms regarding the significant energy of the observed disturbances, with the highest value reached around 4 MHz. The noise is broadband, occurring in the ranges from 0 to 11 MHz and again, from 33 to 52 MHz.

2. Elimination methods of electromagnetic disturbances

Verification of the measurement method requires a series of measurements.

The use of popular and common EMI-reducing elements can confirm the validity of the proposed solution. During the measurements of circuit breakers several disturbances occurring in the circuits were observed, however it is difficult to clearly identify the dominant type of disturbances existing in the circuit. The most characteristic are disturbances in the form of voltage peaks, very similar to the defined test parameters from IEC 61000:4:4 (fast transients). The first proposed method is to connect a gas discharge tube in parallel to the commutator. Attempt of the use of the three popular elements is shown on Fig. 7.

The oscillograms from Fig. 7 clearly show that the variant with three leads has the lowest overvoltage values, the duration of which has been almost halved. One of the possible reasons for this situation is the use of the third lead, which can be connected directly to the protective earth, so that possible disturbances will be discharged into the mentioned circuit. For a more detailed comparative analysis, transformations of the recorded emission spectrums into frequency waveforms were performed.

The frequency analysis from Fig. 8 confirms the observations, highlighting a reduction in the frequency range of the disturbances – from 0 to 13.2 MHz without protection, from 0 to 5.4 MHz in the best variant. The peak value in both cases is at 4.1 MHz, while the energy carried at this frequency has decreased by about 5 dBm.

Another component tested against overvoltage was a 7 mm diameter disk varistor from Würth Elektronik (p/n: 820571406). The oscillograms and frequency analysis of this solution is shown on Fig. 9 and Fig. 10.

The varistor has significantly reduced the short voltage pulses energy, which is also confirmed by the frequency analysis (see Fig. 10). With this type of protection, there was no peaks in the frequency domain and the significantly reduced broadband noise was limited to 6.2 MHz. Comparing the results with the gas discharge element, the tested varistor definitely reduced the disturbances and overvoltage values.

Subsequently, it was decided to use a filter consisting of a capacitor and an inductor, in series connection. During tests on this protection type, it was found that the capacitance had a significant effect on the system performance, compared to the inductance value of the coil. The measurement results are shown on Fig. 11 and Fig. 12.

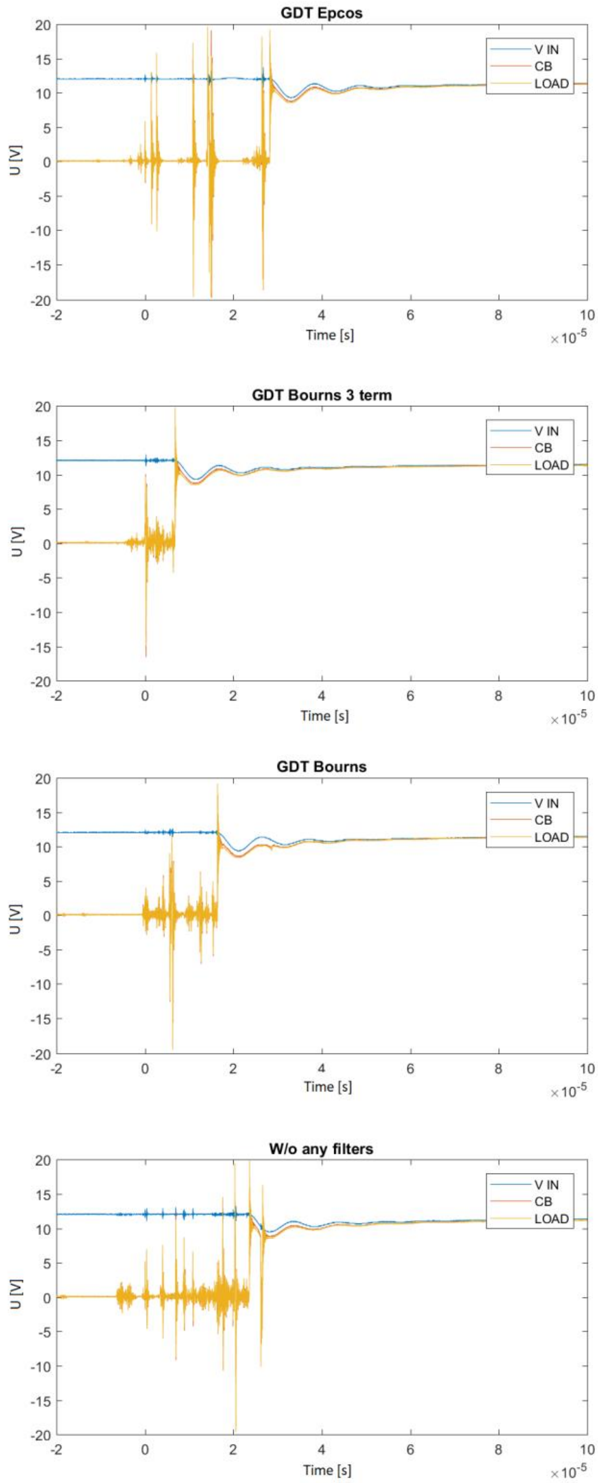

Fig. 7. Results of the analysis of observed disturbances using GDT [Epcos SA24500, Bourns 2020–15T–C2LF (3–term version) and 2031–15T–SM–RPLF + result without any filters

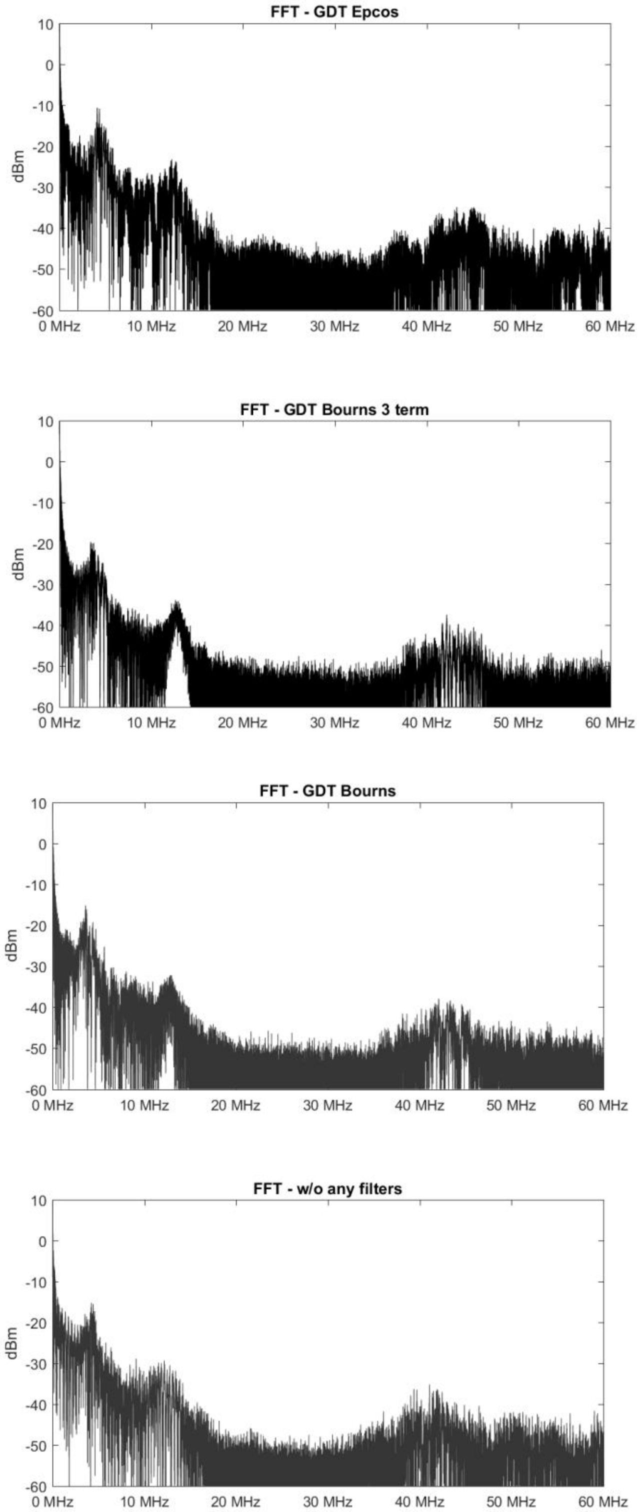

Fig. 8. Frequency analysis of the GDT + result without any filters

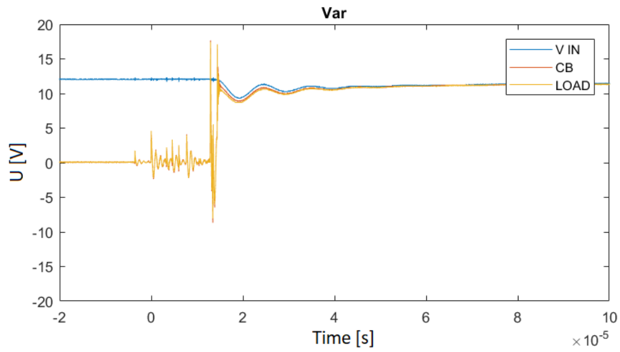

Fig. 9. Oscillograms – disturbance measurement with varistor

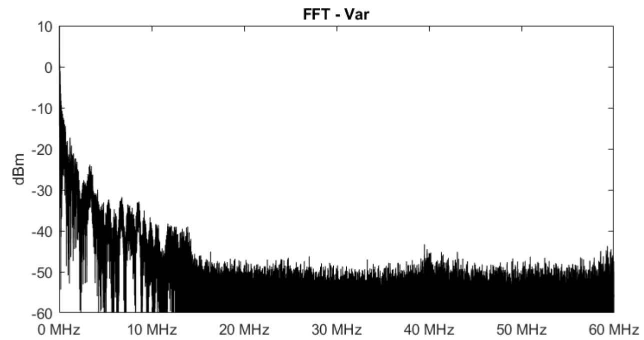

Fig. 10. Frequency analysis at the commutator – varistor

Table 1. List of components used for the construction of the suppressor circuit

	Coil	Capacitors
LC	Würth 744711015	Würth FTXX 680nF
LC small		Würth FTXX 68nF
LC middle		Würth FTXX 15nF

The first variant in figure 11 excels among the presented solutions in terms of significantly reduced voltage spikes.

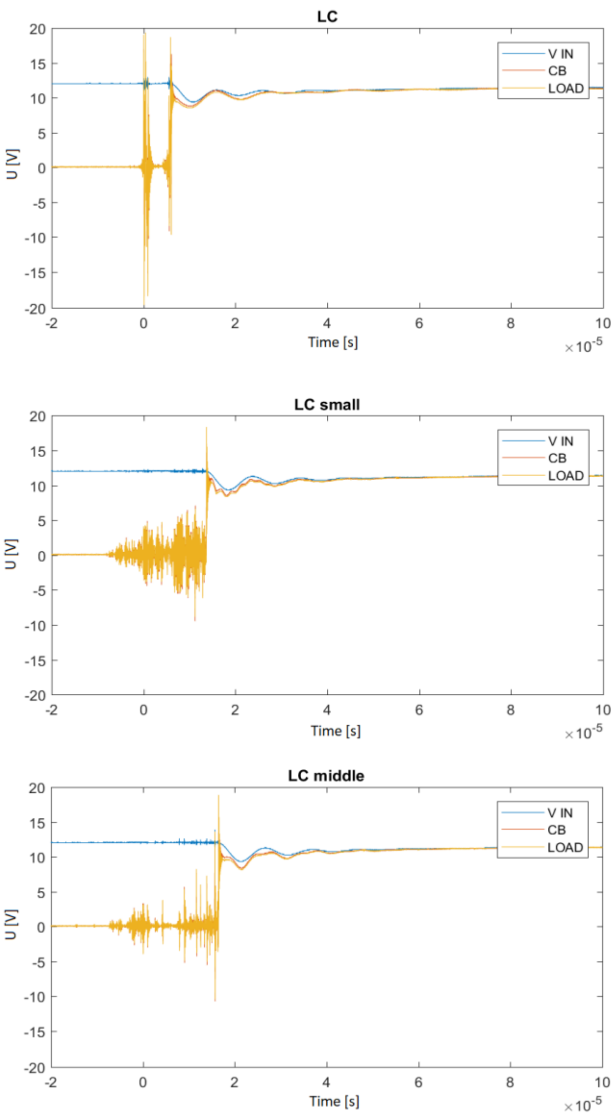

Fig. 11. Time waveforms of the observed disturbances with the use of LC filters

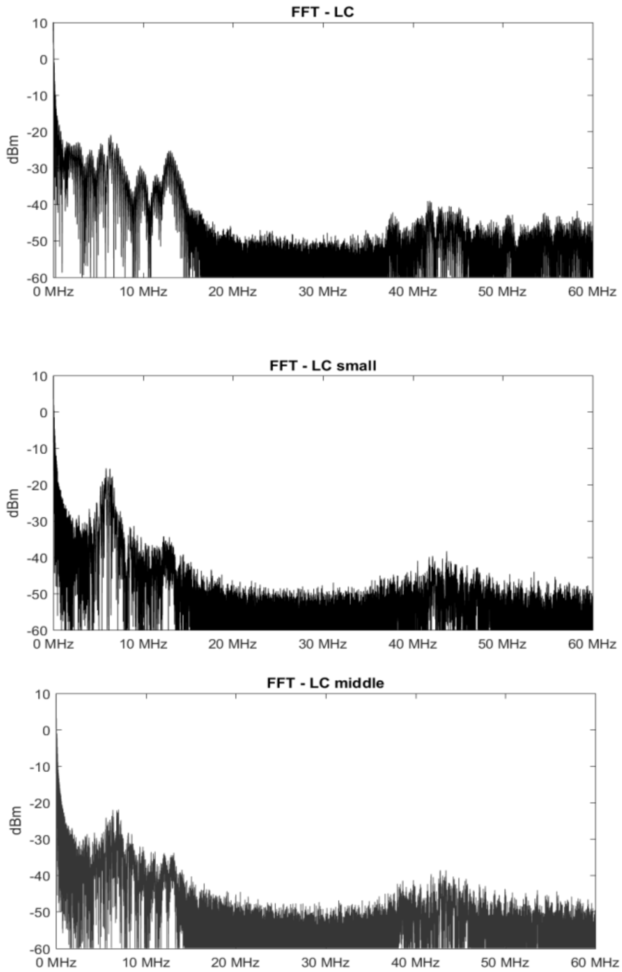

Fig. 12. LC filter frequency analysis

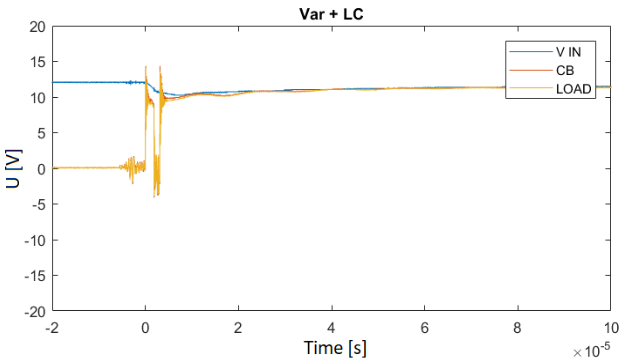

Fig. 13. Time waveforms of measured disturbances – hybrid solution

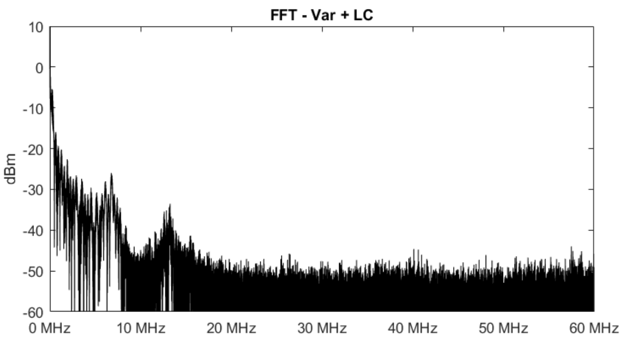

Fig. 14. Frequency analysis of the proposed solutions

The analysis in the frequency domain confirms the observation – the noise was significantly reduced, but the applied filtering circuitry did not achieve the voltage spikes reduction. In an attempt to remove these disturbances, it was decided to attach a previously tested varistor in parallel to the filter. The measurement results are presented in the waveforms in the Fig. 13 and Fig. 14.

The use of an LC filter and a varistor has given the best results so far – a significant reduction of the series of impulses and therefore a significant reduction of the wideband noise. The solution can be successfully mounted in a DIN housing (like a circuit breaker). Installation of such filter may increase the number of on-off cycles (increase mean time between failures) of such the commutator and enables safe analysis of the cycle of switching or disconnection. When the solution is applied to three-phase commutators, facilitate the analysis of commutation between channels without affecting the rising edge of the voltage. For sensitive electronic devices that will be on the load side of the commutator, the disturbance level generated by the commutator + varistor filter may still be too high, so it was decided to investigate further elements to reduce disturbance.

Due to the occurrence of suspected common mode disturbances, a solution that attenuates common-mode disturbances with a current-compensated choke was tested, a variant with added X capacitors, that created a filter for differential type disturbances and then an extended second variant with Y capacitors. These solutions enable to further reduction of common-mode disturbances creating a full first stage filter (see Fig. 17 + Table 2).

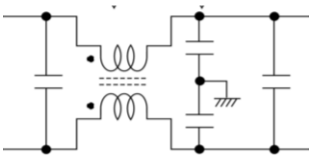

Fig. 17. Filter schematic

The time waveforms from the measurements of the constructed filters are shown on Fig. 18.

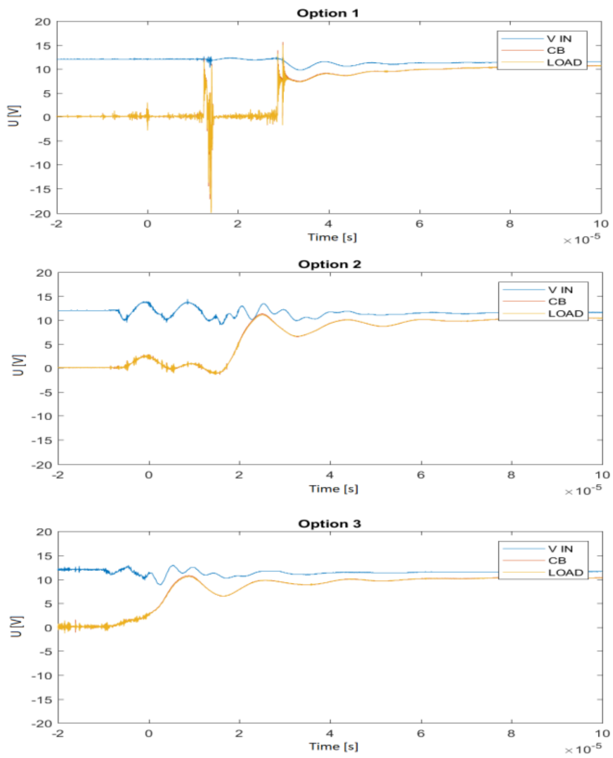

Fig. 18. Time analysis of the constructed filters

Table 2. Components used to create the filter

Option 1	Option 2	Option 3
–	–	Würth CSSA 2.2nF
–	Würth FTXX 680nF	Würth FTXX 680nF
CMC Würth 7448251201	CMC Würth 7448251201	CMC Würth 7448251201

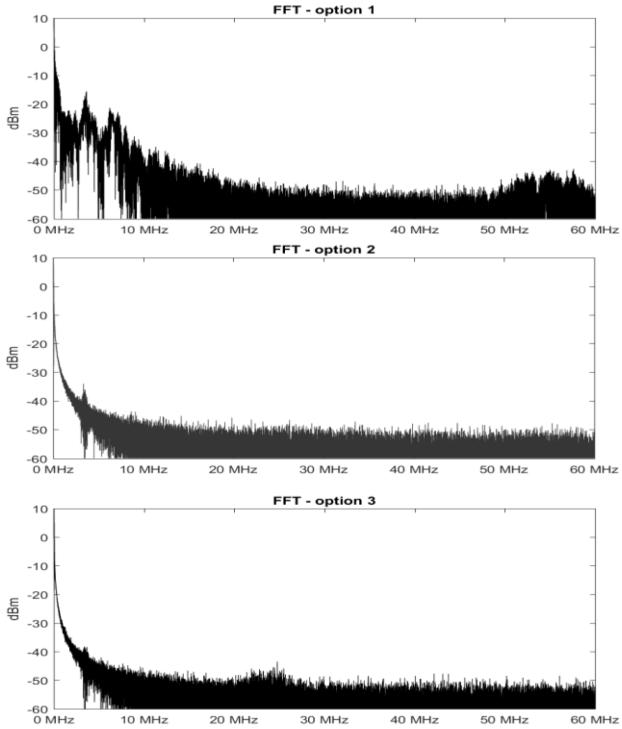

Fig. 19. Frequency domain analysis of constructed filters

The measurements show a significant reduction in the disturbance in all cases. The first option reduced the voltage impulses energy. The wideband noise, in spite of significant reduction, can still cause falsification of results of switch-on time measurements or can constitute a risk for sensitive electronic devices. For options 2 and 3, the disturbance was suppressed. Adding Y-type capacitors to the circuit reduced oscillations and noise at the moment of commutation. However adding capacitance extended the rising edge duration. This should be taken into account when analyzing the circuit.

For the case where a change in the slope of switching is not desired, a filter was constructed based on the current-compensated choke analyzed and the varistor tested earlier. Measurement results are presented on Fig. 20 and 21.

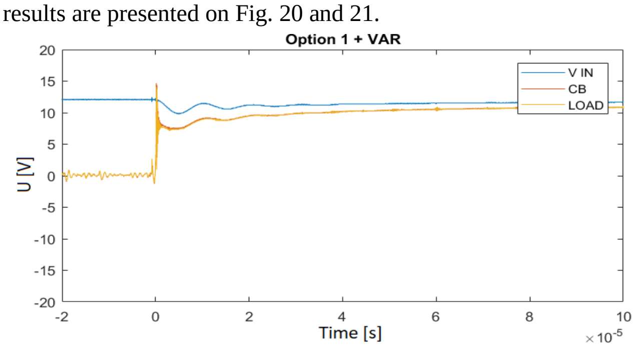

Fig. 20. Analysis of a solution using a combination of CMC and varistor

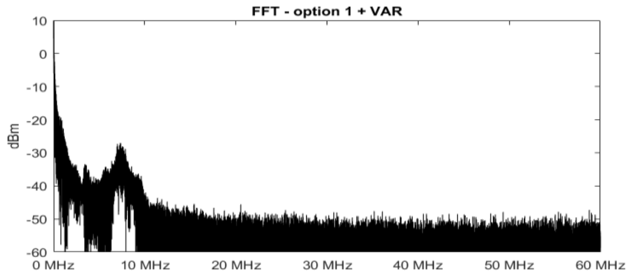

Fig. 21. FFT spectrum analysis of the CMC+VAR solution

The fluctuations have been greatly suppressed (compare graphs on Fig. 21), and only a small part remains, with a peak at 7.4 MHz. There was no significant change in the slope of the voltage at commutation, so the presented solution is more advantageous in this respect, and the filter circuit – less complicated. The filter built from a current-compensated choke with X and Y type capacitors has its equivalent in the integrated version, in a metal casing. For this reason, two filters was tested – the single stage and two stage from Würth Elektronik, with the p/n, respectively: 810911010 and 810913020. The measurement results are given on Fig. 22 and 23.

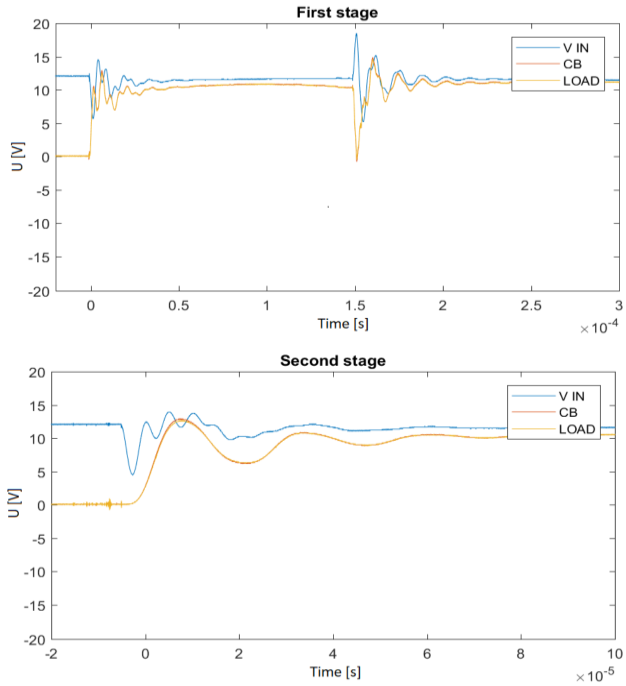

Fig. 22. Time analysis of integrated filters from Würth Elektronik

Filters noticeably reduced the disturbances level. On the oscillogram of the first option, a repeated oscillation was observed, which occurred each time the commutator was switched on. One of the possibilities is the filter resonance. In the second case, the oscillation prolongation was observed. Both cases have a softened voltage slope, however not as much as in the variant on discrete elements soldered to the PCB. One of the reasons for this situation is the use of a metal casing to enclose the filter structure. The other is filling the empty space with a special glue, which affects the filter elements characteristics, especially the current-compensated choke. The mentioned choke can change its parameters even under the influence of the force applied to its core.

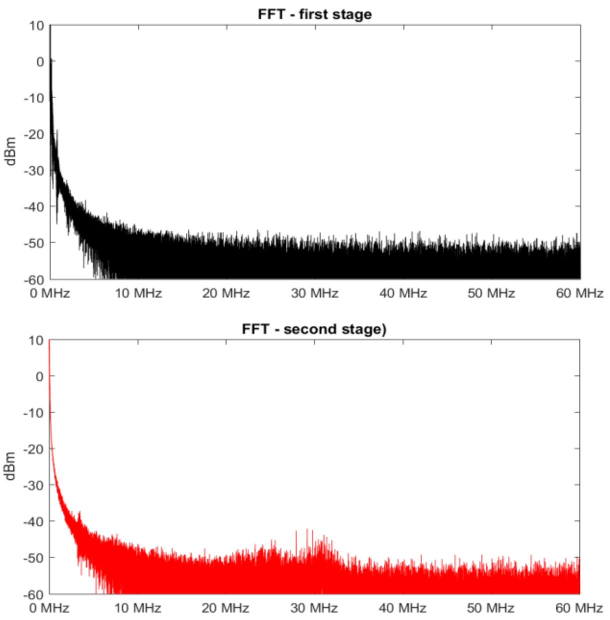

Fig. 23. Frequency analysis of integrated filters from Würth Elektronik

3. Conclusion

The measurements confirmed the effectiveness of the proposed fast, reliable and portable measurement method. The research performed has shown that commutators are a source of electromagnetic disturbances. Moreover, the disturbance level can be high enough to interfere with devices that do not have adequate protection in the coupling path protection form or other protective components. The commutation process is one of the most important moments when the disturbance is emitted into a circuit. After the switching process is completed, there is no emission of disturbances coming from the commutator due to the characteristic internal circuit breaker construction, which, after the switching process is completed, leaves the contacts stationary and protects them against uncontrolled disconnection. It is therefore preferable to use this method over a portable spectrum analyzer. The method, together with selected passive components, can be used to measure multi-channel circuit breakers, where correctly set switching times between channels are important.

The analyses of circuit breakers conducted as part of the study, using the bench built and using passive components, made it possible to identify the types of disturbance. The dominant disturbance is the differential type with a significant amount of common mode noise as well. Relevant differences in emission levels were observed, depending on the power supply circuit used. As expected, an increased disturbance level was observed with the DC supply, while lower values were observed with the AC supply. In the third point, systems were proposed and tested to reduce the disturbances emitted by a commutator with B characteristics.

Among the solutions reviewed, there are at least three most effective filters: LC with a varistor connected in parallel, a current-compensated choke with a varistor, and an integrated filter (or its equivalent on a printed circuit board, such as variant 3 with a current-compensated choke). The choice of solution is determined by the amount of space available to install the solution, the budget allocated for disturbance elimination and the objective the installer or user wants to achieve. If the intention is to protect the commutator, the first-mentioned variant should be chosen, which enables elimination of disturbances, which results in more stable commutation. If the purpose is to attenuate disturbances for measurements of switching times of commutator, e.g. with multi-position switches, the second solution should be chosen, or LC filter with varistor should be multiplied, and if the purpose is a complete elimination of disturbances from the system, irrespective of voltage edge on the commutator, it is necessary to install either integrated filter, preferably of two stage type, or a filter built from elements from presented option 3 (capacitors X, Y, and current-compensated choke).

References

[1] Bander T., Gerfer A., Bernhard R., Heinz Z.: Trilogy of Magnetics. Adolf Würth GmbH & Co. KG, Waldenburg 2019.
[2] Clayton R. P.: Introduction to Electromagnetic Compatibility. Wiley 2006.
[3] Gerfer A. et al.: Trilogy of Connectors. Adolf Würth GmbH & Co. KG, Waldenburg 2015.
[4] Ibrahim, A. I. et al.: A Knowledge Base for Switching Surge Transients. International Conference on Power Systems Transients (IPST), 2005.
[5] Martinez J. A., Natarajan R., Camm E.: Comparison of statistical switching results using Gaussian, uniform and systematic switching approaches. Power Engineering Society Summer Meeting, 2002.
[6] Mroczka J.: The cognitive process in metrology. Measurement 46, 2013, 2896−2907.
[7] Ott H. W.: Electromagnetic Compatibility Engineering. Wiley, 2009.
[8] Phaniraj V., Phadke A. G.: Modelling of circuit breakers in the electromagnetic transients program. IEEE Transaction on Power System 3(2), 1988, 799–805.
[9] Popov M. et al.: Investigation of the Circuit Breaker Reignition Overvoltages Caused by No-load Transformer Switching Surges. European Transactions on Electrical Power 11(6), 2001, 413–422.
[10] Rachard H. et al.: Numerical study of coupled electromagnetic and aerothermodynamic phenomena in a circuit breaker electric arc. International Journal of Heat and Mass Transfer 42(9), 1999, 1723–1734.
[11] Uglešić I. et al.: Transients Caused by Uncontrolled and Controlled Switching of Circuit Breaker. The International Symposium on High-Voltage Technique "Höfler's Days", Portoroz, Slovenia, 2013.
[12] Wen W. et al.: Transient Current Interruption Characteristics of a Novel Mechanical DC Circuit Breaker. IEEE Transactions on Power Electronics 33, 2018, 9424–9431.
[13] Legrand TX3 B16 691223-Model Datasheet. Available online: https://www.tme.eu/Document/957dfb2ffaa80d87ef4a3a3f44f22512/LEGRAND-TX.pdf (accessed on 8.11.2021).
[14] PicoScope 3000D Series Data Sheet. Available online: https://www.picotech.com/download/manuals/picoscope-3000d-series-oscilloscopes-data-sheet.pdf (accessed on 8.11.2021).
[15] Portable spectrum analyzer Aaronia Spectran 6 Datasheet. Available online: https://aaronia.com/download/14538/ (accessed on 13.06.2021).
[16] TA189 Current Clamp User's Guide. Available online: https://www.picotech.com/download/manuals/ta189-30a-current-clamp-users-guide.pdf (accessed on 8.11.2021).

M.Sc. Eng. Patryk Dariusz Wąsik
e-mail: patryk.wasik@pwr.edu.pl

Patryk Dariusz Wąsik received the M.Sc. degree from WUST, Poland, in 2019. He is currently an assistant on Chair of Electronic and Photonic Metrology, Wroclaw University of Science and Technology, Poland. His current research focuses on Electromagnetic Interferences in HF connectors.

http://orcid.org/0000-0002-1927-4111

otrzymano/received: 8.11.2021 *przyjęto do druku/accepted: 15.12.2021*

http://doi.org/10.35784/iapgos.2826

INCREASING THE COST-EFFECTIVENESS OF IN VITRO RESEARCH THROUGH THE USE OF TITANIUM IN THE DEVICE FOR MEASURING THE ELECTRICAL PARAMETERS OF CELLS

Dawid Zarzeczny
Lublin University of Technology, Department of Electrical Engineering and Electrotechnologies, Lublin, Poland

Abstract. *Currently, various methods are used to assess the biocompatibility of materials. After an in-depth and detailed review of the literature, the method used in the research was selected. As part of the experiments, a method based on the analysis of the values of electrical parameters of cell cultures measured in the presence of electrodes was used. The electrode is a structure made of a thin layer of metallization. It measures the change in resistance, impedance and capacity of a mixture of cells and the substance in which they are grown. The plate containing the electrode assembly is called the measurement matrix. Currently, commercially used test matrices are made of gold or platinum. However, their high price means that large-scale research is significantly limited. In order to increase the access to the widespread use of this method, it was decided that it was necessary to use cheaper materials, reducing the necessary costs of conducting experiments. Considering this, an attempt was made to use a different conductive material to build matrices compatible with the ECIS® Z-Theta measurement system. Their use would enable in vitro research on living cells. In the presented work, titanium was used as a material that may turn out to be an alternative to the materials currently used. Its application to the production of matrices will allow to study the influence of this metal on the behavior of cells.*

Keywords: bioimpedance, titanium, MEMS, thin films

ZWIĘKSZENIE EFEKTYWNOŚCI KOSZTOWEJ PROWADZENIA BADAŃ IN VITRO POPRZEZ ZASTOSOWANIE TYTANU W URZĄDZENIU DO POMIARU PARAMETRÓW ELEKTRYCZNYCH KOMÓREK

Streszczenie. *Obecnie, do oceny biokompatybilności materiałów wykorzystywane są różne metody. Po dogłębnym i szczegółowym przeglądzie literatury wybrano metodę, którą wykorzystano podczas prac badawczych. W ramach przeprowadzonych eksperymentów wykorzystano metodę bazującą na analizie wartości parametrów elektrycznych kultur komórkowych, zmierzonych w obecności elektrod. Elektroda jest strukturą wykonaną w cienkiej warstwie metalizacji. Służy do pomiaru zmiany wartości rezystancji, impedancji oraz pojemności mieszaniny złożonej z komórek i substancji, w której są one hodowane. Płytka zawierająca zestaw elektrod nazywana jest matrycą pomiarową. Aktualnie, komercyjnie stosowane matryce testowe wykonane są ze złota lub platyny. Ich wysoka cena powoduje jednak, że prowadzenie badań na szeroką skalę jest znacząco ograniczone. Aby zwiększyć dostęp do powszechnego korzystania z tej metody zdecydowano, że koniecznym jest stosowanie tańszych materiałów, redukując niezbędne koszty prowadzenia eksperymentów. Zważywszy na to, podjęto próbę zastosowania innego materiału przewodzącego do budowy matryc kompatybilnych z systemem pomiarowym ECIS® Z-Theta. Ich użycie umożliwiłoby prowadzenie badań nad komórkami żywymi in vitro. W przedstawionej pracy jako materiał, który może okazać się alternatywą dla materiałów wykorzystywanych obecnie wykorzystano tytan. Jego zastosowanie do wytworzenia matryc pozwoli zbadać wpływ tego metalu na zachowanie komórek.*

Słowa kluczowe: bioimpedancja, tytan, MEMS, cienkie warstwy

1. Purpose of the research

The aim of the research work was to develop a device that would allow conducting medical and biological experiments with a lower financial outlay. The main requirement when designing similar devices is that the materials used, in addition to such properties as corrosion and wear resistance, non-toxicity and appropriate mechanical properties, are characterized by high biocompatibility [9, 12, 13, 30].

Table 1. List of prices of target materials

Material	Symbol	Target diameter [cm]	Target thickness [cm]	Target price [Euro]
Gold	Au	5.08	0.1588	3072.00
Platinum	Pt	5.08	0.1588	3294.72
Titanium	Ti	5.08	0.3175	116.10

A wide range of available raw materials, with a different degree of biocompatibility, allows the selection of such a material that shows a favorable response in a given biological environment, while fulfilling the required function [1, 21]. Usually, noble metals, in particular gold or platinum, are used to build devices that come into contact with a living organism. However, the high cost limits their use in, for example, disposable devices. Looking for an alternative to expensive materials, it was decided to use titanium which, like gold and platinum, is among the non-reactive metals that have little or no effect on the cells surrounding them [5, 11, 25]. Titanium is relatively inert and has good corrosion resistance, which is due to the presence of oxides on its surface. It also has very good mechanical properties. It has low thermal conductivity, relatively low density, low modulus of elasticity and high reactivity. These features are extremely important when used in sensitive areas of the human body [19, 25].

2. Research method

When assessing the possibilities of using a given material in medical applications, it is necessary to conduct a number of biological experiments. The test carried out under strictly defined conditions is to determine whether the properties of the material are sufficient and meet the requirements. Most often, such verification is aimed at finding out the regularities governing a specific biological system in various situations. The observation of cellular behavior changing over time or under the influence of external factors provides a lot of important information. It enables, among others clarification of the toxicological profile of the test substance [17]. In this work, the method of measuring cell impedance in real time in vitro was used to determine the potential possibility of using titanium in a safe way for the tested cells [1, 3, 10, 22, 27, 29]. The methodology of conducting in vitro tests is described in the ISO 10993-5 standard – "In vitro cytotoxicity tests" [16, 20].

Live biological cell impedance measurements are marker-free, non-invasive methods of quantitative analysis. They are used to assess the condition of cells, their biological activity and reactions related to the influence of external factors and chemicals [32]. During the measurement, the signal is supplied to the system in the form of alternating current with a current of less than 1 mA [4] (4 mA/cm^2), the frequency value of which ranges from 10 Hz to 64 kHz [15]. At frequencies below 2 kHz, a significant amount of current flows between the intercellular spaces, providing information about cell adherence. The use of a relatively high frequency, above 40 kHz, causes a direct current flow through cell membranes [2, 4, 15, 18, 28].

Commercial software of the Applied Biophysics measuring system using special mathematical transformations, generates results and plots the characteristics of impedance change. Each value read is plotted as a point in ohms (Ω) or nanofarads (nF) per unit time [2, 28]. The impedance value is at its highest when the cell culture is at its maximum confluence. The obtained resistance value corresponds to the resistance of the current flowing through the tested cell, while the capacitance causes the polarization of the separation of electrons in the isolated layer of the cell membrane. The duration of the experiment is set by the user and may last from a few seconds to several days. The differences between the measurement values are submitted for analysis, which determines the influence of individual factors and other external stimuli on the properties of the tested cells [7, 8, 31, 34].

The basic process of increasing the number of cells by multiplying and dividing is proliferation. It increases the degree of coverage of the electrode with the non-conductive cell membrane. This results in a significant increase in the measured impedance. Monitoring the process of cell proliferation using the bioimpedance measurement method is not a direct method of counting the number of cells, but a registration of changes resulting from a change in the coverage of the measuring electrode area. There is a close relationship between the number of cells and the normalized impedance value [24, 31, 32].

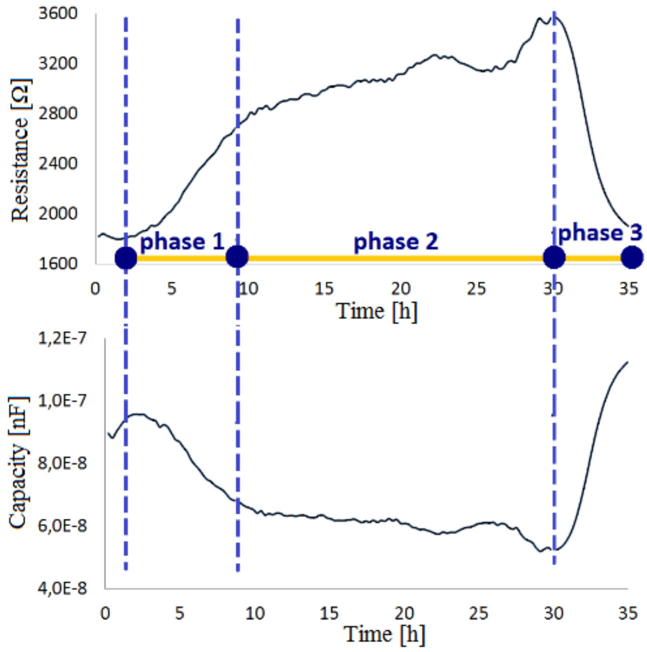

Fig. 1. The expected nature of changes in the measured resistance for 4 kHz and capacity for 64 kHz (measurements made with the use of commercial matrices with gold electrodes)[6]

3. Experiment

Based on the Applied Biophysics measurement system and commercial test matrices, a proprietary device was constructed to check the possibility of using conductive materials other than commercially used gold. The experiment begins with the preparation of a test plate on the surface of which a set of thin-layer detection electrodes is made [31]. The electrodes are defined as very small holes in the dielectric layer revealing the metallization deposited on the biocompatible substrate. Cells are grown on their surface. Commercially available standard backing plates used during measurements are made of biocompatible plastics, i.e. Lexan polycarbonate or polyethylene terephthalate – PET [23]. The arrangement and shape of the electrodes on the measuring plate have a significant impact on the data obtained during the measurement. The most common are 8-well plates, which contain round electrodes or electrodes with a comb structure. The diameter of round electrodes varies from 250 µm to 350 µm. The surface area of the comb structure electrodes ranges from 1.96 mm^2 to 3.92 mm^2. The number and shape of electrodes for a single well affects the number of cells that can be tested at one time. Single-electrode plates are used when the cell populations are small. The small total area of the electrodes causes all current to flow through the cell layer. This makes it possible to obtain a relatively high electric field with a moderately low alternating current. There is a possibility of full or partial electroporation and observation of uncontrolled morphological changes in small groups of cells (<100). Multi-electrode plates allow you to analyze the properties of larger groups of cells, providing an estimate of the morphological response of a large population (> 1000) [2, 23]. Above each pair of electrodes there is a special container attached with a biocompatible silicone. Tested cell cultures are applied to its interior. In order to provide the necessary nutrients for the culture, the test cells are placed in a medium. The set thus completed is placed in an incubator that provides the cells with appropriate environmental conditions [23, 28].

4. Production technology

The process of producing matrices for measuring cell impedance began with formulating the requirements that should be met. The aim of the work was to create structures enabling in vitro tests with the use of cell cultures at acceptable costs of conducting experiments. Using the method of analyzing the electrical parameters of cell culture by measuring their impedance, it was necessary to determine the properties of the test plate. Currently used matrices are made entirely of biocompatible materials. As a base material, Lexan or PET that is harmless to cells and allows them to grow on its surface is used. The electrodes, on the other hand, are made of gold or platinum metallization. In addition, there is a layer of biocompatible dielectric on their surface. The cells are in contact with the electrodes thanks to the holes created on its surface. While the use of the abovementioned substrates does not generate high costs, the abovementioned metals and the dielectric layer consume a significant part of the expenditure. In order to limit the means necessary to conduct research, it was decided to use different conductive materials than those used so far. In addition, the dielectric layer was removed, so that the cells would have direct contact with the material.

The next stage of work was the selection of the optimal shape of the electrodes, which were to be placed on the target plate for measuring cell impedance. Based on the currently used configurations, it was decided that comb structures would be the best choice. Following the example of commercial 8W10E plates, a mask with eight electrodes placed on a single substrate was designed. Thanks to the same pin arrangement as in the case of standard boards supplied by the manufacturer of the measuring equipment, the set can be adapted to conduct experiments in the ECIS® Z-Theta system apparatus. After a series of experiments, comb capacitors with dimensions of 200 µm × 200 µm were selected for the next stages of development works on matrices for measuring cell impedance. The structures produced were the result of using the lift-on method, with the use of positive photosensitive emulsion – Positiv 20. The patterns were obtained with the use of the universal developer for photolists and positive plates AGT – 087 or sodium metasilicate pentahydrate. Sodium persulfate B327 was used to etch the metallization layers.

After selecting the shape of the electrodes and designing the technological masks, the next stage of the work was to select the appropriate substrate on which the target structures were to be produced. The main requirement determining the selection was that the material should not adversely affect and be indifferent to living organisms. In addition to high biocompatibility, necessary when conducting research with the use of living organisms, the base material should be resistant to chemical compounds used during technological processes and mechanical resistance, guaranteeing the appropriate strength of the matrix during its use. In the end, polycarbonate turned out to be a substrate that met all the assumptions and allowed it to be used freely. The 2 mm thick transparent plates kept their original shape. Moreover, they did not react chemically with any of the substances used in the photolithography process [7, 33].

The material from which the measuring electrodes were made was titanium (purity 99.995%). The first deposited layer was ~ 40 nm thick (Fig. 2A). After measuring the resistance of the leads, it turned out that the value is too high (larger than 20 kΩ) and it will not be possible to measure the electrical parameters of the cell culture. The test station was unable to detect the test plate inserted in its holders. Therefore, in the subsequent sputtering process, a layer of titanium with a thickness of ~ 400 nm was deposited (Fig. 2B). The measured value of the resistance of the leads ranged from ~ 960 Ω to almost 18 kΩ. However, these were acceptable values, allowing the measurements of resistance, impedance and capacitance to be carried out.

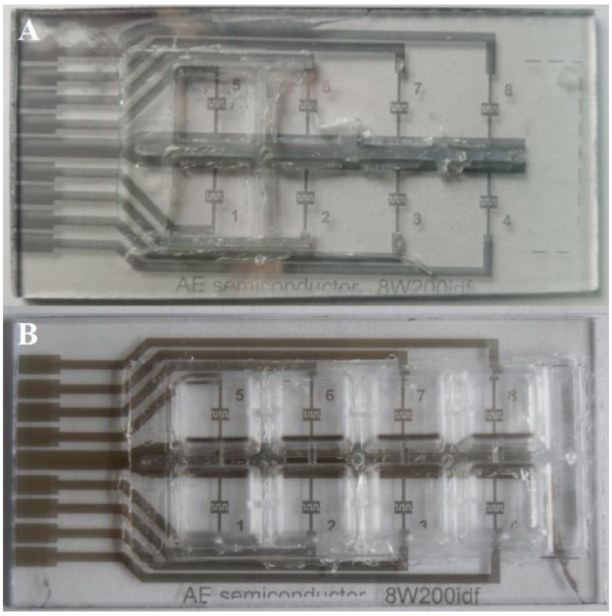

Fig. 2. Plates with titanium electrodes with a metallization layer thickness of 40 nm (A) and 400 nm (B)

After the deposition of the metallization layer and photolithography have been carried out, the next step is to prepare the finished plate for testing. For this purpose, special containers are placed above the electrodes, into which the tested organic compounds are introduced. It is attached using a special biocompatible silicone. To obtain adequate sterility, plates with approved wells are exposed to UV irradiation for approx. 15 minutes, which is bactericidal. The set prepared in this way is used for cell culture and research [33].

All biological experiments were carried out at the Chair and Department of Human Physiology of the Medical University of Lublin. The first step is to apply 600 μl of the culture medium to check the tightness of the wells. Then, the matrices are fixed in the measuring station located in a special incubator. After stabilization of the conditions inside the chamber, the electric parameters of the dies are calibrated. The next step is to place cell cultures inside the wells [24]. The final step is to provide cells with the environmental conditions necessary for their development by regulating temperature, oxygen and/or carbon dioxide concentration. After their stabilization, the measurement of electrical parameters begins.

The optimal frequency values at which the results are interpreted are 4 kHz for resistance, 16 kHz for impedance and 64 kHz for capacitance [15, 18, 26]. All obtained data are presented in a normalized form. The obtained results are presented in the graphs in a normalized form, which allows to observe the changes in the value and compare the trend of changes without the influence of the resistance of the leads. The work uses the min - max normalization expressed by the formula [14]:

$$x' = \frac{x - x_{min}}{x_{max} - x_{min}} \quad (1)$$

where x' is the normalized value within the range from 0 to 1, while x, x_{min}, x_{max} mean the normalized value and the smallest and largest value of the normalized interval, respectively.

The next stage of the work was to measure the electrical parameters of the cell culture. Cell lines from the American Type Culture Collection (ATCC) were used in the laboratory studies. All the cells used were used due to their current availability at the time when it was possible to use the measuring equipment of the Department of Human Physiology of the Medical University of Lublin. The mouse fibroblast L 929 cell line and the simian VERO cell line were used in the experiments. The obtained results are presented in the graphs in a normalized form, which allows to observe the changes in the value and compare their tendency of change without the influence of the resistance of the leads.

5. Measurement results

The first cells tested were murine fibroblasts designated as L929. During the experiment, results were obtained from all wells containing cultured cells. However, the cell cycle did not enter the apoptotic phase. The software of the measurement system allows you to monitor changes in real time, displaying the measured values in the form of generated graphs. During the experiment, the displayed characteristics curves were straight lines, where no significant changes could be observed (Fig. 3). The supervisor of the experiment stated that this was due to a lack of cellular activity. Therefore, the measurement of electrical parameters was interrupted and only the proliferation stage was recorded.

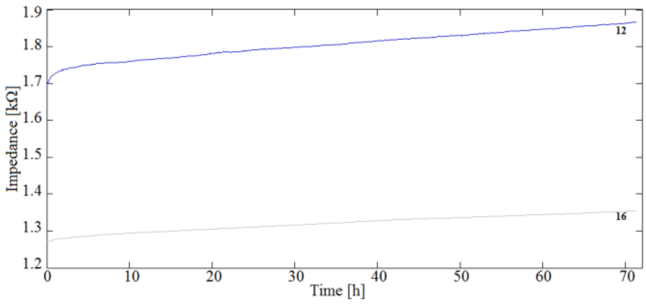

Fig. 3. Measured impedance of L 929 cell culture grown on a plate with titanium electrodes, for the 16 kHz signal, for wells 12 and 16 (graph from the ECIS Z-Theta system)

During the preparation of the results and their normalization, it was noticed that the nature of the changes showed an increasing tendency, and the invisible changes resulted from slight differences between the recorded changes and the measured value. The change of several hundred ohms against the background of several kiloohms required the normalization of the results in order to be noticed. The general trend of changes recorded in the wells allows for the conclusion that there was cell proliferation, which is visible in the change of the measured parameters. A linear change of the measured parameters can be observed, which allows to conclude that the cultured cells had no problems with multiplication and spreading over the electrode surface. By its action, titanium did not disrupt the cell cycle of mouse fibroblasts. Throughout the measurement period, an increase in resistance (Fig. 4) and a decrease in capacitance (Fig. 5) resulting from the continuous multiplication of cells are observed.

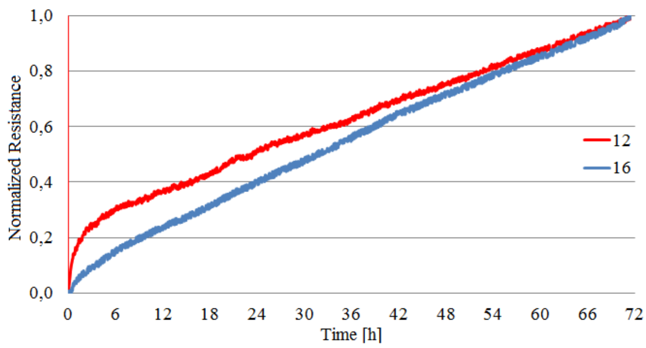

Fig. 4. Normalized resistance of L 929 cell culture carried out on a plate with titanium electrodes, for a signal of 4 kHz, for wells 12 and 16

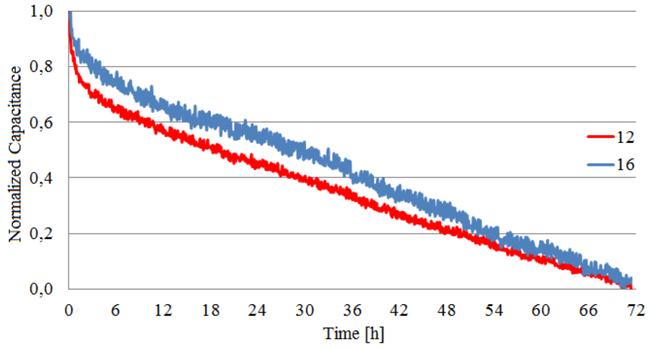

Fig. 5. Normalized capacity of the L 929 cell culture carried out on a plate with titanium electrodes, for a signal of 64 kHz, for wells 12 and 16

The fact that the titanium made it possible to register changes despite the high resistance of the leads is not changing. The measurement matrices showed slight changes in the resistance in relation to the high resistance of the lead paths. Based on the obtained data, it can be concluded that measuring arrays with titanium electrodes can be used for in vitro research on L929 cells.

Successive arrays with titanium electrodes were used to measure the electrical parameters of the VERO monkey cell culture (Fig. 6). In order to better notice the changes occurring, also in this case the normalization of the measured values was applied.

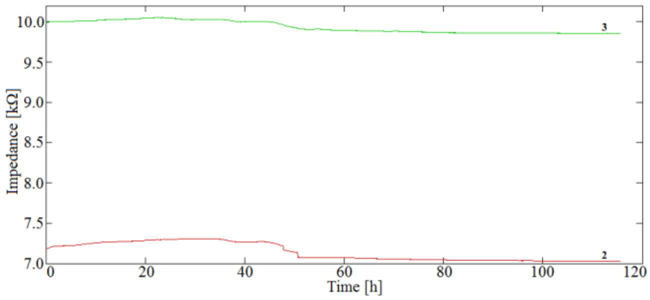

Fig. 6. Measured impedance of VERO cell culture grown on a plate with titanium electrodes, for the 16 kHz signal, for wells 2 and 3 (graph from the ECIS Z-Theta system)

Changes in the parameters value, despite the initial instability, tend to change in time. The cultivation was carried out for over 115 hours, but the most noticeable changes are visible up to 48 hours of measurements. This has been shown in the charts showing the normalized resistance and capacitance.

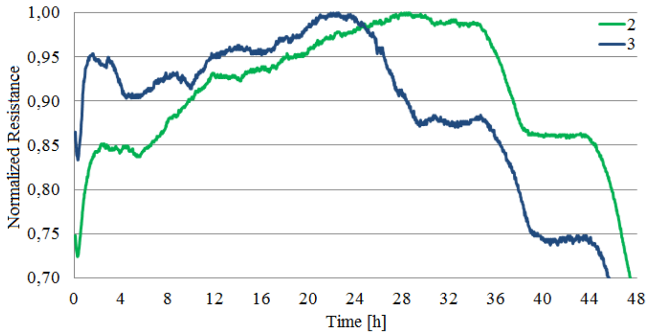

Fig. 7. Normalized resistance of VERO cell culture carried out on a plate with titanium electrodes, for a 4 kHz signal, for wells 2 and 3

By limiting the measurement period to 48 hours, it is possible to observe all the changes that have occurred. All steps of the cell life cycle can be observed. After the initial fluctuation of the resistance (Fig. 7), its value increases. These changes indicate the proliferation and migration of cells over the surface of the measuring electrodes. Thereafter, growth is inhibited, which indicates that the cell culture is completely confluent. Cells there are on the entire surface of the bottom of the well and cannot develop further. The last stage of a cell's life is apoptosis. The cells increase in volume and lose their adhesion to the electrode surface. This causes the resistance value to drop.

The results of the capacitance measurements carried out at a frequency of 64 kHz are characterized by large fluctuations. The results of measurements at a frequency of 16 kHz show changes more clearly (Fig. 8). The nature of the changes tends to increase, which is not as expected. However, after consultation with researchers from the Medical University of Lublin, information was obtained that such changes were acceptable. Nevertheless, the answer to the question why the measured capacity value has increased belongs to in vitro research specialists. From an engineering point of view, the produced matrices made it possible to cultivate two types of cells and measure their electrical parameters.

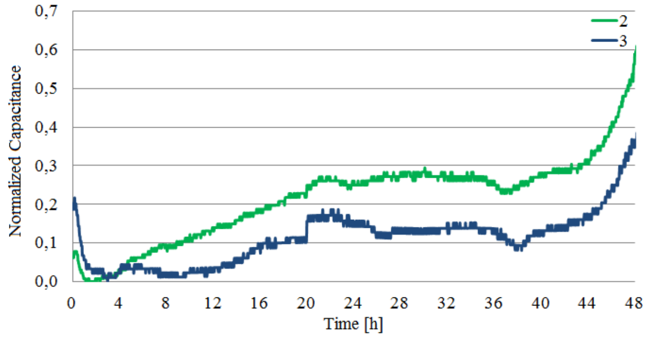

Fig. 8. Normalized capacity of the VERO cell culture carried out on a plate with titanium electrodes, for a 16 kHz signal, for wells 2 and 3

6. Conclusions

The article presents the research results obtained with the use of measuring arrays with titanium electrodes. Two types of cells were used, mouse fibroblast L 929 cell line and the simian VERO cell line. In both cases, cell growth was observed on the surface of the measuring arrays. Titanium had no negative effect on the tested biological objects and made it possible for them to grow in his presence. The presented test results confirm the effectiveness of the use of arrays with titanium electrodes for in vitro testing of cells. Nevertheless, there is a need for further research.

In the presented experiment, animal and human cells were used successfully. It allows to argue that it is possible to make arrays from a material other than gold or platinum to conduct research on various types of cells. At the same time, this reduces the costs associated with conducting in vitro experiments.

References

[1] Ananth H., Kundapur V., Mohammed H. S., Anand M., Amarnath G. S., Mankar S.: A review on biomaterials in dental implantology. International Journal of Biomedical Science 11(3), 2015, 113–120.

[2] Applied BioPhysics, Inc., Product Guide, [https://www.biophysics.com/whatIsECIS.php] (available: 26.11.2021).

[3] Gangadoo S., Chapman J.: Emerging biomaterials and strategies for medical applications: A review. Materials Technology 30, 2015, B3–B7 [http://doi.org/10.1179/1753555714Y.0000000206].

[4] Giaever I., Keese C. R.: Electric Cell-Substrate Impedance Sensing and Cancer Metastasis. Springer 17, 2012, 1–19 [http://doi.org/10.1007/978-94-007-4927-6_1].

[5] Jiang G.: Design challenges of implantable pressure monitoring system. Frontiers in Neuroscience 4, 2010, 1–4 [http://doi.org/10.3389/neuro.20.002.2010].

[6] Kociubiński A., Zarzeczny D., Prendecka M., Pigoń D., Małecka-Massalska T.: Nichrome Capacitors on Polycarbonate Substrate for Monitoring Cell Culture Using Impedance Sensing Technique. Archives of Metallurgy and Materials 65, 2020, 493–496 [http://doi.org/10.24425/amm.2020.131752].

[7] Kociubiński A., Zarzeczny D., Szypulski M.: Kondensatory grzebieniowe z miedzi do monitorowania funkcji życiowych komórek hodowlanych. Przegląd Elektrotechniczny 1, 2018, 61–63 [http://doi.org/10.15199/48.2018.09.15].

[8] Kociubiński A., Zarzeczny D.: Nickel comb capacitors for real-time monitoring of cancer cell cultures. Przegląd Elektrotechniczny 9, 2020, 149–152 [http://doi.org/10.15199/48.2020.09.31].
[9] Kohane D. S., Langer R.: Biocompatibility and drug delivery systems. Chemical Science 1, 2010, 441–446 [http://doi.org/10.1039/c0sc00203h].
[10] Langer R., Tirrell D. A.: Designing materials for biology and medicine. Nature 428, 2004, 487–492 [http://doi.org/10.1038/nature02388].
[11] Meng E., Sheybani R.: Insight: implantable medical devices. Lab on a Chip 14, 2014, 3233–3240 [http://doi.org/10.1039/C4LC00127C].
[12] Menzies K. L., Jones L.: The Impact of Contact Angle on the Biocompatibility of Biomaterials. Optometry and Vision Science 87, 2010, 387–399 [http://doi.org/10.1097/OPX.0b013e3181da863e].
[13] Onuki Y., Bhardwaj U., Papadimitrakopoulos F., Burgess D. J.: A review of the biocompatibility of implantable devices: Current challenges to overcome foreign body response. Journal of Diabetes Science and Technology 2, 2008, 1003–1015 [http://doi.org/10.1177/193229680800200610].
[14] Patro S. G. K., Sahu K. K.: Normalization: A Preprocessing Stage. IARJSET 2(3), 2015, 20–22 [http://doi.org/10.17148/iarjset.2015.2305].
[15] Pennington M. R., Walle G. R. Van de, Smith G. A.: Electric Cell-Substrate Impedance Sensing To Monitor Viral Growth and Study Cellular Responses to Infection with Alphaherpesviruses in Real Time. MSphere 2, 2017, 1–12 [http://doi.org/10.1128/mSphere.00039-17].
[16] PN-EN ISO 10993-1:2010 Biologiczna ocena wyrobów medycznych, 2015, http://www.urpl.gov.pl/en/node/267 (available:26.11.2021).
[17] Porta M.: A Dictionary of Epidemiology (6 ed.). Oxford University Press, Oxford 2014 [http://doi.org/10.1093/acref/9780199976720.001.0001].
[18] Prendecka M., Małecka-Massalska T., Mlak R., Magdalena J., Osińska-Jaroszuk M., Jakubiak-Hulicz M., Leibold C., Bieser A., Wójcik W.: Effect of exopolysaccharide from Ganoderma applanatum on the electrical properties of mouse fibroblast cells line L929 culture using an electric cel-substrate impedance sensing (ECIS). Annals of Agricultural and Environmental Medicine 23, 2016, 293–297 [http://doi.org/10.5604/12321966.1203891].
[19] Rack H. J., Qazi J. I.: Titanium alloys for biomedical applications. Materials Science and Engineering C 26(8), 2006, 1269–1277 [http://doi.org/10.1016/j.msec.2005.08.032].
[20] Rozporządzenie Ministra Zdrowia z dnia 16 lutego 2016 r. w sprawie szczegółowych wymagań dotyczących planowania, prowadzenia, monitorowania i dokumentowania badania klinicznego wyrobu medycznego (Dz. U. z 2016 r. poz. 209).
[21] Saini M.: Implant biomaterials: A comprehensive review. World Journal of Clinical Cases 3, 2015, 52–57 [http://doi.org/10.12998/wjcc.v3.i1.52].
[22] Scholten K., Meng E.: Materials for microfabricated implantable devices: a review. Lab on a Chip 15, 2015, 4256–4272 [http://doi.org/10.1039/C5LC00809C].
[23] Stolwijk J. A., Matrougui K., Renken C. W., Trebak M.: Impedance analysis of GPCR-mediated changes in endothelial barrier function: overview and fundamental considerations for stable and reproducible measurements. Pflügers Archiv - European Journal of Physiology 467, 2015, 2193–2218 [http://doi.org/10.1007/s00424-014-1674-0].
[24] Szulcek R., Bogaard H. J., van Nieuw Amerongen G. P.: Electric Cell-substrate Impedance Sensing for the Quantification of Endothelial Proliferation, Barrier Function, and Motility. Journal of Visualized Experiments 85, 2014, 1–12 [http://doi.org/10.3791/51300].
[25] Veiga C., Davim J. P., Loureiro A. J. R.: Properties and applications of titanium alloys. Reviews on Advanced Materials Science 32, 2012, 133–148.
[26] Voiculescu I., Li F., Nordin A. N.: Impedance Spectroscopy of Adherent Mammalian Cell Culture for Biochemical Applications: A Review. IEEE Sensors Journal 21, 2021, 5612–5627 [http://doi.org/10.1109/JSEN.2020.3041708].
[27] Walkowiak B.: Biomedyczne skutki kontaktu tkanki z implantem. Inżynieria Biomateriałów 7, 2004, 38–42.
[28] Wegener J., Keese C. R., Giaever I.: Electric cell-substrate impedance sensing (ECIS) as a noninvasive means to monitor the kinetics of cell spreading to artificial surfaces. Experimental Cell Research 259, 2000, 158–166 [http://doi.org/10.1006/excr.2000.4919].
[29] Wesolowski R. A., Wesolowski A. P., Petrova R. S.: Biomaterials. In: The World of Materials. Springer International Publishing, Cham 2020, 75–78 [http://doi.org/10.1007/978-3-030-17847-5_12].
[30] Williams D. F.: On the mechanisms of biocompatibility. Biomaterials 29, 2008, 2941–2953 [http://doi.org/10.1016/j.biomaterials.2008.04.023].
[31] Xiao C., Luong J. H. T.: On-line monitoring of cell growth and cytotoxicity using electric cell-substrate impedance sensing (ECIS). Biotechnology Progress 19, 2003, 1000–1005 [http://doi.org/10.1021/bp025733x].
[32] Xu Y., Xie X., Duan Y., Wang L., Cheng Z., Cheng J.: A review of impedance measurements of whole cells. Biosensors and Bioelectronics 77, 2016, 824–836 [http://doi.org/10.1016/j.bios.2015.10.027].
[33] Zarzeczny D.: Projekt i technologia kondensatorów grzebieniowych do monitorowania hodowli komórek. In: Problemy Współczesnej Inżynierii – Wybrane zagadnienia elektroniki i inżynierii biomedycznej. Politechnika Lubelska, Lublin, 2017, 155–168, [http://bc.pollub.pl/Content/13165/PDF/sneie.pdf] (available: 26.11.2021).
[34] Zarzeczny D. A.: Thin film capacitors made of various metals for impedance sensing technique. Proc. SPIE 11176, 2019, 1117654 [http://doi.org/10.1117/12.2536787].

M.Sc. Eng. Dawid Zarzeczny
e-mail: d.zarzeczny@pollub.pl

He graduated in Mechatronics at the Lublin University of Technology. Ph.D. student at the Lublin University of Technology. Since 2021, he has been employed as a didactic and research worker at the Lublin University of Technology. His research area focuses on microeletronics, semiconductor technology, plasma technology and biomedical engineering.

http://orcid.org/0000-0003-2029-9962

otrzymano/received: 19.11.2021 *przyjęto do druku/accepted: 15.12.2021*

http://doi.org/10.35784/iapgos.2855

ELLIPSOMETRY BASED SPECTROSCOPIC COMPLEX FOR RAPID ASSESSMENT OF THE $Bi_2Te_{3-x}Se_x$ THIN FILMS COMPOSITION

Vladimir Kovalev[1], Saygid Uvaysov[2], Marcin Bogucki[3]

[1]MOCVD Semiconductor Growth Laboratory, Kotelnikov Institute of Radio-Engineering and Electronics of RAS, Fryazino, Russia, [2]MIREA – Russian Technological University, Moscow, Russia, [3]Lublin University of Technology, Faculty of Mechanical Engineering, Lublin, Poland

Abstract. *A comparative analysis of the current state and development of spectral ellipsometry (SE) is carried out, the main limitations typical of popular configurations of measuring devices are determined. An original technical solution is proposed that allows one to create a two-source SE that implements the ellipsometry method with switching orthogonal polarization states. The measuring setup provides high precision of measurements of ellipsometric parameters Ψ and Δ in the spectral range of 270–2200 nm and the speed determined by the characteristics of pulsed sources with a simple ellipsometer design. As objects for experimental researches, confirming the efficiency and high precision qualities of the fabricated SE, we used a GaAs/ZnS-quarter-wave device for a CO_2 laser and SiO_2 on Si calibration plates. The optical properties of $Bi_2Te_{3-x}Se_x$ films were investigated in the range of 270–1000 nm using a multi-angle SE. It was shown that the optical properties of $Bi_2Te_{3-x}Se_x$ films monotonically change depending on the ratio of selenium and tellurium.*

Keywords: thin films, optical properties, spectroscopy, Fourier transform, ellipsometry and polarimetry, optics on surfaces, instrumentation, measurements and metrology

ELIPSOMETRYCZNY SYSTEM SPEKTROSKOPOWY DO SZYBKIEJ OCENY SKŁADU CIENKICH WARSTW $Bi_2Te_{3-X}Se_X$

Streszczenie. *W artykule najpierw dokonano analizy porównawczej obecnego stanu rozwoju elipsometrii spektroskopowej oraz określono główne ograniczenia typowe dla popularnych konfiguracji urządzeń pomiarowych. Zaproponowano oryginalne rozwiązanie techniczne pozwalające na stworzenie dwuźródłowego elipsometu spektroskopowego z przełączaniem ortogonalnych stanów polaryzacji. Układ pomiarowy zapewnia wysoką precyzję pomiarów parametrów elipsometrycznych Ψ i Δ w zakresie spektralnym 270–2200 nm i prędkości wyznaczonej przez charakterystyki źródeł impulsowych przy prostej konstrukcji elipsometru. Jako obiekty do badań eksperymentalnych potwierdzających wydajność i wysoką precyzję proponowanego elipsometu spektroskopowego, wykorzystano ćwierćfalowy przyrząd GaAs/ZnS dla lasera CO_2 oraz płytki kalibracyjne SiO_2 na krzemie. Właściwości optyczne warstw $Bi_2Te_{3-x}Se_x$ zbadano w zakresie 270–1000 nm przy użyciu wielokątowego elipsometu spektroskopowego. Wykazano, że właściwości optyczne cienkich warstw $Bi_2Te_{3-x}Se_x$ zmieniają się monotonicznie w zależności od stosunku zawartości selenu i telluru.*

Słowa kluczowe: cienkie warstwy, właściwości optyczne, spektroskopia, transformata Fouriera, elipsometria i polarymetria, optyka cienkowarstwowa, oprzyrządowanie, pomiary i metrologia

Introduction

Over the past years, the method of spectral ellipsometry (SE) has become well studied [10]. This method of analytical measurements is beginning to play an increasing role in various industrial and scientific industries [18]. SE finds application in such applications as the determination of the optical characteristics of thin films [22], in-situ monitoring of semiconductor thin films and their functionality [2, 7], as well as currently topical surface probing in biochemical reactions [16, 17]. In addition, ellipsometry provides exceptional measurement sensitivity, which makes it possible to use it for monitoring the epitaxial growth of thin films with submonolayer resolution [14, 20].

SE measures the changes in the polarization of light that occur when reflected from the surface of a sample depending on the wavelength of light to determine material properties such as complex dielectric function, carrier structure, crystalline nature, and thin film thickness [21]. This change can be described by the ellipsometric angles Ψ and Δ, which represent the amplitude and phase of the complex reflectance.

$$\rho = \frac{r_p}{r_s} = tg\Psi\, exp(i\Delta), \tag{1}$$

where the parameters r_p and r_s are the complex reflection coefficients for parallel and perpendicular polarizations of light, respectively. In a conventional SE the ellipsometric parameters are obtained from measurements of the optical intensity resulting from modulation of the polarization state of light interacting with the sample material.

The spectral regions of the SE cover the ultraviolet (UV), visible and infrared (IR) spectral ranges. Relevant problems in the development of new SE are expansion in the IR spectral range, increasing the accuracy and speed of measuring ellipsometric parameters, simplifying the design of the measuring path with the exclusion of moving polarizing optical elements [3]. Well-known firms solve complex problems of development and manufacture of such SE for various purposes with extremely high technical characteristics [9]. At the same time, the most widely represented on the commercial market are SE based on the use of rotating polarizing elements [4–6] and ellipsometers with phase modulation [1, 8, 19]. For these configurations of spectral ellipsometers, typical examples with distinctive features can be given.

The ellipsometer (RC2, JAWoollam Co. Inc.) with a double rotary compensator and Muller Matrix (MM) measurement [5] is the first commercial MM ellipsometer that uses the latest InGaAs thermoelectric cooled strained array to record hundreds of wavelengths in the IR range up to 2500 nm. The Sentech SE uses a method of discrete change in the azimuths of the polarizing elements. However, this mechanical modulation of polarization limits the stability in the presence of vibrations and the stability of such SE. An ellipsometer (UVISEL Plus, HORIBA) based on phase modulation technology covers a spectral range of 190–2100 nm. Very fast acquisition rate of up to 50 ms/point, ideal for real-time kinetic studies. But the wavelength range and temperature dependence of polarization modulation provided by such devices is a limiting factor. In addition, the fast polarization modulation produced by PEM or EOM (usually from several tens of kilohertz to several tens of megahertz) makes it difficult to use a multichannel spectrometer equipped with a CCD or CMOS camera.

To overcome these limitations, we propose a SE with switching orthogonal polarization states (SOPS), since it has a number of advantages and does not contain moving polarization elements. In publications [12, 13, 15] technical indicators of spectral ellipsometers with switching orthogonal polarization states for various purposes are given.

The use of a set of eight light-emitting diodes (LEDs) in a multichannel SE with binary modulation of the polarization state [12] made it possible to develop a simple ellipsometer with a full wavelength range of 350–810 nm and high characteristics. The obtained reproducibility and stability of measurements of ellipsometric parameters Ψ and Δ are 0.01 and 0.03°, respectively. An LED ellipsometer with an extended wavelength range of 260–1000 nm is described in [13]. The precision of measurements and the stability of the ellipsometric parameters Ψ and Δ for silicon with its own dioxide at the maximum wavelengths of LED radiation are not worse than 0.001 and 0.01°, respectively. At peak wavelengths corresponding to LEDs 365, 375, 390, 405, 420, and 465 nm, the precision of Ψ and Δ measurements of metal films is 0.0003 and 0.001°, respectively. The use of an original built-in monochromator provides a spectral resolution of 4 nm. LED magneto-optical SEs with SOPS [15] are the implementation of the deepest azimuthal modulation, the use of a two-channel detector, the use of a set of LEDs providing a high signal/noise ratio, and the absence of moving polarizing elements. These features significantly increased the accuracy of measuring the ellipsometric parameters Ψ and Δ of ferromagnetic materials and their changes (δΨ and δΔ) in a magnetic field. The results of measurements and calculations [11] are presented, confirming the possibility of creating stable reflective compensators for the spectral range of 200–2200 nm.

However, the use of miniature monochromators and optical shutters in the measuring paths of the above ellipsometers significantly limits their technical characteristics. The availability of commercially available automatic spectral complexes with a set of diffraction gratings for a wide spectral range (from 200 to 25000 nm) makes it possible to develop and create on their basis highly sensitive spectral ellipsometers with switching of orthogonal polarization states. This provides a high adjustable spectral resolution and a low level of scattered radiation.

This paper demonstrates the efficiency of using dual radiation sources and Glan–Thompson (GT) prisms with separation and convergence of orthogonally polarized beams, which made it possible to exclude a rather complex and intensity-weakening switch of orthogonal polarization states in the SE device. The peculiarity of the used prisms is the absence of changes in the geometry of the beams with the radiation wavelength, which makes it possible to use photodetectors with a small active area and high sensitivity. This implementation of SE measurements based on a slit monochromator opens up new ways and possibilities for future studies in the near IR spectral range. We used multi-angle spectroscopic ellipsometry (SE) to study the optical properties in the spectral range 260–1000 nm of $Bi_2Te_{3-x}Se_x$ films grown by the MOVPE method on sapphire substrates.

1. Material and methods

1.1. Experimental setup

The configuration of the developed spectral ellipsometer is shown in figure 1.

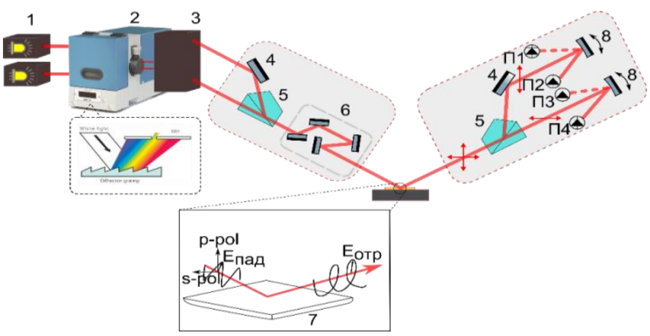

Fig. 1. TSSE optical configuration: 1 – broadband light source; 2 – monochromator; 3 – mirror system; 4 – silicon mirror; 5 – Glan-Thompson beamsplitting prism; 6 – reflective compensator; 7 – sample; 8 – rotary mirror; P1, P3 – InGaAs photodiodes; P2, P4 – silicon photodiodes

In the block of the radiation source, the halogen lamp 1 illuminates the entrance slit of the grating monochromator 2 (MDR-41, "OKB SPECTR" LLC). At the exit slit of the monochromator, there are two diaphragms 1 mm high and adjustable in width, separated by the slit height. A system of four flat and two spherical mirrors 3 (F = 65 mm) forms collimated radiation beams directed to two inputs of the GT 5 prism (calcite GBC08, Bluebean Optical Tech Ltd) with convergence of incident beams. Sequential interruption of the radiation beams from the diaphragms makes it possible to obtain collimated radiation beams with orthogonal azimuths of linear polarization P1 and P1 + 90° (P1 = 30°) at the output of the GT prism. Polarized radiation beams passing through a reflective compensator of four aluminum mirrors 6 successively fall on the sample 7 under study at an angle θ = 70°. The radiation beams reflected from the sample are divided by the second prism GT 5 into beams with orthogonal polarization azimuths A1 and A1 + 90° (A1 = 10°), which are focused by rotating mirrors 8 onto two pairs of photodetectors: P1, P3 – photodiodes InGaAs and P2, P4 – silicon photodiodes. The desired spectral dependences of the ellipsometric parameters Ψ and Δ are determined from the measured signal ratios on the photodetectors.

The method we propose can also be implemented on spectroscopic ellipsometers. In this case, the key issue is that the phase retardation of the compensator is wavelength dependent. Therefore, the optical implementation of the optimal measurement matrix must be adapted to the wavelength. On the other hand, we can also use achromatic compensators, which can provide almost the same phase delay over a wide spectral range, to implement our method for spectroscopic ellipsometers.

Compared to existing commercial ellipsometers, which use continuously rotating motors and spread the total integration time over a large number of data points, the distinct advantage of the proposed method is that it requires only four optimal intensity measurements, and the entire available integration time can be allocated to four points, which further reduces the effect of noise.

In this case, the most natural is configuration of a spectral ellipsometer with switching polarization P and P + 90° in the PSG unit using an original modulator of polarization states that does not have moving polarization elements. In this case, for the implemenatation of two more polarization states A and A + 90° in the PSA unit, a similar modulator of polarization states or a birefringent prism can be used, dividing the optical beam along the front into two orthogonal components.

Based on the proposed model of static ellipsometry with a limited number of degrees of polarization of the optical beam in the measuring path, it is possible to design a spectral ellipsometer with SOPS, which is devoid of the fundamental limitations described in the first chapter of the research, inherent in commercially available ellipsometers with rotating polarizing elements and photoelastic modulators.

Based on this scheme, we will write down an expression for the radiation intensity reaching the photodetector:

$$I_n = I_0(\sin^2 A_n \sin^2 P_n + \cos^2 A_n \cos^2 P_n \tan^2\Psi + \\ + \frac{1}{2}\sin 2A_n \sin 2P_n \cos\Delta \tan\Psi) \quad (2)$$

here P_n and A_n are the azimuths of the polarizer and analyzer; I_0 is an independent coefficient obtained during calibration.

Writing equation (2) for the case of four orthogonal azimuths of polarizing devices, we get:

$$\begin{aligned} I_1 &= h_a I_0(\sin^2 A \sin^2 P + \cos^2 A \cos^2 P \tan^2\Psi + \\ &+ \frac{1}{2}\sin 2A \sin 2P \cos\Delta \tan\Psi) \\ I_2 &= I_0(\cos^2 A \sin^2 P + \sin^2 A \cos^2 P \tan^2\Psi + \\ &- \frac{1}{2}\sin 2A \sin 2P \cos\Delta \tan\Psi) \\ I_3 &= h_a I_0(\sin^2 A \cos^2 P + \cos^2 A \sin^2 P \tan^2\Psi + \\ &- \frac{1}{2}\sin 2A \sin 2P \cos\Delta \tan\Psi) \\ I_4 &= I_0(\sin^2 A \cos^2 P + \sin^2 A \sin^2 P \tan^2\Psi + \\ &+ \frac{1}{2}\sin 2A \sin 2P \cos\Delta \tan\Psi) \end{aligned} \quad (3)$$

where h_a is the coefficient describing the ratio of the sensitivities of the two channels of the analyzer unit.

Accordingly, therefore we get the ellipsometric parameters:

$$\tan^2\Psi = \frac{(x_1 - b_1 b_2 x_2 + c)}{(b_1 b_2 x_1 - x_2 + c)} \quad (4)$$

$$\cos\Delta = \frac{b_1 x_3 - \sin^2 A \sin^2 P + (b_1 x_4 - \cos^2 A \cos^2 P)\tan^2\Psi}{\frac{1}{2}(b_1 + 1)\sin 2A \sin 2P \tan\Psi} \quad (5)$$

Here

$$c = b_2(\sin^2 A \sin^2 P - \cos^2 A \cos^2 P) + b_1(x_4 - x_3)$$
$$x_1 = \sin^2 A$$
$$x_2 = \cos^2 A$$

$$x_3 = \cos^2 A \sin^2 P$$
$$x_4 = \sin^2 A \cos^2 P \qquad (6)$$

At the same time, in order to calibrate the measuring channel, it is easy to implement a method with finding the azimuths of the analyzer, at equal intensities observed on the photodetectors.

$$\tan A_{1,2} = \tan\Psi \frac{(\sin 2P_2 - a \sin 2P_1)\cos\Delta}{(a \sin^2 P_1 - \sin^2 P_2)} + \tan\Psi \frac{[\cos^2\Delta(\sin 2P_2 - a\sin 2P_1)^2 - 4(a\sin^2 P_1 - \sin^2 P_2)(a\cos^2 P_1 - \cos^2 P_2)]^{1/2}}{2(a \sin^2 P_1 - \sin^2 P_2)} \qquad (7)$$

where a is the ratio of the intensities of the switched beams.

When calibrating the measuring path, the spectral dependences of h_a and the difference (A-P) are to be determined. According to expressions (3):

$$I_1 = I_0\, h_a \cos^2(A - P)$$
$$I_2 = I_0 \sin^2(A - P)$$
$$I_3 = I_0\, h_a \sin^2(A - P)$$
$$I_4 = I_0 \cos^2(A - P) \qquad (8)$$
$$h_a^2 = \frac{I_1 I_3}{I_2 I_4}$$
$$\tan^2(P - A) = \left(\frac{I_3 I_2}{I_1 I_4}\right)^{1/2}$$

Calibration of this SE is very simple and is carried out in two stages. At the first stage, the spectrum of the ratio of the channel sensitivities $h_a(\lambda)$, corresponding to the two polarizations after the analyzer and the difference between the angles of the polarizer and the analyzer P-A are measured in the position to the transmission. The formulas given in (8) for four combinations of polarizations for the position in the transmission are simplified:

$$R_1 = \frac{h_a}{tg^2(P-A)};\ R_2 = h_a tg^2(P - A) \qquad (9)$$

where R_1, R_2 are the intensity ratios on two photodetectors.

Therefore

$$h_a = (R_1 R_2)^{\frac{1}{2}};\ P - A = arctg\left(\left(\frac{R_2}{R_1}\right)^{\frac{1}{4}}\right) \qquad (10)$$

At the second stage, at an angle of incidence of 70° with a silicon sample and a known thin oxide, the ratios of the intensities of the beams R_1, R_2 are measured. By solving the inverse problem, the polarizer angle P, the angle of incidence of radiation on the sample, and the silicon oxide thickness are determined.

1.2. Near-IR 4 mirror achromatic compensator

The proposed compensator should have good transmission characteristics and smooth energy dependence in the range from 260–2000 nm. The restrictions on the total phase shift require in our case $0° < \Delta_r < 90°$ in the entire energy range. In this case, the coaxiality of the incoming and outgoing beams is required.

Based on this, we will design a compensator acting on the principle of phase shift caused by reflection from a metal mirror.

An optimal mirror material must meet the following requirements to function as a good reflective quarter-wave plate:

$$|r_s| = |r_p|;\ \Delta\varphi = |\varphi_s - \varphi_p| = 90° \qquad (11)$$

The material must also provide high reflectivity over the entire spectral range, these properties must be nearly constant over a relatively wide range of photon energies and incidence angles to avoid the critical issue of bandwidth and alignment.

Aluminum is a convenient mirror material in the energy range we use. Combined with its high reflectivity, aluminum is a good choice for our purposes.

In addition, it is necessary to find the correct geometry of the phase-shifting device (PD), because the phase difference Δ_r introduced by the compensator depends to a greater extent on the geometry.

Geometric phase analysis showed that a three-mirror PD is capable of rotating the polarization of the incoming beam through the angle $0 < \phi < \pi$. It has been proven that rotation of linear polarization through any angle requires at least four reflections for the final beam path to be collinear with the incoming beam.

Figure 2 shows a diagram of a four-mirror asymmetric PD, which is convenient for implementation.

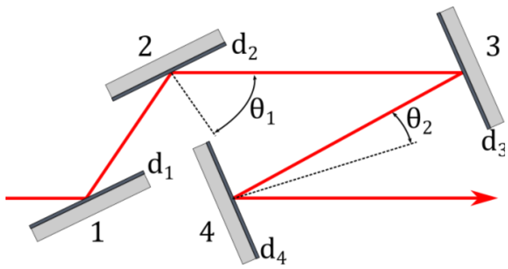

Fig. 2. Optical scheme of a four-mirror asymmetric compensator

The scheme uses four metal mirrors, in pairs (1-2, 3-4), installed at specified angles θ_1 and θ_2 to the incident beam.

The first pair of mirrors are positioned to ensure parallel beam propagation. The second pair of mirrors returns the direction of propagation of radiation to a given axis and are installed in the optical path at a small angle θ_2 to the incident beam to compensate for the sharp increase in Δ with increasing λ.

In this case, the total phase and amplitude displacement is introduced, the values of which can be calculated using the Fresnel reflection coefficients

$$r_p = \frac{n_1\cos\theta_0 - n_0\cos\theta_1}{n_1\cos\theta_0 + n_0\cos\theta_1};\ r_s = \frac{n_0\cos\theta_0 - n_1\cos\theta_t}{n_0\cos\theta_0 - n_1\cos\theta_t} \qquad (12)$$

Obviously, these values depend exclusively on the angle of incidence and the refractive indices of air and aluminum.

High-quality aluminum mirrors can be easily manufactured by sputtering Al onto a glass substrate, but it should be borne in mind that in air it is coated with a layer of Al_2O_3 several nanometers thick. This oxide layer slightly changes the optical properties of aluminum-coated mirrors.

Table 1 shows the angles of incidence on the mirrors and the generated phase shifts and amplitude changes.

Table 1. Dependence of the angles of incidence of the beam and the corresponding phase shifts and changes in amplitude

Mirror No	θ (°)	ψ (°)	Δ (°)
1	32.47	44.93	179.18
2	33.20	44.90	179.14
3	33.20	44.92	179.14
4	32.20	44.91	179.12

To verify the obtained models of prototypes of four-mirror achromatic PDs and to confirm the calculated values, experimental studies were carried out in the following configuration.

The polarization properties of the compensator were obtained in the mode of direct measurement on a spectral ellipsometer with SOPS in the range 260–1000 nm; data from literature sources were used to calculate the optical constants.

Figure 3a shows a good correspondence between the experimental and calculated data when determining the thickness of the Al_2O_3 oxide on Al.

Figure 3b shows the curves of the calculated spectral dependences corresponding to the models of a reflective compensator with a set of variable parameters from two angles of installation of the mirrors and four different thicknesses of aluminum oxide on the surface of the mirrors.

For certain sets of parameters, high quality achromatization has been achieved in a wide spectral range. Curve 1 corresponds to the FMC, in which all mirrors have their own oxide 5.5 nm thick. Blocks of parallel mirrors are inclined to the radiation beam at angles of 49° and 41°, respectively. In the short-wavelength region, a sharp change in Δ is observed, leading to an increase in the errors of ellipsometric measurements. Curve 2 corresponds to the case when the radiation beam is incident at an angle θ_1 = 49° onto a block of mirrors with oxide thicknesses $d_1 = d_2$ = 5.5 nm, and then at an angle θ_2 = 41° onto a block of mirrors with an oxide d_3 = 5.5 nm and d = 36 nm. A decline remains in the wavelength range of 200–250 nm. Curve 3 corresponds to a set of parameters:

$\theta_1 = 49°$, $\theta_2 = 41°$, $d_1 = 14$ nm, $d_2 = 21$ nm, $d_3 = 36$ nm, $d_4 = 70$ nm. Deviations from -90° do not exceed 4° in the spectral range 200–1000 nm. Curve 4 corresponds to a set of parameters: $\theta_1 = 45°$, $\theta_2 = 52°$, $d_1 = 36$ nm, $d_2 = 162$ nm, $d_3 = 36$ nm, $d_4 = 76$ nm. A fairly flat area is observed in the spectral range of 400–2000 nm.

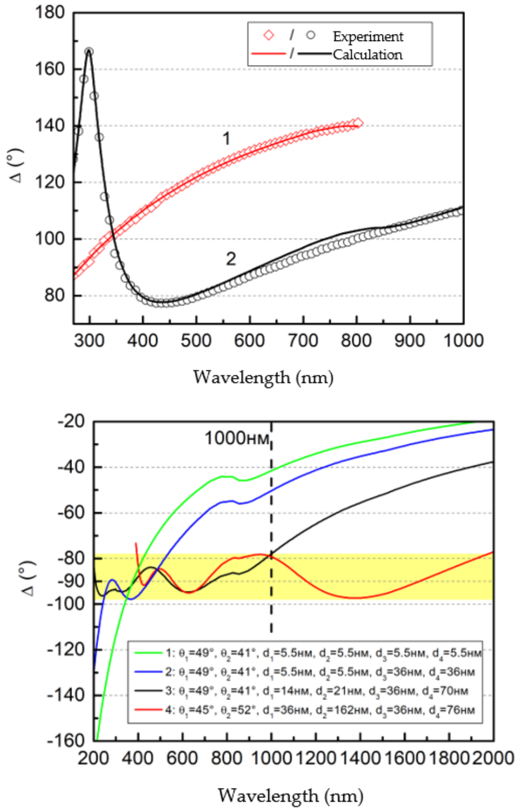

Fig. 3. Spectral dependences of the ellipsometric parameter Δ for: a) layers with a thickness d of Al_2O_3 on Al:1 – d = 5.5 nm; 2 – d = 36 nm, b) a four-mirror asymmetric compensator for different thicknesses d of Al_2O_3 layers on Al and angles of incidence θ_1 and θ_2 of radiation on the mirrors. Curve 1: $\theta_1 = 49°$, $\theta_2 = 41°$, $d_1 = 5.5$ nm, $d_2 = 5.5$ nm, $d_3 = 5.5$ nm, $d_4 = 5.5$ nm. Curve 2: $\theta_1 = 49°$, $\theta_2 = 41°$, $d_1 = 5.5$ nm, $d_2 = 5.5$ nm, $d_3 = 36$ nm, $d_4 = 36$ nm. Curve 3: $\theta_1 = 49°$, $\theta_2 = 41°$, $d_1 = 14$ nm, $d_2 = 21$ nm, $d_3 = 36$ nm, $d_4 = 70$ nm. Curve 4: $\theta_1 = 45°$, $\theta_2 = 52°$, $d_1 = 36$ nm, $d_2 = 162$ nm, $d_3 = 36$ nm, $d_4 = 76$ nm

1.3. Materials

As objects for experimental studies, confirming the efficiency and high accuracy of the fabricated SE, we used a GaAs/ZnS-quarter-wave device for a CO_2 laser and SiO_2 on Si calibration plates (StepWafer, Ocean Optics).

The standard sample, manufactured by Ocean Optics, is a silicon substrate (Si) coated with a thermal oxide layer (SiO_2). The disc has a diameter of 100 mm and 5 steps of oxide thickness on a calibration plate in the range from 0 to 500 nm. It is ideal for use as a standard sample when measuring the thickness of thin transparent layers on a variety of substrates. Each disc is supplied with a calibration certificate containing information on coordinates (x, y) and their corresponding values (ψ, Δ) and film thickness. The plates are calibrated using a verified ellipsometer and their measurement error, guaranteed by the manufacturer, does not exceed 0.1 nm.

In an experimental study, using the developed SE, the optical properties of $Bi_2Te_{3-x}Se_x$ thin films grown by chemical metalorganic vapor phase epitaxy method (MOVPE) on (0001) Al_2O_3 substrates were studied.

To set the research problem, the measured samples and their production process were fully described. In this case, the samples were examined by alternative methods to confirm the physical characteristics.

The films under study were grown at a temperature of 460°C under conditions of a multiple excess of chalcogenes in the gas phase, had a thickness of ~ 0.5 μm and a mirror surface. The epitaxial nature of the films and their crystal structure of tetradymite are confirmed by X-ray studies. The chemical composition of the films was determined on a Jeol JSM-6480LV scanning electron microscope with a built-in X-MaxN energy dispersive spectrometer.

The optical properties of the samples were investigated by spectral ellipsometry in the range 260–1000 nm. The SE data were compared with the results of electron probe studies, a calibration curve was obtained for the express determination by the SE method of the composition of $Bi_2Te_{3-x}Se_x$ thin films in the concentration range ($0 \le x \le 3$). Multi-angle measurements of the spectra of ellipsometric parameters significantly increase the reliability of measurements in the case of investigations of complex structures with initially unknown optical properties.

2. Results and discussions

2.1. SiO_2 on Si calibration plates

Figure 4 shows the measured and calculated ellipsometric parameters Ψ and Δ for Si/SiO_2 calibration plates with oxide thicknesses of 4 nm and 450 nm. Note that the significant smoothing of the peaks in the infrared region of the spectrum is caused by the imperfection of the rear surface of the plates.

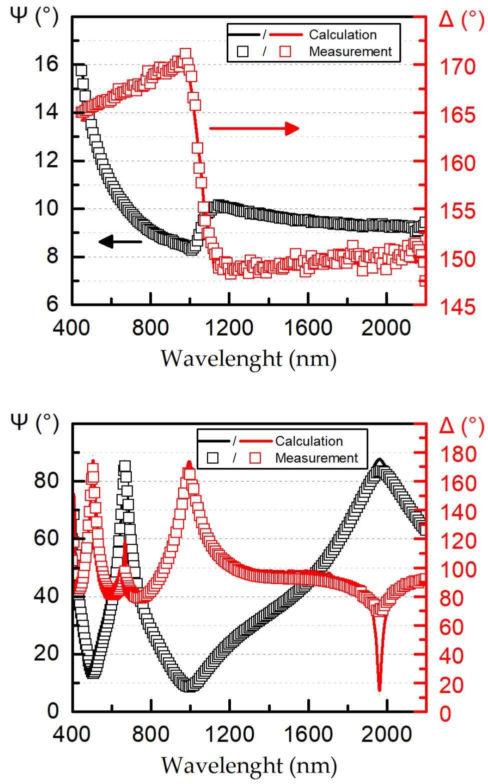

Fig. 4. Spectral dependences of ellipsometric parameters Ψ and Δ for Si/SiO_2: a) SiO_2 thickness 4 nm; b) SiO_2 450 nm thick

Figure 5 shows the dependences of Ψ and Δ on time (noise) for a Si/SiO_2 sample with an oxide thickness of 450 nm at a wavelength of 800 nm and an oxide thickness of 513 nm at a wavelength of 1800 nm. The measurement time for each point was 2 s. The root-mean-square noise at a wavelength of 800 nm and an oxide thickness of 450 nm was 0.0025° (for Ψ) and 0.016° (for Δ); at a wavelength of 1800 nm and an oxide thickness of 513 nm – 0.005° (for Ψ) and 0.03° (for Δ).

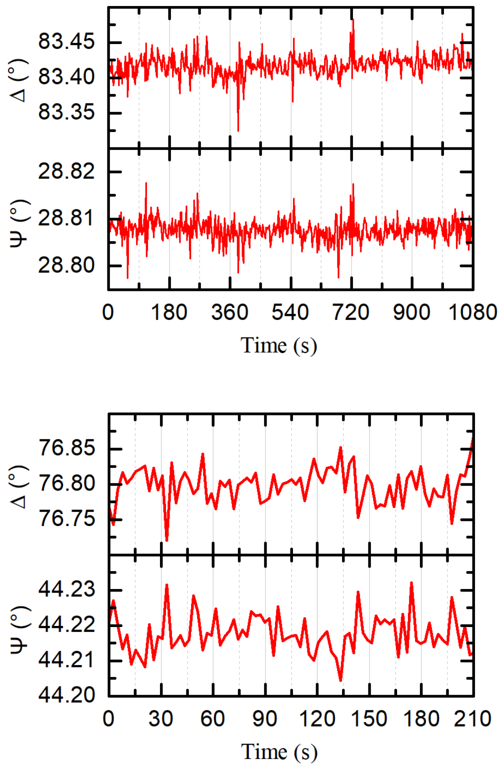

Fig. 5. Time dependences of the parameters Ψ and Δ of the Si/SiO$_2$ sample: a) with a SiO$_2$ thickness of 513 nm at a wavelength of 1800 nm; b) with a SiO$_2$ thickness of 45 nm at a wavelength of 1800 nm. Integration time 2 s

2.2. GaAs/ZnS structures

To calculate the parameters of the ZnS layer, we used the spectral dependence of the refractive index n according to the simplified Sellmeier formula:

$$n(\lambda)^2 = n_0{}^2 + 1/(1 - \frac{\lambda_0{}^2}{\lambda^2}) \tag{13}$$

where n_0 is the value of the refractive index at an infinite wavelength; λ_0 is the wavelength at which n is equal to infinity. To determine n_0, the calculated parameter n_m was used, which corresponds to the value of the refractive index at a wavelength of $\lambda_m = 550$ nm

$$n_m{}^2 = n_0{}^2 + 1/(1 - \frac{\lambda_0{}^2}{\lambda_m{}^2}) \tag{14}$$

The spectral dependence of the absorption coefficient k was approximated by an exponential dependence:

$$k(\lambda) = \mathrm{k_m} \exp((\lambda_m - \lambda)/\lambda_1) \tag{15}$$

where k_m is the value of the absorption coefficient k at a wavelength of $\lambda_m = 550$ nm, λ_1 is the wavelength interval at which k changes by a factor of e.

Figure 6 shows the measured Ψ and Δ spectra for a GaAs/ZnS sample in the 400–2200 nm wavelength range.

Since it is difficult to accurately describe the dispersion in a wide wavelength range with a simplified formula, it was divided into 2 regions: 400–600 nm and 600–2200 nm. In the second range, the ZnS layer thickness d = 1246.6 nm and the parameters $n_m = 2.3667$, $\lambda_0 = 336$ nm, $k_m = 0.001$, $\lambda_1 = 200$ nm were determined by the least squares deviation method. For the same thickness in the first range, the parameters $n_m = 2.3579$, $\lambda_0 = 297$ nm, $k_m = 0.001$, $\lambda_1 = 200$ nm are determined. Figure 7 shows the spectral dependences of the refractive and absorption indices n, k, obtained by the given formulas (13–15) with the indicated coefficients.

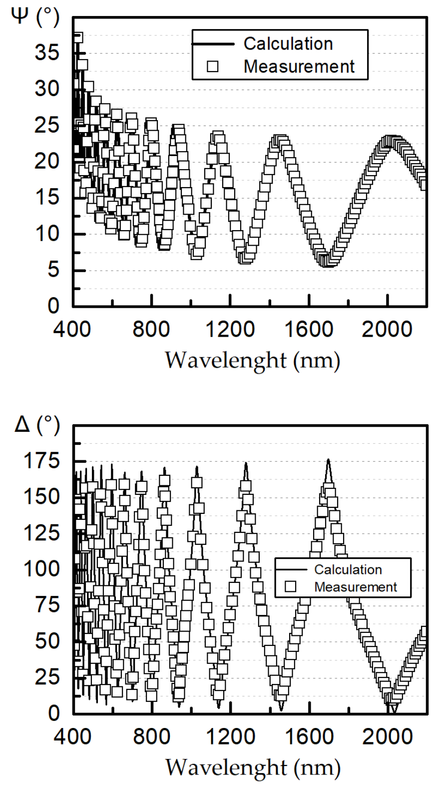

Fig. 6. Spectral dependence of Ψ and Δ for a ZnS film on a GaAs substrate polished on both sides

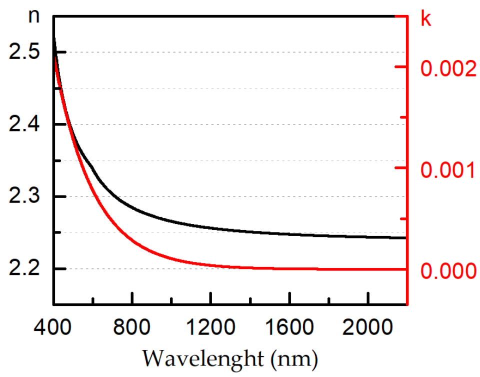

Fig. 7. Spectral dependence of the refractive index n and absorption coefficient k for a ZnS film on a GaAs substrate polished on both sides

2.3. $Bi_2Te_{3-x}Se_x$ topological insulator structures

Figure 8 shows the measured spectral dependence of the ellipsometric angles ψ and Δ of 490 nm thick Bi_2Se_3 and Bi_2Te_3 films deposited on sapphire substrates in the wavelength range 260–1000 nm at incidence angles of 60, 65, and 70°. At these thicknesses, $Bi_2Te_{3-x}Se_x$ films are completely opaque, which makes it possible to use a two-layer (film/surface layer) model to determine its optical properties from the SE spectra.

It was assumed that the surface layer above the films corresponds to the measured ellipsometric spectra. We found that the root-mean-square values of the roughness (rms) of AFM scans over an area of 10 × 10 μm^2 strongly depend on the film thickness. For example, the rms of a 30 nm film was several times higher than that of a 110 nm film. This is due to the transformation of growth modes (3D → 2D) in the process of increasing the film thickness. As a result, upon reaching a thickness of 500 nm, rms was 1–2 nm.

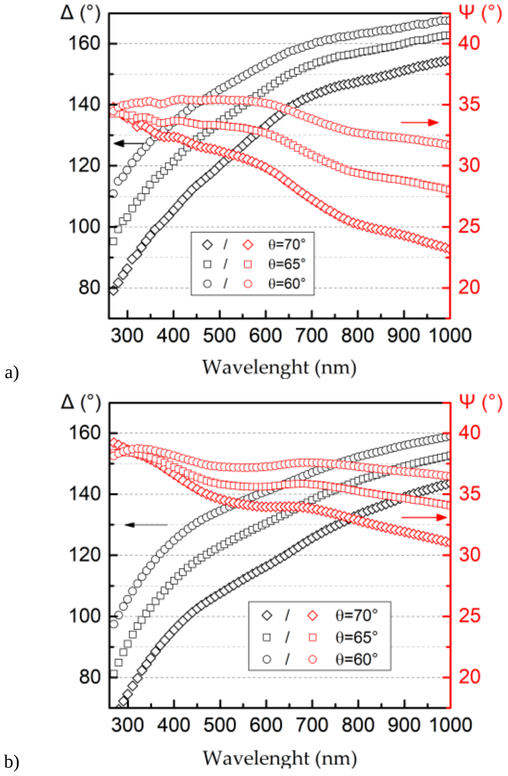

Fig. 8. SE spectra for $Bi_2Te_{3\text{-}x}Se_x$ films: a) x = 3; b) x = 0

AFM micrographs and their profiles for such samples show regular triangular terraces 0.95 nm in height, which correspond to a layered structure of the tetradymite type of $Bi_2Te_{3\text{-}x}Se_x$ films.

It is assumed that the surface (rough) layer is a mixture of 70% diamond and 30% voids. It was described using the Bruggeman effective medium approximation, which can be successfully used to simulate optical functions of surface roughness and interface layers. Modeling was performed using regression analysis and spectra of the real and imaginary parts of the permittivity were obtained for the entire set of $Bi_2Te_{3\text{-}x}Se_x$ films under study (16 samples). To clarify the correlation of some parameters, all spectra were fitted several times using different sets of initial parameters. Each time the fitting procedure gave the same result. The simulation results for five $Bi_2Te_{3\text{-}x}Se_x$ films with different x are shown in figure 9.

The strongest changes in the spectra of optical parameters of $Bi_2Te_{3\text{-}x}Se_x$ films depend on their composition x. Changes in the parameters are observed in the red and near-IR regions of the spectrum, and the short-wavelength part of the spectra is weakly sensitive to the composition of the films.

Figure 10 shows how the spectral position of the maximum of the imaginary ($\varepsilon 2$) parts of the dielectric function depends on their chemical composition of the studied $Bi_2Te_{3\text{-}x}Se_x$ films. It should be noted that this position is observed in the long-wavelength part of the spectra.

In a wide range of concentrations x, a monotonic change in the position of the maximum is observed depending on the composition of the films, which makes it possible to use the SE data to determine the composition of $Bi_2Te_{3\text{-}x}Se_x$ films. The value of the real ($\varepsilon 1$) parts of the dielectric function in the 800–900 nm range is also suitable for a quick assessment of the composition of $Bi_2Te_{3\text{-}x}Se_x$ films using SE measurements (figure 9a).

Published data on the Bi_2Te_3-Bi_2Se_3 system are contradictory. For example, some authors state that the $Bi_2Te_{3\text{-}x}Se_x$ compounds can be considered as a limited solid solution system with the Bi_2Te_2Se compound below the solidus line (500°C). Our XRD and SE data on monotonic changes in the lattice parameters and optical properties of $Bi_2Te_{3\text{-}x}Se_x$ films, depending on their composition, are consistent with the concept of the formation of a continuous series of solid solutions due to the gradual complete filling of selenium atoms into the inner rows in five-layer Te-Bi-Se blocks. (Te)-Bi-Te.

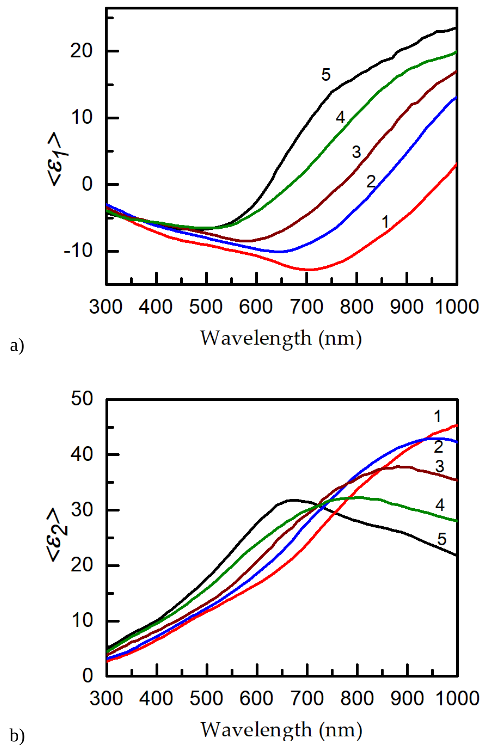

Fig. 9. Spectral dependence of the real ε_1 (a) and imaginary ε_2 (b) parts of the dielectric function for five $Bi_2Te_{3\text{-}x}Se_x$ films with x = 0, 0.25, 0.48, 1.5, 3.0 (curves 1 ÷ 5, respectively)

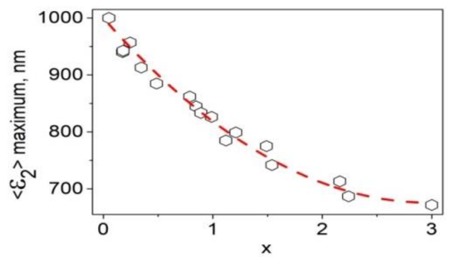

Fig. 10. Correlation between the position of the maxima in the ε_2 spectra of the $Bi_2Te_{3\text{-}x}Se_x$ researched films and their chemical composition

The good crystal structure and high quality of the surface of the films with a thickness of about 500 nm are confirmed by X-ray diffraction and atomic force microscopy. It is shown that multi-angle SE is a powerful method for studying the optical properties of $Bi_2Te_{3\text{-}x}Se_x$ films. There is no expected inflection in the dependence of the optical properties of the researched films on the composition, especially near x = 1, at which selenium atoms completely occupy the inner rows in the five-layer Te-Bi-Se (Te)-Bi -blocks.

The study shows the possibility of joint use of the proposed ellipsometric setup in the system with other analytical methods and means for monitoring the optical and physical properties when obtaining structures based on $Bi_2Te_{3\text{-}x}Se_x$. There are ample opportunities for studying the topological properties and applications of devices based on these compositions.

2.4. Compensator

The phase shift spectra of the FMC, in which two mirrors have an oxide 5.5 nm thick and two mirrors are 36 nm thick are shown in Figure 11. It should be noted that the phase shift deviations of the FMC, from 90° significantly decrease in the measured spectral range from 270 to 800 nm compared with the calculated spectral dependence of the phase shift for the case when all mirrors have only their own oxide.

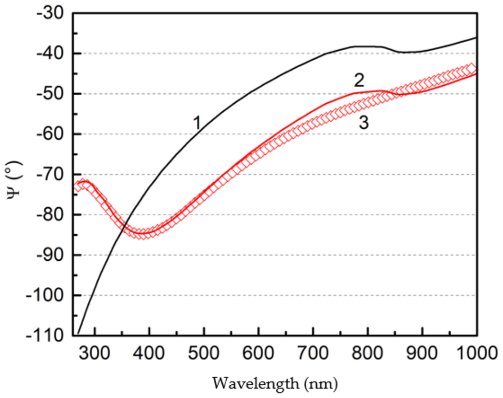

Fig. 11. Spectral dependences of the phase shift of a four-mirror asymmetric compensator with incidence angles of 51° and 30°: 1 – Calculation for the case when 4 mirrors have their own oxide 5.5 nm thick. 2 – two mirrors with their own oxide (51°) and two with an oxide thickness of 36 nm (30°), 3 – measured values

Figure 12 illustrates the possibilities of accurate and unambiguous determination of the spectra of the ellipsometric parameter Δ of the reference sample of thick SiO_2 oxide on Si in the automatic mode of sequential measurements with and without a FMC at each wavelength.

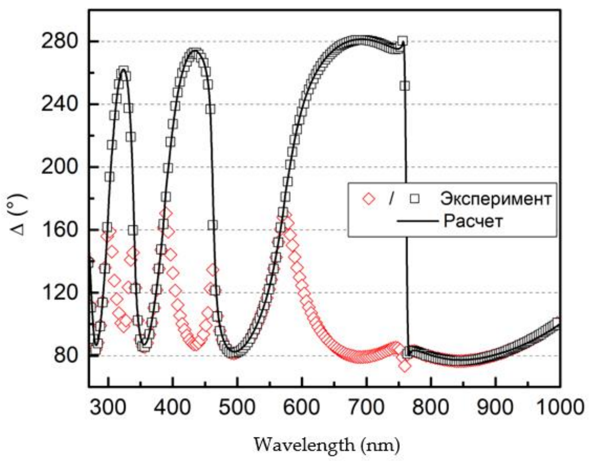

Fig. 12. Spectra of the ellipsometric parameter Δ of the reference sample of SiO_2 oxide with a thickness of 513 nm on Si: 1 – measurements with a compensator; 2 – measurements without compensator (oints – measurements, line – calculation)

The time dependences of the phase shift Δ FMC shown in figure 13, measured at wavelengths of 288 nm and 550 nm, confirm high reproducibility (up to 0.001°) and long-term stability of the compensator under standard laboratory conditions. When measuring the compensator as a sample, Δ is determined in the range of 0–180°.

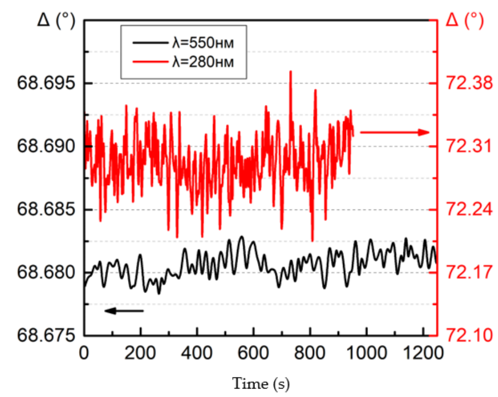

Fig. 13. Time dependences of the phase shift of the. FMC

The results of measurements and calculations confirm the possibility of creating achromatic four-mirror compensators in the spectral range of 200–2000 nm, which is widely used by modern spectral ellipsometers.

The time dependences of the phase shift Δ of the FMC, measured at wavelengths of 288 nm and 550 nm, confirm the high reproducibility and stability of measurements on the LED ellipsometer and the stability of the compensator itself under standard laboratory conditions.

It is planned to manufacture a compensator for the spectral range of 260–1000 nm, the calculated characteristics of which correspond to curve 3 in Figure 3b. It should be noted the low cost of the proposed FMC, the high ratio of the aperture to the length of the compensator, the possibility of precise adjustment of the angles of inclination of the mirrors using a goniometer and autocollimator, as well as the elimination of the need for thermostating of the compensator.

It has been shown experimentally that the use of the proposed simple design of the SE based on the MDR-41 monochromator makes it possible to achieve high technical characteristics. Optimization of the illumination scheme of the entrance slit of the monochromator and the use of GT prisms with a larger aperture will significantly improve the technical characteristics. The described approach provides ample opportunities for creating precision SE with an extended spectral range. Thus, the implementation of a solar cell with an operating wavelength range of 400–5000 nm is possible with a device for aligning orthogonally polarized beams made of YVO4. In this case, it is optimal to use pulsed radiation sources and photodetectors developed for the spectral range of 2–5 microns.

The described ellipsometer using as emitters sets of pairs of identical intense LEDs located, for example, on a disk with a horizontal axis of rotation, does not require interruption of the beams behind the exit slit of the monochromator and provides high-speed ellipsometric measurements at selected wavelengths in the spectral range of 260–1700 nm. The speed of measurements at the wavelengths of LED radiation is completely determined by the time characteristics of switching on and off and their intensity.

The features of the dispersion dependences of the promising material α-BBO do not allow the fabrication of GT prisms with an operating range of 200–3500 nm. We have developed an achromatic device for converging two beams based on a Wollaston prism, at the output of which the combination of orthogonally polarized beams in this spectral range is implemented. Based on this device, it is planned to manufacture a SE with an operating range of 200–3500 nm. Devices for converging orthogonally polarized beams and their separation on the basis of doped silicon wafers installed at the Brewster angle and ZnSe (ZnS) dividing wafers extend the spectral range of SE to 12–18 µm.

3. Conclusions

The new approach developed in the article significantly expands the measuring capabilities of sensitive ellipsometers with switching orthogonal polarization states. The elimination of low-frequency polarization modulators reduces the loss of beam intensity, simplifies the design of the SE, and makes it possible to significantly increase the rate of ellipsometric measurements using high-speed pulsed radiation sources. At the selected wavelengths, it is possible to determine the spatial distribution of ellipsometric parameters over the area of the studied plates, quickly measure the change in the parameters of liquid and gaseous flows in time, and kinetic measurements in the pump/probe configuration. SE can be used to control growth processes. This research shows the possibility of joint use of the proposed ellipsometric setup in the system with other analytical methods and means for monitoring the optical and physical properties when obtaining structures based on $Bi_2Te_{3-x}Se_x$.

References

[1] Acher O., Bigan E., Drévillon B.: Improvements of phase-modulated ellipsometry. Rev. Sci. Instrum. 60, 1989 [http://doi.org/10.1063/1.1140580].

[2] Alonso M. I., Garriga M.: Optical properties of semiconductors. Springer International Publishing Vol. 212, 2018.

[3] Aspnes D. E.: Spectroscopic ellipsometry — Past, present, and future. Thin Solid Films 571, 2014, 334–344 [http://doi.org/10.1016/j.tsf.2014.03.056].

[4] Azzam R. M. A.: Photopolarimetric measurement of the Mueller matrix by Fourier analysis of a single detected signal. Opt. Lett. 2, 1978, [http://doi.org/10.1364/ol.2.000148].

[5] Collins R. W., Koh J.: Dual rotating-compensator multichannel ellipsometer: instrument design for real-time Mueller matrix spectroscopy of surfaces and films. Journal of the Optical Society of America A 16, 1999, 1997 [http://doi.org/10.1364/JOSAA.16.001997].

[6] Fujiwara H.: Spectroscopic Ellipsometry: Principles and Applications. John Wiley and Sons, 2007.

[7] Furchner A., Walder C., Zellmeier M., Rappich J., Hinrichs K.: Broadband infrared Mueller-matrix ellipsometry for studies of structured surfaces and thin films. Appl. Opt. 57, 2018, 7895 [http://doi.org/10.1364/AO.57.007895].

[8] Garcia-Caurel E., de Martino A., Drévillon B.: Spectroscopic Mueller polarimeter based on liquid crystal devices. Thin Solid Films 455–456, 2004, 120–123 [http://doi.org/10.1016/j.tsf.2003.12.056].

[9] Garcia-Caurel E., de Martino A., Gaston J.-P., Yan L.: Application of Spectroscopic Ellipsometry and Mueller Ellipsometry to Optical Characterization. Applied Spectroscopy 67, 2013, 1–21 [http://doi.org/10.1366/12-06883].

[10] Hinrichs K., Eichhorn K. J., Ertl G., Mills D. L., Lüth H.: Ellipsometry of Functional Organic Surfaces and Films. Springer Series in Surface Sciences Vol. 52, Berlin, Heidelberg, 2014.

[11] Kovalev V. I., Rukovishnikov A. I., Kovalev S. V., Kovalev V. V., Rossukanyi N. M.: An achromatic four-mirror compensator for spectral ellipsometers. Opt. Spectrosc. 123, 2017 [http://doi.org/10.1134/S0030400X1707013X].

[12] Kovalev V. I., Rukovishnikov A. I., Kovalev S. V., Kovalev V. V.: An LED multichannel spectral ellipsometer with binary modulation of the polarization state. Instruments and Experimental Techniques 57, 2014 [http://doi.org/10.1134/S002044121405008X].

[13] Kovalev V. I., Rukovishnikov A. I., Kovalev S. V., Kovalev V. V.: LED broadband spectral ellipsometer with switching of orthogonal polarization states. J. Opt. Technol. 2016, 83, 181 [http://doi.org/10.1364/JOT.83.000181.

[14] Kovalev V. V., Kuznetsov P. I., Yakushcheva G. G., Yapaskurt O. V., Kovalev V. I., Rukovishnikov A. I., Kovalev S. V.: MOVPE deposition and optical properties of thin films of a Bi2Te3-xSex topological insulator. J. Phys. Conf. Ser. 1199, 2019, 012038 [http://doi.org/10.1088/1742-6596/1199/1/012038].

[15] Kovalev, V.I., Rukovishnikov, A.I., Rossukanyi, N.M., Kovalev, S. V., Kovalev, V. V., Amelichev, V. V., Kostyuk, D. V., Vasil'ev, D. V., Orlov, E. P. LED magneto-optical ellipsometer with the switching of orthogonal polarization states. Instruments and Experimental Techniques 59, 2016, 707–711 [http://doi.org/10.1134/S0020441216040084].

[16] Kroning A., Furchner A., Aulich D., Bittrich E., Rauch S., Uhlmann P., Eichhorn K. J., Seeber M., Luzinov I., Kilbey S. M., et al.: In Situ Infrared Ellipsometry for Protein Adsorption Studies on Ultrathin Smart Polymer Brushes in Aqueous Environment. ACS Appl. Mater. Interfaces 7, 2015, 12430–12439 [http://doi.org/10.1021/am5075997].

[17] Li K., Wang S., Wang L., Yu H., Jing N., Xue R., Wang Z.: Fast and Sensitive Ellipsometry-Based Biosensing. Sensors 18, 2017, 15 [http://doi.org/10.3390/s18010015].

[18] Losurdo M., Bergmair M., Bruno G., Cattelan D., Cobet C., de Martino A., Fleischer K., Dohcevic-Mitrovic Z., Esser N., Galliet M., et al.: Spectroscopic ellipsometry and polarimetry for materials and systems analysis at the nanometer scale: State-of-the-art, potential, and perspectives. J. Nanoparticle 11, 2009, 1521–1554 [http://doi.org/10.1007/s11051-009-9662-6].

[19] de Martino A., Kim Y.-K., Garcia-Caurel E., Laude B., Drévillon B.: Optimized Mueller polarimeter with liquid crystals. Opt. Lett. 28, 2003, 616 [http://doi.org/10.1364/OL.28.000616].

[20] Schmidtling T., Pohl U. W., Richter W., Peters S.: In situ spectroscopic ellipsometry study of GaN nucleation layer growth and annealing on sapphire in metal-organic vapor-phase epitaxy. J. Appl. Phys. 98, 2005, [http://doi.org/10.1063/1.1999033].

[21] Tompkins H. G., Irene E. A.: Handbook of Ellipsometry. William Andrew Publishing, 2005.

[22] Yim C., O'Brien M., McEvoy N., Winters S., Mirza I., Lunney J. G., Duesberg G. S.: Investigation of the optical properties of MoS2 thin films using spectroscopic ellipsometry. Applied Physics Letters 104, 2014 [http://doi.org/10.1063/1.4868108].

Ph.D. Vladimir Kovalev
e-mail: vladimirkovalev.inc@gmail.com

Scientific researcher – Institute of Radio-Engineering and Electronics of Russian Academy of Sciences. Modern solutions of spectral ellipsometry, the development of new polarization elements and devices.

http://orcid.org/0000-0003-3570-393X

Prof. Saygid Uvaysov
e-mail: uvaysov@yandex.ru

Head of the Radio-Electronic Means Design and Production Department of the Radio Engineering and Telecommunications Systems Institute, MIREA – Russian Technological University.
Scopus Author ID: 55931417100
Researcher ID: H-6746-2015

http://orcid.org/0000-0003-1943-6819

Ph.D. Marcin Bogucki
e-mail: m.bogucki@pollub.pl

Assistant professor on Department of Automation, Faculty of Mechanical Engineering, Lublin University of Technology, Poland.

Research interests: design of experiments, empirical model building, automation, robotics;

http://orcid.org/0000-0001-5296-3827

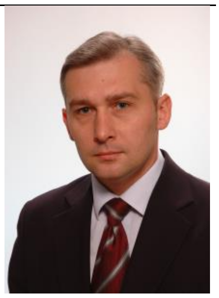

otrzymano/received: 20.11.2021 *przyjęto do druku/accepted: 15.12.2021*

http://doi.org/10.35784/iapgos.2853

APPLICATION OF LOW-COST PARTICULATE MATTER SENSORS FOR MEASUREMENT OF POLLUTANTS GENERATED DURING 3D PRINTING

Jarosław Tatarczak
Lublin University of Technology, Department of Automation and Metrology, Lublin, Poland

Abstract. *This work presents measurement results of pollutants generated during 3D printing. The measure of pollutants is the concentration of particulate matter with a diameter of up to 2.5 µm (PM2.5). Materials acrylonitrile-butadiene-styrene (ABS), polyactide (PLA) for a 3D printer and low-cost particulate matter concentration sensors PMS3003, PMS7003 were used in the research. Research results show that low-cost sensors can be useful for monitoring pollution during 3D printing in offices, laboratories or private homes.*

Keywords: 3D printing, particulate matter, pollution measurement, low-cost sensor

WYKORZYSTANIE NISKOBUDŻETOWYCH CZUJNIKÓW STĘŻENIA CZĄSTECZEK W CELU POMIARU ZANIECZYSZCZEŃ POWSTAJĄCYCH W TRAKCIE PRACY DRUKAREK 3D

Streszczenie. *Praca prezentuje wyniki pomiarów zanieczyszczeń generowanych podczas druku 3D. Miarą zanieczyszczeń jest koncentracja cząstek stałych materii o wymiarach do 2,5 µm (PM2,5). W badaniach zostały wykorzystane materiały aktonitryl-budatien-styren (ABS), poliaktyd (PLA) dla drukarki 3D i niskobudżetowe czujniki koncentracji cząstek stałych materii PMS3003, PMS7003. Wyniki badań pokazują, że niskobudżetowe czujniki mogą być przydatne do monitorowania zanieczyszczeń podczas druku 3D w biurach, laboratoriach czy domach.*

Słowa kluczowe: druk 3D, pyły zawieszone, pomiar zanieczyszczeń, czujniki niskobudżetowe

Introduction

Air quality has a significant impact on health and quality of life. A number of scientific publications describe the negative impact of high concentrations of pollutants on human health [3, 4, 10]. For example, in Poland in 2018, the main producer of particulate matter - PM2.5, were households using coal and wood for heating purposes. It accounted for 40.80% of the total cumulative PM2.5 (particles with a diameter of up to 2.5 µm) emission in Poland [9]. This is a significant problem in zones with dense single-family housing. It is possible to avoid exposure to particulate matter by using appropriate air filters in domestic ventilation systems. The study attempts to characterize a less obvious source of pollution – 3D printers. The popularity of 3D printers is constantly increasing. Such devices are successfully used in offices, laboratories or private homes. The most common materials used in desktop 3D printers are acrylonitrile-butadiene-styrene (ABS) and polyactide (PLA) [7, 8]. The melting point of plastic filament in fused filament fabrication (FFF) technology is in the range of 180ºC -270ºC and depends on the type of material [12].

The literature review presents various ways to measure pollutants during 3D printing. There are two main types of measurements: in an insulated chamber [5, 13, 14] and in standard operating conditions [11, 13]. Measurement in an insulated chamber involves placing the entire printer inside a sealed chamber. The printing process is started and the emission of pollutants is monitored. In the second method, the 3D printer works under typical conditions, i.e. in an open space inside the building room. The sensors are placed near the print head or at a distance from the 3D printer.

Currently, particulate matter concentration sensors [1, 2, 6] can be successfully applied at home. Some of them have a direct interface for monitoring the concentration of particulate matter. However, such sensors typically come at a higher cost.

The aim of the work is to investigate the usefulness of low-cost PM2.5 particulate matter concentration sensors for monitoring pollution during 3D printing in the conditions of an office, laboratory or private home.

1. Methods

The experiment was divided into two stages. In the first stage, pollutants generated during the uniform extrusion of the material were examined under special conditions (an insulated chamber). In the second stage, the measurements were made under typical operation conditions of the printer. In both stages, the print head placed in the Creality Ender 3 desktop printer was used. To measure the concentration of particulate matter, PMS3003 and PMS7003 sensors were applied, their basic parameters are presented in table 1.

Table 1. Basic parameters of the sensors used in the experiment

	PMS3003	PMS7003
Function in test	main measurment	background measurment
Price	89 PLN, 20 EUR	
Error	10% and ±10 µg/m³	
Resolution	1 µg/m³	
Counting efficiency	50% for 0.3 µg/m³ 98% for ≥ 0.5 µg/m³	
Communication	UART, baud rate 9600	
	24 byte frame	32 byte frame
Operating mode	passive or active, response time < 1s	
Software for data collection	e.g. LabVIEW	

The special conditions of experiment consisted in connecting the outlet of the print head nozzle with a tubular container with a diameter of 100 mm and a height of 125 mm. At the other end of the tubular container there is a tight shutter with a small hole to which the air inlet of the PMS3003 sensor is attached. In this way, all contaminants that could arise in the container would either have to settle on the wall of the container or would pass through the PMS3003 sensor, which is the main sensor. A second particulate matter concentration sensor – PMS7003 was placed outside the container for control purposes. Its task was to measure the background. The diagram of the first stage of the experiment is shown in figure 1A.

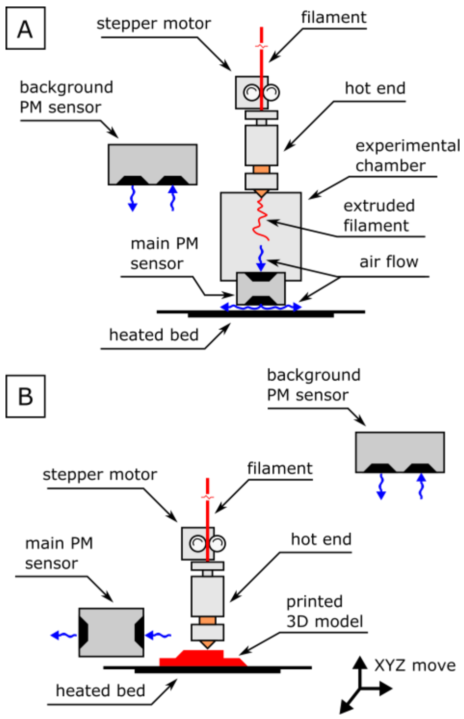

Fig. 1. Two stage of the experiment, measuring the concentration of particulate matter PM2.5, for the 3D printer: A – special working conditions, B – typical working conditions

After loading the material, the printer head was heated to the typical operating temperature of the material: PLA: 200ºC, ABS: 240ºC. Then, after stabilizing the temperature of the print head, the filament was extruded with the following lengths: 50 mm, 75 mm, 100 mm for ABS and 100 mm, 200 mm for PLA. After the airborne particulate matter concentration dropped to a level close to the background level as measured by PMS7003, repeated next extrusion. Five repetitions were performed for each material.

In the second stage, measurements were carried with the Creality Ender 3 printer with an open structure (without a housing) and the movement of the heated bed in the Y axis and the movement of the print head in the X axis. This is important from a measurement point of view because the print head is in motion and can therefore disperse airborne particulate. In addition, during the typical operation of the 3D printer, fans were used to lower the temperature of the print head cooling block and a fragment of the printed model (blowing of air on the print head nozzle). Therefore, the PMS3003 sensor is mounted in such a way that it is located at a constant, short distance from the print head. The diagram of the system during typical working conditions of the 3D printer is shown in figure 1B. At this stage measured particulate matter during the printing of a simple 3D model shown in figure 2. The total printing time was: 39 minutes. About 4 g of plastic were used (PLA: 1.41 m, ABS: 1.47 m of filament with a diameter of 1.75 mm). The concentration of PM2.5 particulate matter was measured for two types of materials: PLA and ABS, and for printing temperatures as in the first stage of the study. The heated working bed of the printer was set to the temperature 70ºC for ABS material and 50ºC for PLA. The measurements were carried out in a technical room with the dimensions 6.0 mm × 3.6 mm × 3.5 mm.

Fig. 2. Printed 3D model with dimensions: 6.0 mm × 3.6 mm × 3.5 mm. LUT – Lublin University of Technology

Data from PMS3003 and PMS7003 sensors were sent via UART connection directly to the PC station. The measurement results were recorded with an LabVIEW application, at an interval of 800 ms.

2. Results

On the basis of figure 3, it can be observed that with the increase in the amount of extruded material – ABS – the concentration of particulate matter in the air inside the chamber increases. For the test in which 100 mm of ABS material was extruded (which corresponds to a mass of 0.25 g), the maximum concentration of PM2.5 particulate matter above the measuring range (based on the datasheet) of the PMS3003 sensor can be observed. During the extruding of PLA material, it turned out that the main measurement is similar to the background measurement. The concentration of PM2.5 particulate matter in single trials did not show any significant increase, as it was noticeable when extruding ABS plastic. Due to the low PM2.5 particulate emission, shorter sections of the material were not extruded. In the case of extruding PLA with a length of 200 mm, the time between individual extruding commands was twice as long (10 minutes per cycle) as for extruding a 100 mm long section (5 minutes per cycle). The result is shown in figures 3.

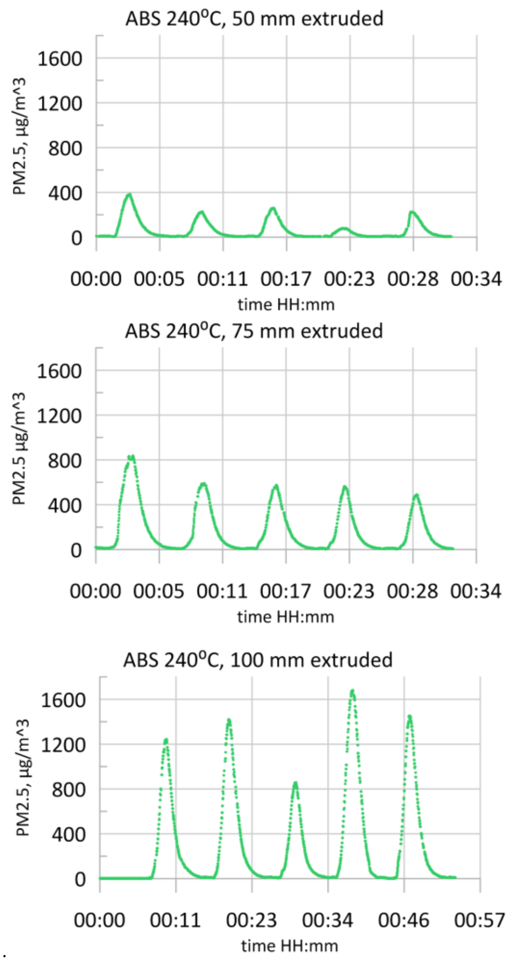

Fig. 3. Results for the special conditions (insulated chamber) in which the following lengths of ABS were extruded: 50 mm, 75 mm and 100 mm. The measurement background fluctuated in the range: (0-4) $\mu g/m^3$

Measurements of the concentration of PM2.5 under typical operating conditions of the 3D printer, for PLA and ABS, did not show any significant differences between the main measurement and the background measurement. In the case of printing with ABS, a peak was observed, it was related to the spraying of the preparation, which was to increase the level of adhesion of the heated working bed. This was required so that the printed 3D model did not detach from the surface during printing. In the case of PLA printing, the abovementioned preparation was not used. Figure 5 shows the measurement results of PM2.5 for the typical operation of the 3D printer.

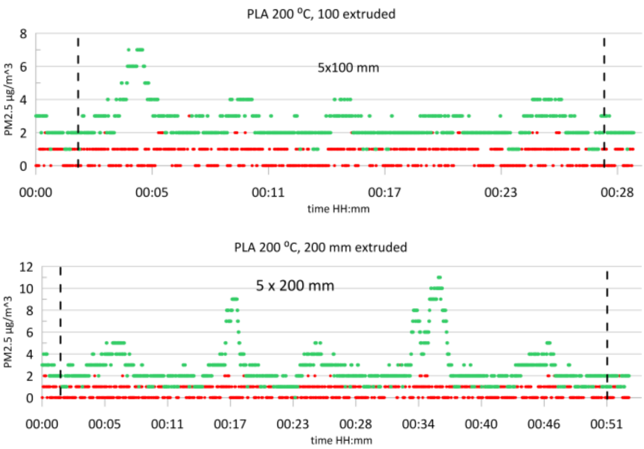

Fig. 4. Measurement results of PM2,5 concentration under special operating conditions (insulated chamber), for lengths of PLA material 100 mm and 200 mm. The results of the main measurement (PMS3003) are marked in green and background measurement (PMS700) in red

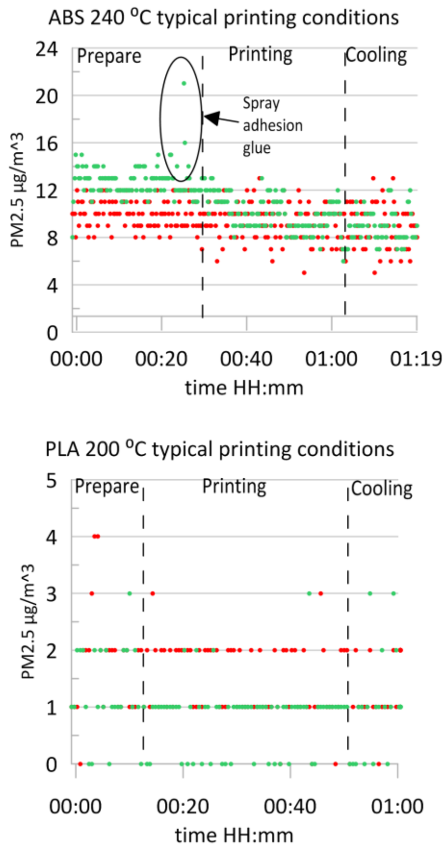

Fig. 5. Measurement results of particulate matter concentration during typical operation of the 3D printer, green colour – main measurement, red colour – background measurement

The statistics of data from measurements during printing with ABS and PLA plastics, for typical printer operating conditions are presented in table 2.

Table 2. Statistics of particulate matter concentration measurements for materials ABS and PLA (typical printer operating conditions)

Material	ABS		PLA	
Sensor role	Background	Main	Background	Main
Minimum	5.00 $\mu g/m^3$	7.00 $\mu g/m^3$	0.00 $\mu g/m^3$	0.00 $\mu g/m^3$
Maximum	14.00 $\mu g/m^3$	13.00 $\mu g/m^3$	3.00 $\mu g/m^3$	3.00 $\mu g/m^3$
Mean	9.48 $\mu g/m^3$	10.16 $\mu g/m^3$	0.90 $\mu g/m^3$	1.43 $\mu g/m^3$
Standard error	0.03 $\mu g/m^3$	0.03 $\mu g/m^3$	0.01 $\mu g/m^3$	0.01 $\mu g/m^3$

3. Conclusions

The measurements results show a significant difference in the level of the maximum concentration of PM2.5 particulate matter for ABS and PLA materials. In the case when a 100 mm long section was extruded at a uniform velocity, the average value of the five maximum values was 1329 $\mu g/m^3$ for ABS and 4.6 $\mu g/m^3$ for PLA. For ABS, the maximum concentration of particulate matter is almost 290 times higher than in the case of PLA extruding.

According to the data in table 2, under typical printer working conditions, the average value of the particulate matter concentration for ABS material is more than ten time higher compared to PLA material. It is worth mentioning, that the annual average limit value of particulate matter PM2.5 concentration should not exceed 25 $\mu g/m^3$[15].

The presented research confirm, in my opinion, the usefulness of low-cost sensors for monitoring pollution during 3D printing in offices, laboratories or private homes.

References

[1] Alfano B, Barretta L, Del Giudice A, De Vito S, Di Francia G, Esposito E, Formisano F, Massera E, Miglietta ML, Polichetti T.: A Review of Low-Cost Particulate Matter Sensors from the Developers' Perspectives. Sensors 20(23), 2020, 6819.

[2] Badura M., Batog P., Drzeniecka-Osiadacz A., Modzel P.: Optical particulate matter sensors in PM2.5 measurements in atmospheric air. E3S Web of Conferences 44, 2018, 00006.

[3] Crinnion W.: Particulate Matter Is a Surprisingly Common Contributor to Disease. Integrative Medicine 16(4), 2017, 8–12.

[4] Du Y., Xu X., Chu M., Guo Y., Wang J.: Air particulate matter and cardiovascular disease: the epidemiological, biomedical and clinical evidence. Journal of Thoracic Disease 8(1), 2016, 8–19.

[5] Gu J., Wensing M., Uhde E., Salthammer T.: Characterization of particulate and gaseous pollutants emitted during operation of a desktop 3D printer. Environment International 123, 2019, 476–485.

[6] Jovašević-Stojanović M., Bartonova A., Topalović D., Lazović I., Pokrić B., Ristovski Z.: On the use of small and cheaper sensors and devices for indicative citizen-based monitoring of respirable particulate matter. Environmental Pollution 206, 2015, 696–704.

[7] Krishnanand, Soni S., Taufik M.: Design and assembly of fused filament fabrication (FFF) 3D printers. Materials Today: Proceedings 46(11), 2021, 5233–5241.

[8] Ngo T. D., Kashani A., Imbalzano G., Nguyen K. T. Q., Hui D.: Additive manufacturing (3D printing): A review of materials, methods, applications and challenges. Composites Part B: Engineering 143, 2018, 172–196.

[9] Poland National Centre for Emissions Management, Poland's Informative Inventory Report 2020, website: https://www.kobize.pl/uploads/materialy/materialy_do_pobrania/krajowa_inwentaryzacja_emisji/IIR_2018_POL.pdf (last access: April 2021).

[10] Raaschou-Nielsen O., Beelen R., Wang M., Hoek G., et al.: Particulate matter air pollution components and risk for lung cancer. Environment International 87, 2016, 66–73.

[11] Stephens B., Azimi P., Orch Z., Ramos T.: Ultrafine particle emissions from desktop 3D printers. Atmospheric Environment 79, 2013, 334–339.

[12] Trhlíková L., Zmeskal, O. Psencik P., Florian P.: Study of the thermal properties of filaments for 3D printing. AIP Conference Proceedings 1752, 2016, 040027.

[13] Yi J., LeBouf R. F., Duling M. G., Nurkiewicz T., Chen B. T., Schwegler-Berry D., Virji M. A., Stefaniak A. B.: Emission of particulate matter from a desktop three-dimensional (3D) printer. Journal of Toxicology and Environmental Health A 79(11), 2016, 453–465.

[14] Zhang Q., Wong J. P. S, Davis A. Y., Black M. S., Weber R. J.: Characterization of particle emissions from consumer fused deposition modeling 3D printers. Aerosol Science and Technology 51(11), 2017, 1275–1286.

[15] Obwieszczenie Ministra Klimatu i Środowiska z dnia 12 kwietnia 2021 r. w sprawie ogłoszenia jednolitego tekstu rozporządzenia Ministra Środowiska w sprawie poziomów niektórych substancji w powietrzu, Dziennik Ustaw Rzeczypospolitej Polskiej, Warszawa, dnia 5 maja 2021 r.

M.Sc. Jarosław Tatarczak
e-mail: j.tatarczak@pollub.pl

Research assistant in Department of Automation and Metrology, Lublin University of Technology. Research field: thermionic emission, renewable energy sources, energy conversion, and 3D printing.

http://orcid.org/0000-0002-3432-7787

otrzymano/received: 18.11.2021 *przyjęto do druku/accepted: 15.12.2021*

LIST OF REVIEWERS COOPERATING WITH THE JOURNAL IN 2021

LISTA RECENZENTÓW WSPÓŁPRACUJĄCYCH Z CZASOPISMEM W ROKU 2021

Prof.	Avrunin	Oleg	Kharkiv National University of Radio Electronics (Kharkiv, Ukraine)
Ph.D.	Babyuk	Natalya	Vinnytsia National Technical University (Vinnytsia, Ukraine)
Prof.	Drevetskiy	Volodymyr	National University of Water and Environmental Engineering (Rivne, Ukraine)
Prof.	Gromaszek	Konrad	Lublin University of Technology (Lublin, Poland)
Ph.D.	Holuk	Mariusz	State School of Higher Education Chelm (Chelm, Poland)
Ph.D.	Hrytsiuk	Yurii	Lutsk National Technical University (Lutsk, Ukraine)
Ph.D.	Iwaszenko	Sebastian	Central Mining Institute (Katowice, Poland)
Prof.	Junisbekov	Mukhtar	M. Kh. Dulaty Taraz State University (Taraz, Kazakhstan)
Ph.D.	Kalizhanova	Aliya	Institute of Information and Computational Technologies SR MES RK (Almaty, Kazakhstan), Al-Farabi Kazakh National University (Almaty, Kazakhstan)
Ph.D.	Kapczyński	Adrian	Silesian University of Technology (Gliwice, Poland)
Prof.	Kisała	Piotr	Lublin University of Technology (Lublin, Poland)
Prof.	Kotyra	Andrzej	Lublin University of Technology (Lublin, Poland)
Ph.D.	Kozieł	Grzegorz	Lublin University of Technology (Lublin, Poland)
Prof.	Kusznier	Jacek	Bialystok University of Technology (Bialystok, Poland)
Ph.D.	Ławicki	Tomasz	Lublin University of Technology (Lublin, Poland)
Prof.	Lytvynenko	Volodymyr	Kherson National Technical University (Kherson, Ukraine)
Prof.	Miaskowski	Arkadiusz	University of Life Sciences in Lublin (Lublin, Poland)
Ph.D.	Michałowska	Joanna	State School of Higher Education Chelm (Chelm, Poland)
Ph.D.	Momot	Alina	Silesian University of Technology (Gliwice, Poland)
Ph.D.	Naumchuk	Oleksandr	National University of Water and Environmental Engineering (Rivne, Ukraine)
Ph.D.	Omiotek	Zbigniew	Lublin University of Technology (Lublin, Poland)
Prof.	Pavlov	Sergey	Vinnytsia National Technical University (Vinnytsia, Ukraine)
Prof.	Pidchenko	Sergey	Khmelnytsky National University (Khmelnytsky, Ukraine)
Ph.D.	Polishchuk	Mykola	Lutsk National Technical University (Lutsk, Ukraine)
Prof.	Rudyk	Andrii	National University of Water and Environmental Engineering (Rivne, Ukraine)
Ph.D.	Samila	Andriy	Yuriy Fedkovych Chernivtsi National University (Chernivtsi, Ukraine)
Prof.	Sikora	Jan	Research & Development Centre Netrix SA (Lublin, Poland)
Prof.	Simiński	Krzysztof	Silesian University of Technology (Gliwice, Poland)
Ph.D.	Smailova	Saule	D. Serikbayev East Kazakhstan State Technical University (Ust-Kamenogorsk, Kazakhstan)
Prof.	Smolarz	Andrzej	Lublin University of Technology (Lublin, Poland)
Prof.	Sochacki	Mariusz	Warsaw University of Technology (Warsaw, Poland)
Ph.D.	Stelmakh	Nataliia	National Technical University of Ukraine „Kyiv Polytechnic Institute" (Kyiv, Ukraine)
Ph.D.	Stepanchenko	Olga	National University of Water and Environmental Engineering (Rivne, Ukraine)
Ph.D.	Styński	Sebastian	Warsaw University of Technology (Warsaw, Poland)
Prof.	Sulemenov	Batyrbek	Kazakh National Research Technical University after K.I.Satpayev (Almaty, Kazakhstan)
Ph.D.	Sydorchuk	Bogdan	National University of Water and Environmental Engineering (Rivne, Ukraine)
Prof.	Szcześniak	Paweł	University of Zielona Góra (Zielona Góra, Poland)
Ph.D.	Tkachuk	Anatolii	Lutsk National Technical University (Lutsk, Ukraine)
Prof.	Uvaysov	Saygid	Moscow Technological University (Moscow, Russia)
Prof.	Wójcik	Waldemar	Lublin University of Technology (Lublin, Poland)
Ph.D.	Yesmakhanova	Laura	M. Kh. Dulaty Taraz State University (Taraz, Kazakhstan)
Prof.	Zabolotnii	Serhii	Cherkasy State Technological University (Cherkasy, Ukraine)
Ph.D.	Zagorodna	Natalia	Ternopil Ivan Puluj National Technical University (Ternopil, Ukraine)
Ph.D.	Żelazna	Agnieszka	Lublin University of Technology (Lublin, Poland)